ERCOFTAC Series

Mikhael Gorokhovski
Fabien S. Godeferd *Editors*

Turbulent Cascades II

Proceedings of the Euromech-ERCOFTAC Colloquium 589

Springer

ERCOFTAC Series

Volume 26

Series Editors

Bernard Geurts, Faculty of Mathematical Sciences, University of Twente, Enschede, The Netherlands
Maria Vittoria Salvetti, Dipartimento di Ingegneria Civile e Industriale, Pisa University, Pisa, Italy

Aims and Scope of the Series

ERCOFTAC (European Research Community on Flow, Turbulence and Combustion) was founded as an international association with scientific objectives in 1988. ERCOFTAC strongly promotes joint efforts of European research institutes and industries that are active in the field of flow, turbulence and combustion, in order to enhance the exchange of technical and scientific information on fundamental and applied research and design. Each year, ERCOFTAC organizes several meetings in the form of workshops, conferences and summerschools, where ERCOFTAC members and other researchers meet and exchange information.

The ERCOFTAC Series will publish the proceedings of ERCOFTAC meetings, which cover all aspects of fluid mechanics. The series will comprise proceedings of conferences and workshops, and of textbooks presenting the material taught at summerschools.

The series covers the entire domain of fluid mechanics, which includes physical modelling, computational fluid dynamics including grid generation and turbulence modelling, measuring-techniques, flow visualization as applied to industrial flows, aerodynamics, combustion, geophysical and environmental flows, hydraulics, multiphase flows, non-Newtonian flows, astrophysical flows, laminar, turbulent and transitional flows.

More information about this series at http://www.springer.com/series/5934

Mikhael Gorokhovski · Fabien S. Godeferd
Editors

Turbulent Cascades II

Proceedings of the Euromech-ERCOFTAC Colloquium 589

Springer

Editors
Mikhael Gorokhovski
Laboratoire de Mécanique des Fluides et d'Acoustique CNRS
Université de Lyon, École centrale de Lyon
Écully, France

Fabien S. Godeferd
Laboratoire de Mécanique des Fluides et d'Acoustique CNRS
Université de Lyon, École centrale de Lyon
Écully, France

ISSN 1382-4309 ISSN 2215-1826 (electronic)
ERCOFTAC Series
ISBN 978-3-030-12546-2 ISBN 978-3-030-12547-9 (eBook)
https://doi.org/10.1007/978-3-030-12547-9

Library of Congress Control Number: 2019930367

This Springer imprint is published by the registered company Springer Nature Switzerland AG.
The registered company address is: Gewerbestrasse 11, 6330 Cham, Switzerland

Organization

The Colloquium EC 589 was organized by the Laboratory of Fluid Mechanics and Acoustics (LMFA), which is a joint laboratory of CNRS, University of Lyon, École Centrale de Lyon (ECL), Université Claude Bernard Lyon I (UCBL), and Institut National des Sciences Appliquées de Lyon (INSA), under the auspices of Euromech and ERCOFTAC.

Executive Committee

Colloquium Chairs	Mikhael Gorokhovski (LMFA, ECL, FR)
	Bernard Geurts (University of Twente, NL)
	Joachim Peinke (University of Oldenburg, GE)
Organizing Chair	Fabien S. Godeferd (LMFA, CNRS, FR)

Organizing Committee

Colloquium Chair	Mikhael Gorokhovski (LMFA, ECL, FR)
	Wouter Bos (LMFA, CNRS, FR)
	Mikhael Bourgoin (LP-ENSL, CNRS, FR)
	Anne Cadiou (LMFA, CNRS, FR)
	Claude Cambon (LMFA, CNRS, FR)
	Alexandre Delache (LMFA, U. St-Étienne, FR)
	Fabien S. Godeferd (LMFA, CNRS, FR)
	Raffaele Marino (LMFA, CNRS, FR)
	Nicolas Mordant (LEGI, CNRS, FR)

Sponsoring Institutions

European Mechanics Society (Euromech), EU
European Research Community on Flow, Turbulence And Combustion (ERCOFTAC), EU
Office of Naval Research (ONR), USA
Laboratory of Fluid Mechanics and Acoustics (LMFA), FR
École Centrale de Lyon (ECL), FR
Laboratory of Physics, École Normale Supérieure de Lyon (LP-ENSL), FR
Laboratory of Geophysical and Industrial Flows (LEGI), FR
Engineering Federation of Lyon-Saint-Étienne (IngéLySE), FR
European Research Council (ERC), EU
National Research Agency (ANR), FR

Preface

This book contains papers presented at the Euromech-ERCOFTAC Colloquium "Turbulent Cascades II," held on December 5–7, 2017, at LMFA laboratory in the Ecole Centrale, Lyon, France.

In 1941 in the framework of –5/3 power law, Kolmogorov and Obukhov (KO-41) formulated the Richardson idea of the energy cascade along with fragmentation of turbulent eddies. Considering the turbulence at very high Reynolds number, the main assumption in KO-41 is that statistical characteristics of turbulence on small scales are unaffected by the structure of large-scale turbulence; i.e., adopting the large time-varying energy flux, handed down from large scales, the high-frequency fluctuations on small scales attain quickly a universal statistically homogeneous state, referred to as equilibrium state. Thereby, the mean flux of transferred energy becomes in KO-41 the only dimensional parameter, supposed to be homogeneous, and in the condition of equilibrium, it is equal to the local mean viscous dissipation rate. The KO-41 cascade model has yielded different approaches to the closure problem of averaged Navier–Stokes equations, and consequently, the efficient solutions were found in many practical applications (the drag reduction for cars, trains, planes, ships, *etc.*, is an example). However, there are some difficulties in interpretation of turbulence in terms of KO-41. On the one hand, even from formal consideration of purely kinematic coupling constraints it turns out that small- and large-scale motions, i.e., local and non-local interactions, are statistically interdependent. The evidence of non-local interactions in the high Reynolds number turbulence is provided by direct numerical simulations and experiments. On smallest turbulent scales, these studies revealed the highly energetic, stable vortical filaments which may persist on large times and may interact directly with other structures. The intersection of such filaments may lead to the violent gradients of velocity giving rise to long-range correlations. In this situation, the assumption that mean viscous dissipation is the only one controlling parameter of turbulent characteristics appears to be questionable. On the other hand, the –5/3 law of KO-41 is always confirmed, and it is confirmed by most studies not only in a wide range of hydrodynamic flows, but also in astrophysics and biological systems. This raises the following question: Do we have another mechanism of the kinetic energy transfer between different length

scales which works differently from the KO-41 cascade picture and which nonetheless provides the celebrated –5/3 law? This question was addressed already in the first edition of the "Turbulent Cascades" colloquium, held in Lille in December 2015. Two years later in Lyon, we decided to continue our discussions. A part of this discussion can be found in this book. At the same time, the scope of our colloquium in Lyon was enlarged beyond the turbulent cascade in simplest flows; many discussions concerned the physics of turbulence in complex conditions. In this book, one can find papers on the turbulence modulation through the finite size of dispersed inertial particles or bubbles, as well as through wavy structures of the gas/liquid interface and its surface tension. Some papers are devoted to effects of compressibility, of shear, of body forces (Coriolis and Lorentz forces, buoyancy effects). After our colloquium in Lyon, the number of open questions about turbulence in complex conditions was not decreased but increased. So much the better. This motivates for the future work and for future meetings. Look below at the photograph of Basilica of Notre-Dame de Fourviere in Lyon. An absolutely stunning picture! Look at the stable boundary between horizontal streaks and large structures, and look at the vertical persisting small-scale structures. How is working such a whole machine of turbulence in the complex conditions?

There are people to whom the theme of turbulent cascade appears as a "literary genre" and who are rather skeptical to bring together scientists for the umpteenth time for discussions on turbulence and frames of KO-41. We believe that a majority of people think otherwise.

Picture courtesy of Philippe Bleicher

Écully, France

Mikhael Gorokhovski
Fabien S. Godeferd

Contents

Part I
Multi-scales Interactions and Non-stationary Cascades: Physics, Models and Tools

Infrared Dynamics and Decay of Helicity in Homogeneous Isotropic Turbulence

Antoine Briard and Thomas Gomez


Abstract The decay of helicity and its impact on kinetic energy is analyzed at very large Reynolds numbers in homogeneous isotropic turbulence lacking mirror symmetry, using the Eddy-Damped Quasi-Normal Markovian closure. A theoretical time decay exponent for helicity is derived and assessed numerically. In addition to the initial well-known slowing down of non-linear transfers, it is further shown that helicity slightly accelerates the decay of kinetic energy in Batchelor turbulence, because it decreases the k^4 back transfers, which is proved analytically using non-local expansions. Finally, unlike the kinetic energy spectrum in Batchelor turbulence, the permanence of large eddies is verified for the helical spectrum.

A. Briard (✉)
Sorbonne Universités, UPMC Univ Paris 06, CNRS, UMR 7190, d'Alembert, 75005 Paris, France
e-mail: antoine.briard92@gmail.com

T. Gomez
Université Lille Nord de France, 59000, Lille, France

M. Gorokhovski and F. S. Godeferd (eds.), *Turbulent Cascades II*,
ERCOFTAC Series 26, https://doi.org/10.1007/978-3-030-12547-9_1

1 Introduction

In three-dimensional homogeneous isotropic turbulence, the scalar product of the velocity and vorticity fields $\langle \boldsymbol{u}.\boldsymbol{\omega} \rangle$, called kinetic helicity, is an inviscid invariant of the Navier-Stokes equations [1]. As a consequence, numerous theoretical and numerical studies were dedicated to helicity [2–7]. Indeed, helicity is not sign-definite unlike kinetic energy, which makes notably the prediction of its cascade direction rather complex.

The presence of kinetic helicity can also be viewed as the simplest anisotropy in a homogeneous turbulent flow since it breaks only the invariance by mirror symmetry of the statistics. Therefore, it is of fundamental interest to predict the dynamics of $\langle \boldsymbol{u}.\boldsymbol{\omega} \rangle$. For this purpose, we consider freely decaying turbulence in which helicity is initially injected at large scales, and focus on the prediction of the asymptotic decay of helicity at large Reynolds numbers. This task is made possible by investigating precisely the large scales properties of a turbulent flow with non-zero helicity: indeed, by analogy, it is known that in the fully isotropic case large scales drive the decay of kinetic energy.

Note that helicity can be created in real (inhomogeneous) atmospheric turbulent flows because of solid boundary conditions for example, and could be responsible for the persistence of tornadoes [8]. In the simplified framework of homogeneous turbulence however, helicity cannot be created if zero initially. This is why for simplicity we choose to inject at $t = 0$ helicity at large scales along with kinetic energy according to $H(k, t = 0) = kE(k, t = 0)$, where H and E are respectively the kinetic helicity and energy spectra, which is the limit case of the realizability condition of Kraichnan [9]. This further allows us to perform analytical calculations in the infrared range of the kinetic spectra. Nonetheless, remark that this simplified configuration of homogeneous turbulence remains relevant: indeed, one could imagine that once created, positive and negatives helical modes are distributed so that $H(k, t = 0) \neq 0$ but $\int_0^\infty H(k)\mathrm{d}k = 0$, so that there is creation of mean helicity during the decay. In simulations not presented here, we have observed that a particular initial helical spectrum like this, or simply $H(k, t = 0) = kE(k, t = 0)$, yields the same asymptotic results at large Reynolds numbers.

In what follows, after briefly recalling the numerical method and the equations, spectral scalings are briefly addressed. Then, the decay of helicity is investigated, with the emphasis put on both the infrared dynamics of the spectra and the prediction of the kinetic energy and helicity decay laws at large Reynolds numbers.

2 Equations in Spectral Space and Modelling

The dynamics of helicity is investigated at large Reynolds numbers using an adapted Eddy-Damped Quasi-Normal Markovian (EDQNM) approximation, originally developed in [3]. In this framework, the evolution equations of the kinetic energy spectrum $E(k, t)$ and helical spectrum $H(k, t)$ read

$$\left(\frac{\partial}{\partial t}+2\nu k^2\right)E(k,t)=S_E(k,t),\quad \left(\frac{\partial}{\partial t}+2\nu k^2\right)H(k,t)=S_H(k,t),\qquad (1)$$

where S_E and S_H are the total spherically-averaged non-linear transfer terms for kinetic energy and helicity, whose explicit expressions within the EDQNM framework can be found in [10]. S_E can be decomposed into the classical isotropic contribution $S^{(\mathrm{iso})}$ plus the term reflecting the retro-action of helicity $S^{(\mathrm{hel})}$. The time evolution of $E(k,t)$ and $H(k,t)$ is obtained by solving the two previous equations using a third-order Runge Kutta scheme with implicit treatment of viscous terms. The wavenumber space is discretized using a logarithmic mesh $k_{i+1}=rk_i$, $r=10^{1/f}$, $f=17$ being the number of points per decade. This mesh extends from $k_{\min}=10^{-6}k_L$ to $k_{\max}=10k_\eta$, where $k_L=1/L$ is the integral wavenumber and $k_\eta=(\epsilon/\nu^3)^{1/4}$ is the Kolmogorov wavenumber. The initial Reynolds number based on the Taylor microscale is $Re_\lambda(0)\simeq 5.10^4$. Finally, the helical spectrum is initialized as $H(k,t=0)=kE(k,t=0)$, which is the maximal helicity condition according to the realizability condition [9], with $E(k,t=0)\sim k^\sigma\exp(-\sigma k^2/2)$, where σ is the infrared slope.

3 Spectral Scalings and Non-linear Transfers

The kinetic energy and helical spectra $E(k,t)$ and $H(k,t)$ are first presented in Fig. 1a for Saffman turbulence, and they both scale in $k^{-5/3}$ in the inertial range spanning four decades, from the integral wavenumber k_L to the dissipative Kolmogorov wavenumber k_η, in agreement with the direct numerical simulations of [5]. Such a $k^{-5/3}$ scaling is consistent with joint-cascades of kinetic energy and helicity

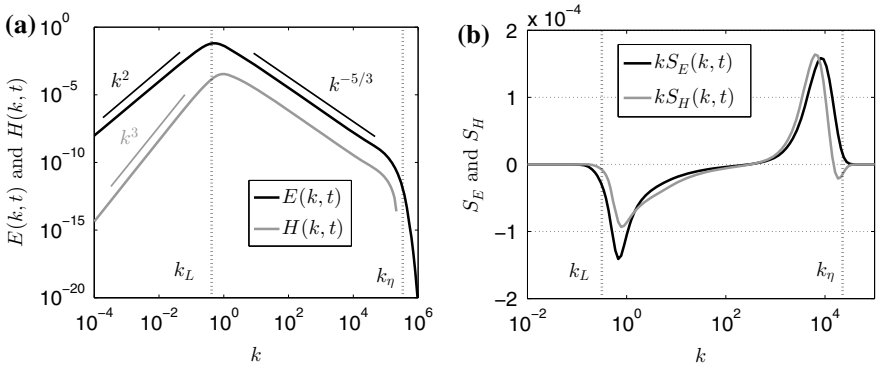

Fig. 1 Spectra and transfers for Saffman turbulence ($\sigma=2$), with the integral and Kolmogorov wavenumbers k_L and k_η: black for kinetic energy, and grey for helicity. **a** Kinetic and helical spectra E and H. **b** Total kinetic and helical non-linear transfers S_E and S_H

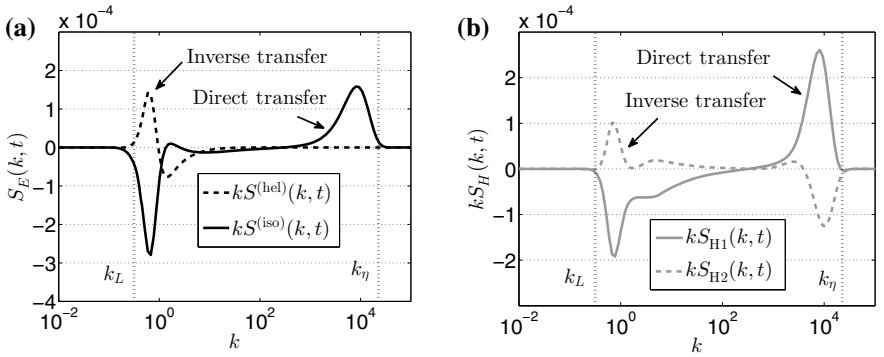

Fig. 2 Kinetic and helical non-linear transfers S_E and S_H, with the integral and Kolmogorov wavenumbers k_L and k_η: black for kinetic energy, and grey for helicity, $-$ for the direct transfer, and $--$ for the inverse one. **a** Parts $S^{(\mathrm{iso})}$ and $S^{(\mathrm{hel})}$ of S_E. **b** Parts S_{H1} and S_{H2} of S_H

[2], as further shown in Fig. 1b, where both S_E and S_H are direct transfers, negative at large scales, and positive at small scales.

Nevertheless, the fact that the cascades of kinetic energy and helicity are direct does not mean that there are no inverse transfers mechanisms. Indeed, both S_E and S_H contain subdominant inverse transfers as shown numerically in Fig. 2: for the non-linear kinetic energy transfer S_E, the usual isotropic part $S^{(\mathrm{iso})}$ is a direct transfer, from large to small scales, whereas the non-linear retro-action of helicity $S^{(\mathrm{hel})}$ is a localized large scales inverse transfer. For the non-linear helicity transfer S_H, it can be shown analytically that it is divided into two terms S_{H1} and S_{H2}, each with zero integral over the whole wavenumber space. More precisely, S_{H1} is a direct transfer like $S^{(\mathrm{iso})}$, and S_{H2} an inverse one, but unlike $S^{(\mathrm{hel})}$, it spans the entire inertial range.

4 Decay of Helicity

In this part, we aim at predicting the decay of helicity and its impact on kinetic energy. But first, it is of great importance to determine the large scales dynamics of homogeneous helical turbulence: indeed, it is known that large scales are crucial and drive the decay of the kinetic energy in the fully isotropic case [11].

4.1 Infrared Dynamics of $E(k,t)$ and $H(k,t)$

The emphasis is put here on the infrared dynamics of the kinetic energy and helical spectra, to determine if the *permanence of large eddies* (PLE) is verified in Batchelor turbulence, where at large scales $E \sim k^4$ and $H \sim k^5$ with the initial condition $H =$

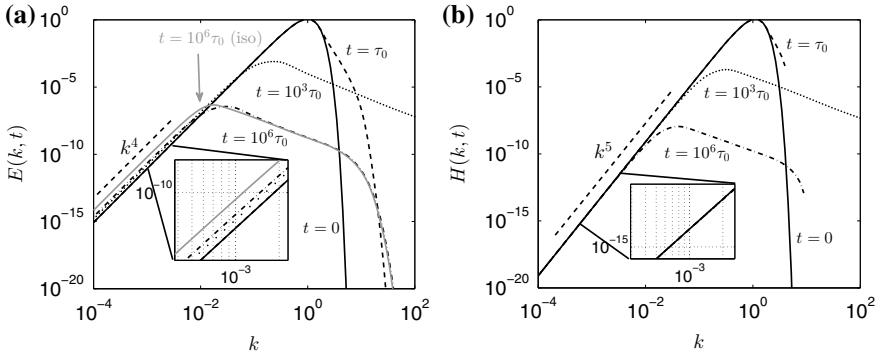

Fig. 3 Time evolution of the kinetic and helical spectra $E(k,t)$ and $H(k,t)$ in Batchelor turbulence ($\sigma = 4$), from $t = 0$ to $t = 10^6\tau_0$, where τ_0 is the characteristic eddy turnover time. **a** $E(k,t)$; grey curve for an isotropic simulation without helicity, plotted at $t = 10^6\tau_0$ and the same Re_λ as the helical simulation. **b** $H(k,t)$

kE. This is of great importance to further predict the asymptotic decay of kinetic energy and helicity.

For a spectrum, scaling in the infrared range like $E(k,t) \sim B(t)k^\sigma$, the *permanence of large eddies* is said to be verified in decaying turbulence if both B and σ remain constant throughout the decay.

It is known in fully isotropic turbulence that the PLE is verified in Saffman turbulence, but not in Batchelor turbulence. For the latter, it is revealed in Fig. 3a that $E(k,t)$ still experiences strong backscatter of energy in the presence of helicity. On the contrary (still for Batchelor turbulence where $H \sim k^5$), the PLE is verified for $H(k,t)$ in Fig. 3b. Furthermore, it appears in Fig. 3a that helicity tends to reduce the backscatter of $E(k,t)$ compared to the fully isotropic case: indeed, the spectrum E in grey, corresponding to an isotropic simulation, has experienced more backscatter than with helicity at $t = 10^6\tau_0$ and the same Re_λ.

It is possible to prove this point analytically using non-local expansions, as already done in the fully isotropic case in [12]. The inverse non-local energy transfer acting in the infrared range is

$$T_-^{(\mathrm{iso})}(k) = \frac{14}{15}k^4 \int_{k_L}^{\infty} \theta_{0pp} \frac{E(p)^2}{p^2} \mathrm{d}p - \frac{2}{15}k^2 E(k) \int_{k_L}^{\infty} \theta_{0pp} \left(5E(p) + p\frac{\partial E}{\partial p}\right) \mathrm{d}p, \tag{2}$$

where θ_{kpq} is the characteristic time of the third-order correlations within the EDQNM framework [3, 10–12]. Such an expression was derived in [12]. The first rhs term is responsible for the backscatter of energy that breaks the PLE hypothesis. The second rhs term is classically written under the eddy-viscous form $-2\nu_t k^2 E$, and represents the damping of large scales by small-scale turbulence. To understand why back transfers on $E(k,t)$ are decreased by helicity, one has to expand $S^{(\mathrm{hel})}$ when $k \ll p \sim q$, which gives

$$T_-^{(\mathrm{hel})}(k) = \frac{2}{15}k^2 H(k) \int_{k_L}^{\infty} \frac{\theta_{0pp}}{p^2} \left(9H(p) - p\frac{\partial H}{\partial p}\right) \mathrm{d}p - \frac{14}{15}k^4 \int_{k_L}^{\infty} \theta_{0pp} \frac{H(p)^2}{p^4} \mathrm{d}p. \tag{3}$$

The second rhs term modifies the backscatter of energy whereas the first one can also be interpreted as a pseudo helical dissipation term in $-2\nu_t^H k^2 H$. Combining this expression with (2) reveals the impact of helicity on the total inverse non-local kinetic transfer $T_-^E = T_-^{(\mathrm{iso})} + T_-^{(\mathrm{hel})}$ in HHT

$$T_-^E(k) = \frac{14}{15}k^4 \int_{k_L}^{\infty} \theta_{0pp} \frac{E(p)^2}{p^2} \underbrace{\left(1 - \left(\frac{H(p)}{pE(p)}\right)^2\right)}_{\leq 1} \mathrm{d}p - 2k^2(\nu_t E(k) + \nu_t^H H(k)). \tag{4}$$

Because of the realizability condition $0 \leq |H|/kE \leq 1$, the parenthesis in the first rhs term is lower than unity, thus showing that the k^4 backscatter of $E(k,t)$ is decreased by helicity, with respect to fully isotropic turbulence. Similar calculations for the inverse non-local helical transfer T_-^H show that there is no term in k^4 in the expansion, thus proving that the PLE should hold for $H(k,t)$, as shown numerically in Fig. 3b.

4.2 Prediction of the Helicity Decay

The prediction of the decay of helicity is made possible by the determination, at large Reynolds numbers, of theoretical decay exponents: our method relies essentially on dimensional analysis. It is well-known that one effect of helicity is to slow-down non-linear transfers [3]: this is a transitory initial feature [4, 10], and the effect of helicity on the decay when the turbulence is fully developed is more subtle.

Effect of helicity on the energy decay: Simulations show that the decay exponent α of the kinetic energy K, where $K(t) \sim t^{\alpha}$, is not modified by helicity, except in the case of Batchelor turbulence ($\sigma = 4$), because of the reduction of the non-local inverse transfers analyzed in the previous section. Hence, one would expect the decay of $K(t)$ to be faster in Batchelor helical turbulence than in Batchelor isotropic turbulence: indeed, the non-local inverse transfers bring back less energy to the large scales, thus accelerating the decay. This is recovered in Fig. 4. To analytically take into account the breakdown of the PLE hypothesis, a backscatter parameter p is usually introduced for isotropic turbulence [12], which is $p(\sigma = 4) = 0.55$ and $p(\sigma \leq 3) = 0$. Here, in Batchelor helical turbulence, $K(t) \sim t^{-1.417}$ is obtained, which provides a new backscatter parameter $p_H = 0.14$. Consequently, only the backscatter parameter changes from p to p_H for the decay of kinetic energy from fully isotropic to helical turbulence

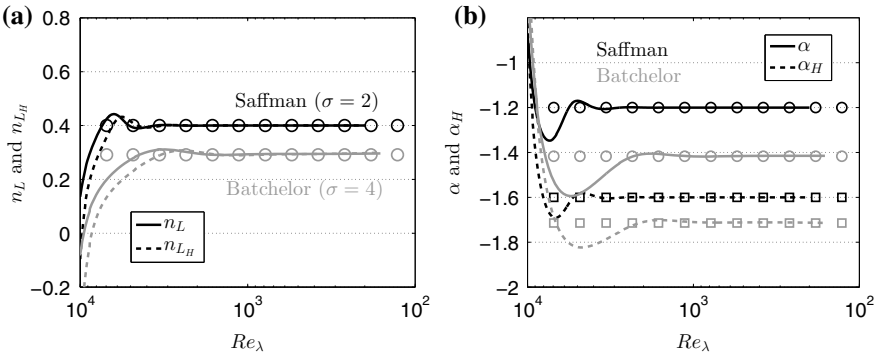

Fig. 4 Decay laws for the kinetic (−) and helical (−−) fields, in Saffman (black) and Batchelor (grey) turbulence. Symbols refer to the theoretical predictions given in (5) for α, (7) for α_H, and (6) for L and L_H. **a** Growth exponents of L and L_H. **b** Decay exponents of K and K_H, where ∘ and □ refer to the kinetic and helical theoretical predictions respectively

$$K(t) \sim t^{\alpha}, \qquad \alpha = -2\frac{\sigma - p_H + 1}{\sigma - p_H + 3}, \qquad \begin{cases} p_H(\sigma = 4) = 0.14 \\ p_H(\sigma \leq 3) = 0 \end{cases} . \tag{5}$$

These decay exponents for the kinetic energy are assessed in Fig. 4 for Saffman and Batchelor turbulence

The decay of helicity: The method to predict the decay of helicity K_H is similar to the one of an advected passive scalar, and even more simple. Indeed, as revealed in Fig. 3b, $H(k, t)$ experiences no strong back transfers, so that the PLE hypothesis is verified. Therefore, there is no need to introduce a backscatter parameter. It is recalled that given the present initial conditions, the spectral infrared slope of $H(k, t)$ is $\sigma + 1$. Then, it is reasonable to assume that the kinetic and helical integral scales $L(t)$ and $L_H(t)$ decay similarly, so that their algebraic exponents n_L and n_{L_H} are equal

$$L_{(H)}(t) \sim t^{n_{L_{(H)}}}, \qquad n_{L_H} = \frac{2}{\sigma + 3} \simeq n_L = \frac{2}{\sigma - p_H + 3}. \tag{6}$$

This assumption is completely assessed in Fig. 4. Then, using $K_H \sim K/L_H$ gives

$$K_H(t) \sim t^{\alpha_H}, \qquad \alpha_H = -2\frac{\sigma + 2}{\sigma + 3}. \tag{7}$$

Theoretical values of this expression for α_H are in excellent agreement with simulations presented in Fig. 4: one can remark that the more σ increases, the more K_H decays rapidly, similarly to the dynamics of $K(t)$.

5 Conclusion

Three features were addressed in the present work: the prediction of the asymptotic decay of helicity, its impact on kinetic energy at large Reynolds numbers, and the infrared dynamics of the kinetic energy and helical spectra E and H. First, it was shown using non-local expansions in the infrared range for Batchelor turbulence that helicity reduces the inverse transfers of kinetic energy, so that the backscatter of E is less intense than in the fully isotropic case. On the contrary, the helical spectrum H experiences no backscatter so that the permanence of large eddies is verified even in Batchelor turbulence.

Then, and consistently with the infrared dynamics analysis, it was shown that helicity slightly accelerates the decay of kinetic energy in Batchelor turbulence. Finally, a theoretical decay exponent has been proposed for helicity, based on dimensional analysis notably, and assessed numerically: in particular, helicity decays faster than kinetic energy for a given initial condition at large scales.

References

1. Moffatt, H.K.: The degree of knottedness of tangled vortex lines. J. Fluid Mech. **35**, 117–129 (1969)
2. Brissaud, A., Frisch, U., Leorat, J., Lesieur, M., Mazure, A.: Helicity cascades in fully developed isotropic turbulence. Phys. Fluids **16**(8), 1366–1367 (1973)
3. André, J.C., Lesieur, M.: Influence of helicity on the evolution of isotropic turbulence at high Reynolds number. J. Fluid Mech. **81**, 187–207 (1977)
4. Polifke, W., Shtilman, L.: The dynamics of helical decaying turbulence. Phys. Fluids A **1**(12), 2025–2033 (1989)
5. Chen, Q., Chen, S., Eyink, G.L.: The joint cascade of energy and helicity in three-dimensional turbulence. Phys. Fluids **15**(2), 361–374 (2003)
6. Biferale, L., Musacchio, S., Toschi, F.: Inverse energy cascade in three-dimensional isotropic turbulence. Phys. Rev. Lett. **108**, 164501 (2012)
7. Briard, A., Biferale, L., Gomez, T.: Closure theory for the split energy-helicity cascades in homogeneous isotropic homochiral turbulence. Phys. Rev. Fluids **2**, 102602 (2017)
8. Moffatt, H.K., Tsinober, A.: Helicity in laminar and turbulent flow. Annu. Rev. Fluid Mech. **24**, 281–312 (1992)
9. Kraichnan, R.H.: Helical turbulence and absolute equilibrium. J. Fluid Mech. **59**, 745–752 (1973)
10. Briard, A., Gomez, T.: Dynamics of helicity in homogeneous skew-isotropic turbulence. J. Fluid Mech. **821**, 539–581 (2017)
11. Meldi, M., Sagaut, P.: On non-self-similar regimes in homogeneous isotropic turbulence decay. J. Fluid Mech. **711**, 364–393 (2012)
12. Lesieur, M.: Turbulence in Fluids, 4th edn. Springer, Dordrecht (2008)

Dual Cascades in Axisymmetric Turbulence

Bo Qu, A. Naso and Wouter J. T. Bos



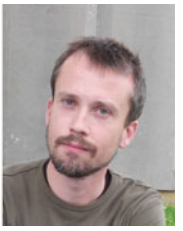

Abstract A spectral analysis of strictly axisymmetric turbulence is performed. We investigate in particular by direct numerical simulation the possible cascades of energy and helicity. Decaying and forced flows at moderate Reynolds numbers are considered. A dual cascade, in which energy is transferred to the large scales and helicity to the small ones, is first evidenced in helical flows. A similar scenario is then shown to hold in the absence of a net helicity: in this case, energy also cascades to the largest scales, and positively and negatively polarized helicity are transferred to the small ones.

1 Introduction

One of the key concepts in turbulence is the existence of cascades of the global inviscid invariants of the Navier-Stokes equations: energy and helicity in three-dimensional (3D) turbulence, energy and enstrophy in two-dimensional (2D) tur-

B. Qu · A. Naso · W. J. T. Bos (✉)
Laboratoire de Mécanique des Fluides et d'Acoustique, Univ Lyon, Ecole Centrale de Lyon, Univ Claude Bernard, CNRS, INSA de Lyon, 69134 Ecully, France
e-mail: wouter.bos@ec-lyon.fr

B. Qu
e-mail: bo.qu@doctorant.ec-lyon.fr

A. Naso
e-mail: aurore.naso@ec-lyon.fr

M. Gorokhovski and F. S. Godeferd (eds.), *Turbulent Cascades II*,
ERCOFTAC Series 26, https://doi.org/10.1007/978-3-030-12547-9_2

bulence. We focus here on turbulent cascades in strictly (that is, instantaneously) axisymmetric turbulence, a system intermediate between 2D and 3D. There has been recently a growing interest for this idealized system, essentially due to the fact that theories based on statistical mechanics can be transposed to it [1–4] and gave some results in qualitative agreement with those obtained in the (statistically axisymmetric) von Kármán flow [5–7].

We perform here a spectral analysis of axisymmetric turbulence and investigate possible cascades of the first quadratic invariants of the axisymmetric Euler equations, i.e., energy E and helicity H_1. For this, the axisymmetric Navier-Stokes equations are integrated by direct numerical simulation using a spectral method. Decaying and forced flows are both investigated.

The methodology is first described in Sect. 2. The results are then summarized in Sect. 3. The conclusions are finally given in Sect. 4.

2 Methodology

The system considered in the present investigation is described by the axisymmetric Navier-Stokes equations (the Navier-Stokes equations in cylindrical coordinates in which all the azimuthal derivatives ∂/∂_θ are set to zero). In the absence of viscosity and forcing, these equations conserve an infinite number of quantities, the so-called inviscid invariants. We will focus here on the quadratic invariants, i.e. kinetic energy $E^{tot} = \langle \mathbf{u}^2 \rangle/2$ and helicity $H^{tot} = \langle \mathbf{u} \cdot \boldsymbol{\omega} \rangle$, by analogy with two- and three-dimensional turbulence and since spectra measured experimentally in the (statistically axisymmetric) von Kármán flow were interpreted in terms of cascades of these quantities [8].

The axisymmetric Navier-Stokes equations are integrated in a cylindrical domain using a fully spectral method based on an expansion of the velocity field in a basis consisting of Chandrasekhar-Kendall eigenfunctions of the curl [9, 10]. No fast transform (similar to the fast Fourier transforms) is currently available for these modes, and the nonlinear term must therefore be calculated in spectral space. The results of our simulations will be therefore very accurate, but limited to moderate values of the Reynolds number. The flow is periodic in the axial direction and a non-penetration condition is imposed on the cylindrical boundary. A forcing term (naturally set to zero in the decaying simulations) based on the negative viscosity method widely used in 3D isotropic turbulence [11] allows to maintain a statistically stationary level of turbulence. Using this forcing scheme allows to control the injection of (zero or finite) net helicity in the flow. Both helical and nonhelical stationary regimes will be therefore considered thereafter.

More details on the numerical method can be found in [10, 12].

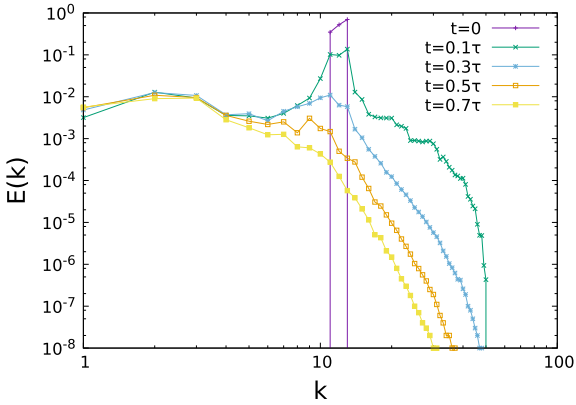

Fig. 1 Typical energy spectra, at different times, in the decaying case

3 Results

3.1 Decaying Turbulence

Decaying turbulence is first considered so as to guarantee that the results obtained are not spurious effects of the forcing scheme. As illustrated in Fig. 1, the energy spectrum unambiguously shows the existence in this system of both direct and inverse cascades. The same result was obtained for all the initial conditions considered (helical or nonhelical flows, vanishing or finite angular momentum, …).

3.2 Stationary Turbulence

Statistically steady flows are then investigated. The energy spectrum obtained at different times in a statistically stationary helical flow is shown in Fig. 2a. A dual cascade clearly develops, as in the decaying case. In the stationary regime, the spectrum displays a scaling compatible with $E(k) \sim k^{-5/3}$ for the inverse cascade and $E(k) \sim k^{-6}$ for the direct one. Such a dual cascade is also visible in the helicity spectrum (see Fig. 2b), which is furthermore found to satisfy the relation $H_1(k) \sim kE(k)$. The scaling $E(k) \sim k^{-5/3}$ obtained in the small wavenumbers range is compatible with an inverse energy cascade scenario.

The previously evidenced cascades are further characterized by measuring the time-averaged transfer rates of energy and helicity. These quantities show unambiguously that energy is preferentially transferred to the large scales of the flow and helicity to the small ones, thereby evidencing the existence of an *inverse energy cascade* and of a *direct helicity cascade*. The same scenario is compatible with energy spectra measured in the experimental von Kármán flow (only axisymmetric on average) [8].

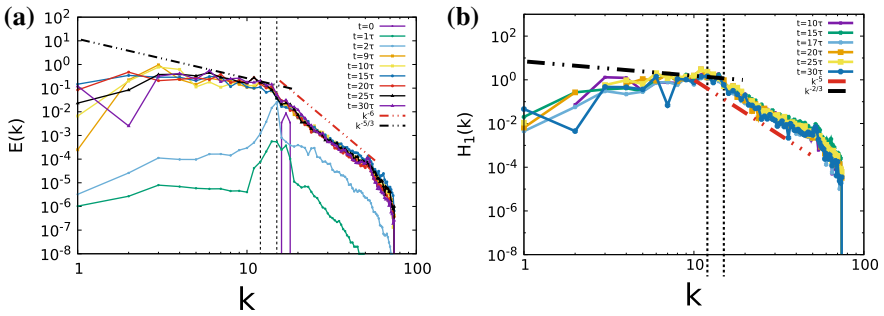

Fig. 2 **a** Energy and **b** helicity spectra, at different times in the forced helical case. The vertical dashed lines indicate the wavenumbers range in which the forcing is applied

Another interesting feature is the fact that in nonhelical steady flows, a dual cascade persists, which transfers energy to the large scales, and positively and negatively polarized helicity fluctuations towards the small ones.

These results are presented in more details in [12].

4 Conclusion

It is tempting to compare the spectral analysis of axisymmetric turbulence performed in the present paper to the well-known features of 3D and 2D isotropic turbulence. As in 3D, the (main) inviscid invariants of the axisymmetric system are energy and helicity. However, as in 2D the energy is transferred to the large scales of the axisymmetric flow, as part of a dual cascade in which helicity is transferred towards the small scales.

It would be interesting to carry out similar investigations at higher Reynolds numbers, which would be made possible by using other numerical methods. This would allow to characterize more precisely the inertial ranges and the associated scaling laws, in particular in the direct cascade regime (large wavenumber range).

Acknowledgements The authors would like to thank Shuojun Li for providing his code of 2D turbulence and Bérengère Dubrulle for suggesting them to carry out this investigation. BQ's PhD thesis was funded by a grant of the China Scholarship Council. This work benefited from the HPC resources of the PMCS2I.

References

1. Leprovost, N., Dubrulle, B., Chavanis, P.-H.: Dynamics and thermodynamics of axisymmetric flows: theory. Phys. Rev. E **73**(4), 046308 (2006)
2. Naso, A., Monchaux, R., Chavanis, P.-H., Dubrulle, B.: Statistical mechanics of Beltrami flows in axisymmetric geometry: theory reexamined. Phys. Rev. E **81**(6), 066318 (2010)

3. Naso, A., Thalabard, S., Collette, G., Chavanis, P.-H., Dubrulle, B.: Statistical mechanics of Beltrami flows in axisymmetric geometry: equilibria and bifurcations. J. Stat. Mech.: Theory Exp. **2010**(06), P06019 (2010)
4. Thalabard, S., Dubrulle, B., Bouchet, F.: Statistical mechanics of the 3D axisymmetric Euler equations in a Taylor-Couette geometry. J. Stat. Mech.: Theory Exp. **2014**(1), P01005 (2014)
5. Ravelet, F., Marié, L., Chiffaudel, A., Daviaud, F.: Multistability and memory effect in a highly turbulent flow: experimental evidence for a global bifurcation. Phys. Rev. Lett. **93**(16), 164501 (2004)
6. Monchaux, R., Ravelet, F., Dubrulle, B., Chiffaudel, A., Daviaud, F.: Properties of steady states in turbulent axisymmetric flows. Phys. Rev. Lett. **96**(12), 124502 (2006)
7. Thalabard, S., Saint-Michel, B., Herbert, E., Daviaud, F., Dubrulle, B.: A statistical mechanics framework for the large-scale structure of turbulent von Karman flows. New J. Phys. **17**, 063006 (2015)
8. Herbert, E., Daviaud, F., Dubrulle, B., Nazarenko, S., Naso, A.: Dual non-Kolmogorov cascades in a von Kármán flow. EPL (Europhys. Lett.) **100**(4), 44003 (2012)
9. Li, S., Montgomery, D., Jones, W.B.: Inverse cascades of angular momentum. J. Plasma Phys. **56**(03), 615–639 (1996)
10. Qu, B., Naso, A., Bos, W.J.T.: Cascades of energy and helicity in axisymmetric turbulence. Phys. Rev. Fluids **3**, 014607 (2018)
11. Kaneda, Y., Ishihara, T., Yokokawa, M., Itakura, K., Uno, A.: Energy dissipation rate and energy spectrum in high resolution direct numerical simulations of turbulence in a periodic box. Phys. Fluids **15**(2), L21 (2003)
12. Qu, B., Bos, W.J.T., Naso, A.: Direct numerical simulation of axisymmetric turbulence. Phys. Rev. Fluids **2**, 094608 (2017)

A Rigorous Entropy Law for the Turbulent Cascade

André Fuchs, Nico Reinke, Daniel Nickelsen and Joachim Peinke




Abstract There is a lack of high precision results for turbulence. Here we present a non-equilibrium thermodynamical approach to the turbulent cascade and show that the entropy generation ΔS_{tot} of the turbulent cascade fulfills in high precision the rigorous integral fluctuation theorem $\langle e^{-\Delta S_{tot}} \rangle_{u(\cdot)} = 1$. To achieve this result the turbulent cascade has to be taken as a stochastic process in scale, for which Markov property is given and for which an underlying Fokker-Planck equation in scale can be set up. For one exemplary data set we show that the integral fluctuation theorem is fulfilled with an accuracy better than 10^{-3}. Furthermore, we show that other basic turbulent features are well taking into account like the third order structure function or the skewness of the velocity increments.

A. Fuchs (✉) · N. Reinke · J. Peinke (✉)
Institute of Physics and ForWind, University of Oldenburg, Carl-von-Ossietzky-Str. 9-11, Oldenburg, Germany
e-mail: andre.fuchs@uni-oldenburg.de

N. Reinke
e-mail: nico.reinke@uni-oldenburg.de

J. Peinke
e-mail: joachim.peinke@uni-oldenburg.de

D. Nickelsen
Institute of Theoretical Physics, University of Stellenbosch, Stellenbosch, South Africa
e-mail: d.nickelsen@uni-oldenburg.de

M. Gorokhovski and F. S. Godeferd (eds.), *Turbulent Cascades II*,
ERCOFTAC Series 26, https://doi.org/10.1007/978-3-030-12547-9_3

1 Introduction

One important question of turbulence theory is to get a profound understanding of turbulence as a cascade process, that can be understood as the evolution of turbulent structures on different spatial or temporal scales. There have been many works to achieve a better understanding but rigorous results, like the Kármán-Howarth equations or Kolmogorov's 4/5th law, are still rare, cf. [7]. Although these laws are derived from the Navier Stokes equation, the experimental verification is not of high precision. The reason for that probably is that the mentioned rigorous results only hold exactly for the ideal case of infinite Reynolds numbers and homogeneous and isotropic flow fields. These conditions are difficult to meet for real turbulent flows. One therefore may state that high precision results are still lacking in turbulence research.

We present an analysis of the turbulent cascade with respect to the evolution process of velocity increments towards smaller scales. The analysis of this data includes 2- as well as 3-point statistics. Evidence of the Markov property for the turbulent cascade process in scale, which corresponds to a three-point (two-scale) closure of general joint multi-scale statistics, has been shown in previous studies [4, 9]. Based on an estimation method by Kramers-Moyal coefficients, a Fokker-Planck equation for the cascade process can be estimated directly from the measured data, thus the whole multi-point statistics is expressed by a differential equation, the Fokker-Planck equation. This approach is very general and can reproduce all structure functions, including the third order one, accurately. Interestingly this statistical approach can be linked to the non-equilibrium thermodynamics of microscopic systems [12]. This analogy enables to define the thermodynamical quantity of entropy. Furthermore, precision results on entropy statistics can be shown.

For each cascade trajectory, which we define as the complete evolution of a velocity increment from the integral length L to the Taylor length λ, the entropy change can be determined, using concepts from stochastic thermodynamics. Such entropy changes will fluctuate from cascade trajectory to cascade trajectory and may become positive (in case of entropy production) and negative (in case of entropy consumption). As a new feature, we find that the entropy fluctuations fulfill nearly perfectly the integral fluctuation theorem (IFT), which is a fundamental entropy law of non-equilibrium thermodynamics.

In this contribution, we report on results obtained from a free air-jet experiment [9]. Constant temperature hot-wire anemometry measurements of velocity were done at a distance of 125 nozzle diameters at the centerline. The data acquisition comprises 12.5×10^6 samples at a sampling frequency of 8 kHz. This experiment is characterized by a nozzle-based Reynolds number of about 2.7×10^4, an integral length $L = 67$ mm and a Taylor length scale of $\lambda = 6.6$ mm which corresponds to $Re_\lambda = 166$.

The paper is organized as follows, firstly the theoretical framework is explained, secondly results of the stochastic analysis are presented and finally our findings are summarized.

2 Theoretical Framework

2.1 Fokker-Planck Equation of Velocity Increment Series u_r

The turbulent cascade is taken as a stochastic process described by a Fokker-Planck equation Eq. (2) and its Kramers-Moyal coefficients [1, 10, 13]. Here we use the assumption that the turbulent energy cascade possesses a Markov property in scale down to the so-called Einstein-Markov length (order of Taylor length) [4], which corresponds to a three-point (two-scale) closure of general joint multi-scale statistics. We estimate Kramers-Moyal coefficients $D^{(k)}$ directly from experimental data by using the definition

$$D^{(k)}(u_r, r) = \lim_{\Delta r \to 0} \frac{1}{k!\,\Delta r} \int_{-\infty}^{\infty} (u_{r-\Delta r} - u_r)^k \, p\,(u_{r-\Delta r}|u_r)\; du_{r-\Delta r}, \tag{1}$$

where u_r is the longitudinal velocity increment series.

Based on the first two terms of the Kramers-Moyal expansion $D^{(1,2)}$ (drift and diffusion coefficient), which strongly dominate the expansion [1, 10] and the Markov property in scale r, a stochastic description of the energy cascade process by a Fokker-Planck equation ($r < r_0$)

$$\begin{aligned} -\partial_r p\left(u_r|u_{r_0}\right) = &- \partial_u \left[D^{(1)}(u_r, r)\, p\left(u_r|u_{r_0}\right)\right] \\ &+ \partial_u^2 \left[D^{(2)}(u_r, r)\, p\left(u_r|u_{r_0}\right)\right] \end{aligned} \tag{2}$$

can be estimated directly from the measured data. Here the abbreviations $\partial_r = \partial/\partial r$ and $\partial_u = \partial/\partial u_r$ are used. As found in many experimental data (see [5, 8–10]) we find a linear function for $D^{(1)}$ and a parabolic function for $D^{(2)}$

$$\begin{aligned} D^{(1)}(u_r, r) &= d_{11}(r) u_r, \\ D^{(2)}(u_r, r) &= d_{22}(r) u_r^2 + d_{21}(r) u_r + d_{20}(r). \end{aligned} \tag{3}$$

The drift and diffusion coefficient, together with an initial probability density function $p(u_L)$ contain the complete stochastic information about the Markov cascade process in scale r.

2.2 Reconstruction of Structure Functions

From the Fokker-Planck equation Eq. (2) it is possible to derive equations for the structure functions $S^k(r) = \langle u_r^k \rangle$. To verify the validity of estimated $D^{(1)}$ and $D^{(2)}$ we investigate the scaling of second, third and sixth order structure function $S^k(r)$. The self-similar eddy hierarchy in a statistical sense suggests scaling laws for

turbulence of the form $S^k(r) \propto r^{\zeta_k}$ with a power law exponent ζ_k, initiated by works of Kolmogorov 41 and 62 [2, 3]. This feature of the turbulent cascade process is investigated in Sect. 3. Structure function $S^k(r)$ is calculated as

$$S^k(r_1) = \int_{-\infty}^{\infty} u_{r_1}^k \, p(u_{r_1}) du_{r_1}, \tag{4}$$

with use of $(r_1 < r_2)$

$$p(u_{r_1}) = \int_{-\infty}^{\infty} p_{stp}(u_{r_1}|u_{r_2}) p(u_{r_2}) du_{r_2}. \tag{5}$$

To reconstruct the conditional PDF $p_{stp}(u_{r_1}|u_{r_2})$ we use the estimated Kramers-Moyal coefficients and the so called short time propagator in Eq. (6) [9, 11], that solely depends on $D^{(1)}$ and $D^{(2)}$, for $r_2 = \lim_{\Delta r \to 0} r_1 + \Delta r$

$$p_{stp}(u_{r_1}|u_{r_2}) = \frac{1}{\sqrt{4\pi D^{(2)}(u_{r_2}, r_2)\Delta r}} exp\left(-\frac{\left(u_{r_1} - u_{r_2} - D^{(1)}(u_{r_2}, r_2)\Delta r\right)^2}{4D^{(2)}(u_{r_2}, r_2)\Delta r} \right). \tag{6}$$

We are especially interested in the scale-wise evolution equation for the third order structure function

$$\partial_r S^3(r) = S^3(r)/r. \tag{7}$$

In this context, we mention the Kolmogorov's 4/5-law [7], derived from the Navier-Stokes equation

$$\partial_r S^3(r) = -4/5\langle\epsilon\rangle + 6\nu\partial_r^2 S^2(r) + q(r), \tag{8}$$

where $q(r)$ is related to the correlation function of the external forcing, ν is the kinematic viscosity and $\langle\epsilon\rangle$ is the mean energy dissipation rate per unit mass. In [9] the connection between the Fokker-Planck equation of u_r and structure functions was discussed. Integrating Eq. (2) leads to

$$\partial_r S^k(r) = -k\langle u_r^{(k-1)} D^{(1)}(u_r, r)\rangle - k(k-1)\langle u_r^{(k-2)} D^{(2)}(u_r, r)\rangle. \tag{9}$$

Using parametrization given in Eq. (3) one obtains for the third order structure function

$$\partial_r S^3(r) = -3\big(d_{11}(r) + 2d_{22}(r)\big)S^3(r) - 6d_{21}(r)S^2(r). \tag{10}$$

The term $d_{21}(r)$ couples $S^2(r)$ with the equation for $S^3(r)$, accordingly $d_{21}(r)$ and $S^2(r)$ model a source of skewness throughout the cascade process. In this case, the set of equations for $S^k(r)$ are closed as they can be solved step by step starting with $S^0(r) = 1$ and $S^1(r) = 0$. Next, we discuss a simplified case for $D^{(1)}$ and $D^{(2)}$ where we set $d_{21}(r) = 0$. The parametrization in terms of $d_{11}(r)$, $d_{20}(r)$ and $d_{22}(r)$, implies a relaxation of an initial skewness down to smaller scales according to

$$\partial_r S^3(r) = -3\big(d_{11}(r) + 2d_{22}(r)\big)S^3(r). \tag{11}$$

The sign of skewness is given by the initial skewness in $S^3(L) \neq 0$ which is known to be negative. Note the additive term $d_{20}(r)$ in the diffusion coefficient $D^{(2)}$ does not contribute to the third order structure function, whereas it mixes lower order structure functions $\big(d_{20}(r)S^{k-2}(r)\big)$ to all structure functions $S^k(r)$ with $k \neq 3$.

2.3 Integral Fluctuation Theorem (IFT)

The corresponding stochastic process defined in Sect. 2.1 can be interpreted as an analogue of a non-equilibrium thermodynamic process [6, 12]. In particular, this allows to apply concepts of stochastic thermodynamics to turbulent flows [6, 8]. It enables to determine an entropy production of the turbulent cascade, in particular for every individual velocity increment trajectory $u(\cdot) = \{u_r; r = L \ldots \lambda\}$ evolving from the integral length $L = 67\,\text{mm}$ to the Taylor length scale $\lambda = 6.6\,\text{mm}$, the total entropy production ΔS_{tot} is given by

$$\begin{aligned} \Delta S_{tot}\,[u(\cdot)] &= \Delta S_{med} + \Delta S_{sys} \\ &= -\int_L^\lambda \partial_r u_r \partial_u \varphi(u_r) dr - \ln\left(\frac{p(u_\lambda, \lambda)}{p(u_L, L)}\right). \end{aligned} \tag{12}$$

The total entropy production is given by the sum of two contributions, ΔS_{med} being the entropy variation due to the exchange of energy with the surrounding medium which depends on the evolution through the hierarchy of length scales r in the cascade and ΔS_{sys} gives the entropy change associated with the change in state of the system itself. In Eq. (12) $\varphi(u_r)$ is the stochastic potential from the stationary solution of the estimated Fokker-Planck equation

$$\varphi(u_r) = \ln\left(D^{(2)}\,(u_r, r)\right) - \int_{-\infty}^{u} \frac{D^{(1)}(w_r, r)}{D^{(2)}(w_r, r)} dw. \tag{13}$$

Within stochastic thermodynamics, the integral fluctuation theorem (IFT)

$$\langle e^{-\Delta S_{tot}} \rangle_{u(\cdot)} = 1, \tag{14}$$

where $\langle \ldots \rangle$ is the average over many fluctuating velocity increments trajectories, is a fundamental entropy law of non-equilibrium thermodynamics [12], which holds for any Markov process. It is a relation which expresses the balance between the relative frequency of entropy-consuming ($\Delta S_{tot} < 0$) as compared to entropy-producing ($\Delta S_{tot} > 0$) trajectories associated with the stochastic evolution of velocity increment trajectories $u(\cdot)$ (individual stochastic trajectories).

3 Verification of Fokker-Planck Equation

There is the crucial question if the estimated Fokker-Planck equation correctly captures the cascade process of the turbulent flow. Using Eq. (1) it is always possible to obtain the functional dependency of $D^{(1,2)}$. With the knowledge of $D^{(1,2)}$ one can calculate by using Eq. (6) the conditional PDF $p_{stp}(u_{r_1}|u_{r_2})$. The comparison of p_{stp} with estimated conditional PDF from the measured data can be taken as a quality check [5, 9, 13]. With this approach, it is possible to find the leading terms of $D^{(1,2)}$, but it is difficult to judge the meaning of small other functional contributions.

To quantify the accuracy of $D^{(1,2)}$ we will analyze here two-point-statistics in terms of structure functions and furthermore we will apply concepts of stochastic thermodynamics as aforementioned in Sects. 2.2 and 2.3. To be more precisely we conduct a case study on the functional contributions as presented in Table 1. According to the different cases **a–d** we use the specific estimated parameterization of $D^{(1,2)}$ to reconstruct the selected structure functions. In addition, we compute from Eq. (12) the total entropy balance and test the validity of the IFT (see Eq. (14)).

3.1 Structure Functions as a Criterion for $D^{(1)}$ and $D^{(2)}$

Figure 1a–c show a good agreement between the directly calculated structure functions from the experimental data and the "reconstructed" structure functions using the estimated Fokker-Planck equation (case **a**, **c**, and **d**). We see that the different Fokker-Planck equations reproduce all structure functions, including the third order one, accurately. Since structure functions are 2-point (one scale) quantities, there is a wide range of Fokker-Planck equations that can reproduce these structure functions, which also include the correct deviations from scaling behavior by Kolmogorov 41 and 62 [2, 3]. The dashed line in Fig. 1b represents the $-4/5$ law, that only holds for ideal flow conditions (homogeneous isotropic turbulence) and for infinite Reynolds numbers. For case **b** where $D^{(2)} = 0$ the short time propagator in Eq. (6) is not defined thus it is not possible to reconstruct the structure function via a Fokker-Planck equation.

Table 1 Case study for simplified parametrization of $D^{(1,2)}$ (for all cases $d_{11} \neq 0$)

	$D^{(1,2)}$	$S^k(r)$	IFT
a	$d_{20}(r) \neq 0$, $d_{22}(r) \neq 0$	✓	0.98
b	(K41) $d_{20}(r) = 0$, $d_{22}(r) = 0$	×	×
c	$d_{22}(r) = 0$	✓	∞
d	(K62) $d_{20}(r) = 0$	✓	∞

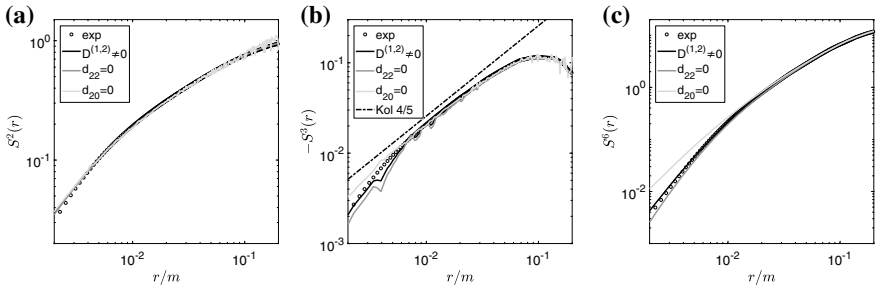

Fig. 1 **a** Second, **b** third and **c** sixth order structure function $S^k(r)$ as a function of scale r. Shown are the results obtained from the experimental data (exp) and for different parameterization of the Kramers-Moyal coefficients presented in Table 1. We plot $-S^3(r)$ since the third order structure function is negative in the inertial range. Dashed line represents $-4/5$ law. Note that the Einstein-Markov length is about 5.5 mm

3.2 Validity of the Integral Fluctuation Theorem

Next, we use the sensitivity of IFT to quantify the applicability of the estimated Fokker-Planck equation for describing the turbulent cascade process. As the IFT must hold for a system that is given by a Fokker-Planck equation, a good convergence of the integral fluctuation theorem to the theoretical value 1 ensures the validity of the estimated $D^{(1,2)}$.

For a detailed parameterization ($D^{(1)}$ polynomial of order three and $D^{(2)}$ of order two) we obtain the results presented in Fig. 2. Using this form of parameterization the total entropy fluctuations ΔS_{tot}, estimated from the experimental data, fulfill with an accuracy better than 10^{-3} the validity of the integral fluctuation theorem. Figure 2b, c demonstrates that the convergence of the empirical average $\langle e^{-\Delta S_{tot}} \rangle_N$ to the theoretical value (horizontal dashed line in Fig. 2b) is rather fast. Furthermore the

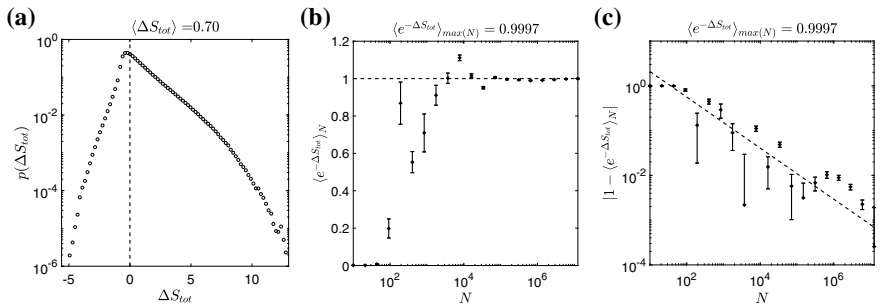

Fig. 2 **a** Probability density function of the total entropy production, **b** empirical average $\langle e^{-\Delta S_{tot}} \rangle_N$ and **c** $|1 - \langle e^{-\Delta S_{tot}} \rangle_N|$ as function of the number of trajectories N. The dashed line in **c** represents a power-law fit by using $f(N) = 5.4N^{-0.5}$

statistics (Fig. 2a) of the total entropy values show that the turbulent cascade process is linked to an overall entropy production $\langle \Delta S_{tot} \rangle > 0$, which is in accordance with the second law of thermodynamics. Moreover Fig. 2a show that the entropy consuming trajectories with $\Delta S_{tot}\,[u(\cdot)] < 0$ occur frequently. Similar results can be obtained for case **a** with an empirical average $\langle e^{-\Delta S_{tot}} \rangle_N = 0.98$.

As already pointed out, case **b** is not defined. For the cases of **c** and **d** the validity of the IFT is not confirmed. Using these classes of parameterization the average in Eq. (14) diverges. Here we should remark that the case **d** corresponds to the ideal log-normal model of Kolmogorov [1].

4 Conclusion

In this contribution, we point out that the concept to take the turbulent cascade as a Markov process in scale and to describe the scale evolution of velocity increments by a Fokker-Plank equation is in good accordance with structure functions. Thus a connection to approved results on turbulence known for structure functions can be drawn. We also see that there are different functional forms of the drift and diffusion coefficients of the Fokker-Planck equation to reproduce the structure functions. This is a consequence of the projection of the multi-scale description by the Fokker-Planck equation onto the one-scale statistics of the structure function.

Based on the concept of a Markov process a local entropy for cascade trajectories can be defined, using the concepts of non-equilibrium thermodynamics known for fluctuations in non-equilibrium systems. In addition we show that the IFT as a generalization of the second law of non-equilibrium thermodynamics holds also for turbulent flows. The IFT can be taken as a new law for turbulence, up to now only shown for experimental data but with high precision. The quantities $\partial_r u_r$, $p(u_\lambda, \lambda)$ and $p(u_L, L)$ that are taken directly from the measured data together with the stochastic properties of the cascade process, described by proper drift and diffusion coefficients, are in exact balance for the fulfilment of the IFT. Taking the IFT as a valid law for turbulence it can be used to rule out different functional dependencies of the underlying Fokker-Planck equation.

Acknowledgements We acknowledge helpful discussions with A. Abdulrazek, A. Engel, A. Girard, G. Gülker, M. Wächter and T. Wester.

References

1. Friedrich, R., Peinke, J.: Description of a turbulent cascade by a Fokker-Planck equation. Phys. Rev. Lett. **78**(5), 863 (1997)
2. Kolmogorov, A.N.: Dissipation of energy in locally isotropic turbulence. Dokl. Akad. Nauk SSSR **32**, 16–18 (1941)

3. Kolmogorov, A.N.: A refinement of previous hypotheses concerning the local structure of turbulence in a viscous incompressible fluid at high Reynolds number. J. Fluid Mech. **13**(1), 82–85 (1962)
4. Lueck, S., Renner, C., Peinke, J., Friedrich, R., et al.: The Markov-Einstein coherence length—a new meaning for the Taylor length in turbulence. Phys. Lett. A **359**(5), 335–338 (2006)
5. Nawroth, A., Peinke, J., Kleinhans, D., Friedrich, R.: Improved estimation of Fokker-Planck equations through optimization. Phys. Rev. E **76**(5), 056,102 (2007)
6. Nickelsen, D., Engel, A.: Probing small-scale intermittency with a fluctuation theorem. Phys. Rev. Lett. **110**(21), 214,501 (2013)
7. Pope, S.B.: Turbulent Flows (2001)
8. Reinke, N., Fuchs, A., Nickelsen, D., Peinke, J.: On universal features of the turbulent cascade in terms of non-equilibrium thermodynamics. J. Fluid. Mech. **848**, 117–153 (2018). https://doi.org/10.1017/jfm.2018.360
9. Renner, C., Peinke, J., Friedrich, R.: Experimental indications for markov properties of small-scale turbulence. J. Fluid Mech. **433**, 383–409 (2001)
10. Renner, C., Peinke, J., Friedrich, R., Chanal, O., Chabaud, B.: Universality of small scale turbulence. Phys. Rev. Lett. **89**(12), 124,502 (2002)
11. Risken, H.: The Fokker-Planck Equation. Methods of Solution and Applications, vol. 18 of. Springer Series in Synergetics (1989)
12. Seifert, U.: Stochastic thermodynamics, fluctuation theorems and molecular machines. Rep. Prog. Phys. **75**(12), 126,001 (2012)
13. Stresing, R., Peinke, J.: Towards a stochastic multi-point description of turbulence. New J. Phys. **12**(10), 103,046 (2010)

Evolution of Local Structure of Turbulent Flow Along Pathlines

Joseph Mathew

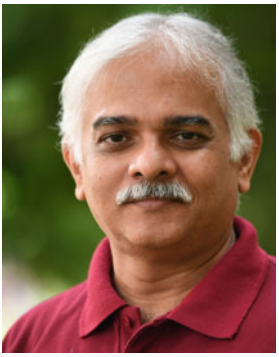

Abstract The evolution of invariants of the velocity gradient tensor is examined to determine local topologies of flow within shear flow turbulence. In a temporal direct numerical simulation of a round jet, a large number of fluid pathlines were computed simultaneously, and values of invariants at locations along pathlines were stored. It turns out that trajectories in the invariant space, corresponding to fluid pathlines, are far more varied than those of the conditional mean field that has been determined before. Several trajectories have segments where the invariants have much larger values than that expected from their joint pdfs. Corresponding large changes are also observed in the space of the invariants of the strain rate tensor. Although less frequent, these large departures may have consequences for the evolution of turbulent flow fields.

1 Introduction

Studies of the velocity gradient tensor (VGT) have revealed several features of the local structure of flows. In several types of flows, such as homogeneous isotropic turbulence, boundary layer, channel and pipe, and free shear flows, isolines of the

J. Mathew (✉)
Department of Aerospace Engineering, Indian Institute of Science, Bangalore 560012, India
e-mail: joseph@iisc.ac.in

M. Gorokhovski and F. S. Godeferd (eds.), *Turbulent Cascades II*,
ERCOFTAC Series 26, https://doi.org/10.1007/978-3-030-12547-9_4

joint pdf of the 2nd and 3rd invariants (Q and R, respectively; defined below) of the VGT have obviously similar, teardrop shapes. This implies a prevalence of regions in the flow which are sheet-like, and those where vortices are being stretched, or compressed, axially. The analyses have taken flowfields at instants from direct numerical simulations (DNS) to obtain statistics and infer such properties. Although most studies have taken homogeneous, isotropic turbulence of incompressible flow and found similar results, qualitative variations have been observed in other situations; e.g., when compressibility effects are significant, both expected [8] and unexpected [5] changes have been observed. The present study is of the local structure and changes to it along fluid pathlines with an aim of uncovering a mechanistic understanding of shear flow turbulence.

The velocity gradient tensor $\mathbf{A}$ has elements $A_{ij} = \partial u_i/\partial x_j$, which are the spatial derivatives of the Eulerian velocity field u_i. It has three invariants: $P = -\text{trace}\mathbf{A}$; $Q = \frac{1}{2}\left[P^2 - \text{trace}(\mathbf{A^2})\right]$; $R = -\det(\mathbf{A})$. For incompressible flow $P = 0$. The discriminant surface $D = 0$, where $D = 27R^2 + (4P^3 - 18PQ)R + (4Q^3 - P^2Q^2)$, separates the region in Q-R space where eigenvalues of $\mathbf{A}$ are complex ($D > 0$) and local topology is focal—like that in vortices—from the region where they are real. $\mathbf{A}$ can be split into symmetric strain-rate and skew-symmetric rotation-rate parts: $\mathbf{A} = \mathbf{S} + \mathbf{W}$. With subscripts S and W to denote invariants of these two tensors, $P_W = R_W = 0$ for all flows; $P_S = P$, $Q_S = -(1/2)S_{ij}S_{ji}$, $R_S = -(1/3)S_{ij}S_{jk}S_{ki}$ and $Q_W = -(1/2)W_{ij}W_{ji}$ (see Chong et al. [3] for details). In the analyses presented below, the flow is incompressible and $P \equiv 0$.

Most studies of the VGT have sought to find the joint pdf of the invariants Q and R, and changes to shapes of isolines of this pdf in different regions of a turbulent flow, such as the layers in channel flows. Others have been to find closures for some terms in the transport equations for the VGT, so that solutions of the model equations may, at least qualitatively, resemble the exact evolution. Cantwell [2] showed that the restricted Euler model, which sets the pressure Hessian term to zero, predicts that (Q, R) states evolve toward $R > 0$, close to the discriminant $D(Q, R) = 0$ curve. This is correct for a range of $|R|$ that is not too large and $D(Q, R) > 0$, but is generally wrong for $D(Q, R) < 0$. A summary of later models is available [6]. It is useful to note that modeling has been considered successful when there is a correspondence to the shapes of the isolines of the joint pdf.

Ooi et al. [7] went further by computing the conditional mean growth rates of invariants in stationary, homogeneous, isotropic turbulence. They computed vectors and trajectories in the spaces of the invariants of the VGT, its symmetric and antisymmetric parts and of stretching. Trajectories in the conditional mean growth rate vector field provide a picture of the likely evolution of local topology of fluid packets. They observed cyclical changes from, say, sheet-like regions to stretching and then compressing vortical ones, spiralling towards the origin, where invariants and all gradients are small. Ooi et al. [7] had noted that following fluid pathlines may be useful but would require expensive computations. Here, results of just such a computation involving simultaneous tracking of a large number of fluid particles in a DNS of a turbulent round jet is presented. From data of the invariants at successive locations of these fluid particles, a direct determination of their history and implied

topological changes was obtained. A striking observation is that trajectories of individual fluid particles in Q-R space are quite different from those of the conditional mean trajectories.

2 Preparation of DNS Data

A temporal DNS of a round jet was performed. The initial state is a model of a round jet where it emerges from a nozzle, with a top-hat streamwise velocity profile bounded by a thin, tanh shear layer. Jet centerline velocity U and initial mean diameter D are the scales used. The DNS employs a Fourier pseudospectral method in a cube of side 4 and a grid of $128 \times 128 \times 128$. The jet occupies a cylindrical region whose axis coincides with the z-axis of a Cartesian coordinate system. Initial positions of fluid particles are at gridpoints on a cross-sectional plane x-y over a 90° sector of radius equal to four times the initial jet radius. Successive positions of 3278 particles were computed simultaneously and local values of vorticity and invariants Q, R, Q_s and R_s were stored.

The initial, jet boundary shear layer rolls up into 4 vortex rings per period, adjacent rings undergo pairing, rings undergo azimuthal instability followed by a rapid breakdown into a roughly cylindrical region of turbulence. Features this simulation have been discussed at length before [4]; here, the Reynolds number based on U and D is 2400.

Figure 1 shows a longitudinal section at three instants from the DNS; filled contours of vorticity magnitude are shown. At $t = 3$, the cylindrical shear layer has rolled up into 4 vortex rings per period. At $t = 8$ adjacent vortex rings have merged into two rings per period. At $t = 25$ the fine scale structure of the turbulent jet is evident. Curves in Fig. 2 are indicators of the evolution of the flow in terms of the kinetic energy E and enstrophy E_ω integrated over the simulation volume and scaled with their initial values $E(0)$ and $E_\omega(0)$, respectively. Enstrophy grows as the vortex

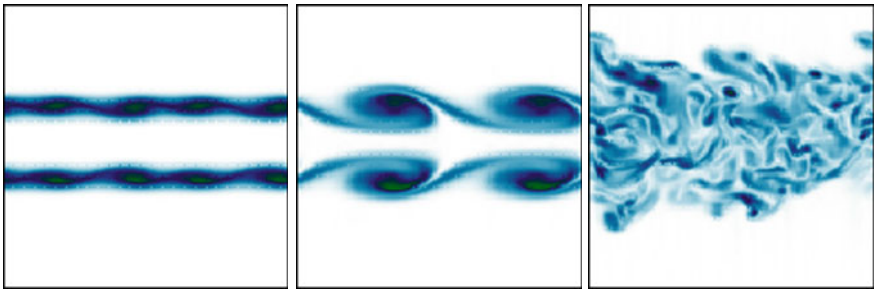

(a) $t = 3$ (b) $t = 8$ (c) $t = 25$

Fig. 1 Vorticity magnitude on longitudinal plane $y = 0$. A sequence of 4 vortex rings per period at $t = 3$, adjacent rings have merged at $t = 10$, and a turbulent flow has set in at $t = 25$

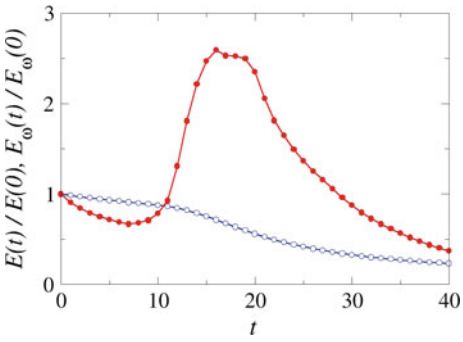

Fig. 2 Evolution of kinetic energy (–o–o–) and enstrophy (–●–●–) in simulation

rings undergo azimuthal instability and breaks down rapidly and then falls slowly due to net dissipation of the turbulent flow.

3 Analyses of Local Structure

Chong et al. [3] classified the local topology of flow in terms of the nodes, saddles and foci of critical point analyses of dynamical systems. For incompressible flow, most regions have one of the four types of local structure shown in Fig. 3a. Special forms occur along the axes and the discriminant curves. Regions above the discriminant curve $D(Q, R) = 0$ have structures that are vortex-like, stretching in quadrant 2, and compressing in quadrant 1. Below, in $D < 0$, the structure is sheet-like in quadrant 4, and tube-like in quadrant 3. Figure 3b shows isolines of the joint pdf $f(Q, R)$ from all points along all computed fluid pathlines of the present simulation. Only the three standard deviation range ($\pm 3\sigma(Q)$, $\pm 3\sigma(R)$) has been shown. Isolines cover 3 decades of pdf levels. The shape resembles that usually observed [6].

Values of Q and R at successive positions along many representative fluid pathlines were stored after every integration time-step. The corresponding trajectories in Q-R space for pathline subsets are shown in Fig. 4. In each subset, the initial position on the pathline is at gridpoints which are at roughly the same radius. In Fig. 4a, pathlines originate from the sheet-like region of the initial cylindrical shear layer from radial positions $r(t = 0) \approx 0.5$. Values of Q and R are much larger than the 3σ range of the joint pdf (Fig. 3b). Pathlines that originate from $r(0) \approx 1$, which is well outside the jet, enter the turbulent region later—after these fluid packets are entrained. Values of Q and R over some parts of these pathlines are also outside the 3σ ranges. Of course, these large excursions are not very frequent. The overall shape of the region occupied by these extreme trajectories is a distortion of the shape of the isolines of the joint pdf: in $Q \gg 0$, the trajectories occupy a greater range of values of R; in $Q \ll 0$, the trajectories form a much thinner tail about the discriminant curve in $R > 0$. In these figures, larger spacing between symbols on curves indicate faster

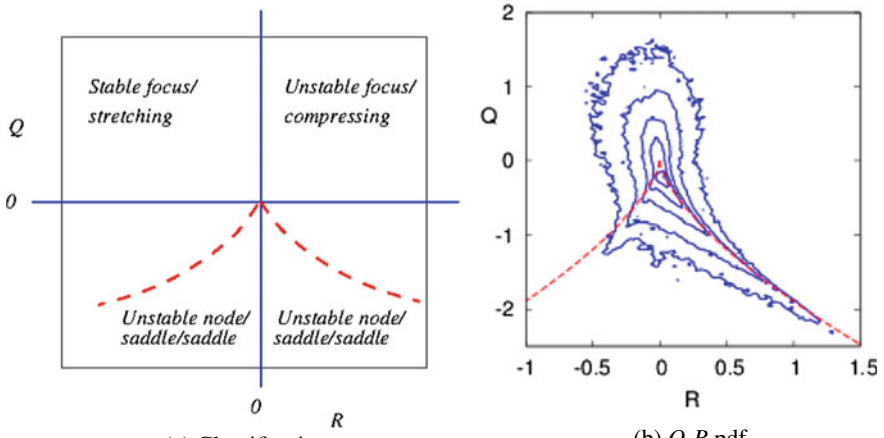

(a) Classification (b) Q-R pdf

Fig. 3 Local structure for incompressible flow. **a** topology types; **b** isolines of the joint pdf (——). Discriminant curves $D(Q, R) = 0$ (– – –)

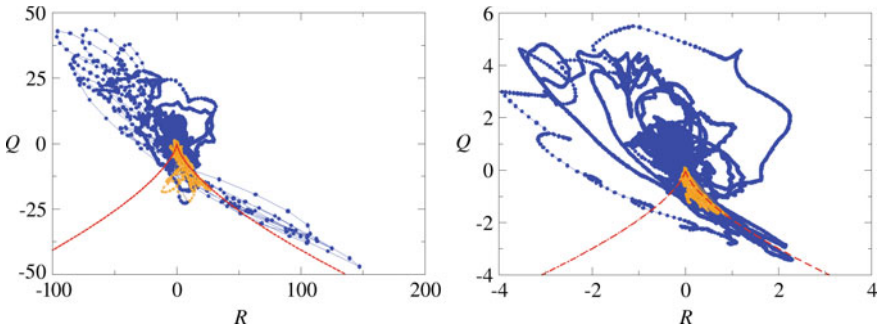

(a) $r(0) \approx 0.5$ (b) $r(0) \approx 1.0$

Fig. 4 Trajectories in Q-R for fluid particles whose initial radial position $r(0)$ is roughly the same. In turbulent region (–●–●–), and in nonturbulent region (–●–●–). $D(Q, R) = 0$ (– – –)

changes. Over several segments we can observe that changes are also more rapid where the invariants' values are larger.

Q-R trajectories for four pathlines originating from radial positions $r(0) \approx 1.0$ are shown in Fig. 5. Arrows indicate direction of increasing time. Figure 5a shows a simple trajectory: (Q,R) states begin near the origin, move towards the quadrant 4 slowly, and then travel rapidly to quadrant 2 and 1, with minor detours, then slowly within quadrant 1, and eventually to the origin again. The trajectory in Fig. 5b has the following sequence: origin, along $D(Q, R > 0) = 0$, retrace past the origin and along $Q > 0$, $R \approx 0$, a partial anticlockwise circuit in quadrant 2 before reversal, a rapid foray through quadrants 1, 4, 2, and back to the origin. Besides, the broad

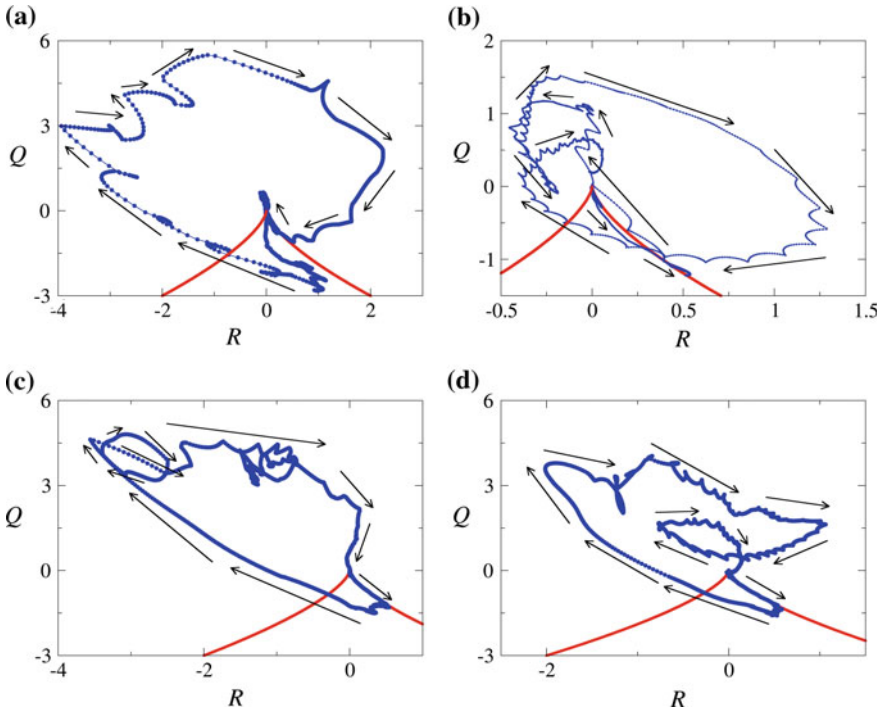

Fig. 5 A few trajectories in Q-R of particles from radial position $r(t = 0) \approx 1.0$

similarity of the trajectories in Fig. 5c, d, note that the initial segments are along $D = 0$, and the final segments are along $Q = 0$, $R \approx 0$.

From stationary, homogeneous, isotropic turbulence simulations, Ooi et al. (1998) extracted mean trajectories in Q-R space. They found the trajectories to spiral clockwise to the origin. Also, these trajectories have roughly the same shape, though spiralling inward, as the tear-drop contours of the isolines of the pdf $f(Q, R)$. The present studies show that trajectories along *fluid pathlines* are more diverse than has been inferred from such means and model equations. For ensembles, there are perhaps many that resemble the pdf (trajectories near the origin in Fig. 4), as indeed they should to realize the pdf, but there are significant departures on some. The shapes of the trajectories in Fig. 5 look nothing like that of the pdf! We should expect this to be significant because because the values of Q and R are *everywhere* significantly larger, with consequences for the overall structure and evolution of the turbulent region.

The progression from 4th to 2nd quadrant can be understood as a sheet-like region rolling up into a stretching vortex. A large scale version occurs during the initial stages of the present simulation. The pathlines begin within a *large scale* cylindrical vortex sheet and (Q,R) states are along $D(Q, R > 0) = 0$. The sheet then rolls up into a sequence of vortex rings and the Q-R trajectories go to the 3rd quadrant and remain

there for some time. In the turbulent regime, any sheet-like region would be of much smaller extent, but a similar process of roll-up into a single scroll, or into several neighboring vortex filaments is possible.

The 1st quadrant flow is that of a compressing vortex. So the progression from 2nd to 1st quadrant is of a fluid particle in a region with a stretching vortex to a compressing vortex. While this can be achieved by a relaxation and reversal of background strain, it is tempting to speculate that when $Q \gg 0$ in quadrant 2, the travel to quadrant 1 may, sometimes, involve vortex breakdown at high swirl; most often it may be merely a (vortical) fluid packet travelling into a region of smaller strain, and the vortex relaxes. It is nevertheless intriguing that in Fig. 5c, d, the eventual return to the origin is along $R \approx 0$, $Q > 0$, after travelling right in quadrant 2. Typically, the subsequent travel from 1st quadrant to 4th is a very much slower process (Fig. 5a), but not always (Fig. 5b). Over some intervals, trajectories go from quadrant 1 to 2 also (Fig. 5d).

3.1 Q_s-R_s Trajectories

The corresponding trajectories in Q_s-R_s are simpler and qualitatively similar. The Q_s-R_s plane can be divided into regions where flow is expanding ($R_s > 0$) or contracting ($R_s < 0$); along the discriminant $D(Q_s, R_s) = 0$ the flow is axisymmetric (Fig. 6a); on $R_s = 0$ the flow is 2-dimensional. These local flow types can be understood by examining the ratios among eigenvalues of the strain-rate tensor $\mathbf{S}$ [1].

Ooi et al. [7] found that conditional mean trajectories in Q_s-R_s spiral outward from a point $0 < R_s < D(Q_s, R_s) = 0$, lying close to the right discriminant curve. Here, such spiralling trajectories were not observed. There is a preference for $R_s > 0$

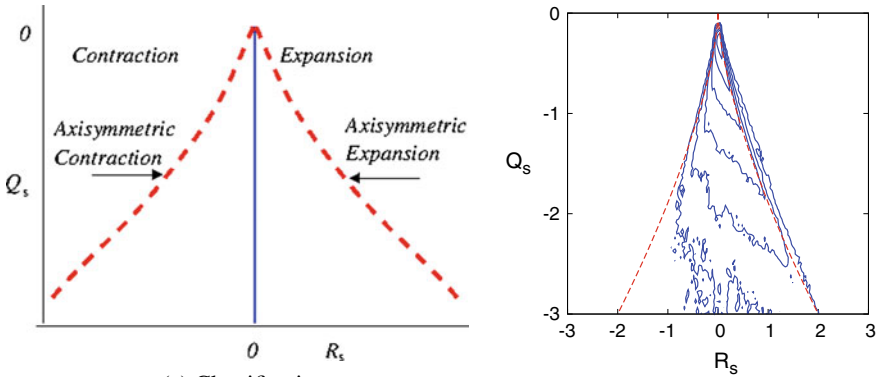

(a) Classification (b) Q_s-R_s pdf

Fig. 6 Local structure for incompressible flow. **a** topology types; **b** isolines of the joint pdf (——). Discriminant curves $D(Q_s, R_s) = 0$ (– – –)

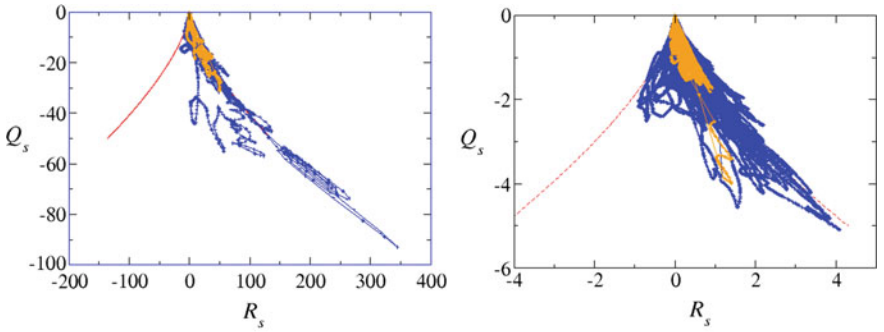

(a) $r(0) \approx 0.5$ (b) $r(0) \approx 1.0$

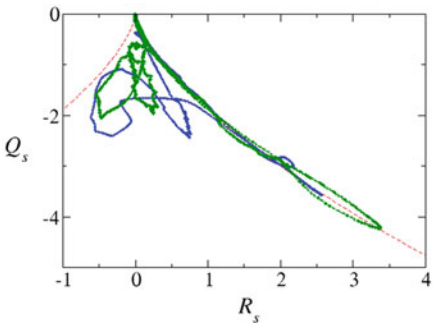

(c) $r(0) \approx 1.0$

Fig. 7 Trajectories in Q_s-R_s for fluid particles from initial radial position $r(0)$. In turbulent region (–●–●–), and in nonturbulent region (–●–●–). $D(Q, R) = 0$ (– – –). In **c**, only two trajectories corresponding to the curves in Fig. 5c, d are shown

at large $|Q_s|$, but not at smaller values. Note, again, that there are large excursions to values much larger than the 3σ range of the joint pdf $f(Q_s, R_s)$ (Fig. 7).

4 Conclusions

Trajectories in the plane of the 2nd and 3rd invariants Q and R of the velocity gradient tensor were found corresponding to pathlines in an axisymmetric, turbulent shear flow from a direct numerical simulation. Many of these trajectories have the teardrop shape and spiral inward to the origin, as could be expected from the joint pdf $f(Q, R)$, or conditional mean trajectories. Surprisingly, there are several trajectories that travel through parts that are far from the origin, and with a wide variety of changes that are quite different from the simple inward spiralling. Although such trajectories are less frequent, since the values of the invariants are large, there may be consequences to the structure and evolution of turbulence, like internal or fine-scale intermittency.

References

1. Blackburn, H.M., Mansour, N.N., Cantwell, B.J.: Topology of fine-scale motions in turbulent channel flow. J. Fluid Mech. **310**, 269–292 (1996)
2. Cantwell, B.J.: On the behavior of velocity gradient tensor invariants in direct numerical simulations of turbulence. Phys. Fluids A **5**(8), 2008–2013 (1993)
3. Chong, M.S., Perry, A.E., Cantwell, B.J.: A general classification of three-dimensional flow fields. Phys. Fluids A **2**(5), 765–777 (1990)
4. Mathew, J., Basu, A.J.: An economical method for direct numerical simulation studies of transitional round jets. Comput. Fluids **30**(5), 543–554 (2001)
5. Mathew, J., Ghosh, S., Friedrich, R.: Changes to invariants of th velocity gradient tensor at the turbulent-nonturbulent interface of compressible mixing layers. Int. J. Heat Fluid Flow **59**, 125–130 (2016)
6. Meneveau, C.: Lagrangian dynamics and models of the velocity gradient tensor in turbulent flows. Ann. Rev. Fluid Mech. **43**, 219–245 (2011)
7. Ooi, A., Martin, J., Soria, J., Chong, M.S.: A study of the evolution and characteristics of the invariants of the velocity-gradient tensor in isotropic turbulence. J. Fluid Mech. **381**, 141–174 (1999)
8. Suman, S., Girimaji, S.S.: Velocity gradient invariants and local flow-field topology in compressible turbulence. J. Turbul. **11**(2), 2 (2010)

Renormalized Equations in Turbulent Immiscible Gas-Liquid Flows—The Target on LES-Formulation

M. A. Gorokhovski and V. L. Saveliev

Abstract In the group-theoretical model of stationary homogeneous turbulence (PRE 72, 016302, 2005), the renormalized form of the Navier-Stokes equations includes the turbulent viscosity, which appears not from averaging of the nonlinear term, but from the molecular viscosity term. The next raised question is as follows. In the immiscible gas-liquid turbulent flow, the motion equation is completed by the surface tension force, acting on the interface. When such a flow is averaged over some length-scale, there is no more interfaces. Then at the high Reynolds number, what is the renormalized form of governing equations in this flow? In the framework of approach of the aforementioned paper, the result is this: similar to the Smagorinsky viscosity, the "effective surface tension coefficient" appears in the invariant to scaling transformation form. Its expression is discussed in this paper.

M. A. Gorokhovski (✉)
Laboratoire de Mécanique des Fluides et d'Acoustique, École Centrale de Lyon, CNRS-Université Claude Bernard Lyon 1-INSA Lyon, Ecully, France
e-mail: mikhael.gorokhovski@ec-lyon.fr

V. L. Saveliev
Institute of Ionosphere, Almaty 480020, Kazakhstan

M. Gorokhovski and F. S. Godeferd (eds.), *Turbulent Cascades II*,
ERCOFTAC Series 26, https://doi.org/10.1007/978-3-030-12547-9_5

1 Introduction

In our earlier paper [1] the group-theoretical model for stationary developed turbulence was developed in lines of classical idea of renormalization group (Kadanoff [2], Bogolubov and Shirkov [3], Wilson [4]). In relation to Kadanoff's "block picture" for the spin field in Ising's model, the approach in that paper stemmed from the following statement: If instead of turbulent field $\mathbf{v}(\mathbf{r})$, an averaged (or filtered) on the length-scale σ field, $\langle \mathbf{v} \rangle_\sigma (\mathbf{r})$, is considered, then the last one will "resemble" the original turbulent field $\mathbf{v}(\mathbf{r})$. The exact sense of "resemble" was determined by the group of renormalization transformations, derived explicitly for both the field of velocity and its governing equation. In this way the renormalized form of Navier-Stokes equation was obtained where the turbulent viscosity appeared not from the gradient approximation of averaged nonlinear term, but from the molecular viscosity term. Let us consider now the unsteady turbulent flow of the mixture of two incompressible immiscible fluids which are identifiable at any fixed point of the flow, say one fluid is the liquid, and another fluid is the gas. The density of such continua is represented by the step function with two values, either the gas or the liquid density:

$$\rho(\mathbf{r}, t) = \begin{cases} \rho_g \\ \rho_l \end{cases} \tag{1}$$

The simplest model of this flow is given by the following equation:

$$\frac{\partial \mathbf{v}}{\partial t} = -\nabla \cdot \mathbf{v}\mathbf{v} - \frac{1}{\rho}\nabla p \tag{2}$$

where $\mathbf{v}$ represents the velocity field, continuous at each and every material point:

$$\nabla \cdot \mathbf{v} = 0 \tag{3}$$

Although the viscous term in Eq. (2) is omitted for simplicity, the role of viscosity is not discarded, and the corresponding discussion is postponed to Sect. 2. The momentum equation is completed simultaneously by the mass conservation equation:

$$\frac{\partial \rho}{\partial t} = -\nabla \cdot \rho \mathbf{v} \tag{4}$$

The following question is addressed in this paper: what is the form of Eqs. (2)–(4) after averaging over some spatial scale σ? One way to answer this question is proposed in the aforementioned paper [1]. We will first remind the renormalized averaging formula obtained in that paper. With the help of this formula, we will average Eqs. (2)–(4) over a small, residual, length-scale σ_0. Using then the renormalization group transformation, we will transform this averaged equation to the equation for the velocity field $\langle \mathbf{v} \rangle_\sigma (\mathbf{r})$, averaged over any larger length-scale $\sigma > \sigma_0$. If that length-

scale σ represents the resolved scale in simulation, the renormalized form of the momentum equation can be regarded in the framework of Large Eddy Simulation (LES) approach.

2 The Modified "Turbulent" Pressure and, the Momentum Equations Averaged over a Small Length-Scale

The general averaging operation of a function $\mathrm{v}(\mathbf{r})$, depending on radius vector $\mathbf{r}$, is defined by $\langle \mathrm{v} \rangle(\mathbf{r}) = \int_{-\infty}^{\infty} \mathrm{v}(\mathbf{r}')\Psi(\mathbf{r}-\mathbf{r}')d\mathbf{r}'$, where $\Psi(\mathbf{r})$ is weight function. When this function is Gaussian:

$$\Psi_\sigma(\mathbf{r}) = \frac{1}{(\sqrt{4\pi\sigma})^3} e^{-\frac{\mathbf{r}^2}{4\sigma}} \tag{5}$$

the average is given by Gauss transform (filtering):

$$\langle \mathrm{v} \rangle(\mathbf{r}) = \int_{-\infty}^{\infty} \mathrm{v}(\mathbf{r}')\Psi(\mathbf{r}-\mathbf{r}')d\mathbf{r}' \tag{6}$$

Considering the averaged product $\langle \mathrm{v}u \rangle_\sigma$ of two fields, $\mathrm{v}(\mathbf{r})$ and $u(\mathbf{r})$, the following renormalized averaging formula was derived in [1]:

$$\begin{aligned} \langle \mathrm{v}u \rangle_\sigma &= \langle \mathrm{v} \rangle_\sigma \langle u \rangle_\sigma + 2\sigma \nabla \langle \mathrm{v} \rangle_\sigma \cdot \nabla \langle u \rangle_\sigma \\ &+ 2 \int_0^\sigma d\sigma' 2\sigma' \langle \langle \nabla_{l_1} \nabla_{l_2} \mathrm{v} \rangle_{\sigma'} \langle \nabla_{l_1} \nabla_{l_2} u \rangle_{\sigma'} \rangle_{\sigma-\sigma'} \end{aligned} \tag{7}$$

Here the last term represents the integral contribution of all scales. The usage of this formula was demonstrated in [1] by introducing a simple model velocity field

$$\mathrm{v}_i(\mathbf{r}) = \mathrm{v}_i + a_{ij} r_j + \mathrm{v}_i^{rnd}(\mathbf{r}) \tag{8}$$

where along with translation, straining and rotation of a fluid particle (a smooth part with constant v_i and a_{ij}), the velocity includes also the component from random field $\mathrm{v}_i^{rnd}(\mathbf{r})$. The latter represents the statistically homogeneous and isotropic field; it is characterized by the internal length-scale σ_*, such that above this scale the randomness leads to: $\langle \mathrm{v}_i^{rnd} \rangle_{\sigma' > \sigma_*} = 0$, while below this scale, the field is no more random $\langle \mathrm{v}_i^{rnd} \rangle_{\sigma' \le \sigma_*} = \mathrm{v}_i^{rnd}(r)$, due to eventual effects of viscosity, or surface tension. To remove the ambiguity with the upper index rnd in the last case of $\sigma' \le \sigma_*$, we denote: $\langle \mathrm{v}_i^{rnd} \rangle_{\sigma' \le \sigma} = \mathrm{v}_i^{rnd}(r) \equiv \mathrm{v}_i^*(r)$. For the model field (8), the averaging formula (7) gives:

$$\langle \mathrm{v}_i \mathrm{v}_k \rangle_\sigma = \langle \mathrm{v}_i \rangle_\sigma \langle \mathrm{v}_k \rangle_\sigma + 2\sigma \nabla \langle \mathrm{v}_i \rangle_\sigma \cdot \nabla \langle \mathrm{v}_k \rangle_\sigma + \delta_{ik} P_{tur} \tag{9}$$

where δ_{ij} is the Kronecker delta and P_{tur} is the scalar function defined by:

$$P_{tur} = \frac{2}{3}\int_0^{\sigma_*} d\sigma' 2\sigma' \langle \nabla_{l_1} \nabla_{l_2} \mathrm{v}^*_{l_3} \nabla_{l_1} \nabla_{l_2} \mathrm{v}^*_{l_3} \rangle_{\sigma_* - \sigma'} \tag{10}$$

where $l_1, l_2 = 1, 2, 3$. For one-fluid continua this scalar function is absorbed in a modified pressure to remain the averaged velocity field be solenoidal [1]. In the case of two incompressible immiscible fluids, the situation is more complex, and motivates the supplementary interpretation of the pressure modification. Both equations together, Eqs. (3) and (4), make up the zero material derivative, $D\rho/Dt = 0$, i.e. a fluid particle does not change the density along its trajectory. Thereby the interfaces of relative motion between two fluids are formed in the transporting mixture. If this mixture field is averaged over some spatial scale σ, there will be no more interfaces between fluids. In this case, let us consider a new variable per unit volume of mixture—the kinetic energy $\langle E \rangle_\sigma$ averaged conditionally on one of two fluids, flowing relatively to another fluid, and thereby straining the latter. It is clear that the variation of such energy with the change of the mixture density plays the role of a "potential" for the mutual motion of two fluids. Its contribution to the pressure modification we associate with the scalar function P_{tur} in the following form:

$$P_{tur} = \frac{\partial \langle E \rangle_\sigma}{\partial \langle \rho \rangle_\sigma} \tag{11}$$

The derivative in Eq. (11) should be taken at the constant momentum of the flowing fluid, and since the density of this fluid and the density of the mixture are proportional, we have:

$$\frac{\partial \langle E \rangle_\sigma}{\partial \langle \rho \rangle_\sigma} = -\frac{\langle E \rangle_\sigma}{\langle \rho \rangle_\sigma} \tag{12}$$

Considering $\dfrac{\partial \langle E \rangle_\sigma}{\partial \langle \rho \rangle_\sigma}$ in two neighboring points, the modification for the pressure gradient has due to (12) the following form:

$$\nabla P_{tur} = -\langle E \rangle_\sigma \nabla \frac{1}{\langle \rho \rangle_\sigma} \tag{13}$$

Let us average Eq. (2) over some small scale σ_0. With Eqs. (9) and (13), we have:

$$\frac{\partial \langle \mathbf{v} \rangle_{\sigma_0}}{\partial t} + \nabla \cdot \langle \mathbf{v} \rangle_{\sigma_0} \langle \mathbf{v} \rangle_{\sigma_0} + \frac{1}{\rho} \nabla p = \langle E \rangle_{\sigma_0} \nabla \frac{1}{\langle \rho \rangle_{\sigma_0}} \tag{14}$$

Here an appraisal of σ_0 and of $\langle E \rangle_{\sigma_0}$ in the right hand side is made by including the overall action of the surface tension effects. Due to turbulence in the flowing fluid relatively to another one, the latter is also involved into turbulent flow and thereby

is stretched by the turbulent stresses up to the moment when the balance with the capillary forces is reached. We assume that at the scale σ_0 the capillary effects absorb the effects of "turbulent" stretch characterized here by $\langle E\rangle_{\sigma_0}$:

$$\sigma_0 = \left(\frac{\gamma}{\langle E\rangle_{\sigma_0}}\right)^2 \tag{15}$$

where γ is the surface tension coefficient. It is known from [5] that the averaged relative velocity between the turbulent gas at the high Reynolds number and the inertial particle is controlled by two main parameters: the viscous dissipation of turbulent energy ϵ and the typical time of relaxation for particle velocity, referred to as the Stokes time. In this case, σ_0, usually referred to as critical, or maximum probably length scale, has the following expression [6]:

$$\sigma_0 = \left(\frac{\gamma v}{\epsilon \rho_p}\right)^{2/3} \tag{16}$$

where v is the gas viscosity, and ρ_p is the density of inertial particle. Using the definition of viscous dissipation $\langle\epsilon\rangle_{\sigma_0} = 2v\langle S_{ik}\rangle_{\sigma_0}\langle S_{ik}\rangle_{\sigma_0}$, where the elements of the strain rate tensor are $\langle S_{ik}\rangle_{\sigma_0} = \frac{1}{2}\left(\nabla_i\langle \mathbf{v}_k\rangle_{\sigma_0} + \nabla_k\langle \mathbf{v}_i\rangle_{\sigma_0}\right)$, Eq. (14) may be rewritten in the following form:

$$\frac{\partial\langle \mathbf{v}\rangle_{\sigma_0}}{\partial t} + \nabla\cdot\langle \mathbf{v}\rangle_{\sigma_0}\langle \mathbf{v}\rangle_{\sigma_0} + \frac{1}{\rho}\nabla p = -2\sigma_0\langle S_{ik}\rangle_{\sigma_0}\langle S_{ik}\rangle_{\sigma_0}\frac{\nabla\langle\rho\rangle_{\sigma_0}}{\langle\rho\rangle_{\sigma_0}} \tag{17}$$

Note that in terms of the mixture specific volume $\theta = \rho^{-1}$ (see Eq. (1) for definition), Eq. (4) may be expressed as $\frac{1}{\theta}\frac{D\theta}{Dt} = \nabla\cdot\mathbf{v}$, and Eq. (17) takes the following form:

$$\frac{\partial\langle \mathbf{v}\rangle_{\sigma_0}}{\partial t} + \nabla\cdot\langle \mathbf{v}\rangle_{\sigma_0}\langle \mathbf{v}\rangle_{\sigma_0} + \theta\nabla p = -2\sigma_0\langle S_{ik}\rangle_{\sigma_0}\langle S_{ik}\rangle_{\sigma_0}\frac{\nabla\langle\theta\rangle_{\sigma_0}}{\langle\theta\rangle_{\sigma_0}} \tag{18}$$

The right hand side of Eqs. (17) and (18) represents the effective contribution of surface tension effects on the length-scale σ_0. Let us introduce the ffective surface tension coefficient γ_{eff,δ_0}:

$$\gamma_{eff,\delta_0} = 2\sigma_0^{3/2}\langle\rho\rangle_{\sigma_0}\langle S_{ik}\rangle_{\sigma_0}\langle S_{ik}\rangle_{\sigma_0} \tag{19}$$

and represent Eqs. (17) and (18) as:

$$\frac{\partial\langle \mathbf{v}\rangle_{\sigma_0}}{\partial t} + \nabla\cdot\langle \mathbf{v}\rangle_{\sigma_0}\langle \mathbf{v}\rangle_{\sigma_0} + \theta\nabla p' = \gamma_{eff,\sigma_0}\sigma_0^{-1/2}\nabla\langle\theta\rangle_{\sigma_0} \tag{20}$$

We complete this equation by continuity and mass-conservation equations:

$$\nabla \cdot \langle \mathbf{v} \rangle_{\sigma_0} = 0 \tag{21}$$

$$\frac{\partial \langle \rho \rangle_{\sigma_0}}{\partial t} = -\nabla \cdot \rho \langle \mathbf{v} \rangle_{\sigma_0} \tag{22}$$

or, equivalently:

$$\frac{\partial \langle \theta \rangle_{\sigma_0}}{\partial t} = -\frac{\langle \theta \rangle_{\sigma_0}^2}{\theta^2} \nabla \cdot \theta \langle \mathbf{v} \rangle_{\sigma_0} \tag{23}$$

3 Renormalization of the Averaged Equations

Consider in this chapter the continuous scaling transformation from one length-scale, σ_0, to another σ, $\sigma > \sigma_0$ (the time variable is not involved into this transformation):

$$\begin{cases} \mathbf{r} \to e^{\tau\beta}\mathbf{r} \\ e^{\tau\beta(1-\mathbf{r}\cdot\nabla)}\mathbf{v}(\mathbf{r}) = e^{\tau\beta}\mathbf{v}\left(e^{-\tau\beta}\mathbf{r}\right) \\ e^{\tau\beta(1-\mathbf{r}\cdot\nabla)}\rho(\mathbf{r}) = e^{\tau\beta}\rho\left(e^{-\tau\beta}\mathbf{r}\right) \end{cases} \tag{24}$$

where β is the rate of the homogeneous scaling, relatively to the evolution parameter τ:

$$\tau\beta = \ln\sqrt{\sigma/\sigma_0} \tag{25}$$

The transformation of rotation and translation should complete (24), as it is done in [1], but here the emphasis is put on the scaling transformation (24)–(25) only, for the sake of simplicity. It is easy to show the invariance of Eqs. (2)–(4) to scaling symmetry transformation (24)–(25). By analogy with [1], the stationary turbulence is associated here with dynamics of specific class of self-similar solutions of the Euler equation (2)–(3), for which the evolution in time is the result of continues space symmetry transformations of the velocity field $\mathbf{v}(\mathbf{r}, t)$, relevantly to translation, rotation and scaling. E.g. concerning the scaling symmetry transformations, the time evolution of $\mathbf{v}(\mathbf{r}, t)$ is determined by one-parameter sub-group generator $\beta(1 - \mathbf{r} \cdot \nabla)$:

$$\mathbf{v}(\mathbf{r}, t) = e^{(t-t_0)\beta(1-\mathbf{r}\cdot\nabla)}\mathbf{v}(\mathbf{r}, t_0) \tag{26}$$

$$e^{\tau\beta(1-\mathbf{r}\cdot\nabla)}\mathbf{v}(\mathbf{r}, t) = e^{(t-t_0+\tau)\beta(1-\mathbf{r}\cdot\nabla)}\mathbf{v}(\mathbf{r}, t_0) = \mathbf{v}(\mathbf{r}, t+\tau) \tag{27}$$

An interesting invariance property of such a turbulent state was found in [1]: the application of scaling transformation (24)–(25) to the averaged field $\langle \mathbf{v} \rangle_{\sigma_0}$ acts equivalently (with the accuracy up to the change of stochastic phases) to the averaging over the length scale $\sigma > \sigma_0$, i.e.

$$e^{\ln\sqrt{\frac{\sigma}{\sigma_0}}(1-\mathbf{r}\cdot\nabla)}\langle\mathbf{v}\rangle_{\sigma_0} = \langle\mathbf{v}\rangle_{\sigma} \tag{28}$$

Therefore applying the scaling transformation (24)–(25) with (28) to Eqs. (19)–(23) we obtain:

$$\frac{\partial\langle\mathbf{v}\rangle_{\sigma}}{\partial t} + \nabla\cdot\langle\mathbf{v}\rangle_{\sigma}\langle\mathbf{v}\rangle_{\sigma} + \theta\nabla p' = \gamma_{eff,\sigma}\sigma^{-1/2}\nabla\langle\theta\rangle_{\sigma} \tag{29}$$

where the "effective" surface tension coefficient is introduced:

$$\gamma_{eff,\delta} = 2\sigma^{3/2}\langle\rho\rangle_{\sigma}\langle S_{ik}\rangle_{\sigma}\langle S_{ik}\rangle_{\sigma} \tag{30}$$

with the continuity and the mass-conservation equations in the following form

$$\nabla\cdot\langle\mathbf{v}\rangle_{\sigma} = 0 \tag{31}$$

$$\frac{\partial\langle\theta\rangle_{\sigma}}{\partial t} = -\frac{\langle\theta\rangle_{\sigma}^2}{\theta^2}\nabla\cdot\theta\langle\mathbf{v}\rangle_{\sigma} \tag{32}$$

References

1. Saveliev, V.L., Gorokhovski, M.A.: Phys. Rev. E **72**, 016302 (2005)
2. Kadanoff, L.: Physics **2**, 263 (1966)
3. Bogoliubov, N.N., Shirkov, D.V.: Introduction to the Theory of Quantum Fields (1980)
4. Wilson, K.: Phys. Rev. B **4**, 3184 (1971)
5. Kuznetsov, V.R., Sabel'nikov, V.A.: Turbulence and Combustion (1990)
6. Gorokhovski, M.: Atom. Sprays **11**, 505 (2001)

The Turbulence Cascade in Physical Space

Javier Jiménez, José I. Cardesa and Adrián Lozano-Durán

Abstract Some recent developments on the physical mechanism of turbulence cascades are summarised. It is first shown that the energy cascade in statistically steady isotropic turbulence is local in scale, at least on average, and that temporal variations of the large-scale forcing are transferred to smaller scales as a 'wave' consistent with the classical Kolmogorov model. It is further shown that, when energy-containing structure are individually tracked in band-pass filtered velocity fields, they also behave classically. The correlation of their physical position with larger (or smaller) structures is highest towards the beginning (or end) of their lifetimes. The analysis is then extended to the structures of momentum flux in the logarithmic layer of turbulent channels. Small structures grow and shrink smoothly along their lifetimes, but larger ones change size mostly by splits and mergers involving structures of similar size. For the largest structures, splits predominate, although not overwhelmingly.

1 Introduction

Cascades are required whenever a conserved quantity has to be transferred across a range of scales but, beyond that generic idea, every particular instance of multiscale transport requires a physical implementation that does not have to be the same in all cases. In fact, it is probably always true in high-dimensional systems that cascades include a variety of mechanisms that transfer the conserved quantity in different directions, in such a way that a one-directional transfer across scales is only true as a statistical average. The main problem lies in the traditional idea of scale, which, because of the Fourier uncertainty principle, only takes a definite meaning when averaged over a region of space larger than the scale in question. Based on the general idea that the Navier–Stokes equations are local PDEs in physical, but not in scale space (e.g. Fourier), our group have tried for some time to ascertain whether

J. Jiménez (✉) · J. I. Cardesa · A. Lozano-Durán
School of Aeronautics, Universidad Politécnica Madrid, 28040 Madrid, Spain
e-mail: jimenez@torroja.dmt.upm.es
URL: https://torroja.dmt.upm.es

M. Gorokhovski and F. S. Godeferd (eds.), *Turbulent Cascades II*,
ERCOFTAC Series 26, https://doi.org/10.1007/978-3-030-12547-9_6

some component of the various transfers in turbulence can be identified locally in physical space, and to clarify their mechanisms. We primarily do this by isolating individual intense structures, and tracking them in space, time and, occasionally, also across scales.

2 The Energy Cascade

The best-known example of a turbulent cascade is the transfer of kinetic energy in equilibrium isotropic turbulence [4]. If energy is fed by some large-scale forcing, it is transferred to the Kolmogorov scale, η, to be dissipated by viscosity, but the manner in which this happens has been the subject of endless discussions. We will first present evidence that the transfer is local in scale, at least on average. For example, Fig. 1a shows that, when the flow is separated into scale bands by filtering, and the forcing is unsteady, the unsteadiness of the sub-grid energy transfer, $\Sigma = -\langle \tau_{ij} \overline{S}_{ij} \rangle$, where τ_{ij} is the subgrid Reynolds stress tensor at the chosen filter width, and $\overline{S}_{ij}$ is the filtered rate of strain, moves towards bands of smaller scale as a 'wave' [1]. The mean $\langle \cdot \rangle$ refers to the time-dependent instantaneous average over the whole computational box. Moreover, the evolution of the transfer rate is self-similar, as posited by Kolmogorov, in the sense that the delay required by the energy to cross an octave of scales centred at r is proportional to the local eddy turnover, $r^{2/3}/\varepsilon^{1/3}$, where ε is the ensemble-averaged energy dissipation rate (Fig. 1b).

The energy cascade in isotropic turbulence is also local in physical space [2]. The band-filtered fields used in [1] can be segmented into individual structures of intense energy, and these structures can be followed in time. In a first approach, the evolution in this five-dimensional space (three spatial dimensions, scale, and time)

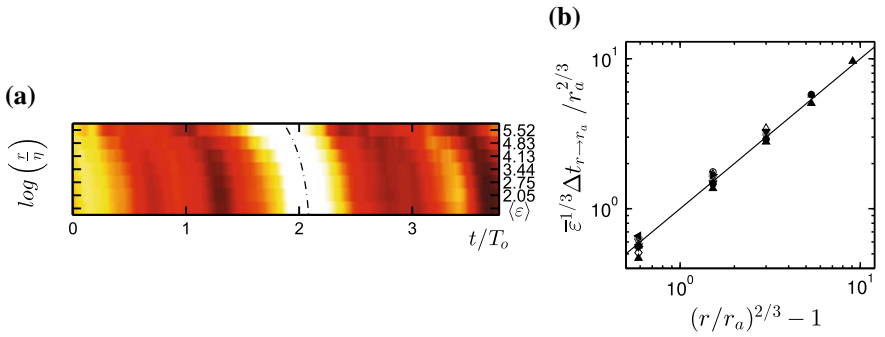

Fig. 1 **a** Time-scale diagram of $\Sigma(r)$, with the filter width r decreasing from top to bottom and the instantaneous mean dissipation $\langle\varepsilon\rangle$ added as the bottom band. Isotropic turbulence at microscale Reynolds number $Re_\lambda = 384$. The dashed-dotted line corresponds to $\varepsilon^{1/3}\Delta t = (250\eta)^{2/3} - r^{2/3}$. **b** Dimensionless average delay between the energy transfer at two filter widths, $r > r_a$. Several homogeneous flows. The slope of the solid line is linear. Reproduced with permission from [1]

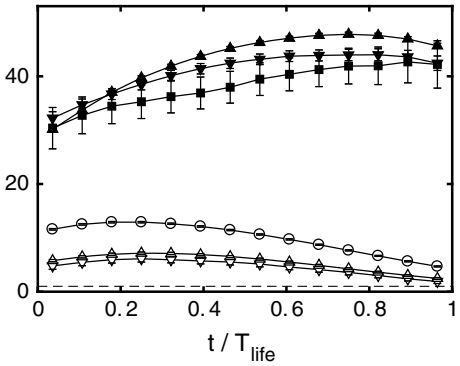

Fig. 2 Intersection ratio of individual structures of size r_A with the set of all structures of size r_B, separated from r_A by a factor of two. Normalised to unity for random sets, and plotted as function of the time within the life of each structure. ○, $r_A/\eta = 30$; △, 60; ▽, 120; □, 240. Solid symbols are for $r_B = r_A/2$; open ones are $r_B = 2r_A$. Error bars are two standard deviations. Adapted with permission from [2]

is too complex to have allowed tracking each structure individually up to now, but it can be handled statistically. A measure of how related are the location of two flow scales is the volume of the intersection of their intense structures, which has to be compared to the null hypothesis of randomly located point sets with the same overall volume fractions. It is found that structures in energy bands separated by a factor of 2 are more correlated than random, but that those separated by 4 or more are not [2]. This could simply be a sign of spectral leakage in the filter, but the structures are also tracked in time, so that each of them has a lifetime (which, not surprisingly, is proportional to $r^{2/3}$), and the evolution of its correlation can be measured. Figure 2 shows that structures of size r are more strongly correlated with those of size $2r$ at the beginning of their life than at the end. The opposite is true for their correlation with smaller structures of size $r/2$, in strong agreement with a process in which energy passes from larger to smaller structures at the same physical location.

3 Momentum Transfer in Shear Flows

Another conserved quantity whose transfer is important is the flux along the wall-normal (y) direction of streamwise momentum in turbulent shear flows. Traditionally, momentum is considered to be carried by the tangential Reynolds stress, uv, defined as the product of the streamwise and wall-normal velocity fluctuations. The structures (Qs) of particularly intense uv are often treated as important momentum carriers [8], and their organisation is different from that of the energy structures in isotropic turbulence. Only 'large' structures couple strongly enough to the shear of the mean velocity, $S = \partial_y U$, to carry net mean momentum. But the shear in the

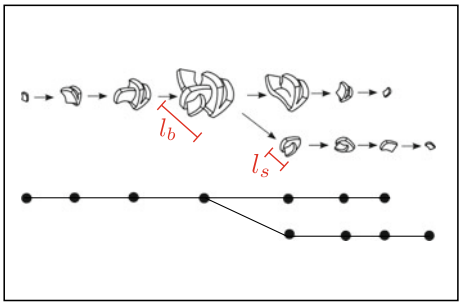

Fig. 3 Sketch of a simple evolution graph for Qs. Time increases from left to right, and the graph includes a split. Structure size is characterised by the diagonal ℓ of its circumscribed parallelepiped

inertial (logarithmic) layer of a wall-bounded flow changes as the inverse of the distance from the wall, and the result is that the inertial momentum-carrying Qs form a self-similar hierarchy of different scales in which most relevant Qs are attached to the wall, in the sense that their size is proportional to their distance from it. The transfer of momentum across this hierarchy is a problem that has to be understood as much as the Kolmogorov energy cascade, because equilibrium has to be maintained across scales, and the result determines the scaling parameters for the overall flow; for example, it defines the friction velocity as the uniform velocity scale in wall-bounded turbulence (and therefore the drag coefficient).

Three-dimensional Qs are studied for turbulent channels in [5], and tracked individually in time in [7]. They are found to grow and decay while they merge and split in complicated temporal graphs that have to be parsed to understand their evolution (Fig. 3). In agreement with their inertial character, their lifetime is proportional to their size, but, somewhat surprisingly given that they are mostly attached to the wall, they are not found to be particularly connected with it. Roughly half of the Qs are born near the wall and move away from it, while the other half do the opposite. In fact, Qs were studied in [3] for homogeneous shear turbulence, which shares with wall-bounded turbulence the role of the shear as a source of momentum transfer and of turbulent energy, but which has no walls. Its Qs differ very little from those in wall-bounded flows, showing that they are a consequence of the shear, rather than of the neighbourhood of the wall. The relevant condition for Qs to participate in momentum transfer is that they should be larger than the local Corrsin scale, $L_c = (S^3/\varepsilon)^{1/2}$. But $L_c \sim y$ in the logarithmic layer of wall-bounded flows, and most Qs larger than L_c are also too large to fit in the flow without hitting the wall. They are therefore attached.

From the point of view of the present paper, the most interesting question is the relevance of merging and splitting in the growth and decay of the momentum-carrying structures. Because Qs are defined by thresholding an intense property (uv), they are born and die as small structures, which at first grow in volume and later shrink. Part of this evolution is a smooth variation with time as a consequence of their intensification and weakening. Figure 4a shows that this accounts for most of the change in volume for Qs smaller than about 100 wall units (defined by the kinematic viscosity and the friction velocity, and denoted by a '+' superscript). Above that threshold, all Qs

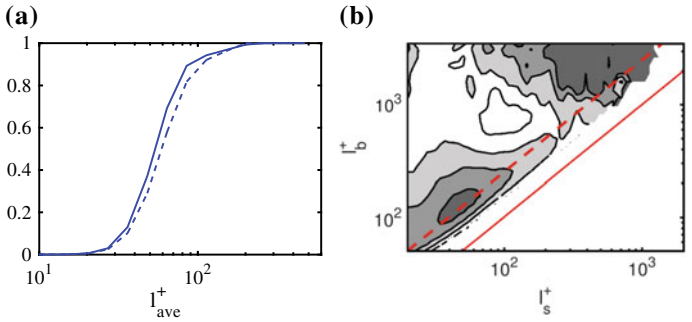

Fig. 4 **a** Fraction of the number of Qs that split (solid line) or merge (dashed) at least once in their lives, as a function of their mean diagonal size averaged over their lifetime. **b** Volume ratio between the direct (splits) and inverse (merge) cascade events, as a function of the size of the smallest and largest fragments in the interaction. The dashed line is $\ell_s = 0.4\ell_b$, and the solid one in $\ell_s = \ell_b$. Contours are, from light to dark, 1.1(0.2)1.7. Both figures refer to Qs above the viscous wall layer of a turbulent channel with friction Reynolds number $Re_\tau = 4200$ [6]

merge or split at least once in their life, and it can be shown that between 50 and 70% of the volume change of the largest Qs is due to these discontinuous events. If we interpret the mergers as an inverse cascade to larger volumes, and the splits as a direct cascade, the direct cascade predominates, although not by a large margin (rough 1.3 on average). Figure 4b shows that, disregarding the smallest Qs that cascade seldom, the direct cascade is a property of large structures that break into (or merge from) fragments of comparable size. Small fragments of large eddies have almost the same probability of merging as of splitting, but a large attached Q is roughly twice more likely to break in half than to be created from two comparable fragments.

In summary, the above examples show that cascades in turbulence can be associated to definite interactions that take place locally in physical space between entities of comparable size. In general, both direct and inverse events occur, leading respectively to the generation of smaller and of larger structures, but, in all our examples, the direct cascade predominates.

Funded in part by the Multiflow and Coturb projects of the European Research Council.

References

1. Cardesa, J.I., Vela-Martín, A., Dong, S., Jiménez, J.: The temporal evolution of the energy flux across scales in homogeneous turbulence. Phys. Fluids **27**, 111702 (2015)
2. Cardesa, J.I., Vela-Martín, A., Jiménez, J.: The turbulent cascade in five dimensions. Science **357**, 782–784 (2017)
3. Dong, S., Lozano-Durán, A., Sekimoto, A., Jiménez, J.: Coherent structures in statistically stationary homogeneous shear turbulence. J. Fluid Mech. **816**, 167–208 (2017)

4. Kolmogorov, A.N.: The local structure of turbulence in incompressible viscous fluids at very large Reynolds numbers. Dokl. Akad. Nauk. SSSR **30**, 301–305 (1941)
5. Lozano-Durán, A., Flores, O., Jiménez, J.: The three-dimensional structure of momentum transfer in turbulent channels. J. Fluid Mech. **694**, 100–130 (2012)
6. Lozano-Durán, A., Jiménez, J.: Effect of the computational domain on direct simulations of turbulent channels up to $Re_\tau = 4200$. Phys. Fluids **26**, 011702 (2014)
7. Lozano-Durán, A., Jiménez, J.: Time-resolved evolution of coherent structures in turbulent channels: characterization of eddies and cascades. J. Fluid Mech. **759**, 432–471 (2014)
8. Lu, S.S., Willmarth, W.W.: Measurements of the structure of the Reynolds stress in a turbulent boundary layer. J. Fluid Mech. **60**, 481–511 (1973)

Effects of Regenerating Cycle on Lagrangian Acceleration in Homogeneous Shear Flow

A. Barge and M. A. Gorokhovski


Abstract The aim of this paper is to identify the effects of the regenerating cycle phases on the Lagrangian acceleration statistics. Direct Numerical Simulation of fluid and inertial particles ($St = 3.0$) moving in a stationary homogeneous shear flow is performed and the autocorrelation functions of the norm and components of the Lagrangian acceleration vector are calculated. The energy balance between turbulent scales is first observed, and the range of scales, sensitive to growth and collapse phases, is identified. In link to this range, it was shown that the acceleration norm is correlated longer during a growth phase and shorter during a collapse phase. This effect is amplified when inertia of particles is increased. At the same time, it was shown that the acceleration vector components are invariant to the regenerating cycle.

A. Barge · M. A. Gorokhovski (✉)
Laboratoire de Mécanique des Fluides et d'Acoustique, École Centrale de Lyon, CNRS-Université Claude Bernard Lyon 1-INSA Lyon, Ecully, France
e-mail: mikhael.gorokhovski@ec-lyon.fr

M. Gorokhovski and F. S. Godeferd (eds.), *Turbulent Cascades II*,
ERCOFTAC Series 26, https://doi.org/10.1007/978-3-030-12547-9_7

1 Introduction

A DNS study of Lagrangian acceleration was mostly focused on the case of homogeneous isotropic turbulence. The case of homogeneous shear flow is more close to realistic flows. However such flows are less studied in terms of Lagrangian statistics of acceleration. The flow with homogeneous shear are characterized by the growth of turbulent structures with time [1, 2]. In computation, this growth takes place until the structures reach the size of the computational domain [3]. They then collapse, and the phase of growth restarts again. These phases are accompanied by successive increase and decrease of energy and of rate of dissipation (see Fig. 2). Thereby surprisingly, as it is shown in [3], the flow characteristics represent a statistically stationary process. Several studies [3, 4] demonstrated that properties and the mechanisms of such regenerative cycle of structure growth and collapse is similar to phenomena that appear in wall-bounded flows. This motivates the DNS study of flows with homogeneous shear, as a proper tool to isolate and to study Lagrangian properties of flows which mimic the flows closely to the wall. However at our knowledge, the only DNS observation of the Lagrangian acceleration in flows with homogeneous shear is the paper [5], in which the authors showed that the norm of acceleration of the fluid particle is long time correlated and linked to the largest turbulent scales whereas the acceleration orientation is correlated on times of order of the Kolmogorov time, and is linked to the dissipative scales. This study was limited to initial phase of the flow when the structures were only growing. The following question is raised: are the results of [5] valid when the flow is in the statistically stationary state, and how statistics of the fluid particle acceleration may be affected by growth and collapse phases? The next question is this: If particles are inertial, what is their reaction on growth and collapse phases and how inertia effects react to the process of regenerative cycle of turbulent structures? This motivated our work to perform statistics conditionally on those phases.

The paper is organized as follows: In Sect. 2, numerical methods are presented. In Sect. 3, a first part shows the sensitivity of turbulent scales to the growth and collapse phase of the regenerating cycle. In a second part, effects of these phases on Lagrangian autocorrelations functions of particles acceleration are discussed. Finally, conclusion will be drawn in Sect. 4.

2 Numerical Methods

We perform DNS of fluid and inertial particles moving in a turbulent flow confined in a periodic cubic box of size $L = 2\pi\ m$, discretized on 512^3 grid points and with an uniform mean shear $S = 3.2\,\mathrm{s}^{-1}$ imposed in one spatial direction. The kinematic viscosity is chosen as $\nu = 0.005\,\mathrm{m}^2\mathrm{s}^{-1}$. The mean velocity field is then:

$$\mathbf{U}(x_1, x_2, x_3) = (Sx_2, 0, 0) \tag{1}$$

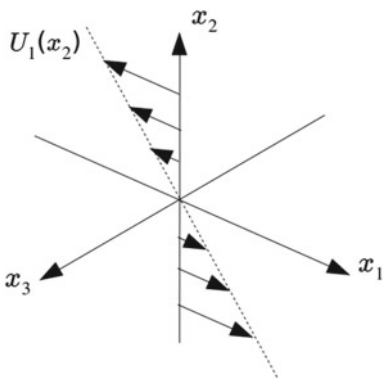

Fig. 1 Mean velocity profile in the homogeneous shear flow. Mean shear is here negative

and is illustrated on Fig. 1. The advection by the mean shear makes impossible to look for periodic solutions of the Navier-Stokes equations in the x_2 direction. To cope with this problem, we followed Rogallo [6] method of moving frame defined by:

$$x_1' = x_1 - Stx_2; \quad x_2' = x_2; \quad x_3' = x_3 \tag{2}$$

and we applied the remeshing operation to avoid the numerical instabilities increasing with the mesh deformation. Using periodicity in x_1 direction, the computational domain is transformed like if the box would have been skewed in the opposite direction of the mean flow. Then the domain moves back to a cubic state and the cycle starts again. Remeshing is done every time $S \cdot t = n + \dfrac{L_1}{2L_2}$; $n = 0, 1, 2, \ldots$ Navier-Stokes equations for the fluctuating velocity field are:

$$\frac{\partial u_i}{\partial t} + \frac{\partial u_i u_j}{\partial x_j} + Su_2\delta_{i1} = -\frac{1}{\rho}\frac{\partial p}{\partial x_i} + \frac{\partial u_i}{\partial x_j \partial x_j} \tag{3}$$

$$\frac{\partial u_i}{\partial x_i} = 0 \tag{4}$$

The Eqs. (3)–(4) are solved by pseudo-spectral methods in space; non-linear terms are directly solved with the classical 2/3 rule to avoid aliasing errors and the linear terms are implicitly calculated. Time integration is performed by a second order Runge-Kutta scheme. Particles are injected when the flow reaches the statistically stationary state and their displacements are calculated by integration of their motion equations:

$$\frac{d\mathbf{x}_p}{dt} = \mathbf{u}_p(t) + \delta_{i1} S x_{p2}(t) \tag{5}$$

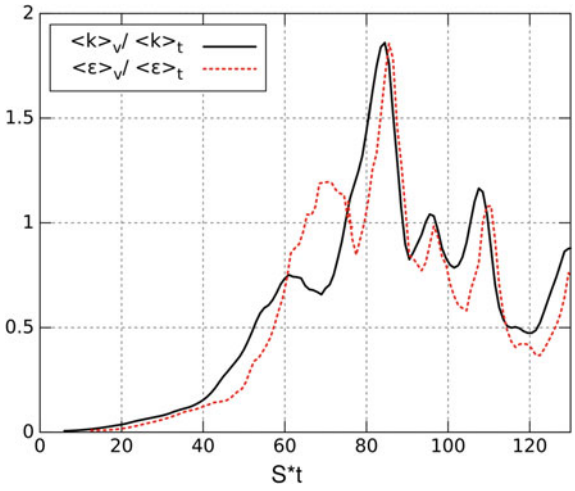

Fig. 2 Time evolution of energy $k = \frac{1}{2}\langle u_i u_i \rangle_V$ and dissipation $\varepsilon = 2\nu\langle S_{ij}^2 \rangle_V$ in the homogeneous shear flow. $\langle \bullet \rangle_V$ is the average over the volume of fluid and $\langle \bullet \rangle_t$ is the average over the volume of fluid and time from stationary state

$$\frac{d\mathbf{u}_p}{dt} = \frac{\mathbf{u}_f(\mathbf{x}_p(t), t) - \mathbf{u}_p(t)}{\tau_p} + \delta_{i1} Su_{p2}(t) \tag{6}$$

Here $\mathbf{u}_p(t)$ is the particle velocity, $\mathbf{u}_f(\mathbf{x}_p(t), t)$ is the fluid velocity at the particle position and $\tau_p = \frac{\rho_p d_p^2}{18\rho_f \nu}$ the typical response time of the particles. Henceforth the Stokes number is introduced as $St = \tau_p/\tau_\eta$. For each simulations, we consider the displacement of two types of particles: a fluid tracer and a heavy particle, the latter is characterized by the Stokes number $St = 3.0$. From Eq. (6) we can see that the longitudinal acceleration of particles $a_1 = a_1' + Su_{p2}$ has a mean acceleration term Su_{p2}. It has been shown [5] that this term has a negligible contribution to particles dynamics. Therefore hereafter we will consider only the fluctuating components of acceleration denoted by a_1, a_2 and a_3. Results are discussed in the next section (Fig. 2).

3 Results

The Lagrangian statistics are performed conditionally on different phases of the regenerating cycle by identification of two periods of observation. The first one is defined between the moment where energy is just stabilized after a decay period and the moment corresponding to the half of the following increasing period. This allows to isolate moments where structures are developing and growing. This period is called hereafter by Energy Rise (ER). The second time window is taken between the moment where energy is just stabilized after its increasing period and the moment

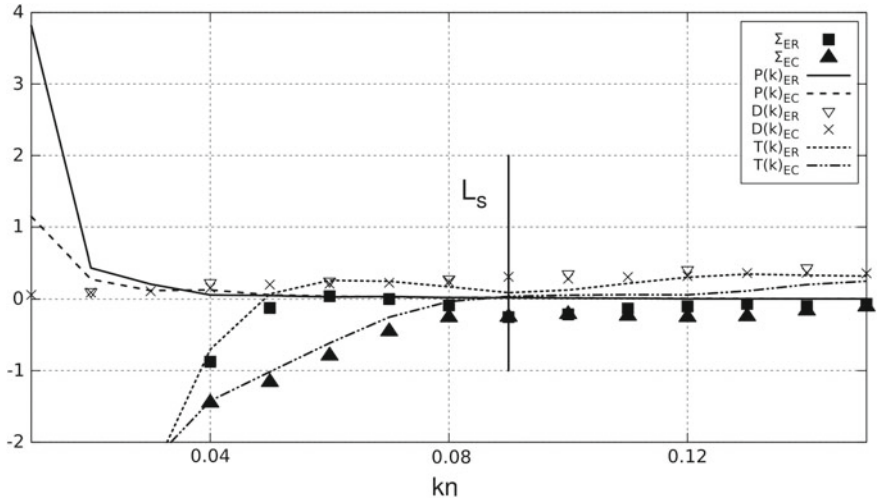

Fig. 3 Production $P(\mathbf{k})$, transfer $T(\mathbf{k})$ and dissipation $D(\mathbf{k})$ terms of the energy balance equation in the homogeneous shear flow as a function of spatial scales conditioned to the growth (ER) and collapse (EC) phases

corresponding to the half of the next decay period. This period is called by Energy Collapse (EC).

Because [5] showed that the acceleration statistics are related to different sizes of turbulent scales, we first identify which scales are sensitive to the regenerating cycle by focusing on the evolution of energy in the Fourier spectral space of spatial scales $\mathbf{k}$. Figure 3 shows the different terms of the energy balance equation $\Sigma(\mathbf{k}, t) = \dfrac{\partial E(\mathbf{k}, t)}{\partial t} = P(\mathbf{k}, t) + T(\mathbf{k}, t) - D(\mathbf{k}, t)$ as a function of turbulent scales and growth/collapse phases. It is seen that a range of scales larger than the shear scale $L_S = \sqrt{\varepsilon/S^3}$ (those scales are dominated by the anisotropy of the mean shear [7] and characterized by a transverse cascade [8]) are characterized by an equilibrium state during the growth phase while these large scales are losing the energy during the collapse phase due to transfer towards smaller scales. The difference can easily be explained because the very large structures have collapsed and the intermediate scales can not receive energy anymore from those structures. Consequently, the scales smaller than the shear scale (these scales are dominated by classic inertial cascade [7]) are mostly insensitive to the regenerating cycle.

The next step concerns observation of the autocorrelation functions of the amplitude and components of the particles acceleration vector. Since the flow can be considered as an instationary one on short times, the correlation coefficient was introduced in the following form:

$$\rho_A(\tau) = \frac{\langle A'(t)A'(t+\tau)\rangle}{\sqrt{\langle A'(t)^2\rangle\langle A'(t+\tau)^2\rangle}} \tag{7}$$

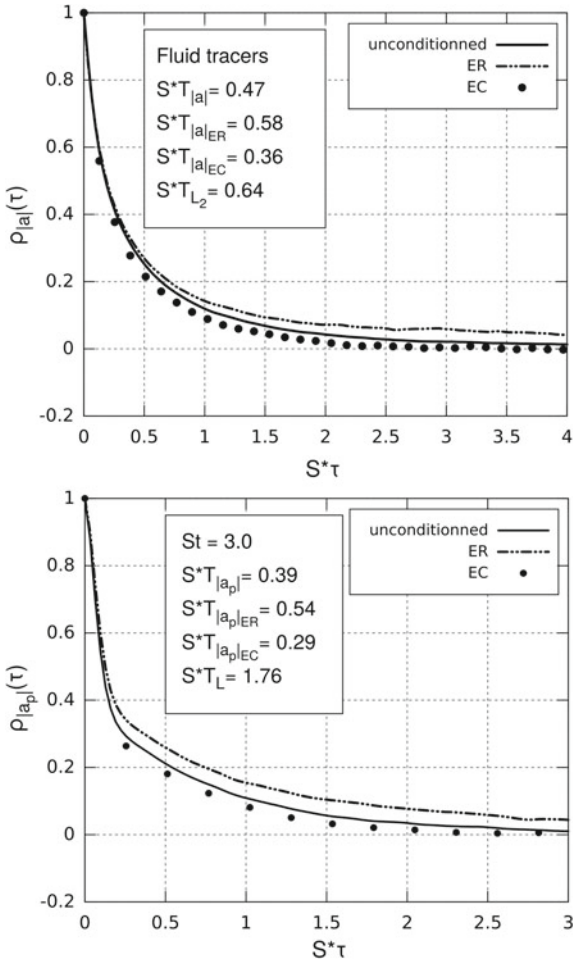

Fig. 4 Top panel: Autocorrelation functions of the acceleration norm of fluid particles in the homogeneous shear flow averaged over the complete simulation (—) and conditioned to the growth phase (— · ·—) and to the collapse phase (•). Bottom panel: Same figure for inertial particles with $St = 3.0$

where the angled brackets $\langle \bullet \rangle$ denote the average on all particles and A' the fluctuating value of A obtained by subtracting $\langle A \rangle$ calculated at the considered time. Preliminary to Lagrangian statistics on different phases of regenerating cycle, the unconditional statistics show in Figs. 4 and 5 that the acceleration norm of fluid particles is always correlated on long time while its components are correlated on the Kolmogorov time. The same observation is addressed to inertial particles (results for inertial acceleration components are not shown here). Since the norm of acceleration is correlated on large times which are linked to large structures of the homogeneous shear flow, one can expect the sensitivity of the acceleration norm to regenerating cycle. Figure 4 shows the autocorrelation functions of the acceleration norm for fluid and inertial particles conditioned to the growth and collapse phase of the cycle. It is seen that the time correlation of the acceleration norm is larger during a growth phase: the turbulent structures persist in time. After the collapse, the turbulent structures are smaller,

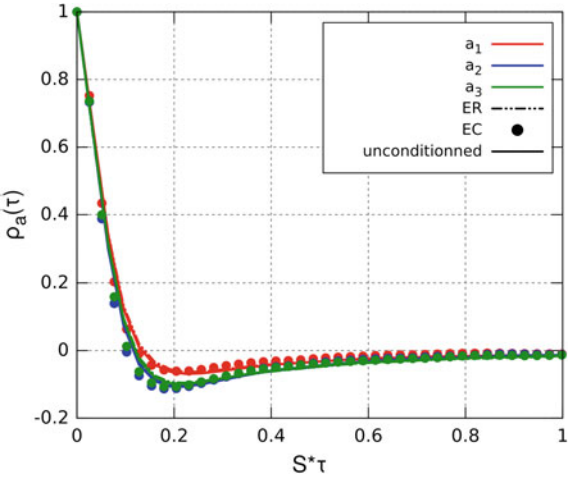

Fig. 5 Autocorrelation functions of the acceleration vector components of fluid particles in the homogeneous shear flow averaged over the complete simulation (—) and conditioned to the growth phase (— · ·—) and to the collapse phase (•)

and their typical lifetime is shorter. It is seen from Fig. 4 that such sensitivity is increased with inertia of particles ($T_{|a_p|_{ER}}/T_{|a_p|_{EC}} \sim 1.8$; $T_{|a|_{ER}}/T_{|a|_{EC}} \sim 1.6$). Unlike to the fluid particles, an inertial particle respond to larger turbulent scales due to filtering effects, being not disturbed by smaller fluctuations in the carrier phase. Then it turns out that in average, and specifically during the collapse phase, the time correlation of the acceleration norm is shorter when inertia increases. Concerning the autocorrelation functions of the acceleration vector components, it is shown in Fig. 5 that the time correlation of the acceleration orientation is, as expected, invariant with the regenerating cycle: the acceleration orientation is linked to small scales. The same conclusion can be made for the vector components of inertial particles (not shown here).

4 Conclusion

In homogeneous shear flow, this communication is addressed to effects of growth and collapse phases in the regenerative cycle on the Lagrangian autocorrelation functions of the acceleration of fluid and inertial particles. As it was observed in [5]: the acceleration norm is long time correlated and linked to the large turbulent scales, while components of the acceleration vectors are correlated on the Kolmogorov time. This property is also valid for inertial particles. However it was shown that acceleration statistics is sensitive to the regenerating cycle. Since scales larger than the shear scale intervene into growth and collapse phases, whereas scales smaller than shear scales do not, the acceleration norm is correlated longer during a growth phase and shorter during a collapse phase. This effect is amplified when inertia of particles is increased. At the same time the acceleration vector components are invariant to the regenerating cycle.

References

1. Tavoularis, S., Karnik, U.: Further experiments on the evolution of turbulent stresses in uniformly sheared turbulence. J. Fluid Mech. **204**, 457 (1989)
2. Rogers, M., Moin, P.: The structure of the vorticity field in homogeneous turbulent flows. J. Fluid Mech. **176**, 33–66 (1987)
3. Pumir, A.: Turbulence in homogeneous shear flows. Phys. Fluids (1994-present) **8**(11), 3112–3127 (1996)
4. Sekimoto, A., Dong, S., Jimenez, J.: Direct numerical simulation of statistically stationary and homogeneous shear turbulence and its relation to other shear flows. Phys. Fluids **28** (2016)
5. Yeung, P.K.: One- and two-particle lagrangian acceleration correlations in numerically simulated homogeneous turbulence. Phys. Fluids **9**(10), 2981–2990 (1997)
6. Rogallo, R.S.: Numerical experiments in homogeneous turbulence. In: NASA Technical Memorandum (1981)
7. Casciola, C.M., Gualtieri, P., Benzi, R., Piva, R.: Scale-by-scale budget and similarity laws for shear turbulence. J. Fluid Mech. **476**, 105–114 (2003)
8. Mamatsashvili, G., Khujadze, G., Chagelishvili, G., Dong, S., Jiménez, J., Foysi, H.: Dynamics of homogeneous shear turbulence: a key role of the nonlinear transverse cascade in the bypass concept. Phys. Rev. E **94** (2016)

Part II
Compressibility ⇔ Turbulence; Turbulence ⇔ Atomization

Energy Transfer and Spectra in Simulations of Two-Dimensional Compressible Turbulence

Alexei G. Kritsuk

Abstract We present results of high-resolution numerical simulations of compressible 2D turbulence forced at intermediate spatial scales with a solenoidal white-in-time external acceleration. A case with an isothermal equation of state, low energy injection rate, and turbulent Mach number $M \approx 0.34$ without energy condensate is studied in detail. Analysis of energy spectra and fluxes shows that the classical dual-cascade picture familiar from the incompressible case is substantially modified by compressibility effects. While the small-scale direct enstrophy cascade remains largely intact, a large-scale energy flux loop forms with the direct acoustic energy cascade compensating for the inverse transfer of solenoidal kinetic energy. At small scales, the direct enstrophy and acoustic energy cascades are fully decoupled at small Mach numbers and hence the corresponding spectral energy slopes comply with theoretical predictions, as expected. At large scales, dispersion of acoustic waves on vortices softens the dilatational velocity spectrum, while the pseudo-sound component of the potential energy associated with coherent vortices steepens the potential energy spectrum.

A. G. Kritsuk (✉)
University of California, San Diego, USA
e-mail: akritsuk@ucsd.edu

M. Gorokhovski and F. S. Godeferd (eds.), *Turbulent Cascades II*,
ERCOFTAC Series 26, https://doi.org/10.1007/978-3-030-12547-9_8

1 Introduction

Interstellar turbulence [17] is believed to play an important role regulating star formation [31] in molecular clouds [20]. However, our understanding of large-scale energy cycle in the interstellar medium (ISM) of disk-like galaxies remains incomplete. In particular, it is unclear how the energy injected in the ISM by stellar feedback and gravitational instabilities at scales comparable to the disk scale height h cascades to larger and smaller scales, shaping the structure and global stability of interstellar clouds. The phenomenology of such split energy cascade in quasi-two-dimensional turbulent thin layers of incompressible fluid has been discussed in [5, 34]. While the feasibility of inverse energy transfer in the galactic context has attracted some attention [7, 17], compressibility effects have never been studied quantitatively in sufficient detail. An important observational signature of the inverse energy cascade that can be verified numerically is the scaling of the column density spectrum, which exhibits a break at $\sim h^{-1}$ in a number of nearby disk-like galaxies observed face-on [4, 11, 14–16, 41]. Using numerical simulations of two-dimensional (2D) compressible turbulence, we recently demonstrated that the inverse cascade is truncated at turbulent Mach numbers approaching unity, when vortices get destabilized due to acoustic emission [19]. The acoustic vortex instability [8, 22, 23, 35] ultimately provides for a direct acoustic energy cascade, closing the energy flux loop above the injection scale [19].

In this communication we further detail energy transfer across scales in 2D, using numerical simulations of forced isothermal turbulence in a so-called dual-cascade setting. A high-order accurate low-dissipation numerical method provides enough scale separation to resolve both large- and small-scale 2D cascades on a $16{,}384^2$ grid. Energy transfer is analyzed in spectral space using our new formalism for compressible turbulence developed in [2] and generalized to magnetohydrodynamics in [3].

2 Numerics

We carried out implicit large eddy simulations (ILES) of compressible turbulence in a square periodic domain $L \times L$ covered with a uniform Cartesian grid of $N \times N$ points. The system is governed by the compressible Euler equations

$$\partial_t \rho + \nabla \cdot (\rho \boldsymbol{u}) = 0, \tag{1}$$

$$\partial_t (\rho \boldsymbol{u}) + \nabla \cdot (\rho \boldsymbol{u}\boldsymbol{u} + p\mathbf{I}) = \boldsymbol{f}, \tag{2}$$

$$\partial_t \mathscr{E} + \nabla \cdot [(\mathscr{E} + p)\,\boldsymbol{u}] = \boldsymbol{u} \cdot \boldsymbol{f}, \tag{3}$$

where ρ is the density, $\boldsymbol{u}$—velocity, p—pressure, and $\mathscr{E} = \rho(u^2/2 + e)$—total energy density, $\mathbf{I} = \{\delta_{ij}\}_{i,j=1}^{2}$—identity matrix. A solenoidal, white-in-time random external force per unit mass $\boldsymbol{a} = \boldsymbol{f}/\rho$ is applied at an intermediate pumping scale

Table 1 Simulations and parameters

Case	N	λ_f	ε_f	$t_{\rm start}$	$t_{\rm cnd}$	$t_{\rm sat}$	$t_{\rm end}$	$M_{\rm end}$
A	8192	0.012	0.001	0	158	390	450	0.52
B	16,384	0.006	0.001	124	–	–	180	0.34

$\lambda_f = 2\pi/k_f$. The system is closed by an ideal gas equation of state $p = (\gamma - 1)\rho e$ with the ratio of specific heats set very close to unity, $\gamma \equiv c_p/c_v = 1.001$, e.g., [27]. The dimensionless units are chosen so that the box size $L = 1$, the mean density $\rho_0 = 1$, and the speed of sound $c_{s,0} = 1$. The rate of kinetic energy injection by the forcing is relatively small, $\varepsilon_f \in [0.001, 0.01]$, as substantially higher rates would inhibit the inverse cascade with most of the added energy dissipated in shocks right at the injection scale. The force correlation time is $\sim 10^4$ times shorter than the characteristic vortex turn-over time at λ_f, $\tau_f = \rho_0^{1/3}\lambda_f^{2/3}\varepsilon_f^{-1/3}$. In this formulation, each case is fully defined by three input parameters $(N, \varepsilon_f, \lambda_f)$, see Table 1.

While we computed about a dozen different cases, here we shall focus only on the two highest resolution weakly forced cases A and B. Case A was evolved through $t_{\rm end} = 450$ box-crossing times $\tau = L/c_{s,0}$ with the piecewise parabolic method [10], reaching the turbulent Mach number $M \approx 0.54$. We distinguish the following evolutionary stages: (i) a quasi-incompressible regime with linear total energy growth $E \equiv \int \mathscr{E} d\boldsymbol{x} \sim 0.92\varepsilon_f t$ at $t \in [0, 50]$ and Mach numbers $M \in [0, 0.25]$, (ii) a weakly compressible turbulence regime with shocklets at $t \in [50, 158]$ and $M \in [0.25, 0.3]$, with $E \propto 0.35\varepsilon_f t$, (iii) an energy condensation event at $t \approx 158$, marking a fully developed inverse energy cascade, followed by (iv) further growth of the condensate at $t \in [158, 380]$ still with $E \propto 0.35\varepsilon_f t$, and (v) energy saturation at $t \in [380, 450]$ and $M \sim 0.54$ [19].

Case B was restarted from case A at $t = 124$ after doubling the inverse cascade range by combining 4 identical boxes into one larger square box covered with a $16{,}384^2$ grid. We then evolved case B for 26 box-crossing times to get rid of all transients associated with the restart and to further develop the inverse cascade in the new enlarged domain. Finally, we evolved the case for $\Delta t = 30\tau$ at $M \sim 0.34$ and collected 600 data snapshots at $t \in [150, 180]$ to study turbulence statistics. For this simulation, we used a more accurate method described below, which allowed us to double the spectral bandwidth in the inertial range of the direct enstrophy cascade (i.e. below the energy injection scale). Hence, we essentially doubled the extent of inertial ranges for both incompressible cascades compared to case A.

To evolve case B, we used a variable high-order 3D solver developed for problems involving turbulence with strong shocks and density variations at flow speeds that range from nearly incompressible to hypersonic [24, 39] and implemented in the ADPDIS3D code. Our production runs used an optimal subset of numerical methods, which includes: (i) 8th-order-accurate central spatial base scheme that employs a split form of the inviscid flux derivative for better numerical stability [13]; (ii) non-linear Ducros et al. sensor [12] to filter the solution and provide extra dissipation where needed, using a dissipative portion of the 7th-order WENO scheme and limiting the use of numerical dissipation away from discontinuities with a control parameter,

distinguishing shocks from vortical flow types; and (iii) 4th-order Runge-Kutta time integration.

3 Results

Time-averaged velocity power spectra for case B are shown in Fig. 1. The spectrum is defined by $P(\boldsymbol{u},k) \equiv \int |\widehat{\boldsymbol{u}}(\boldsymbol{\kappa})|^2 \delta(k-|\boldsymbol{\kappa}|) d\boldsymbol{\kappa}$, where $\widehat{\boldsymbol{u}}(\boldsymbol{k})$ denotes the Fourier transform of the velocity $\boldsymbol{u}(\boldsymbol{x})$ and $\delta(k)$ is the Dirac delta function. Averaging over a short period of time $\Delta t = 30\tau$ at $t > 150$ is justified because at $\varepsilon_f = 0.001$ the energy growth $E(t) \propto 0.33\varepsilon_f t$ is slow and only affects the tip of the spectrum at the lowest wave numbers, while the rest of the spectrum remains statistically stationary. As can be seen in Fig. 1, the spectral slopes deviate from classical predictions for incompressible turbulence in two dimensions [25, 26].

With a well-resolved stochastic forcing, we obtain $P(\boldsymbol{u},k) \propto k^{-2}$ at $k < k_f$ instead of $P(\boldsymbol{u},k) \propto k^{-5/3}$. The same scaling was measured at similar Mach numbers in case A, just before the energy condensation occurred [19]. At $k > k_f$, where one would normally expect to see $P(\boldsymbol{u},k) \propto k^{-3}$, the spectrum does not show any clear power-law scaling range, even though the numerical method used in case B is sufficiently accurate to resolve an inertial range.

To discuss the origin of these deviations in compressible turbulence, we use Helmholtz decomposition $\boldsymbol{u} = \boldsymbol{u}_s + \boldsymbol{u}_d$, separating solenoidal $\boldsymbol{u}_s$ and dilatational $\boldsymbol{u}_d$ velocity components. The decomposed spectra $P(\boldsymbol{u}_s,k)$ and $P(\boldsymbol{u}_d,k)$ are also shown in Fig. 1. The solenoidal component $\boldsymbol{u}_s$ clearly dominates over the dilatational one at all wave numbers, except for $k \gtrsim 5k_f$. A local peak in $P(\boldsymbol{u}_s,k)$ at k_f is associated with the forcing, while $P(\boldsymbol{u}_d,k)$ does not show any feature at k_f because the external acceleration $\boldsymbol{a} = \boldsymbol{f}/\rho$ is divergence-free.

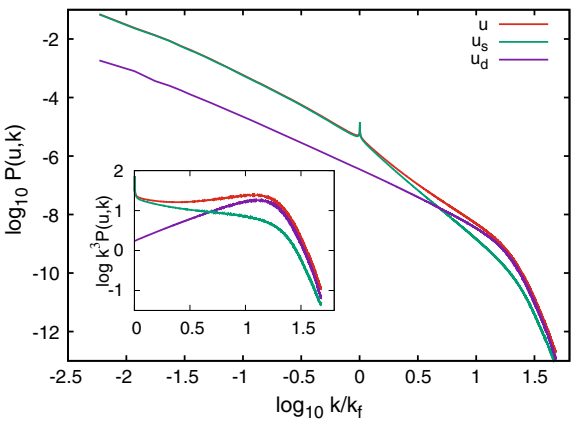

Fig. 1 Power spectra of the velocity $\boldsymbol{u}$ (red) and its solenoidal $\boldsymbol{u}_s$ (green) and dilatational $\boldsymbol{u}_d$ (purple) components. The solenoidal component dominates at large scales, $k \lesssim k_f$, while the dilatational one dominates at small scales, $k \gg k_f$, resulting in a 'bottleneck' in the velocity spectrum, see the inset for k^3-compensated small-scale spectra

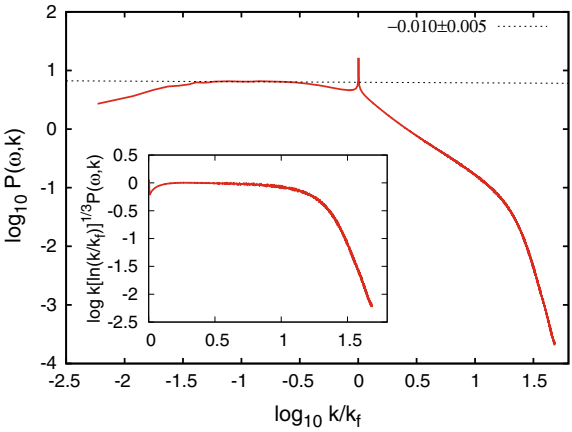

Fig. 2 Vorticity power spectrum is essentially flat at $k < k_f$, $P(\omega, k) \propto k^0$, consistent with $P(\boldsymbol{u}_s, k) \propto k^{-2}$. At $k > k_f$, the spectrum closely follows Kraichnan's prediction $P(\omega, k) \propto k^{-1}[\ln(k/k_f)]^{-1/3}$ [26], see compensated spectrum in the inset

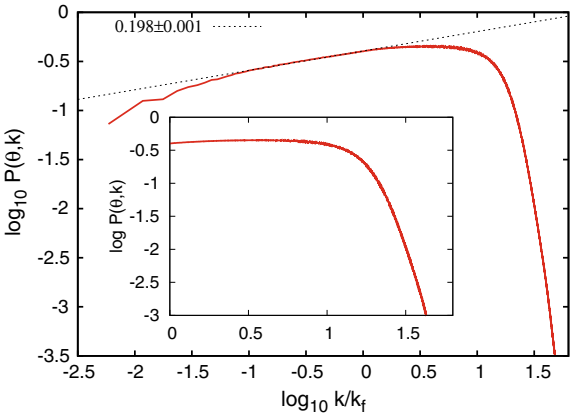

Fig. 3 Power spectrum of the velocity divergence $\theta \equiv \nabla \cdot \boldsymbol{u}$. At large scales, $P(\theta, k) \propto k^{1/5}$, while at $k > k_f$ the spectrum scales approximately as $P(\theta, k) \propto k^0$, reflecting $P(\boldsymbol{u}_d, k) = k^{-2} P(\theta, k) \propto k^{-2}$, see the inset

To detail the velocity scaling further, we show spectra of the vorticity $\boldsymbol{\omega} \equiv \nabla \times \boldsymbol{u} = \nabla \times \boldsymbol{u}_s$ and dilatation $\theta \equiv \nabla \cdot \boldsymbol{u} = \nabla \cdot \boldsymbol{u}_d$ in Figs. 2 and 3, respectively. Above the injection scale, at $k/k_f \in [0.03, 0.3]$, the vorticity spectrum is flat $P(\boldsymbol{\omega}, k) \propto k^0$, corresponding to $P(\boldsymbol{u}_s, k) \propto k^{-2}$. There is a slight deep in the spectrum just above the injection scale at $k/k_f \in [0.3, 1]$, where a small fraction of pumped up solenoidal kinetic energy is being converted into acoustic energy.

At $k > k_f$, the vorticity spectrum is steeper than k^{-1} and hence $P(\boldsymbol{u}_s, k)$ is steeper than k^{-3}, as can also be seen in the inset of Fig. 1. The logarithmic correction $[\ln(k/k_f)]^{-1/3}$, however, is sufficient to have a compensated spectrum approximately flat for about a decade in k (see inset in Fig. 2). The solenoidal velocity spectrum, thus, closely follows Kraichnan's prediction [26] for the direct enstrophy cascade in incompressible 2D turbulence, i.e. $P(\boldsymbol{u}_s, k) \propto k^{-3}[\ln(k/k_f)]^{-1/3}$ at $k > k_f$. It is worth noting that smooth flows in ideal 2D compressible hydrodynamics conserve the potential vorticity $\boldsymbol{\omega}/\rho$ of any streamline, but when compressibility is small, the enstrophy cascade persists, much as in the incompressible case [19].

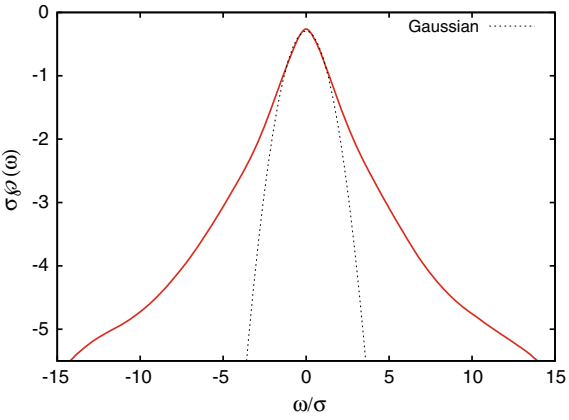

Fig. 4 The vorticity PDF is strongly non-Gaussian, reflecting the presence of coherent vortices. Vorticity ω is normalized by its rms fluctuations σ

At the same time, the spectrum of solenoidal velocity $P(\boldsymbol{u}_s, k) \propto k^{-2}$ is substantially steeper than $k^{-5/3}$ at $k < k_f$. Similar spectral slopes were previously seen in 2D simulations of incompressible turbulence with stochastic forcing in which the forcing scale λ_f is sufficiently well resolved and large-scale friction is not included [37]. The steep spectra were associated with the emergence of coherent vortices, which usually coexist with the inverse energy cascade in 2D [9]. The vortices do not form if λ_f is unresolved; they also may get destabilized if a stationary external force is used [32] or if the order of hypodissipation is small enough [6]. The presence of coherent vortices is reflected in the strongly non-Gaussian shape of single-point vorticity PDF (see Fig. 4 and Ref. [37]). Moreover, scaling exponents ζ_p of the transverse solenoidal velocity structure functions $|\Delta \boldsymbol{u}_s^{\perp}(\ell)|^p \propto \ell^{\zeta_p}$ also show anomalies with $\zeta_p > p/3$ at $p < 3$ and saturate at $\zeta_p \approx 1$ for order $p \in [3, 6]$ due to the presence of vortices [38], cf. [6]. Overall, the emerging population of vortices appears to substantially control the dynamics of 2D turbulence in our cases A and B.

Let us now consider the spectrum of dilatation (Fig. 3), which has a small positive slope $P(\theta, k) \propto k^{0.2}$ at $k < k_f$ and then flattens to $P(\theta, k) \propto k^0$ at $k > k_f$. The dilatational velocity spectrum at small scales $P(\boldsymbol{u}_d, k) \propto k^{-2}$ is consistent with theoretical prediction for the potential velocity component in acoustic turbulence by Kadomtsev and Petviashvili [21]. Indeed, at small Mach numbers, the direct acoustic energy and enstrophy cascades proceed independently of each other at $k \gtrsim k_f$.

At $k < k_f$, we observe a slightly more shallow spectrum of dilatational velocity $P(\boldsymbol{u}_d, k) \propto k^{-1.8}$. Due to dispersion of acoustic waves on large-scale coherent vortices, the slope is expected to lie approximately half-way between -2 (the case of purely potential velocity [21]) and $-11/7 \approx -1.57$ (as suggested for 2D in Ref. [18] based on arguments similar to those advanced for 3D acoustic turbulence by Zakharov and Sagdeev [40], see also [28–30, 33]).

Besides the velocity spectra, it is worth inspecting the spectral densities of kinetic and potential energy, $K(k) = P(\rho \boldsymbol{u}, \boldsymbol{u}; k)/2$ and $U(k) = P(\rho, e; k)/2 + U_0 \delta(k)/2$, respectively (here $U_0 \equiv \int \rho e d\boldsymbol{x}$). Indeed, the total energy $E = \int_0^\infty E(k) dk =$

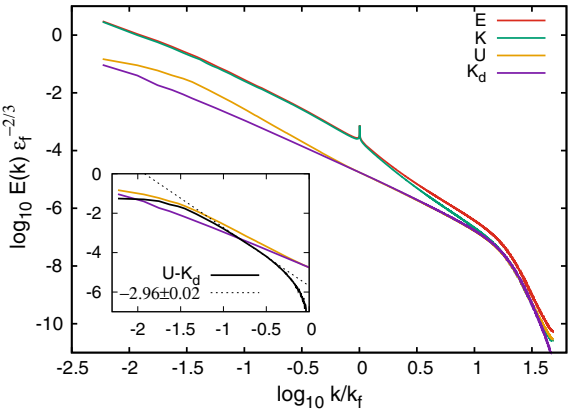

Fig. 5 Total $E(k)$ (red), kinetic $K(k)$ (green), and potential $U(k)$ (brown) spectral energy densities. Also shown is the dilatational component $K_d(k)$ (purple) of the kinetic energy in detailed equipartition with the potential one $K_d(k) \approx U(k)$ at $k \gtrsim k_f$

$K + U = \int_0^\infty [K(k) + U(k)]dk$ is an ideal invariant of the isothermal system. Following Ref. [2], we define the spectral densities as cospectra $P(\boldsymbol{a}, \boldsymbol{b}; k) \equiv \int [\widehat{\boldsymbol{a}}(\boldsymbol{\kappa}) \cdot \widehat{\boldsymbol{b}}^*(\boldsymbol{\kappa}) + \widehat{\boldsymbol{a}}^*(\boldsymbol{\kappa}) \cdot \widehat{\boldsymbol{b}}(\boldsymbol{\kappa})]\delta(k - |\boldsymbol{\kappa}|)d\boldsymbol{\kappa}/2$, with $\boldsymbol{a} = \rho\boldsymbol{u}$, $\boldsymbol{b} = \boldsymbol{u}$ in case of the kinetic energy and $a = \rho$, $b = e$ for the potential energy. While these generic definitions are valid for arbitrary degree of compressibility, in the Mach number regimes realized in case B, the kinetic energy spectra can be reasonably well approximated by $K(k) \approx \rho_0 P(\boldsymbol{u}, k)/2$ at all resolved wave numbers. Likewise, the kinetic energy spectral density can be approximately decomposed into solenoidal and dilatational parts $K(k) \approx K_s(k) + K_d(k)$, where $K_s(k) = \rho_0 P(\boldsymbol{u}_s, k)/2$ and $K_d(k) = \rho_0 P(\boldsymbol{u}_d, k)/2$.

Figure 5 shows the relevant spectral energy densities: total $E(k)$, kinetic $K(k)$, potential $U(k)$, and dilatational kinetic $K_d(k)$. Overall, these look similar to the corresponding velocity spectra, except for $U(k)$, which is new. One can clearly see the detailed acoustic energy equipartition $U(k) \approx K_d(k)$ at $k \gtrsim k_f$ [2, 36]. However, at large scales, the presence of coherent vortices breaks this equipartition, as pseudo-sound component of $U(k)$ associated with the vortices makes the potential energy exceed $K_d(k)$ at $k < k_f$. The inset in Fig. 5 details the pseudo-sound contribution $U(k) - K_d(k)$ shown in black, which scales approximately as k^{-3}. This scaling can be readily derived, assuming that centrifugal force is balanced by the pressure gradient in coherent vortices and $P(\boldsymbol{u}, k) \propto k^{-2}$. We thus see a large-scale excess of $U(k)$ as another (purely compressible) signature of the presence of coherent vortices in the inertial range of inverse energy cascade.

Finally, spectral energy fluxes computed using the formalism developed in Ref. [2] are shown in Fig. 6. The kinetic $\Pi_K(k)$ (green) and potential $\Pi_U(k)$ (brown) energy fluxes form a flux loop at $k < k_f$, as solenoidal kinetic energy inversely cascades to large scales, where it gets converted into acoustic energy, which then directly cascades to small scales [19]. The net total energy flux $\Pi(k) = \Pi_K(k) + \Pi_U(k)$ (red) is split in two roughly equal parts: one cascading inversely to feed the continuing energy growth of the system, and another cascading directly to rid the system of the excessive

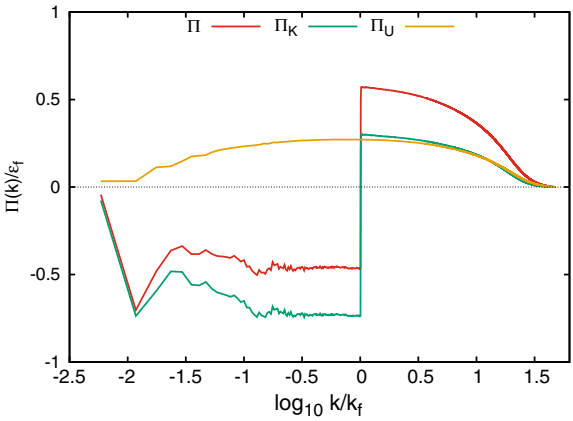

Fig. 6 Net $\Pi(k)$ (red), kinetic $\Pi_K(k)$ (green), and potential $\Pi_U(k)$ (brown) spectral energy fluxes normalized by the kinetic energy injection rate ε_f. Note that the total energy $E(t)$ is not statistically stationary and continues to grow at a rate of approximately $0.33\varepsilon_f$ within the time-averaging interval $t \in [150, 180]$

acoustic noise. In the mean time, shock dissipation actively drains the kinetic energy of the isothermal system across scales. It is worth noting that the kinetic and potential components of the net flux are comparable, while the kinetic-to-potential energy ratio generally oscillates around 10%. Thus, even small compressibility can alter or even reverse the energy transfer across scales. Another remark due here is on the notion of 'kinetic energy cascade' sometimes used in compressible turbulence, even though K is not an invariant of the dynamics, e.g., [1]. Our 2D case provides a curious illustration, as the solenoidal and dilatational components of the kinetic energy cascade in opposite directions at $k < k_f$.

4 Summary

We presented results of high-resolution numerical simulations of compressible 2D turbulence forced at intermediate spatial scales with a solenoidal white-in-time external acceleration. We studied in detail a case with an isothermal equation of state, low energy injection rate, and turbulent Mach number $M \approx 0.34$ without energy condensate. Our analysis of energy spectra and fluxes shows that the classical dual-cascade picture familiar from the incompressible case is substantially modified by compressibility effects. While the small-scale direct enstrophy cascade remains largely intact, a large-scale energy flux loop forms with the direct acoustic energy cascade compensating for the inverse transfer of solenoidal kinetic energy. At small scales, the direct enstrophy and acoustic energy cascades are fully decoupled at low Mach numbers, and hence the corresponding spectral energy slopes comply with theoretical predictions [21, 26], as expected. At large scales, dispersion of acoustic waves on vortices softens the dilatational velocity spectrum [33, 40], while pseudo-sound component of the potential energy associated with coherent vortices steepens the potential energy spectrum.

Acknowledgements This research was supported in part by the National Science Foundation through Grant No. AST-1412271 as well as through XSEDE allocation MCA07S014 on *Stampede*-1/2 at TACC (production runs) and on *Comet* at SDSC (data analysis).

References

1. Aluie, H., Li, S., Li, H.: Conservative cascade of kinetic energy in compressible turbulence. ApJL **751**, L29 (2012)
2. Banerjee, S., Kritsuk, A.G.: Exact relations for energy transfer in self-gravitating isothermal turbulence. Phys. Rev. E **96**, 053116 (2017)
3. Banerjee, S., Kritsuk, A.G.: Energy transfer in compressible magnetohydrodynamic turbulence for isothermal self-gravitating fluids. Phys. Rev. E **97**, 023107 (2018)
4. Block, D.L., Puerari, I., Elmegreen, B.G., Bournaud, F.: A two-component power law covering nearly four orders of magnitude in the power spectrum of spitzer far-infrared emission from the large magellanic cloud. ApJL **718**, L1 (2010)
5. Boffetta, G., Celani, A., Musacchio, S.: Split energy cascade in quasi-2D turbulence. In: Eckhardt, B. (ed.) Advances in Turbulence XII. Springer Proceedings in Turbulence, vol. 132, p. 173 (2009)
6. Boffetta, G., Celani, A., Vergassola, M.: Inverse cascade in two-dimensional turbulence: deviations from Gaussian behavior. Phys. Rev. E **61**, R29 (2000)
7. Bournaud, F., Elmegreen, B.G., Teyssier, R., Block, D.L., Puerari, I.: ISM properties in hydrodynamic galaxy simulations: turbulence cascades, cloud formation, role of gravity and feedback. MNRAS **409**, 1088 (2010)
8. Broadbent, E.G., Moore, D.W.: Acoustic destabilization of vortices. Philos. Trans. R. Soc. A **290**, 353 (1979)
9. Burgess, B.H., Scott, R.K., Shepherd, T.G.: Kraichnan-Leith-Batchelor similarity theory and two-dimensional inverse cascades. J. Fluid Mech. **767**, 467 (2015)
10. Colella, P., Woodward, P.R.: The piecewise parabolic method (PPM) for gas-dynamical simulations. J. Comput. Phys. **54**, 174 (1984)
11. Combes, F., Boquien, M., Kramer, C., et al.: Dust and gas power spectrum in M 33. A&A **539**, A67 (2012)
12. Ducros, F., Ferrand, V., Nicoud, F., Weber, C., Darracq, D., Gacherieu, C., Poinsot, T.: Large-eddy simulation of the shock/turbulence interaction. J. Comput. Phys. **152**, 517 (1999)
13. Ducros, F., Laporte, F., Soulères, T., Guinot, V., Moinat, P., Caruelle, B.: High-order fluxes for conservative skew-symmetric-like schemes in structured meshes: application to compressible flows. J. Comput. Phys. **161**, 114 (2000)
14. Dutta, P., Begum, A., Bharadwaj, S., Chengalur, J.N.: HI power spectrum of the spiral galaxy NGC628. MNRAS **384**, L34 (2008)
15. Dutta, P., Begum, A., Bharadwaj, S., Chengalur, J.N.: The scaleheight of NGC 1058 measured from its HI power spectrum. MNRAS **397**, L60 (2009)
16. Dutta, P., Begum, A., Bharadwaj, S., Chengalur, J.N.: Probing interstellar turbulence in spiral galaxies using HI power spectrum analysis. New Astron. **19**, 89 (2013)
17. Elmegreen, B.G., Scalo, J.: Interstellar turbulence I: observations and processes. ARA&A **42**, 211 (2004)
18. Elsässer, K., Schamel, H.: Energy spectra of turbulent sound waves. Zeitschrift Phys. B **23**, 89 (1976)
19. Falkovich, G., Kritsuk, A.G.: How vortices and shocks provide for a flux loop in two-dimensional compressible turbulence. Phys. Rev. Fluids **2**, 092603 (2017)
20. Hennebelle, P., Falgarone, E.: Turbulent molecular clouds. A & A Rev. **20**, 55 (2012)
21. Kadomtsev, B.B., Petviashvili, V.I.: Acoustic turbulence. Sov. Phys. Doklady **18**, 115 (1973)

22. Klyatskin, V.I.: Sound radiation by a system of vortices. Izv. Akad. Nauk. SSSR, Mekh. Zhidk. Gaza **1**, 87 (1966)
23. Kop'ev, V.F., Leont'ev, E.A.: On acoustic instability of an axial vortex. Akust. Zh. **29**, 192 (1983)
24. Kotov, D.V., Yee, H.C., Wray, A.A., Hadjadj, A., Sjögreen, B.: High order numerical methods for the dynamic SGS model of turbulent flows with shocks. Comm. Comput. Phys. **19**, 273 (2016)
25. Kraichnan, R.H.: Inertial ranges in two-dimensional turbulence. Phys. Fluids **10**, 1417 (1967)
26. Kraichnan, R.H.: Inertial-range transfer in two- and three-dimensional turbulence. J. Fluid Mech. **47**, 525 (1971)
27. Kritsuk, A.G., Norman, M.L., Padoan, P., Wagner, R.: The statistics of supersonic isothermal turbulence. Astrophys. J. **665**, 416 (2007)
28. Lvov, V.S., Mikhailov, A.V.: Sound and hydrodynamic turbulence in a compressible fluid. Zh. Eksper. Teor. Fiziki **74**, 1445 (1978)
29. Lvov, V.S., Mikhailov, A.V.: Scattering and interaction of sound with sound in a turbulent medium. Zh. Eksper. Teor. Fiziki **75**, 1669 (1978)
30. Lvov, V.S., Mikhailov, A.V.: Contribution to the nonlinear theory of sound and hydrodynamic turbulence of a compressible liquid. Physica D **2**, 224 (1981)
31. McKee, C.F., Ostriker, E.C.: Theory of star formation. ARA&A **45**, 565 (2007)
32. Mizuta, A., Matsumoto, T., Toh, S.: Transition of the scaling law in inverse energy cascade range caused by a nonlocal excitation of coherent structures observed in two-dimensional turbulent fields. Phys. Rev. E **88**, 053009 (2013)
33. Moiseev, S.S., Sagdeev, R.Z., Tur, A.V., Ianovskii, V.V.: Structure of acoustic-vortical turbulence. Akad. Nauk SSSR Doklady **236**, 1112 (1977)
34. Musacchio, S., Boffetta, G.: Split energy cascade in turbulent thin fluid layers. Phys. Fluids **29**, 111106 (2017)
35. Naugol'nykh, K.A.: Nonlinear sound waves upon collapse of a vortex dipole. Acoust. Phys. **60**, 424 (2014)
36. Sarkar, S., Erlebacher, G., Hussaini, M.Y., Kreiss, H.O.: The analysis and modelling of dilatational terms in compressible turbulence. J. Fluid Mech. **227**, 473 (1991)
37. Scott, R.K.: Nonrobustness of the two-dimensional turbulent inverse cascade. Phys. Rev. E **75**, 046301 (2007)
38. Wang, L.P., Kritsuk, A.G.: Scaling and intermittency in two-dimensional compressible turbulence. Phys. Rev. (in preparation) (2018)
39. Wang, W., Yee, H.C., Sjögreen, B., Magin, T., Shu, C.-W.: Construction of low dissipative high-order well-balanced filter schemes for non-equilibrium flows. J. Comput. Phys. **230**, 4316 (2011)
40. Zakharov, V.E., Sagdeev, R.Z.: Spectrum of acoustic turbulence. Sov. Phys. Doklady **15**, 439 (1970)
41. Zhang, H.-X., Hunter, D.A., Elmegreen, B.G.: H I power spectra and the turbulent interstellar medium of Dwarf irregular galaxies. ApJ **754**, 29 (2012)

The Exact Solution to the 3D Vortex Compressible Euler Equation and the Clay Millennium Problem Generalization

S. G. Chefranov and A. S. Chefranov

Abstract The general exact solution of the Cauchy problem to the 3D Euler vortex equation for compressible flow in unbound space is obtained. This solution has singularity at finite time and coincides with the vortex solution of the 3D Hopf equation for particles motion by inertia. A closed description of the evolution of enstrophy and all higher moments for the corresponding vortex field is established, giving an exact solution to the problems of closure in the theory of turbulence. On the base of this solution the smooth solution of the Navier-Stokes 3D equation for viscous compressible medium is obtained taking into account the effective viscosity and representation for the pressure field, which follows from the integral entropy balance equation, not from the medium equation of state. The above provides a positive solution for the Clay Millennium Problem (www.claymath.org) just in the case of its generalization on the Navier-Stokes equation for the compressible medium, for which an absence of smooth solutions on finite time interval has been a priori assumed before.

1 Introduction

1. The Euler equations, which express the impulse and mass conservation laws, for the case of ideal compressible medium are well-known for already more than 250 years (since 1755) and have the following form [1–4]:

$$\frac{\partial u_i}{\partial t} + u_j \frac{\partial u_i}{\partial x_j} = \frac{1}{\rho}\left(f_i - \frac{\partial p}{\partial x_i}\right) \tag{1}$$

S. G. Chefranov (✉) · A. S. Chefranov
A.M. Obukhov Institute of Atmospheric Physics Russian Academy of Sciences, Moscow, Russia
e-mail: schefranov@mail.ru; csergei@technion.ac.il

A. S. Chefranov
e-mail: a.chef@bk.ru

S. G. Chefranov
Physics Department, Technion-Israel Institute of Technology, Haifa 32000, Israel

M. Gorokhovski and F. S. Godeferd (eds.), *Turbulent Cascades II*,
ERCOFTAC Series 26, https://doi.org/10.1007/978-3-030-12547-9_9

$$\frac{\partial \rho}{\partial t} + \frac{\partial}{\partial x_i}(\rho u_i) = 0 \tag{2}$$

where according to the repeated indices meant is a summation from 1 to n (n is a dimension of space), and u_i; f_i; p; ρ the components of the velocity field, the external forces field, field of pressure and density, respectively. If we consider not only external forces, but also the force associated with the medium viscosity, then Eq. (1) coincides in form with the Navier-Stokes equation, obtained later and known since 1827 [3].

At the same time Eq. (1) exactly coincides with the Navier-Stokes equation for viscous compressible medium, if for the force f_i in (1) the following representation takes place [3, 4]:

$$f_i = \eta \frac{\partial^2 u_i}{\partial x_k^2} + \left(\zeta + \frac{\eta}{3}\right) \frac{\partial}{\partial x_i} \left(\frac{\partial u_k}{\partial x_k}\right) \tag{3}$$

In (3) η, ζ are the constant coefficients of viscosity and the second viscosity, respectively.

2. Since 2000 the problem of the existence of smooth solutions for the three-dimensional (3D) Navier-Stokes equation is one of the seven fundamental problems for the Millennium Prize formulated at the Clay Mathematical Institute [5]. In [5] this problem is formulated not for the general form of the Navier-Stokes equations (1) and (3), but for the special case when the approximation of an incompressible medium $\rho = const$ is assumed to be fulfilled in (1)–(3) for zero divergence of the velocity field

$$div\mathbf{u} \equiv \frac{\partial u_k}{\partial x_k} = 0 \tag{4}$$

A necessary condition for carrying out this approximation is the assumption that the Mach numbers $Ma = \dfrac{|u|}{c} \ll 1$ are small (where c is the speed of sound in a given medium).

Such a formulation is connected not only with the explicit simplification of the form of system (1)–(3). The main thing here is the a priori idea that the complete system (1)–(3) cannot have smooth solutions on an arbitrarily large time interval. The reason for this is the possibility of appearance of a singularity (collapse) arising in the solution in a finite time, as, for example, in case of collapse of a traveling nonlinear wave in an ideal compressible medium [6]. At the same time it is assumed that the consideration of the viscosity forces cannot lead to the regularization of the corresponding solutions, at least in the case of a 3D vortex solution having the greatest theoretical and applied value. To understand whether this is really so, it is necessary to have at least some class of exact nonstationary 3D solutions of system (1)–(3).

3. L. Euler also noted the complexity of the analysis necessary to obtain the general form of the solution of system (1), (2) and pointed out the importance of obtaining at least particular solutions of these equations [1]. Thus, for example, in [1] (see also [2]), considered is the solution corresponding to an exact hydrostatic equilibrium,

when in (1) the total force on the RHS of Eq. (1) is equal to zero and all the velocity field components are identically equal to zero. In [1] also considered is the case when at zero balance of forces on the RHS of (1) the velocity is no longer zero, but equal to a constant value that is the same for all particles in the medium.

Following this logic of Euler's work [1], and also under the condition of zero balance of forces on the RHS of the Euler equation (1), we can consider that despite the velocity is constant for each particles, it is not necessarily to be the same for different particles of the medium. Besides, the requirement of equality to zero of the LHS of Eq. (1) leads to the following nonlinear equation for the velocity field:

$$\frac{\partial u_i}{\partial t} + u_k \frac{\partial u_i}{\partial x_k} = 0, i = 1, \ldots, n \tag{5}$$

This equation, obtained from (1) under condition of zero balance of forces in the RHS of Eq. (1), describes inertial motion of the medium particles and is the n-dimensional generalization of the well-known one-dimensional equation for nonlinear travelling wave, sometimes called as the Hopf equation [6]. In one-dimensional case Eq. (5) is obtained within the limit of large Mach numbers and from equation, firstly considered by Riemann [3] (see Eq. (101.2) in [3]). Therefore Eq. (5) is sometimes called as the Riemann equation.

The closed (as opposed to (1)–(3)) system of equations of type (5), (2) is also obtained from the equations of hydrodynamics of self-gravitating dust matter when considering the formation of a large-scale structure of the Universe under the assumption of zero pressure $p = 0$ in (1) [7–10]. The same system of Eqs. (5), (2) is also obtained when expanding the Mach numbers $Ma \gg 1$ in inverse powers, for example, in the hydrodynamic description of the granular media dynamics, when the contribution to (1) associated with the pressure gradient is a small value of order $O\left(1/Ma^2\right), Ma \gg 1$ [11–13].

4. It is also known that the Hopf equation (5) can describe the process of the nonlinear travelling wave collapse in compressible medium [6] that, as noted above, has determined the limitation in selecting the formulation of the Clay Millennium Prize problem by limit $Ma \ll 1$, corresponding to the approximation of incompressible medium [5]. In that regard, a special interest attracts just the vortex solution of the Hopf 3D equation (5), for which a potential possibility for realization of the enstrophy explosive growth and the vortex field higher moments is caused by not only the vortex filament stretch effect, but the vortex field generation at the expense of finiteness of the velocity field divergence in the compressible medium flow.

Actually, after applying the curl operator to the Hopf equation (5) the Euler vortex 3D equation (also called the Helmholtz vortex equation) follows from it and has the form:

$$\frac{\partial \omega_i}{\partial t} + u_k \frac{\partial \omega_i}{\partial x_k} = \omega_k \frac{\partial u_i}{\partial x_k} + \omega_i \frac{\partial u_k}{\partial x_k} \tag{6}$$

where $\omega = rotu$. Exactly the same equation is obtained when applying the curl operation to initial Euler equation (1) [if in (1) $rotf = 0$ and $rot(\frac{1}{\rho}\nabla p) = 0$].

Thus, the nonstationary vortex solution of Eq. (5) definitely determines the form of the Eq. (6) solution for the vortex field of the compressible ideal medium flow.

However, all well-known solutions of the Hopf 3D equation (5) are obtained only in Lagrange variables [7, 14]. Therefore they do not give the solution for the Euler vortex 3D equation (6) for the vortex field just in Euler variables. At the same time, for both the problems of astrophysics, considered in [7, 10] and hydrodynamics of granular media [11–13] noted is the importance of just the vortex solutions for the Hopf equation (5) [10–12]. In connection with the Clay Millennium Problem consideration [5] it also attracts great interest to obtain the solution for just the equation for the vortex field (6) with a subsequent evaluation of viscosity force effect on a possibility of regularization of the solution singularity, appearing at the expense of presence of the terms in the RHS of Eq. (6) (the first of which is responsible for 3D effect of vortex filaments stretch).

5. In 1991, in [15], the general exact vortex solution of Eq. (5) was obtained in Euler variables, the vortex field of which strictly satisfies the nonlinear nonstationary Eq. (6) for arbitrary smooth initial fields defined in an infinite space (see also [16], where a more detailed derivation of this solution is given).

In the present paper, as in the preprint [16], on the basis of the solution [15] an analytic solution of the Navier-Stokes equations (1) and (3) for a compressible medium is obtained with a model accounting of the friction force effect. This is necessary for the regularization of solution (5) and (6) that loses its smoothness in a finite time t_0 of the solution collapse realization. The value of the minimum time for the solution t_0 collapse depends on the initial conditions and can be determined in explicit form for the obtained exact solution of Eqs. (5) and (6) (see formula (3.7) in [16]).

In particular, it is shown that when choosing the coefficient of uniform friction, when introducing member $-\mu u_i$ into the RHS of the Hopf equation (5), which satisfies the criterion:

$$\mu > \frac{1}{t_0} \tag{7}$$

the solution already becomes regular and keeps smoothness for arbitrarily large intervals of time of the solution evolution. In condition (7) the value of the friction coefficient is equal to $\mu = \nu/l_{\min}^2$, where ν is the coefficient of kinematic viscosity of the medium, and $l_{\min} \propto 1/k_{\max}$ is the characteristic scale, associated, for example, with the inevitable cutoff wavenumbers at some maximum number $k_{\max}$, that is typical for any numerical simulations on the basis of Eq. (1).

Indeed, in [17] the possibility of the appearance of an effective viscosity associated with spectral cutoff at large wavenumbers is shown in numerical simulations based on the 3D Euler equation for an ideal medium.

Thus, only when we take into account the regularity condition (7), it is possible to avoid the occurrence of instabilities caused by the loss of smoothness of solutions in finite time, that allows us to qualitatively and quantitatively expand the predictability limits on the basis of the corresponding numerical calculations using the hydrodynamic equations. Up to now, numerical calculations based on the Euler equation

did not take into account the need to establish a correlation between the initial data used, which determine the value of t_0 in (7), and the value of the cutoff scale which determines the value of μ in the left side of inequality (7).

It is also shown that when modeling viscous forces by introducing a random Gaussian field $\vec{V}(t)$ (with the substitution of $u_i(x,t) \to u_i(x,t) + V_i(t)$ in (5)), the regularization of the singular modes in the evolution of the solutions of the vortex 3D Euler equation (6) is already achieved for any arbitrarily small effective viscosity coefficient $\vec{V}$, determined in the form

$$\langle V_i(t+\tau)V_j(t)\rangle = 2\nu\delta_{ij}\delta(\tau) \tag{8}$$

where the angular brackets denotes the statistical averaging, δ is a Dirac delta-function, and δ_{ij} is a unity matrix.

Thus, in this paper we establish the possibility of the existence of a smooth solution on an unlimited interval of time for the analytical approximate (only because of the use of the model representation for the viscosity forces) solution of the Navier-Stokes equation describing the flow of a compressible medium. For the pressure field corresponding to this solution, a representation providing a sufficient condition for the positive definiteness of the rate of change in integral entropy is used, which is, as shown below, more correct than the traditional use of the equation of the medium state. As a result, it is shown that a positive answer to the generalization of the Clay Millennium Problem formulated in [5] is possible exactly for the case of a compressible medium.

Besides, the expressions for the integral of the square of the vortex field (enstrophy) and for all higher moments of the vortex field are obtained for the exact solution of the vortex 3D Euler equation (6). This corresponds to the establishment of an exact solution of the well-known closure problem in the theory of turbulence, to the solution of which only approximate approaches have been developed by W. Heisenberg, A. N. Kolmogorov et al. earlier [4].

2 Energy and Entropy Balance Equation

1. The system of the Euler equations for an ideal compressible medium (1), (2) and the corresponding system of Navier-Stokes equations under condition (1)–(3) are not closed, since, for example, in the three-dimensional case it consists of four equations, but, at the same time, contains five unknown functions, namely three components of the velocity field, the pressure field and the field of the medium density.

To close this system in the limit of small Mach number the approximation of an incompressible medium is traditional used when the density is assumed to be a constant value and zero divergence condition (4), which follows from this continuity equation (2) in case of this assumption, takes place.

For the compressible medium usually some additional equation of state [1–3], which connects the functions of density and pressure (here and below, let us consider

an isothermal medium for simplicitys sake) is used to close the system of equations. Besides, it is assumed that the medium is in a locally thermodynamic equilibrium state, when the time of relaxation to this state is much smaller than the typical time of the flow dynamics of the medium. This assumption, however, must certainly be violated in case of velocities of the medium corresponding to not small and especially large Mach numbers, and also in case of slow relaxation processes, for example, in the presence of chemical reactions [3].

Therefore, instead of introducing any equation of state, it seems natural to obtain an additional equation for the pressure field closing the system of Eqs. (1)–(3), as proposed in [3] for the case of slow relaxation processes (see (81.4) and (81.6) in [3]). In the present paper we propose to obtain an equation for the pressure field from the consideration of the integral entropy balance equation and the condition of positive definiteness of the integral entropy rate of growth.

At first, let us obtain from (1) to (3) the following equation of the integral kinetic energy balance for the compressible medium $E = \frac{1}{2}\int d^n x \rho u^2$ flow:

$$\frac{dE}{dt} = -\eta \int d^n x \left(\frac{\partial u_i}{\partial x_k}\right)^2 + \int d^n x \left[p - \left(\zeta + \frac{\eta}{3}\right) div\mathbf{u}\right] div\mathbf{u} \tag{9}$$

This expression under condition (4) exactly coincides with the given in [3] (see (16.3) in [3]) in case of incompressible medium and serves as its generalization for the compressible medium flow.

From the condition of conservation of total energy [3] $E_h = \int d^3 x \left(\rho \frac{u^2}{2} + \rho\varepsilon\right)$ and the balance equation (ε is a density of the internal energy; see derivations in [16]):

$$\begin{gathered} \frac{\partial}{\partial t}\left(\rho\frac{u^2}{2} + \rho\varepsilon\right) = \\ -\frac{\partial}{\partial x_k}\left[u_k\left(\rho\left(\frac{u^2}{2} + \Phi_0\right) + p - \left(\zeta + \frac{\eta}{3}\right) div\mathbf{u}\right) - \eta\frac{\partial}{\partial x_k}\left(\frac{u^2}{2}\right)\right] \\ +T\left(\frac{\partial}{\partial t}(\rho s) - \frac{B}{T}\right), \\ B = \eta\left(\frac{\partial u_i}{\partial x_k}\right)^2 - \left[p - \left(\zeta + \frac{\eta}{3}\right) div\mathbf{u}\right] div\mathbf{u} \end{gathered} \tag{10}$$

follows the balance equation for density (per unit mass) of entropys

$$\frac{\partial}{\partial t}(\rho s) = \frac{B}{T} \tag{11}$$

where T is the temperature.

From (11) we obtain the following equation of the integral entropy $S = \int d^3 x \rho s$ balance:

$$\frac{d}{dt}S = \eta \int d^3x \frac{1}{T}\left(\frac{\partial u_i}{\partial x_k}\right)^2 - \int d^3x \frac{1}{T} div\mathbf{u}\left[p - \left(\zeta + \frac{\eta}{3}\right) div\mathbf{u}\right] \tag{12}$$

Comparing the form of Eqs. (12) and (9), for the considered isothermal case (when $T = T_0 = const$), we obtain the following exact relation:

$$T_0 \frac{dS}{dt} = -\frac{dE}{dt} \tag{13}$$

In [3] (see paragraph 79 in [3]) relation (13) is derived as a certain fundamental relation which must be executed for any mechanical system tending to thermodynamic equilibrium from a given nonequilibrium state.

However, in [3] this relation is not derived directly for the hydrodynamics of a viscous compressible medium, as opposed to the present paper, where relations (12) and (9) are derived independently and lead exactly to equality (13).

In [3] the relation of form (13) is used only for obtaining the value of velocity of changing the integral kinetic energy of compressible medium $\frac{dE}{dt}$, on the basis of the obtained in [3] equation of the integral entropy balance and corresponding expression for derivative $\frac{dS}{dt}$. In this case, however, the expression for $\frac{dE}{dt}$ (see (79.1) in [3]) differs significantly from (9).

This difference is caused by the fact that, as opposed to the derivation of relations (10)–(12), the derivation of the total energy and entropy balance equations in [3] is based on the application of the relations typical for the medium thermodynamic equilibrium state to the nonequilibrium pressure field entering the Navier-Stokes equation for a flow of compressible viscous medium (1.1).

Hence the conclusion follows that the use of thermodynamic equilibrium representations for the pressure field entering the Navier-Stokes equation for a viscous compressible medium, as it has been done in [3], is inadmissible because of the resulting contradiction with the fundamental relation (13) [3], proved in the present paper for also the nonequilibrium hydrodynamics of a viscous compressible medium.

Indeed, the obtained in [3] expression $\frac{dS}{dt}$ does not satisfy Eq. (13) taking into account formula (9), which is obtained only on the basis of Eqs. (1)–(3) without involving any thermodynamic relations.

It means that the use of the equation of state, which is usually applied [1–3] for closing the system (1)–(3), is also inadmissible in describing the flow of a viscous compressible medium, and instead an additional equation for the pressure field must be obtained by other way.

This additional equation is obtained from a sufficient condition for the positive definiteness of the integral entropy (12) growth rate, which has the following form:

$$p = \left(\zeta + \frac{\eta}{3}\right) div\mathbf{u} \tag{14}$$

Equation 14 is an additional equation to system (1)–(3) and makes it closed. In [3] (see (81.4) and (81.6) in [3]), a similar expression for pressure in the form of a linear function of the divergence of the velocity field was also obtained, albeit from other considerations, with a coefficient of proportionality equal to the coefficient of the second viscosity. Moreover, in [3] it is also proposed to consider this relation between the pressure and the divergence of the velocity field instead of the medium state equation. Let us note that the condition for the extremum for the functionals (9) and (12) also yields a relation for determining the pressure as a linear function of the divergence of the velocity field, which corresponds to the already necessary extremum condition for functionals (9) and (12).

When the Eq. (14) is satisfied for the pressure field, the Navier-Stokes equations (1) and (3) reduces to an equation of the three-dimensional Burgers equation type, for which in the next section proposed is an approximate solution based on the assumption of the possibility of modeling the viscosity force either due to a uniform friction $-\mu u_i$, or by means of a random Gaussian velocity field $\vec{V}(t)$ of the white noise type.

3 Analytical Solution of the Navier-Stokes Equation

1. Let us find the solution of closed system (1)–(3) and (14) on the basis of the exact solution of the Hopf equation (5) satisfying the vortex form of the Euler equation (6) obtained in [15] and having the following form (see also [16]):

$$u_i(\vec{x},t) = \int d^n\vec{\xi}\,\vec{u}_{0i}(\vec{\xi})\delta\left(\vec{\xi} - \vec{x} + t\vec{u}_0(\vec{\xi})\right)\det\hat{A} \tag{15}$$

where $\det\hat{A}$ is a determinant of matrix $\hat{A} \equiv A_{nm} = \delta_{nm} + t\dfrac{\partial\vec{u}_{on}}{\partial\vec{\xi}_m}$, and $\vec{u}_{0i}(\vec{x})$ is an arbitrary initial smooth velocity field. This solution preserves smoothness only for time $t < t_0$, for which condition $\det\hat{A} > 0$ is executed, where t_0 is a minimal time, in space coordinates, for which determinant $\det\hat{A} = 0$ vanishes.

In particular, for one-dimensional case $n = 1$ we have $\det\hat{A} = 1 + t\dfrac{du_{01}}{d\xi_1}$ and solution (15) exactly coincides with the solution obtained in [18, 19]. At the same time $t_0 = \dfrac{1}{\max|du_0/dx|} > 0$ and, for example, for initial distribution $u_0(x) = a\exp\left(-x^2/L^2\right)$, $a > 0$ we have $t_0 = \dfrac{L}{a}\sqrt{\dfrac{e}{2}}$, where $x = x_{\max} = L/\sqrt{2}$ and the solution singularity can be realized only for $x > 0$.

2. When introducing into Eq. (5) the homogeneous friction with coefficient $\mu > 0$ the solution for modified equation (5) is obtained from (15) if to substitute in (15) the new time variable by changing $t \to \tau t = \left(1 - e^{-\mu t}\right)/\mu$. Besides, it is obvious that if condition (7) is satisfied, solution (15) remains smooth for any arbitrarily large times.

Actually, under condition (7), even in the limit $t \to \infty$, determinant $\det \hat{A}$ does not vanish, remaining positive, since the condition $\tau(t) < t_0$ is preserved in this limit. At the same time the noted modification of solution (15) satisfies vortex 3D equation (6) when introducing member $-\mu\omega_i$ into the right side (6).

3. If we replace $u_i \to u_i + V_i(t)$ in (5), then solution (15) will still satisfy Eqs. (5) and (6) if we replace $\mathbf{x} \to \mathbf{x} - \mathbf{B}(t)$, $\mathbf{B}(t) = \int_0^t dt_1 \mathbf{V}(t_1)$ in 15.

If we assume that the velocity field $\vec{V}(t)$ is a random Gaussian field of white noise type satisfying the condition (8), then after statistical averaging of this modification of expression 15 we obtain for the average velocity an expression that remains smooth for any time intervals and has the following form:

$$\langle u_i \rangle = \int d^n \xi u_{0i}(\boldsymbol{\xi}) \left| \det \hat{A} \right| \frac{1}{\left(2\sqrt{\pi \nu t}\right)^n} \exp\left[-\frac{(x - \xi - t u_0(\xi))^2}{4\nu t} \right] \tag{16}$$

Thus, a smooth for any times solution of the Navier-Stokes equation for a viscous compressible medium in the form (16) is obtained. It takes place under condition of taking into account the relations (14) in (1) and (3), and it is permissible to use instead of term $\frac{\eta}{\rho} \frac{\partial^2 u_i}{\partial x_i^2}$ in the RHS of (1) for modeling the viscosity force a random Gaussian velocity field whose correlator has the form (8) like for white noise. In limit $\nu \gg \frac{\eta}{\min \rho}$ this substitution seems justified, where value ν is determined in 8 and corresponds to the level of white noise simulating the effect of viscosity forces. This method of simulating the viscosity does not lead to the appearance of hyper viscosity effects (when instead of the Laplacian in the Navier-Stokes equation introduced is a viscosity force proportional to the Laplacian in a degree higher than one [20]).

4. Equation of continuity (2) has a structure which exactly coincides with equation for vortex field (6) in two-dimensional case, when in the RHS of (6) the first term is absent. For solution (15) the vortex field in two-dimensional case exactly satisfies Eq. (6) and has the following form:

$$\omega(\vec{x}, t) = \int d^2 \vec{\xi} \omega_0(\vec{\xi}) \delta\left(\vec{\xi} - \vec{x} + t\vec{u_0}(\vec{\xi}) \right) \tag{17}$$

where $\omega_0(\vec{x})$ is an initial distribution of the vortex field on plane. In case of substitution $\omega_0(\vec{x}) \to \rho_0(\vec{x})$ expression (17) gives the distribution for the density field (not only in two-dimensional, but also in three-dimensional case, if the integration is considered in three-dimensional space in 17 and all the vectors appearing in (17) are also considered as three-dimensional).

The exact solution of the three-dimensional Euler vortex equation (6) corresponding to the velocity field (15) has the following form:

$$\omega_i(\mathbf{x}, t) = \int d^3 \xi \left(\omega_{0j}(\boldsymbol{\xi}) + t\omega_{0j} \frac{\partial u_{0i}(\xi)}{\partial \xi_j} \right) \delta\left(\boldsymbol{\xi} - \mathbf{x} + t\mathbf{u}_0(\boldsymbol{\xi}) \right) \tag{18}$$

where $\omega_0 = rotu_0$. The expression for enstrophy corresponding to exact solution (18) has the following form:

$$\Omega_3 \equiv \int d^3x\omega_i^2\,(\mathbf{x},t) = \int d^3\zeta \left(\omega_{0i} + t\omega_{0j}\frac{\partial u_{0i}}{\partial \zeta_j}\right)^2 / \det \hat{A} \tag{19}$$

The expressions for any higher moments of the vortex field are obtained similarly. For simplicitys sake, let us give them only for two-dimensional case, when they have the following form:

$$\begin{aligned} \Omega_{2(m)} &= \int d^2x\omega^m = \int d^2\xi \frac{\omega_0^m(\xi)}{\det^{m-1}\hat{A}}; \\ \Omega_{2(2m)} &= \int d^2x\omega^{2m} = \int d^2\xi \frac{\omega_0^{2m}(\xi)}{\det^{2m-1}\hat{A}}; \quad m = 1, 2, 3, \ldots \end{aligned} \tag{20}$$

Thus, the exact solution of the closure problem, the main problem in the theory of turbulence, is obtained. In particular, from (20) it follows that in limit $t \to t_0$ we have inequality $\Omega_{2(m)}^2 \ll \Omega_{2(2m)}$, which is typical for realization of the high intermittency of turbulence [20].

Acknowledgements We thank Itamar Procaccia, Pavel Lushnikov, Viktor Lvov and Gregory Falkovich for useful discussions and positive reaction on the results of this paper. The study is supported by RSF, project No. 14-17-00806P and Israel Science Foundation, Grant No. 492/18.

References

1. Euler, L.: Principes generaux du movement des fluids. Acad. Roy. Sci. et des Belles-Lettres de Berlin, Memoires **11**, 217–273 (1757); also Physica D, **237**, 1825–1839 (2008)
2. Darrigol, O., Frisch, U.: Physica D **237**, 1855 (2008)
3. Landau, L.D., Lifshitz, E.M.: Fluid Mechanics, 2nd edn. Pergamon Press, Oxford (1987)
4. Monin, A.S., Yaglom, A.M.: Statistical Hydromechanics, Theory of Turbulence, vol. 1, S.-Petersburg (1992)
5. Fefferman, C.L.: Existence and smoothness of the Navier Stokes equation. In: The Millennium Prize Problems, pp. 57–67. Clay Mathematics Institute, Cambridge, MA (2006). http://claymath.org/millennium/Navier-Stokes-Equation
6. Hopf, G.E.: Comm. Pure. Appl. Math. **1**, 303 (1948)
7. Arnold, V.I., Shandarin, S.F., Zeldovich, Ya.B.: Geophys. Astrophys. Fluid Dyn. **20**, 111 (1982)
8. Shandarin, S.F.: Large Scale Structures of the Universe, p. 273. Audouze, J., Peletan, M.C., Szalay, A. (ed.) Kluwer Acad., Dordrecht (1988)
9. Shandarin, S.F., Zeldovich, Ya.B.: Rev. Mod. Phys. **61**, 185 (1989)
10. Barrow, J.D., Saich, P.: Class. Quantum Grav. **10**, 79 (1993)
11. Glasner, A., Livne, E., Meerson, B.: Phys. Rev. Lett. **78**, 2112 (1997)
12. Efrati, E., Livne, E., Meerson, B.: Phys. Rev. Lett. **94**, 088001 (2005)
13. Kolvin, I., Livne, E., Meerson, B.: Phys. Rev. E **82**, 021302 (2010)
14. Kuznetsov, E.A.: Physica D **184**, 266 (2003)
15. Chefranov, S.G.: Sov. Phys. Dokl. **36**(4), 286 (1991)

16. Chefranov, S.G., Chefranov, A.S.: Exact time-dependent solution to the three-dimensional Euler-Helmholtz and Riemann-Hopf equations for vortex flow of compressible medium and one of the Millennium prize problems. arXiv:1703.07239 v3 [physics.flu-dyn] 22 Mar 2017
17. Krstulovic, G., Brachet, M.E.: Physica D **237**, 2015 (2008)
18. Pelinovsky, E.N.: Izv. VUZov, Radiophys. **19**, 373 (1976)
19. Chefranov, S.G.: JETP **96**, 171 (1989)
20. Zybin, K.P., Sirota, V.A.: Uspekhi Fiz. Nauk **185**, 593 (2015)

A Subgrid-Scale Model for Large-Eddy Simulation of Liquid/Gas Interfaces Based on One-Dimensional Turbulence

A. Movaghar, R. Chiodi, O. Desjardins, M. Oevermann and A. R. Kerstein

Abstract The interface/turbulence interaction between two fluids in a turbulent environment has an important role in many technical processes, e.g. primary liquid atomization in combustion devices. Primary atomization has a significant role in spray formation and its characteristics. The resulting dynamics typically span 4–6 orders of magnitude in length scales, making detailed numerical simulations exceedingly expensive. This motivates the need for modeling approaches based on spatial filtering such as large-eddy simulation (LES). In this paper, a new approach based on One-Dimensional turbulence (ODT) is presented to describe the subgrid interface dynamics. ODT is a stochastic model simulating turbulent flow evolution along a notional one-dimensional line of sight by applying instantaneous maps that represent the effects of individual turbulent eddies on property fields. It provides affordable

A. Movaghar · M. Oevermann
Department of Mechanics, Chalmers University of Technology, Gothenburg, Sweden
e-mail: movaghar@chalmers.se

M. Oevermann
e-mail: michael.oevermann@chalmers.se

R. Chiodi · O. Desjardins (✉)
Sibley School of Mechanical and Aerospace Engineering, Cornell University, Ithaca, USA
e-mail: olivier.desjardins@cornell.edu

R. Chiodi
e-mail: rmc298@cornell.edu

A. R. Kerstein
Consultant, 72 Lomitas Road, Danville, CA, USA
e-mail: alan.kerstein@gmail.com

M. Gorokhovski and F. S. Godeferd (eds.), *Turbulent Cascades II*,
ERCOFTAC Series 26, https://doi.org/10.1007/978-3-030-12547-9_10

high resolution of interface creation and property gradients within each phase, which are key for capturing the local behavior as well as overall trends. ODT has previously been shown to reproduce the main features of an experimentally determined regime diagram for primary jet breakup. Here a new approach called VODT is presented which produces a size-conditioned as well as a total time rate of generation of droplets for given flow conditions at an interface. At the LES level, the total droplet generation from VODT is interpreted as a rate of mass conversion of LES-resolved liquid into unresolved droplets. Preliminary results of applying VODT to a cell with a planar-shear-layer are discussed at the end of the paper.

1 Introduction

The interaction between turbulence and interfaces of immiscible fluids is seen in many engineering applications, e.g., primary atomization in combustion devices. The atomization process plays a significant role in combustion performance, including efficiency and emissions. Despite its importance, a detailed description of primary atomization has remained elusive, due in part to insufficient understanding of how interfaces modulate the surrounding flow field and undergo breakup. Many attempts have been made to describe interfacial instabilities using linear stability analysis, however, these only provide a very limited picture of interfacial dynamics, especially in turbulence and complex geometries. Because of this, there remains a need to understand and model the interactions between two immiscible fluids in a turbulent environment.

Predictive simulations with high spatial and temporal resolution, i.e., Direct Numerical Simulations (DNS), offer an alternative way to study liquid-gas interface dynamics during primary breakup. But despite the significant benefits provided by DNS, the large computational cost precludes their use in many flows of engineering interest. Therefore, there is a need for appropriate interface dynamics models lower the computational cost of predicting the atomization process. While requiring physical models for the small unresolved scales of the flow, Large-Eddy Simulation (LES) has shown to be a useful tool that can provide much more flexibility on resolution coarser than DNS by introducing a spatial filter into the governing equations and resolving only the scales larger than the filter width [3]. However, the LES sub-filter models typically neglect the contribution of the surface tension term and are based on a cascade process hypothesis that may be questionable in the context of surface tension-driven atomization. This leads the need for a new LES subgrid interface dynamics model.

A One-Dimensional Turbulence (ODT) model is considered here as an affordable model for simulating large Reynolds and Weber number flow configurations. ODT is a stochastic model simulating turbulent flow evolution along a notional one-dimensional line of sight by applying instantaneous maps that represent the effects of individual turbulent eddies on the flow properties. ODT has recently been used by

the authors [5, 6] to reproduce the main features of an experimentally determined regime diagram for primary jet breakup.

ODT can be used both as a stand alone tool and as a sub-grid model for LES or RANS. This creates a possibility to use ODT as a subgrid resolution model in LES simulations to describe/model subgrid interface dynamics. This approach is described in detail in the following sections.

2 Governing Equations

The flows investigated in this study are governed by the incompressible Navier-Stokes equations for immiscible two-phase flow. The momentum equation is given by

$$\frac{\partial \rho u}{\partial t} + u \cdot \nabla \rho u = -\nabla p + \nabla \cdot [\mu(\nabla u + \nabla^T u)] + \sigma \gamma \delta(x - x_\Gamma) n, \tag{1}$$

where u is the velocity, ρ the density, p the pressure, and μ is the dynamic viscosity. The last term in Eq. 1 is the singular surface tension force where γ denotes the curvature of the interface, δ is the Dirac delta function, x_Γ is the point on the interface Γ closest to the point x and n is the interface normal vector.

To compute the phase interface, in addition, a transport equation for the liquid volume fraction α in a computational cell is solved

$$\frac{\partial \alpha}{\partial t} + \nabla \cdot (u\alpha) = 0. \tag{2}$$

The interface unit vector n and the interface curvature γ can be theoretically expressed in terms of the liquid volume fraction as

$$n = \frac{\nabla \alpha}{|\nabla \alpha|}, \quad \gamma = \nabla \cdot n. \tag{3}$$

Following the continuum surface force approach [2] the surface tension force in Eq. 1 is modelled as

$$\sigma \gamma \delta(x - x_\Gamma) n = \sigma \gamma \nabla \alpha. \tag{4}$$

LES formulation is based on applying spatial filtering to Eq. 1. The filtered structures or large scales of the flow field are resolved directly, though the terms filtered out need to be modeled. These terms are called sub grid scale (SGS) terms. If they are small enough they behave isotropic and geometry independent. The SGS terms can be closed by applying a model e.g. the Smagorinsky model. However, these models usually neglect the effect of the sub-filter surface tension term and need to be reconsidered.

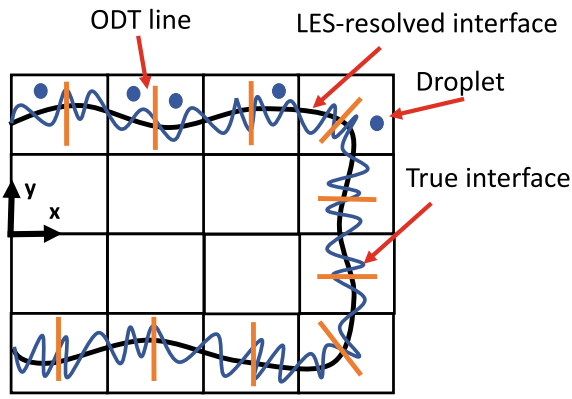

Fig. 1 Using ODT as a sub-filter model for LES

In particular, LES does not see interface wrinkles below its resolution scale, so the LES-resolved interface is much smoother and has less total surface area than the true interface. Therefore it doesn't fully account for the true total amount of stored surface-tension area. As Fig. 1 illustrates, when the Weber number is high enough there are some scales of interface wrinkling that are not resolved by the LES and cause droplet generation. The following sections describe how ODT can be used to model these unresolved scales.

3 One-Dimensional Turbulence (ODT)

The ODT model of Kerstein used in this study is briefly described in this section. For a fully detailed description we refer to Kerstein et al. [4], Ashurst et al. [1], and its extension to modelling primary breakup by Movaghar et al. [6].

ODT is a stochastic model simulating the evolution of turbulent flow along a notional line of sight through a three-dimensional flow. Here ODT line is oriented in the transverse y direction or normal to the interface. This setup provides high lateral resolution of the relevant physics near the interface. On the other hand, one-dimensional formulation provides the affordability needed to capture the full range of scale separation at high Reynolds and Weber numbers.

In ODT formulation the fields on the 1-D line of sight are evolved by two different mechanisms: molecular diffusion or time advancement and eddy events representing advection.

Time advancement of the present ODT formulation is expressed schematically as

$$\frac{\partial u_i}{\partial t} - \nu \frac{\partial^2 u_i}{\partial y^2} = Eddies, \tag{5}$$

where ν is the kinematic viscosity and the indices $i = 1, 2, 3$ denote the streamwise, lateral and spanwise velocity components, respectively, corresponding to the spatial coordinates (x, y, z). This equation formally represents the two processes that can change the value of u_i at a given location y and time t.

The eddy events representing advection may be interpreted as the model analog of individual turbulent eddies. In ODT, an eddy of size l is represented by an instantaneous map acting on each property field within an interval $[y_0, y_0 + l]$ on the line. The mathematical formulation of the map should satisfy measure preservation and continuity of mapped profiles. The new velocity field after the map event is given by,

$$\hat{u}_i(y, t) = u_i(f(y), t) \tag{6}$$

where the inverse of the triplet map is specified by

$$f(y) = y_0 + \begin{cases} 3(y - y_0), & \text{if } y_0 \le y \le y_0 + (1/3)l, \\ 2l - 3(y - y_0), & \text{if } y_0 + (1/3)l \le y \le y_0 + (2/3)l, \\ 3(y - y_0) - 2l, & \text{if } y_0 + (2/3)l \le y \le y_0 + l, \\ y - y_0, & \text{otherwise} \end{cases} \tag{7}$$

If the eddy range $[y_0, y_0 + l]$ contains no phase interfaces, then it is a single-phase eddy whose implementation is the same as in previous ODT formulations. If instead the eddy range contains an interface then it is a multiphase eddy requiring the domain-integrated energy conservation. This requires that the change of kinetic energy after the eddy event, ΔE_{kin} is equal and opposite to any surface-tension potential-energy change, ΔE_σ caused by triplet mapping of phase interfaces.

For this purpose, the kernel functions $c_i K(y)$ and $b_i J(y)$ are added to the u_i profile created formerly by triplet mapping. On this basis Eq. 6 is rewritten as

$$u_i(y) \rightarrow u_i(f(y)) + b_i J(y) + c_i K(y) \tag{8}$$

and

$$\rho(y) \rightarrow \rho(f(y)), \tag{9}$$

where $f(y)$ is the inverse of the triplet map, $K = y - f(y)$, $J = |K|$, and b_i and c_i are assigned based on physical modeling. The requirement $\int K(y)dy = 0$ enforces momentum conservation.

ODT samples eddy events from an instantaneous distribution that evolves with the flow. These events are individually parameterized by position y_0 and size l.

The number of events during a time increment dt for eddies located $[y_0, y_0 + dy]$ in the size range $[l, l + dl]$ is denoted $\lambda(y_0, l; t)dy_0 dl dt$, where the event rate density λ is defined as

$$\lambda(y_0, l; t) = C/(l^2 \tau(y_0, l; t)). \tag{10}$$

with dimensions of $events/(location \times size \times time)$. The adjustable parameter C scales the overall eddy frequency and τ is the eddy time scale. To find this eddy time scale, the square of the velocity implied by l and τ is modeled as

$$(l/\tau)^2 \sim E_{final} - Z(\nu^2/l^2). \tag{11}$$

On the right hand side, the first term is the final value of the available kinetic energy, denoted E_{kin} in the absence of surface-tension effects, $E_{final} = E_{kin} - \Delta E_\sigma$ and the second term involving the parameter Z suppresses unphysically small eddies, such as those smaller than the Kolmogorov scale. Following [6], ΔE_σ is formulated as

$$\Delta E_\sigma = -\frac{4\sigma}{\rho_{\text{eddy}} l}. \tag{12}$$

Because ΔE_σ and the last term in Eq. 11 are both negative, the right-hand side of that equation can be negative but the left-hand side must be positive. This is an indication that the selected eddy is energetically forbidden, corresponding to $\lambda = 0$ for such eddies.

4 Virtual ODT for LES/VOF Closure

As described, ODT can be used as a stand alone computation tool. This creates a possibility to use ODT to compute a subgrid breakup table. As shown in Fig. 1 it is assumed that the ODT closure of LES/VOF can be formulated on an ODT domain locally normal to a given interface element in every interface LES cell. For generality the interface is allowed here to be at any location $y = I$ on the ODT domain where I is the interface location. ODT produces a size-conditioned as well as a total time rate of generation of droplets at a given VOF interface. At the LES level, the total droplet generation is interpreted as a rate $\dot{M}$ of mass conversion of LES-resolved liquid into unresolved droplets that are then deemed to reside in the gas phase. Accordingly, for an interface element within a LES cell, droplet generation causes recession of the interface at a speed $\dot{M}/(A\rho_l)$ inserted as a source term into Eq. 2 and updates the LES governing equations. A reduced formulation of ODT, called virtual ODT (VODT), that is suitable for economical closure in this manner is introduced next.

As discussed earlier, ODT contains two main mechanisms, viscous time advancement and eddy events. For the tabulation purposes, we suppose there is no viscous advancement but only eddy sampling. Nevertheless the accepted eddies are not implemented and just their statistics are collected. Because the VODT state is not time advanced, the only effect of eddy events is droplet generation and the implied recession of the liquid surface. Therefore, eddies entirely contained in one phase have no effect, leaving only multiphase (hence droplet-forming) eddies to be considered. By not implementing the eddies, the eddy rate distribution is stationary. Thus the initial rate distribution is used to evaluate the rate of production of a droplet of any size.

The effect of surface tension (and hence the We dependence), which does not appear in Eq. 5, is brought into the formulation through the physical modeling that specifies the eddy rate distribution.

A VODT droplet-forming eddy ranges from some location $y_0 < I$ to a location $y_0 + l > I$, which implies $l > I - y_0$ where. Based on the triplet-map definition, the eddy transfers 2/3 of the liquid interval $[y_0, I]$ to the droplet, while the rest remains in liquid form as defined in VODT. The implied surface recession is then $\Delta y = \frac{2}{3}(I - y_0)$, corresponding to the LES-level volume conversion $\Delta V = A_s \Delta y$ where A_s is the surface area of VOF interface element.

Δy is the only available length scale from which the droplet diameter D can be inferred, so $D = B\Delta y$ is assumed, where B is a tunable parameter. Then the ODT droplet is deemed to represent N physical droplets, where $N = \Delta V / \left(\frac{\pi}{6} D^3\right)$ is based on assuming spherical droplets. Using $\Delta V = A_s D/B$, this gives $N = 6A_s/(\pi B D^2)$. N need not to be an integer because it is meaningful only in terms of droplet statistics.

At the LES scale, it is assumed that the droplet spectrum in the gas phase is represented by a histogram based on either linear or geometric sized bins. Uniform linear bins of size dD are assumed here for illustration, although the reasoning is more general. To complete the formulation of VODT outputs, the total generation rate $G(D)$ of droplets in the size range $[D, D + dD]$ is evaluated. To do this, the droplets number probability distribution, $g(D) = \frac{dG}{dD}$ per unit diameter increment is first evaluated. Based on the the results that follow, $g(D)$ can be integrated over dD intervals to obtain the binned generation rates $G(D)$.

The fixed VODT flow state is piecewise linear in u, where the slope discontinuity is determined by steady state momentum-flux balance at the phase interface, which is at the domain midpoint. The domain size, velocity difference across the domain, surface tension, and the phase viscosities and densities define a particular case.

The ODT eddy rate distribution $\lambda(y_0, l)$, which has no t dependence, has been evaluated exactly in closed from as a function of y_0 and l for a specified VODT state. To evaluate $g(D)$, this distribution is integrated over its arguments subject to the constraint $D = B\Delta y = \frac{2}{3}B(I - y_0)$, re-expressed as $y_0 = I - \frac{3}{2}\frac{D}{B}$. Formally this involves insertion of $\delta(y_0 - I + \frac{3}{2}\frac{D}{B})$ into the integral over dy_0, and thus

$$
\begin{aligned}
g(D) &= N(D) \int_{\frac{3}{2}\frac{D}{B}}^{h-I+\frac{3}{2}\frac{D}{B}} dl \int dy_0 \, \lambda(y_0, l) \delta(y_0 - I + \frac{3}{2}\frac{D}{B}) \\
&= \frac{6A_s}{\pi B D^2} \int_{\frac{3}{2}\frac{D}{B}}^{h-I+\frac{3}{2}\frac{D}{B}} dl \, \lambda(I - \frac{3}{2}\frac{D}{B}, l).
\end{aligned}
$$

The moments of the drop number probability distribution are then defined by

$$
G_i(D) = \int_{D_{\min}}^{D_{\max}} g(D) \, D^i dD.
$$

G_0 is the total number of droplets generated per unit time, G_1 is the total sum of diameter of the droplets per unit time, πG_2 is the total surface area of the droplets per unit time and $\pi G_3/6$ is the total volume of the droplets per unit time.

5 Results and Conclusion

As discussed, for this simple application VODT reduces to an algebraic system that is economical enough for on-the-fly runtime implementation. This makes VODT a computationally affordable tool to study different atomization processes. Figure 2 shows a normalized droplet atomization rate of interfacial breakup in different Reynolds and Weber numbers. The droplet generation rate, G_0, shows the total number of drops in time and is normalized by local shear $\Delta u/h$. As seen in the Fig. 2, for relatively low injection velocities the atomization rate is primarily governed by the liquid surface tension. In Fig. 2 the density and viscosity ratios are both equal to 1. By varying the liquid/gas density ratio and keeping the viscosity ratio constant, Fig. 3 is generated, showing the atomization rate. As shown, VODT can generate the entire droplet dependent moments of the generation rate, $G_i(D)$ e.g. total volume of the drops per unit time for any flow condition.

As discussed earlier the main scope of this paper is to propose VODT as a subgrid model for LES/VOF simulations. Like ODT, VODT has three adjustable parameters C, Z, B that need to be calibrated for this planar shear layer application.

A possible basis for this that does not require external input is to run LES/VOF/VODT at different LES resolutions for the same case. If VODT is a good closure, then these results should all predict the same flow development and droplet statistics. As resolution improves, some of the droplet generation seen at the VODT level at coarse LES resolution should become LES-resolved, with VODT still giving the same results as at lower LES resolution for droplets still not resolved. This approach is currently under study and outcomes will be a part of discussions in future publications.

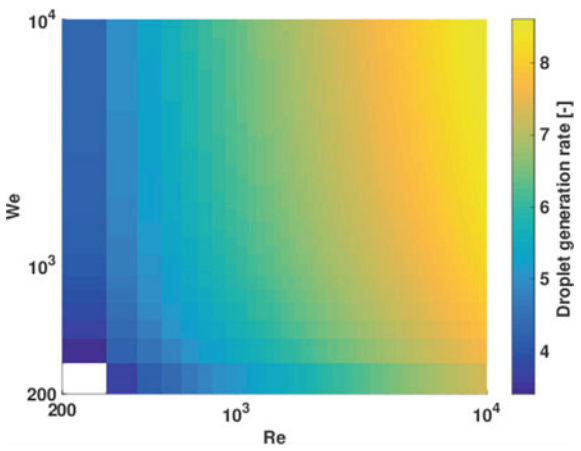

Fig. 2 Normalized droplet generation rate [-]

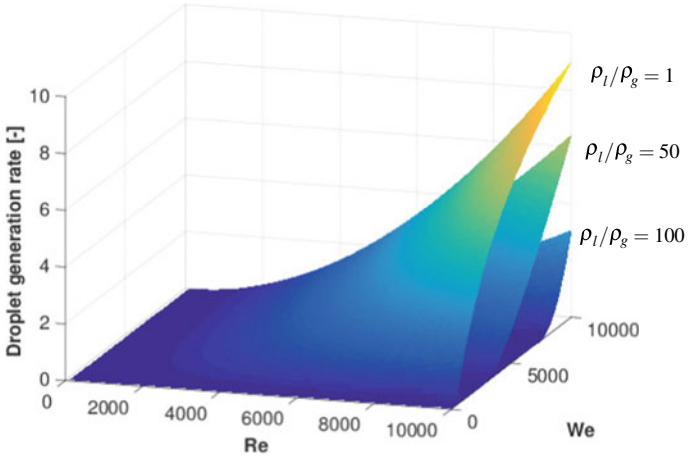

Fig. 3 Normalized droplet generation rate at $\rho_l/\rho_g = 1, 10, 100$ with $\mu_l/\mu_g = 100$

Acknowledgements The authors thank the Knut and Alice Wallenberg Foundation for financial support of this project.

References

1. Ashurst, W.T., Kerstein, A.R.: One-dimensional turbulence: variable-density formulation and application to mixing layers. Phys. Fluids **17**, 025107 (2005)
2. Brackbill, J.U., Kothe, D.B., Zemach, C.: A continuum method for modeling surface tension. J. Comput. Phys. **100**, 335–354 (1992)
3. Desjardins, O., McCaslin, J., Owkes, M., Brady, P.: Direct numerical and large-eddy simulation of primary atomization in complex geometries. Atom. Sprays **23**, 1001–1048 (2013)
4. Kerstein, A.R., Ashurst, W.T., Wunsch, S., Nilsen, V.: One-dimensional turbulence: vector formulation and application to free shear flows. J. Fluid Mech. **447**, 85–109 (2001)
5. Movaghar, A., Linne, M., Oevermann, M., Meiselbach, F., Schmidt, H., Kerstein, A.R.: Numerical investigation of turbulent-jet primary breakup using one-dimensional turbulence. Int. J. Multiph. Flow **89**, 241–254 (2017)
6. Movaghar, A., Linne, M., Herrmann, M., Kerstein, A.R., Oevermann, M.: Modeling and numerical study of primary breakup under diesel conditions. Int. J. Multiph. Flow **98**, 110–119 (2018)

Part III
Effects of Shear and Rotation

Energy Transfer Between Scales and Position in a Turbulent Recirculation Bubble

J.-P. Mollicone, F. Battista, P. Gualtieri and C. M. Casciola

Abstract The energy transfer among the different scales of the turbulent structures is analysed by means of the generalised Kolmogorov equation (GKE). The equation is applied to a turbulent channel with the addition of a bump which creates a strong shear layer and separation bubble. The GKE can provide an intricate description of the energy scale-by-scale budget in both physical and separation space, through the identification of the regions of production and dissipation of energy. Conventional one-point statistics do not allow any analysis across scales. The GKE statistics show that the turbulent structures follow two paths: they are trapped by the recirculation bubble, deformed and dissipated or they are convected downstream by the shear layer and elongated in the streamwise direction. These paths correspond to the direct and inverse energy cascades, respectively. The main feature of this complex flow is that the energy dynamics depends, in a non-trivial way, on both the physical position and separation scales, and does not follow the classical energy path occurring in homogeneous isotropic turbulence.

J.-P. Mollicone
Department of Civil and Environmental Engineering, Imperial College London, London, UK
e-mail: j.mollicone@imperial.ac.uk

F. Battista · P. Gualtieri · C. M. Casciola (✉)
Department of Mechanical and Aerospace Engineering, via Eudossiana 18, 00184 Roma, Italy
e-mail: carlomassimo.casciola@uniroma1.it

F. Battista
e-mail: francesco.battista@uniroma1.it

P. Gualtieri
e-mail: paolo.gualtieri@uniroma1.it

M. Gorokhovski and F. S. Godeferd (eds.), *Turbulent Cascades II*,
ERCOFTAC Series 26, https://doi.org/10.1007/978-3-030-12547-9_11

1 Introduction

The generalisation of the classical Kolmogorov equation [8] has been proposed in various anisotropic and inhomogeneous cases, for example, in shear dominated flows [2, 3] and channel flow [4, 5, 10].

Direct numerical simulation (DNS) and experimental data are analysed to address the energy path in the physical and separation spaces. Concerning the numerical simulations, the generalised Kolmogorov equation (GKE) is used to characterise different scales in the in homogeneous shear flow [3], for example to discern between large scales which are dominated by shear or small scales of dissipative nature. In wall-bounded flows, experimental data [5] explores the large scale dynamics effect on the dissipative small scales at different distances from the walls. For the same geometry, data obtained by DNS have been analysed to address the energy production, transfer and dissipation dependence on the wall distance [4, 10]. Turbulence models and control systems can make use of these knowledges to accurately treat turbulent flows, even in inhomogeneous anisotropic conditions [15].

In the present work, the GKE is used to investigate the energy dynamics in a more complex geometry that involves turbulent channel flow in which one of the walls is decorated with a bump. The bump generates a strong shear layer and recirculation bubble, two features whose inhomogeneity and anisotropy make the GKE analysis challenging but yet interesting. The shear layer is the main source of energy, which is transferred both in space (in the recirculation bubble or downstream in the bulk of the channel) and among the scales, due to the modification of the turbulent structures. This complex dynamics is accessible only through the GKE.

2 Computational Approach

The Navier-Stokes system of equations in incompressible form,

$$\frac{\partial \mathbf{u}}{\partial t} + \mathbf{u} \cdot \nabla \mathbf{u} = -\nabla p + \frac{1}{Re} \nabla^2 \mathbf{u} + \mathbf{f} \qquad \nabla \cdot \mathbf{u} = 0, \tag{1}$$

has been solved by DNS in a channel geometry with a bump at the lower wall. In Eq. (1), $\mathbf{u}$ is the velocity, p is the hydrodynamic pressure and $\mathbf{f}$ is the body force forcing the flow across the channel. The Reynolds number is $Re = h_0 U_b / \nu = 2500$, where h_0 is half the nominal channel height, U_b is the bulk velocity and ν is the kinematic viscosity. h_0, h_0/U_b and ρU_b^2 are the characteristic reference length, time and pressure scales, respectively.

Approximately four hundred time-uncorrelated velocity and pressure fields were collected, at steady state, for statistical analysis. The domain has size $[L_x \times L_y \times L_z] = [26 \times 2 \times 2\pi]$ and is discretised with 120 million grid points. Nek5000 [6],

a solver based on the spectral element method (SEM), see [14], is used to solve the system (1). For additional details on the numerical setup and the flow features see [11, 12].

3 The Generalised Kolmogorov Equation (GKE)

A generalised form of the Kolmogorov equation, meaning it can be applied to inhomogeneous conditions, can be derived using different methods [7, 9, 17]. The Kolmogorov equation, and consequently its generalised form, reveals the turbulence dynamics not only at physical points in the fluid domain but also the dynamics at each scale [1, 16]. In a form that groups together similar terms in relation to their physical interpretation, the GKE reads

$$\nabla \cdot \Phi_6 = \Pi_6 - 4\,\varepsilon^* \,, \tag{2}$$

where $\Phi_6 = (\Phi_X, \Phi_r)$, $\Pi_6 = \Pi_r + \Pi_X$ and ε is the turbulent kinetic energy dissipation. Φ_X and Φ_r are the energy fluxes in the physical space, see Eq. (4), and separation space, see Eq. (4), respectively. $\Pi_6 = \Pi_r + \Pi_X$ is the sum of energy production in the separation and physical spaces, respectively, see Eq. (5).

$$\Phi_r = \langle |\delta\mathbf{u}|^2 \delta\mathbf{u} \rangle + \langle |\delta\mathbf{u}|^2 \delta\mathbf{U} \rangle - 2\nu \nabla_r \langle |\delta\mathbf{u}|^2 \rangle \tag{3}$$

$$\Phi_X = \langle |\delta\mathbf{u}|^2 \mathbf{u}^* \rangle + \langle |\delta\mathbf{u}|^2 \mathbf{U}^* \rangle - \frac{\nu}{2} \nabla_X \langle |\delta\mathbf{u}|^2 \rangle + \frac{2}{\rho} \langle \delta p \delta\mathbf{u} \rangle \,. \tag{4}$$

$$\Pi_r = 2\langle \delta\mathbf{u} \otimes \delta\mathbf{u} \rangle : \nabla_r \delta\mathbf{U} \qquad \Pi_X = 2\langle \mathbf{u}^* \otimes \delta\mathbf{u} \rangle : \nabla_X \delta\mathbf{U} \,, \tag{5}$$

A variable having an apostrophe, such as $\mathbf{x}'$, means it is taken at a position separated by the vector $\mathbf{r} = \mathbf{x}' - \mathbf{x}$ with respect to $\mathbf{x}$. $\mathbf{X_c} = (\mathbf{x} + \mathbf{x}')/2$ defines the coordinate of the mid-point between points $\mathbf{x}'$ and $\mathbf{x}$. Fluctuations are in lower-case whilst averaged quantities are in upper-case. The mid-point average is denoted by an asterisk, e.g. $\mathbf{u}^* = (\mathbf{u}' + \mathbf{u})/2$, whilst an increment is denoted by δ, e.g. $\delta\mathbf{U} = \mathbf{U}' - \mathbf{U}$.

The GKE for our domain reduces to a five-dimensional equation since the spanwise direction is a homogeneous one. The independent coordinates are the two physical X_c and Y_c and the three separation r_x, r_y and r_z coordinates. One-point statistics only give information on the energy behaviour in the physical space, for example using the equation for the mean flow kinetic energy and the equation for the turbulent kinetic energy. On the other hand, Eq. (2) can determine the energy exchange between regions of production and dissipation also in separation space.

4 Results

The main features of interest in the flow domain are the shear layer and the recirculating region which form behind the bump. Figure 1 shows the instantaneous streamwise velocity, at $Re = 2500$, in an (x, y) plane. The bump restricts the flow and causes it to accelerate and separate behind the bump, with a complete re-attachment of the flow downstream of the bump. A description of the flow, including extensive one-point statistics, are discussed by [12]. The present work is dedicated to applying the GKE, see Eq. (2), to investigate the energy fluxes through the space of positions and separations, with particular attention to the shear layer and recirculating region. The phase space that can be scrutinised involves the five dimensions $(X_c, Y_c, r_x, r_y, r_z)$. These correspond to two centre point positions (X_c, Y_c) and the three separations (r_x, r_y, r_z). In the following, with reference to Fig. 2, the results are in two-dimensional sub-spaces. One sub-space is (Y_c, r_x) with fixed $r_z = r_y = 0$ and the other is $\left(Y_c, r_y\right)$ with $r_x = r_z = 0$. The remaining variable is fixed at the streamwise station $X_c = 5.8$, which intersects both the shear layer and the recirculating region after the bump.

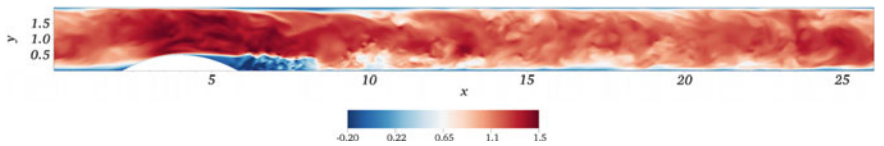

Fig. 1 Snapshot of the instantaneous x-direction (streamwise) velocity in an (x, y) plane at $Re = 2500$

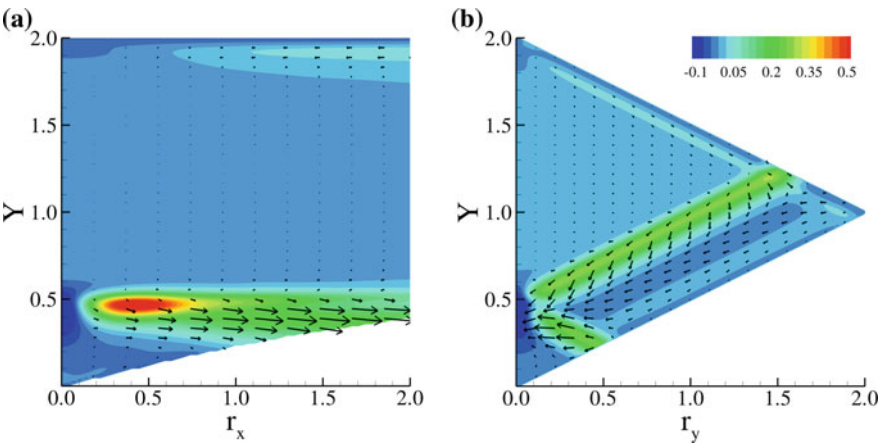

Fig. 2 Net production $\Pi_6 - 4\varepsilon^*$ as contour plots with in-plane flux components Φ_6. Panel (**a**): Φ_Y and Φ_{r_x} in the plane $(Y, r_x)\,|_{r_y=r_z=0}$. Panel (**b**): Φ_Y and Φ_{r_y} in the plane $\left(Y, r_y\right)|_{r_x=r_z=0}$

Figure 2a shows the net production $\Pi_6 - 4\varepsilon^*$ in the plane $(Y, r_x)\,|_{r_y=r_z=0}$. The flux Φ_6 is projected onto the plane and therefore the corresponding components shown as vectors are Φ_Y and Φ_{r_x}. The net production has a peak at $Y = 0.5$ and $r_x \simeq 0.5$. The Y-coordinate corresponds to the distance of the shear layer from the bottom wall. At the top wall, the effect of the bump is minimal and is qualitatively similar to a planar channel flow [4]. The vectors, depicting the flux, transport the squared velocity difference, $|\delta\mathbf{u}|^2$ in both space and across scales. In panel (a), this transport corresponds to displacement in the Y-direction (wall normal direction in space) and to different r_x scales, respectively. The flux is directed towards the small scales, $\Phi_{r_x} < 0$), corresponding to a direct cascade, at the top wall. At the top of the shear layer the trend is similar but less intense. Inside the recirculating region, that is under the shear layer, the vectors point towards the large scales, $\Phi_{r_x} > 0$. The physical explanation to this process is attributed to the formation and progressive elongation in the streamwise direction of turbulent structures which arise from the shear layer.

Figure 2b shows the net production $\Pi_6 - 4\varepsilon^*$ in the plane $\left(Y, r_y\right)|_{r_x=r_z=0}$. The vectors now represent the fluxes Φ_Y and Φ_{r_y}. The upper and lower green regions of the coloured contour plot represent strong net production when one point in the domain is correlated with the shear layer. The upper region is created when the point in the shear layer is correlated with the bulk flow whilst the lower region arises from the correlation of a point in the shear layer with another one below it, that is in the recirculating region. A larger range of scales is present in the upper region with respect to the lower one since the latter is physically limited by the lower part of the domain. In these regions, the net production is a source from which the fluxes in the upper region move towards the wall and the fluxes from both regions move towards small wall-normal separation. This shows that $|\delta\mathbf{u}|^2$ (the squared velocity difference), originating from a larger scale, is transported by the fluxes to smaller r_y scales and into a dissipative region.

Figure 3 shows the fluxes in three coordinates planes in the compound space of positions and separations. The plots refer to $X^0 = 5.8$ and correspond to the planes $\left(Y, r_y\right)|_{r_z=0,r_x=0}$, $(Y, r_x)\,|_{r_y=0,r_z=0}$, and $\left(r_x, r_y\right)|_{Y=0.5,r_z=0}$, respectively. The components of fluxes, represented as vectors, are $\left(\Phi_Y, \Phi_{r_y}\right)$, $\left(\Phi_Y, \Phi_{r_x}\right)$, and $\left(\Phi_{r_x}, \Phi_{r_y}\right)$, respectively. The contour plots indicate the net energy source, $\Pi_6 - 4\varepsilon^*$. The figure links the two-dimensional sub-manifolds previously observed and provides a general idea of the structure function dynamics in these parts of the five-dimensional hyperspace. The effective source $\Pi_6 - 4\varepsilon^*$ is particularly strong when a point in the shear layer is correlated with a point above or below it, explaining the strong oblique structures appearing in the contour plot in the front plane of Fig. 3 (corresponding to Fig. 2b). Fluxes are directed from these sources towards smaller r_y, which in turn are directed to larger scales in the (Y, r_x) plane.

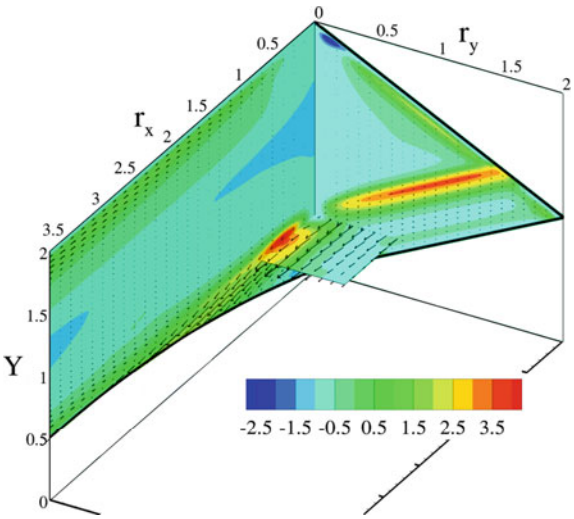

Fig. 3 Fluxes in three coordinates planes in the compound space of positions and separations. The plots refer to $X^0 = 5.8$ and correspond to the planes $(Y, r_y)\,|_{r_z=0, r_x=0}$, $(Y, r_x)\,|_{r_y=0, r_z=0}$, and $(r_x, r_y)\,|_{Y=0.5, r_z=0}$, respectively. On these planes the components of fluxes, represented as vectors in the plane, are (Φ_Y, Φ_{r_y}), (Φ_Y, Φ_{r_x}), and (Φ_{r_x}, Φ_{r_y}), respectively. The contour plots indicate the net energy source, $\Pi_6 - 4\varepsilon^*$

5 Conclusions

The generalised Kolmogorov equation (GKE) is applied to a turbulent channel flow that is modified with a bump at one of the walls. This introduces interesting features such as a strong shear layer and a large recirculating region, which are points of interest since they involve complex energy behaviours. The GKE, generally used in simpler flow domains, has been applied to study the present anisotropic and inhomogeneous domain. The main feature of the GKE is that it accounts for energy dynamics in both the physical and separation spaces and can be applied to more complex flows, extending the original scale-by-scale analysis used by Kolmogorov in homogeneous and isotropic turbulence.

The GKE, projected onto adequate sub-spaces to visualise results, shows intense peaks of net production that are located at points that correlate with the shear layer. This is the main source of turbulent fluctuations in the domain and is responsible for the creation of turbulent structures just after the bump that are then transported downstream and elongated in the streamwise direction. Fluxes from the shear layer are either directed towards bulk of the flow or are captured by the recirculating region. The GKE confirms that complex energy mechanisms are present in all the possible five dimensions [13] and that they arise due to the bump and walls.

Acknowledgements The research leading to these results has received funding from the European Research Council under the ERC Grant Agreement no. 339446. PRACE, under grant no. 2014112647, has awarded access to resource FERMI based in Bologna, Italy.

References

1. Cambon, C., Gracia, B.J.: The role of directionality on the structure and dynamics of strongly anisotropic turbulent flows. J. Turbul. (2013)
2. Casciola, C., Gualtieri, P., Jacob, B., Piva, R.: Scaling properties in the production range of shear dominated flows. Phys. Rev Lett. **95**(2), 024503 (2005)
3. Casciola, C.M., Gualtieri, P., Benzi, R., Piva, R.: Scale-by-scale budget and similarity laws for shear turbulence. J. Fluid Mech. **476** (2003)
4. Cimarelli, A., Angelis, E.D., Casciola, C.M.: Paths of energy in turbulent channel flows. J. Fluid Mech. **715** (2013)
5. Danaila, L., Anselmet, F., Zhou, T., Antonia, R.: Turbulent energy scale budget equations in a fully developed channel flow. J. Fluid Mech. **430**, 87–109 (2001)
6. Fischer, P., Lottes, J.W., Kerkemeier, S.G.: Nek5000—Open source spectral element CFD solver. Argonne National Laboratory, Mathematics and Computer Science Division, Argonne, IL, see http://nek5000.mcs.anl.gov (2008)
7. Hill, R.J.: Exact second-order structure-function relationships. J. Fluid Mech. **468**, 317–326 (2002)
8. Kolmogorov, A.N.: The local structure of turbulence in incompressible viscous fluid for very large reynolds numbers. Dokl. Akad. Nauk SSSR **30**, 299–303 (1941)
9. Kurien, S., Sreenivasan, K.R.: Dynamical equations for high-order structure functions, and a comparison of a mean-field theory with experiments in three-dimensional turbulence. Phys. Rev. E **64**(5), 056302 (2001)
10. Marati, N., Casciola, C.M., Piva, R.: Energy cascade and spatial fluxes in wall turbulence. J. Fluid Mech. (2004)
11. Mollicone, J.P., Battista, F., Gualtieri, P., Casciola, C.: Energy fluxes in turbulent separated flows. J. Phys. Conf. Ser. **759**, 012003 (2016)
12. Mollicone, J.P., Battista, F., Gualtieri, P., Casciola, C.: Effect of geometry and reynolds number on the turbulent separated flow behind a bulge in a channel. J. Fluid Mech. **823**, 100–133 (2017)
13. Mollicone, J.P., Battista, F., Gualtieri, P., Casciola, C.: Turbulence dynamics in separated flows: the generalised kolmogorov equation for inhomogeneous anisotropic conditions. J. Fluid Mech. **841**, 1012–1039 (2018)
14. Patera, A.T.: A spectral element method for fluid dynamics. J. Comput. Phys. **54**, 468–488 (1984)
15. Thiesset, F., Antonia, R.A., Danaila, L., Djenidi, L.: Kármán-howarth closure equation on the basis of a universal eddy viscosity. Phys. Rev. E **88**(1), 011003 (2013)
16. Thiesset, F., Danaila, L., Antonia, R.A.: A look at the turbulent wake using scale-by-scale energy budgets. Fluid Struct Sound Interact. Control (2014)
17. Yakhot, V.: Mean-field approximation and a small parameter in turbulence theory. Phys. Rev. E **63**(2), 026307 (2001)

Nonlinear Transverse Cascade—A Key Factor of Sustenance of Subcritical Turbulence in Shear Flows

D. Gogichaishvili, G. Mamatsashvili, G. Chagelishvili and W. Horton

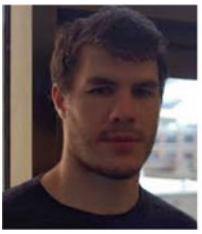


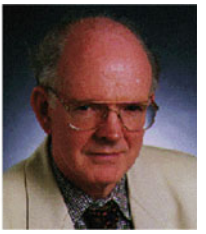

Abstract We analyze the essence of nonlinear processes that underlie turbulence sustenance in spectrally stable shear flows. In these flows, the strong anisotropy of velocity shear-induced nonmodal growth phenomenon in spectral (**k**-)space, in turn, entails the anisotropy of nonlinear processes in this space. Consequently, the main novel nonlinear process is transverse, or angular redistribution of modes in Fourier space referred to as the *nonlinear transverse cascade* rather than a mere direct/inverse cascade. It is demonstrated that nonlinear coherent as well as turbulent states are sustained via a subtle interplay of the linear nonmodal growth (that has transient nature) and the nonlinear transverse cascade. This course of events exemplifies the well-known bypass scenario of subcritical turbulence in spectrally stable shear flows. In this proceedings paper, we present selected results of our simulations of hydrodynamic and MHD 2D plane shear flows to demonstrate the transverse cascade in action.

D. Gogichaishvili (✉)
Department of Physics, The University of Texas at Austin, Austin, TX 78712, USA
e-mail: g.mamatsashvili@hzdr.de

G. Mamatsashvili
Helmholtz-Zentrum Dresden-Rossendorf, P.O. Box 510119, 01314 Dresden, Germany

G. Chagelishvili
Abastumani Astrophysical Observatory, Ilia State University, 0162 Tbilisi, Georgia

G. Chagelishvili
Institute of Geophysics, Tbilisi State University, 0193 Tbilisi, Georgia

W. Horton
Institute for Fusion Studies, The University of Texas at Austin, Austin, TX 78712, USA

M. Gorokhovski and F. S. Godeferd (eds.), *Turbulent Cascades II*,
ERCOFTAC Series 26, https://doi.org/10.1007/978-3-030-12547-9_12

1 Introduction

Delay in the understanding of turbulence phenomenon in smooth shear flows was due to a certain inadequacy of the canonical/modal/spectral approach—spectral decomposition of perturbations in time and subsequent analysis of eigenfunctions—to study their linear stability, which ultimately led to the change of paradigm to, so-called, nonmodal approach [1]. Although, retrospectively a thinking inertia pretty long was clutching on the modal approach, now the phrases: shear flow nonnormality, nonmodal approach, transient growth, bypass concept of turbulence, etc. are already in common parlance of the fluid dynamical and astrophysical disk communities.

In the beginning of the 1990s, the non-normality of shear flows was revealed and extensively studied by the hydrodynamic community [1–3]. Drawbacks of the traditional modal analysis when applied to shear flows have been disclosed. As a result, from the 1990s the mathematical approach was shifted from modal to the nonmodal approach and a breakthrough in the understanding and precise description of linear shear-induced transient phenomena followed. It was shown that in spectrally stable hydrodynamic shear flows perturbations of specific spatial structure (orientation) exhibit linear transient growth and hence are short-lived in the linear limit [2, 4–6]. However, under certain favorable circumstances, finite amplitude perturbations can be maintained over much longer times by the shear flow. Specifically, the imperfect linear transient growth, which is the only energy source for perturbations (turbulence) in these flows, must be bolstered up by nonlinear positive feedback, i.e., the nonlinear processes play a vital role in this case: they close the feedback loop, thereby ensuring the sustenance. This interplay between linear transient growth and nonlinear positive feedback forms the basis for the bypass concept, which was elaborated by the hydrodynamic community to describe the transition to and sustenance of turbulence in spectrally stable shear flows (see, e.g., [7–9]). However, the bypass concept is commonly illustrated on toy models [3] or on phenomenological analysis in physical space [10]. For this reason, it is appropriate to take another route and consider the flow with simplest/constant shear profile and investigate in detail the linear transient and nonlinear processes as well as their interplay in spectral ($\mathbf{k}$-)space. Firstly, a constant shear flow is a quite realistic/useful model and secondly, canonical nonlinear processes, such as direct/inverse cascade, are usually studied in spectral space. Therefore, it is natural to ask how flow shear enriches the canonical nonlinear processes, whether modifies the direct and inverse cascades, or leads to the appearance of a new type of cascade process. The following thoughts can contribute to the clarification of these questions. The shear-induced linear transient growth of a perturbation mode is mainly determined by the orientation of its wavevector (e.g., [5, 11–13]): the spatial Fourier modes that have a wavevector orientated in a certain direction with respect to the flow draw energy from it and amplify, whereas modes with other orientation of the wavevector lose energy to the flow and decay. This anisotropy of the linear energy-exchange processes with respect to wavevector orientation (angle), in turn, causes anisotropy of nonlinear processes in $\mathbf{k}$-space. In particular, as revealed in our studies of hydrodynamic (HD) and magnetohydrodynamic (MHD) smooth shear

flows [14–17], the primary nonlinear process in the presence of flow shear is in fact the so-called, *nonlinear transverse cascade*—transverse, or angular redistribution of Fourier modes in **k**-space—instead of a direct or inverse one. In these papers, we examined in detail key features of the transverse cascade in 2D and 3D constant shear flows by combining direct numerical simulations and, based on that, a detailed analysis of the dynamics in spectral space. The nonlinear transverse cascade represents an alternative to the canonical direct and inverse cascades when large-scale shear of flow velocity is imposed. Nevertheless, apparently, the thinking inertia still persists regarding this new type of shear-induced nonlinear cascade. In this connection, in this proceedings paper, following our studies [14, 15], we intend to show as vividly as possible the action of the nonlinear transverse cascade by analyzing the interplay of the latter with linear transient growth in **k**-space in the 2D case. In Sect. 2, we describe the dynamics of coherent cyclonic and anticyclonic vortices in 2D HD plane constant shear flow. The coherence of perturbations leads to a regular, easily recognizable nonlinear transverse/angular redistribution of modes in (k_x, k_y)-plane, i.e., the transverse cascade. At the same time, we present the corresponding mathematical scheme, clarifying the interplay of the linear transient and nonlinear transverse cascade processes. In Sect. 3, we analyze sustained MHD turbulence in spectrally stable 2D plane constant shear flows with an uniform magnetic field parallel to the flow. The interplay ensuring the sustenance of subcritical turbulence in realistic 3D HD and MHD shear flows are presented in [16, 17].

2 Coherent Vortices in 2D HD Plane Shear Flows—Nonlinear Transverse Cascade

The nonlinear transverse cascade and its interplay with the linear transient growth can be clearly demonstrated in (k_x, k_y)-plane by analyzing the dynamics of coherent cyclonic and anticyclonic vortices in 2D homogeneous constant shear flow, $U_0(x) = (0, Ax)$, with the shear parameter $A > 0$ [14]. The nonlinear dynamical equation for the stream function of perturbations, ψ, is

$$\left[\frac{\partial}{\partial t} + U_0(x)\frac{\partial}{\partial y}\right]\Delta\psi + J(\psi, \Delta\psi) - \nu\Delta^2\psi = 0, \tag{1}$$

where the spatial operators $J(.,.)$ and Δ are, respectively, 2D Jacobian and Laplacian and ν is the viscosity. The velocity and energy density of perturbations are expressed via ψ and density ρ, respectively, as

$$v_x = -\frac{\partial\psi}{\partial y};\quad v_y = \frac{\partial\psi}{\partial x},\quad e(x, y, t) = \frac{1}{2}\rho\left[\left(\frac{\partial\psi}{\partial y}\right)^2 + \left(\frac{\partial\psi}{\partial x}\right)^2\right].$$

Initially we impose coherent vortices with Gaussian shape of stream function in the (x, y)-plane:

$$\psi(x, y, t)|_{t=0} = nb \exp\left(-\frac{x^2 + y^2}{l^2}\right). \tag{2}$$

where $n = -1$ and $n = 1$ corresponds, respectively, to cyclonic and anticyclonic vortices with amplitude $b > 0$. We introduce non-dimensional variables,

$$\tau \equiv At, \quad (X, Y) \equiv \frac{(x, y)}{l}, \quad B \equiv \frac{b}{Al^2}, \quad \Psi \equiv \frac{\psi}{Al^2}, \quad E \equiv \frac{2e}{\rho A^2 l^2}, \quad Re \equiv \frac{Al^2}{\nu},$$

and perform spatial Fourier transform with respect to the coordinates X and Y,

$$\Psi = \int dk_x dk_y \Psi_{\mathbf{k}} \exp(ik_x X + ik_y Y). \tag{3}$$

Substituting Eq. (3) into Eqs. (1) and (2), we obtain evolution equation for $\Psi_{\mathbf{k}}$:

$$k^2 \frac{\partial \Psi_{\mathbf{k}}}{\partial \tau} - k_y \frac{\partial (k^2 \Psi_{\mathbf{k}})}{\partial k_x} + \frac{k^4}{Re} \Psi_{\mathbf{k}} = \sum_{\mathbf{k}=\mathbf{k}'+\mathbf{k}''} (k'_x k''_y - k''_x k'_y) k'^2 \Psi_{\mathbf{k}'} \Psi_{\mathbf{k}''}, \tag{4}$$

with the corresponding initial condition in Fourier plane

$$\Psi_{\mathbf{k}}|_{\tau=0} = nB \exp\left(-\frac{k_x^2 + k_y^2}{4\pi^2}\right),$$

where $k^2 \equiv k_x^2 + k_y^2$. The nonlinear term on the right hand side (rhs) of this equation describes three-wave interactions. Equation (4) forms the basis of the numerical study to explore quantitatively the dynamics of the stream function, spectral energy density, and total energy of cyclonic and anticyclonic vortices. However, to investigate the physics of the phenomena, one has to analyze the dynamical equation for the spectral kinetic energy density, $E_{\mathbf{k}} = k^2 |\Psi_{\mathbf{k}}|^2$, which follows from Eq. (4),

$$\frac{\partial E_{\mathbf{k}}}{\partial \tau} = k_y \frac{\partial E_{\mathbf{k}}}{\partial k_x} + \frac{2k_x k_y}{k^2} E_{\mathbf{k}} - \frac{k^2}{Re} E_{\mathbf{k}} + N_{\mathbf{k}}, \tag{5}$$

where $N_{\mathbf{k}}$ is the nonlinear term:

$$N_{\mathbf{k}} = \sum_{\mathbf{k}=\mathbf{k}'+\mathbf{k}''} (k'_x k''_y - k''_x k'_y) k'^2 (\Psi^*_{\mathbf{k}} \Psi_{\mathbf{k}'} \Psi_{\mathbf{k}''} + \Psi_{\mathbf{k}} \Psi^*_{\mathbf{k}'} \Psi^*_{\mathbf{k}''}).$$

The terms on the rhs of Eq. (5) represent four–three linear and one nonlinear—basic phenomena: (*i*) the linear flux of the spectral kinetic energy parallel to the k_x-axis; (*ii*) the energy exchange between the perturbation modes and the background

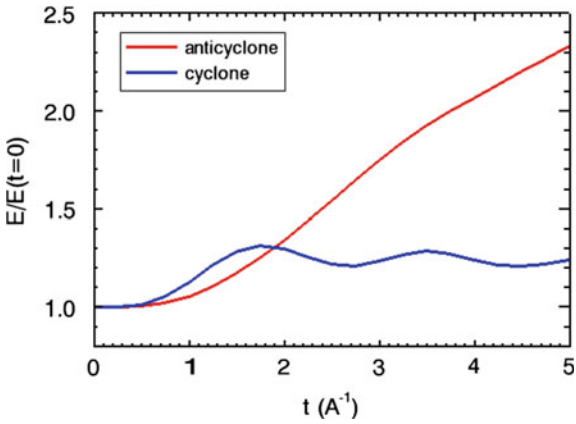

Fig. 1 Normalized total energy versus time for finite amplitude ($B = 3$) coherent anticyclonic (red) and cyclonic (blue) vortex perturbations at $Re = 1000$

flow; (*iii*) the viscous dissipation; (*iv*) the nonlinear processes that redistribute the energy of perturbation modes in **k**-plane via triad interactions, but do not change their total energy. The interplay of these basic phenomena defines $\partial E_{\mathbf{k}}/\partial\tau$. By solving numerically Eq. (4), or equivalently Eq. (5), one can get full information on all the physical quantities and underlying dynamics.

The evolution of the perturbation energy normalized to the initial value E/E_0 for the coherent anticyclonic and cyclonic perturbations are presented in Fig. 1. The energy of the anticyclonic vortex increases monotonically, while the energy of the cyclonic one initially increases and then oscillates weakly around a constant value. Since the linear dynamics of the perturbations are identical, the difference in the energy evolutions is due to the effect of nonlinearity in (k_x, k_y)-plane characterized by $N_{\mathbf{k}}$. For the anticyclonic vortex, this term is presented (at $B = 3$ and $Re = 1000$) in the upper two plots of Fig. 2 at $\tau = 0.5$ and 2. The nonlinearity redistributes the perturbation energy from the blue areas (where $N_{\mathbf{k}} < 0$) to the red ones (where $N_{\mathbf{k}} > 0$). The green refers to areas where $N_{\mathbf{k}} \simeq 0$. As it is seen, as a result of the nonlinear interactions, energy is being transferred from quadrants *II* and *IV* (where $N_{\mathbf{k}}$ is predominantly negative), to quadrants *I* and *III* (where $N_{\mathbf{k}}$ is predominantly positive). This nonlinear angular redistribution, or transverse cascade, repopulates the growing modes, which further extract shear flow energy and are amplified in quadrants *I* and *III* of **k**-plane, where $k_x k_y > 0$, due to the second rhs term in Eq. (5). This nonlinear feedback mechanism results in the growth of the total energy (red curve in Fig. 1) and hence sustenance of the coherent anticyclonic vortical perturbations. In addition, it is seen that the domain of significant nonlinear activity shrinks in time towards lower wavenumbers, i.e., an inverse cascade is also at work. However, the dominant nonlinear process is the transverse cascade.

The lower two plots of Fig. 2 show that the transverse cascade is also strongly pronounced for coherent cyclonic vortex. However, in this case the nonlinear dynamics is more complicated. The positive and negative feedbacks alternate in time. Indeed, we see that nonlinear interactions redistribute energy mainly over wavenumber angle,

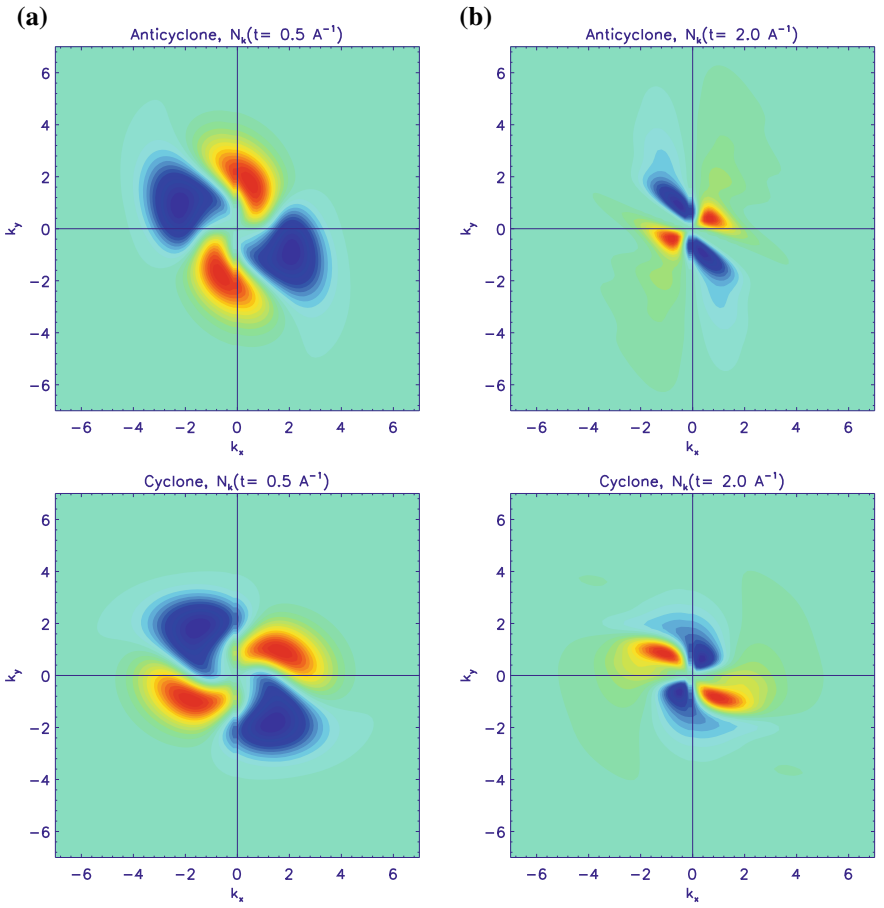

Fig. 2 The spectrum of the nonlinear term $N_{\mathbf{k}}(k_x, k_y, \tau)$ for the coherent anticyclonic (upper two plots) and cyclonic (lower two plots) vortices with $Re = 1000$ and $B = 3$ at times $\tau = 0.5$ and 2, respectively. Nonlinearity redistributes mode energy from the blue areas (where $N_{\mathbf{k}} < 0$) to the red ones (where $N_{\mathbf{k}} > 0$)—the nonlinear transverse cascade is strongly pronounced. (These figures are reproduced from Ref. [14])

from quadrants II and IV to quadrants I and III at $\tau = 0.5$ and vice versa at $\tau = 2$. Hence, the transverse cascade repopulates growing modes (for which $k_x k_y > 0$) at $\tau = 0.5$, contributing to an increase in the cyclonic vortex total energy. By contrast, the repopulation of decaying modes by the transverse cascade leads to a decrease in the total energy at $\tau = 2$. This results in the oscillations in the total energy (blue curve in Fig. 1). So, in the case of the cyclonic vortex, the transverse cascade does not ensure a continuous positive feedback.

3 Sustaining Turbulence in Spectrally Stable 2D MHD Plane Shear Flows

Now we move to the MHD case and, following Ref. [15], demonstrate manifestations of the nonlinear transverse cascade for sustained 2D MHD turbulence in incompressible constant shear flow, $\mathbf{U}_0 = (0, -Ax)$, threaded by an uniform background magnetic field parallel to the flow, $\mathbf{B}_0 = (0, B_{0y})$ (with $A, B_{0y} > 0$). This flow is spectrally stable and hence the turbulence is subcritical by nature, being supported energetically only by shear flow non-normality induced transient (non-modal) growth. As for the essence of the nonlinear processes, it is again a transverse redistribution of kinetic and magnetic spectral energies. We present the results of direct numerical simulations in (k_x, k_y)-plane, demonstrating the dominance of the transverse cascade in 2D MHD plane shear flows too.

We consider basic equations of non-ideal incompressible MHD flow and use normalized variables by taking the shear time, A^{-1}, as the unit of time; the Alfvén speed, $u_A = B_{0y}/(4\pi\rho)^{1/2}$, as the unit of velocity; $\ell \equiv u_A A^{-1}$ as the unit of length; and B_{0y}, as the unit of the magnetic field perturbations (see details in [15]). Figure 3 shows the time-development of the domain-averaged perturbed kinetic, $\langle E_K \rangle$, and magnetic, $\langle E_M \rangle$, energies as well as the Reynolds, $\langle u_x u_y \rangle$, and Maxwell $-\langle b_x b_y \rangle$ stresses. After an initial growth phase, the energies and stresses settle down to a quasi-steady state of sustained turbulence. In this state, the kinetic and magnetic energies are comparable. The Maxwell stress is much larger than the Reynolds stress, indicating that the turbulent transport and energy extraction from the mean flow are ensured by the magnetic field perturbations—the Maxwell stress counteracts dissipative processes and plays a decisive role in the maintenance of the turbulence. Therefore,

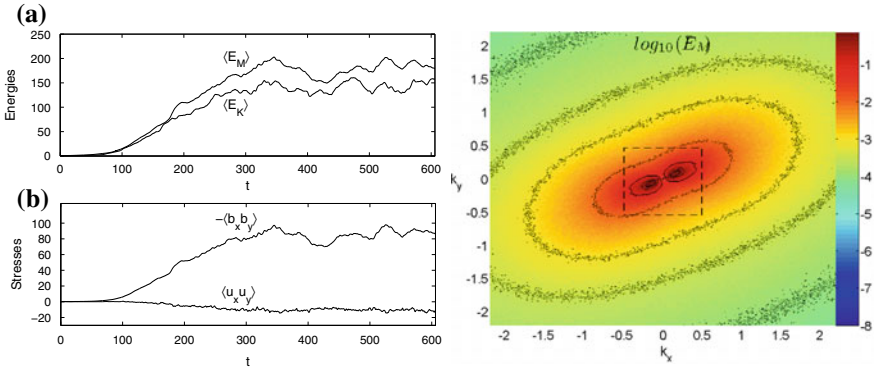

Fig. 3 (left) the domain-averaged **a** perturbed kinetic, $\langle E_K \rangle$, and magnetic, $\langle E_M \rangle$, energies as well as **b** the Reynolds and Maxwell stresses versus time. (right plot) Logarithm of the time-averaged magnetic energy spectra in (k_x, k_y)-plane in the quasi-stationary turbulent state. The dashed rectangle encloses the central, small wavenumber area of (k_x, k_y)-plane that is vital for the sustenance of the turbulence. (These figures are reproduced from Ref. [15].)

we analyze only dynamical equation for nondimensional magnetic spectral energy, $E_M = |b_x|^2 + |b_y|^2$:

$$\frac{\partial E_M}{\partial t} + k_y \frac{\partial E_M}{\partial k_x} = I_M + I_{MK} + D_M + N_M, \tag{6}$$

where, the second term on the left hand side is the flux of the spectral magnetic energy parallel to k_x axis, I_M is the Maxwell stress spectrum, describing the magnetic energy exchange with the mean flow and perturbation modes, I_{MK} is the exchange between the kinetic and magnetic spectral energies, D_M is the resistive dissipation term and N_M is the nonlinear transfer of the magnetic spectral energy in (k_x, k_y)-plane:

$$I_M = -b_x b_y^* - \text{c.c.} = \frac{2k_x k_y}{k^2} E_M, \quad I_{MK} = \mathrm{i}k_y (u_x b_x^* + u_y b_y^* - \text{c.c.}), \quad D_M = -\frac{2k^2}{Rm} E_M$$

$$N_M(\mathbf{k}, t) = \mathrm{i}(k_y b_x^* - k_x b_y^*) \sum_{\mathbf{k}=\mathbf{k}'+\mathbf{k}''} \left[u_x(\mathbf{k}', t) b_y(\mathbf{k}'', t) - u_y(\mathbf{k}', t) b_x(\mathbf{k}'', t) \right] + \text{c.c.}\,.$$

The simulations have indicated that $I_{MK} \ll I_M$, therefore, in Figs. 3 and 4 we show only time-averaged E_M, I_M and N_M in (k_x, k_y)-plane in the quasi-steady turbulent state. With these plots we can understand the action of the last two dynamical terms and the resulting anisotropic energy spectrum (Fig. 3). Similar to the energy spectrum, I_M and N_M are also strongly anisotropic over wavenumbers, being tilted towards the k_x-axis due to the shear (Fig. 4). I_M mainly operates at $0.05 < k < 0.5$ on the $k_x/k_y > 0$ side, where it is positive (red and yellow) and supplies the modes with energy at these wavenumbers. Specifically, a cycle of the sustenance scheme is the following. The modes that are initially on the left side of the injection region, where $I_M > 0$, drifting along the k_x-direction, go into this region. As a result, their magnetic

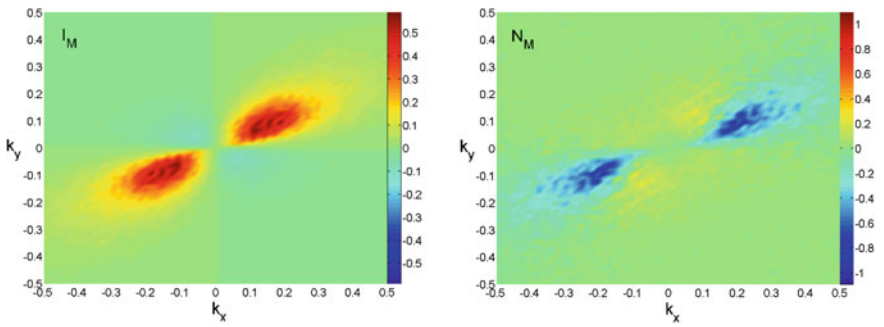

Fig. 4 The time-averaged spectra of I_M (left) and the nonlinear transfer term N_M (right) in $\mathbf{k}-$plane in the state of quasi-steady turbulence. N_M transfers magnetic energy anisotropically (transversely) in wavenumber plane, away from regions where $N_M < 0$ (blue) to regions where $N_M > 0$ (yellow). (These figures are reproduced from Ref. [15].)

energy starts to grow due to the action of I_M. Afterwards, these modes enter the region where the nonlinear term is negative $N_M < 0$ (blue) and hence acts to transfer part of the amplified magnetic energy of these modes back to the area where $N_M > 0$ (yellow), from which these modes started off, thereby replenishing new modes there. This positive nonlinear feedback is an essential link that closes the cycle loop. Thus, in this cycle, the modes acquire magnetic energy from the flow due to the injection term I_M. Part of this energy goes into the kinetic energy due to the nonlinear term in the spectral kinetic energy equation (not given here) and the other part into magnetic energy of the newly generated modes, which go through the cycle again; the rest is eventually dissipated. In this way, a positive feedback loop—interplay of the linear transient amplification and nonlinear transverse cascade of the magnetic spectral energy—is established, ensuring the long-term sustenance of the turbulence.

Acknowledgements D. G. acknowledges the financial support from the US Department of Energy under grant DE-FG02-04ER54742; G. M. is supported by the Alexander von Humboldt Foundation (Germany).

References

1. Schmid, P., Henningson, D.: Stability and Transition in Shear Flows. Springer (2000)
2. Reddy, S., Henningson, D.: J. Fluid Mech. **252**, 209 (1993)
3. Trefethen, L., Trefethen, A., Reddy, S., Driscoll, T.: Science **261**, 578 (1993)
4. Gustavsson, L.: J. Fluid Mech. **224**, 241 (1991)
5. Farrell, B., Ioannou, P.: Phys. Fluids A **5**, 1390 (1993)
6. Chagelishvili, G., Zahn, J.-P., Tevzadze, A., Lominadze, J.: A&A **402**, 401 (2003)
7. Baggett, J., Driscoll, T., Trefethen, L.: Phys. Fluids **7**, 833 (1995)
8. Grossmann, S.: Rev. Mod. Phys. **72**, 603 (2000)
9. Chapman, J.: J. Fluid Mech. **451**, 35 (2002)
10. Waleffe, F.: Phys. Fluids **7**, 3060 (1995)
11. Butler, K., Farrell, B.: Phys. Fluids **4**, 1637 (1992)
12. Farrell, B.: Phys. Fluids **31**, 2093 (1988)
13. Jiménez, J.: Phys. Fluids **25**, 110814 (2013)
14. Horton, W., Kim, J.-H., Chagelishvili, G., Bowman, J., Lominadze, J.: Phys. Rev. E **81**, 066304 (2010)
15. Mamatsashvili, G., Gogichaishvili, D., Chagelishvili, G., Horton, W.: Phys. Rev. E **89**, 043101 (2014)
16. Mamatsashvili, G., Khujadze, G., Chagelishvili, G., Dong, S., Jiménez, J., Foysi, H.: Phys. Rev. E **94**, 023111 (2016)
17. Gogichaishvili, D., Mamatsashvili, G., Horton, W., Chagelishvili, G., Bodo, G.: ApJ **845**, 70 (2017)

Incompressible Homogeneous Buoyancy-Driven Turbulence

Benoît-Joseph Gréa and Olivier Soulard

Abstract We review recent results concerning the idealized framework of incompressible homogeneous buoyancy-driven turbulence, shedding light on the mixing process occurring in variable density fluids subjected to accelerations. Self-similar analysis, results from numerical simulations and anisotropic spectral models establish the sensitivity of the late time dynamics to the distribution of energy at large scales, to the different properties of the mixing and to the resonances inside the mixing zone when a time-varying acceleration is applied. The isotropic and anisotropic part of turbulent spectra are also investigated. Different scenarii are proposed to explain how the turbulent scales within the inertial range are altered by buoyancy forces.

1 Introduction

Turbulent mixing subjected to buoyancy forces is ubiquitous in astrophysics, geophysics and many engineering applications such as inertial confinement fusion (ICF). It often results from accelerations applied at the interfaces of variable density fluids, leading to the classical Rayleigh-Taylor, Richtmyer-Meschkov or Faraday instabilities[1] [1–5]. These destabilization mechanisms, if strong enough, generate non-linear interactions between modes and give birth to turbulent mixing zones.

Among others, two important questions have motivated engineers and researchers for years: What are (i) the dynamics of the mixing zones and (ii) the main features of turbulence driven by this process? Many studies addressing this problem already evidenced how these two aspects are closely entangled. Yet regarding these questions,

[1]Corresponding respectively to constant, impulsive or oscillating accelerations.

B.-J. Gréa (✉) · O. Soulard
CEA, DAM, DIF, 91297 Arpajon, France
e-mail: benoit-joseph.grea@cea.fr

O. Soulard
e-mail: olivier.soulard@cea.fr

M. Gorokhovski and F. S. Godeferd (eds.), *Turbulent Cascades II*,
ERCOFTAC Series 26, https://doi.org/10.1007/978-3-030-12547-9_13

the role of initial conditions and how buoyancy forces influence the cascade remain not fully understood.

Recent results obtained at CEA in collaboration with LFMA allow to get new insights in this problem and we propose to briefly review them in this chapter. As often in fluid dynamics, the present approach extensively uses numerical simulations in order to assess and confront the theory. However, simulation still suffers from inherent limitations due to the difficulty of reaching high Reynolds numbers and to the finite size of computational domains. In order to overcome this problem, two-point anisotropic turbulence models are developed and implemented. This combined strategy relying on theory, simulation and model reveals itself fruitful and constitutes perhaps the principal originality of the present method.

For simplicity, we limit the context of this study to miscible and incompressible fluids as in [3]. In addition, we discuss only unstable configurations discarding important problems such as stably stratified turbulence.

This chapter is organized as follows: First, we introduce the homogeneous framework and the associated spectral anisotropic model in order to explore buoyancy driven turbulence. Then, we investigate the dynamics of turbulent quantities, showing its relation with large scales structures, the characteristics of the mixing and internal gravity waves. Finally, we turn our attention to smaller scales detailing how they are influenced by buoyancy forces.

2 Stratified Homogeneous Turbulence as a Paradigm for Buoyancy-Driven Turbulence

Homogeneous approximations have played an important role in turbulence history, starting from the pioneering works on homogeneous isotropic turbulence (HIT) [6], and extended later to anisotropic flows [7]. Accordingly, many closures introduced for turbulence modelling and fast pseudo-spectral Fourier based algorithms for direct numerical simulations (DNS) have benefited from this idealized concept.

In the context of buoyancy-driven turbulence, in particular related to the Rayleigh-Taylor instability, the homogeneous assumption can apply to turbulent quantities at the center of the mixing zones due to a scale separation between the mean density gradient and the integral scale of turbulence (see [8]). Therefore, many homogeneous frameworks for buoyancy-driven flows have been proposed, in particular by [9–11].

The equations of stratified homogeneous turbulence (SHT) addressing the turbulent velocity $\mathbf{u}(\mathbf{x}, t)$ and concentration $c(\mathbf{x}, t)$ fields in the Boussinesq limit take the following form [12, 13]:

$$\partial_t c + (\mathbf{u} \cdot \nabla) c = -\frac{1}{L} u_3 + \mathscr{D} \Delta c, \tag{1}$$

$$\partial_t \mathbf{u} + (\mathbf{u} \cdot \nabla) \mathbf{u} = -\nabla p + 2\mathrm{A_t} c G(t) \mathbf{n} + \mu \Delta \mathbf{u}, \tag{2}$$

$$\nabla \cdot \mathbf{u} = 0, \tag{3}$$

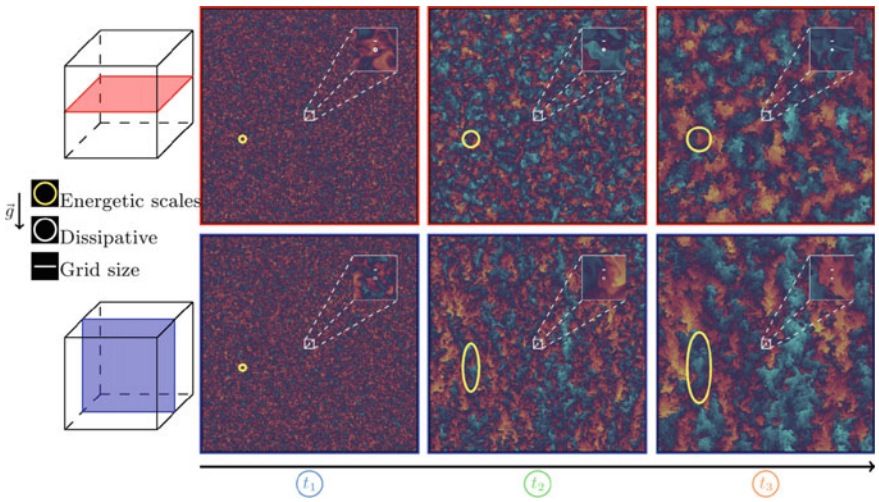

Fig. 1 Fluctuating density field at different times extracted from a DNS of unstably stratified homogeneous turbulence detailed in [16]. The simulation uses 2048^3 grid points. The energetic, dissipative and grid scales are also indicated. Top row: Horizontal plane. Bottom row: vertical plane. From the initial isotropic condition, the work of buoyancy forces can be observed by the growth and elongation along the vertical direction of turbulent structures

$$\dot{L} = 12\frac{\lambda}{L}\langle u_3 c\rangle\,, \tag{4}$$

with $p(\mathbf{x}, t)$ the fluctuating reduced pressure, $G(t)\mathbf{n}$ the acceleration vector aligned with the vertical direction $_3$, $\mathrm{A_t}$ the Atwood number, μ and $\mathscr{D}$ the viscosity and diffusion coefficient. Fluctuating turbulent quantities have zero mean $\langle\mathbf{u}\rangle = \langle c\rangle = \langle p\rangle = 0$ and are assumed homogeneous. Remark that the acceleration $G(t)$ is time varying, allowing various changes of sign.

One important characteristic of this system is the feedback of turbulence on the mean density gradient or equivalently[2] the mixing zone width L. This is expressed by Eq. (4) which has been derived in the context of the rapid acceleration model [14]. Thus, within the SHT framework, it is possible to mimic frozen stratifications by setting $\lambda = 0$, but also evolving mixing zone with $\lambda = 1$, corresponding to Rayleigh-Taylor flows for instance.

The question of how well SHT is able to reproduce the characteristics of turbulence in a mixing zone comes naturally. From [15], it appears that the energetic and smaller scales of turbulence are qualitatively well reproduced in SHT. Besides and as may be expected, the larger ones differ due to inhomogeneous effects.

Despite this limitation, working within the SHT framework presents many advantages. DNS (see Fig. 1) are facilitated as confinement effects due the finite size of the

[2] Assuming the mean density profile is linear inside the mixing zone.

computational domain are delayed.[3] The simplifications provided by the theoretical background allow for the derivation of two-point anisotropic turbulence models as detailed in the following section. It is important to stress that most theories or models dedicated to turbulent mixing layers should also apply to SHT, and can be validated against it.

3 Exploring High Reynolds Number with Spectral Anisotropic Models

The simulations of unstable mixing layers become costly due to the growth of the Reynolds number. This limitation comes from the constraints to keep the resolution of small scales but also to avoid spurious effects when the turbulent eddies reach the size of the computational domain. In consequence, an appealing strategy consists in developing turbulence models not restricted by the Reynolds number values and able to reproduce efficiently the phenomenology of buoyancy-driven turbulence.

The closure choice and the description level for a turbulence model result from a compromise between complexity and accuracy. In that matter, two-point anisotropic spectral models based on eddy-damped quasi-normal Markovian (EDQNM) and applied to SHT seem well adapted (see [16–19]).

These models express the dynamics of anisotropic spectra for the velocity and the buoyancy fields. Due to their axisymmetric description, they can evaluate exactly the buoyancy production and the redistribution by rapid pressure effects. This aspect appears very important to capture the late-time dynamics of the mixing zone. Models which do not fulfil this condition, based on one-point description or even using shell-integrated spectra as [20, 21] for instance, need corrections to produce the right values for the buoyancy production as they underestimate large scales anisotropy.

In order to assess the validity of the model, many comparisons were performed against SHT simulations at different initial conditions [16, 17] (see Fig. 2). This procedure permits to identify various defects. Some have been known for a long time in classical isotropic EDQNM closures, such as the underestimation of backscatter transfers at large scales and of energy values at small scales often attributed to the intermittency problem. Besides, the distortions coming from discarding the buoyancy production in the equation for triple correlations have been corrected by changing the eddy-damping term in the closure. The level of modelling derived by this procedure has been shown to reproduce accurately one-point and two-point turbulent quantities provided by the DNS (see for instance Fig. 2).

The anisotropic EDQNM model can be used with confidence to explore the mixing layers dynamics and the scale-by-scale distribution of turbulent energy at high Reynolds numbers. This also allows to study the influence of initial conditions beyond the reach of simulations, as will be detailed in the next section.

[3] The limitation in SHT simulations principally comes from the growth of the integral scale but not the mixing zone width which is modelled contrary to classical mixing layer simulations.

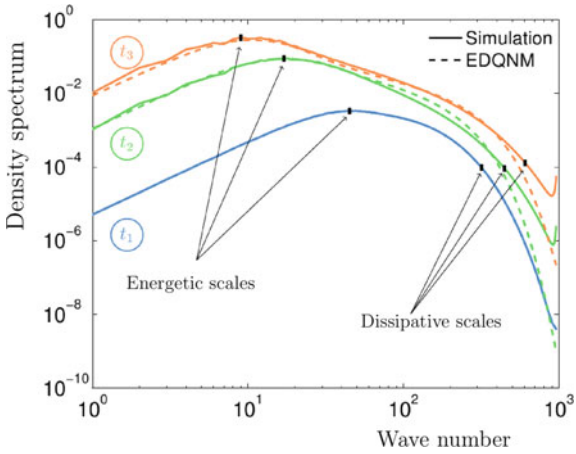

Fig. 2 Density spectra at different times corresponding to the SHT case detailed in [16] and also shown in Fig. 1. Plain lines: DNS. Dashed lines: EDQNM.

4 Self-similar and Non Self-similar Dynamics

Unstably stratified homogeneous turbulence (USHT)[4] reaches self-similar states at late times, similar to Rayleigh–Taylor turbulent mixing zones.

In USHT with frozen stratification, $\lambda = 0$ in Eq. (4), the turbulent quantities experience an exponential growth which is further characterized by a parameter β such that the length scale of the flow ℓ and its kinetic energy K grow as:

$$\text{USHT}(\lambda = 0): \quad \ell(t) \propto e^{\beta t/2}\ , \quad K(t) \propto e^{\beta t}.$$

In Rayleigh–Taylor turbulence and USHT taking into account the feedback on the mean density gradient, $\lambda = 1$, the central self-similar parameter is the growth rate coefficient α. It is such that the mixing zone width L evolves as:

$$\text{Rayleigh} - \text{Taylor or USHT}(\lambda = 1): \quad L(t) = 2\alpha \mathrm{A_t} G_0 t^2\ ,$$

For both flows, it is important to be able to predict the values of coefficient α or β which appear to depend on initial conditions [22]. As in homogeneous isotropic turbulence (HIT), the self-similar properties of USHT are expected to be influenced by large turbulent scales [23, 24], i.e. by scales much larger than the integral scale of turbulence. For instance, in HIT, the decay rate of kinetic energy in the self-similar regime is deduced from the principle of the permanence of large eddies and depends on the power law exponent of the turbulent spectrum at small wave numbers, also called "infrared" exponent [25, 26] and denoted by s_0 (see Fig. 3).

A similar link exists between large scales and self-similarity in USHT. This connection was studied in [27]. In this work, it was shown that equatorial wave vectors

[4] Special SHT case with a constant destabilizing accelerations G_0.

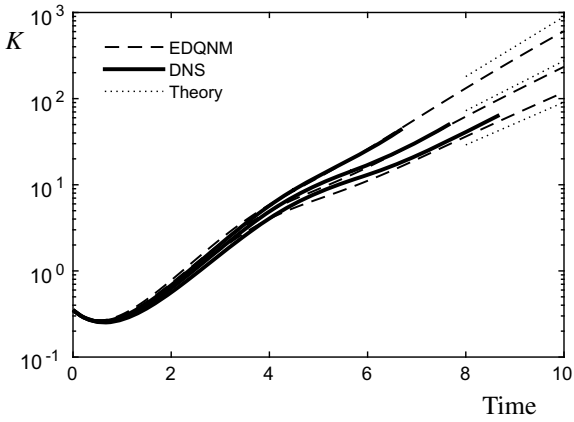

Fig. 3 Time evolution of kinetic energy K for different infra-red slope $s_0 = 2, 3, 4$ from [16]. Plain line: DNS. Dashed line: EDQNM. Dotted line: Theory with $\beta = 4/(s_0 + 3)$.

evolve linearly from their initial conditions when $s_0 < 4$. This is the equivalent of the permanence of large eddies observed in HIT. Note that other directions do not verify this property. Using this result, a relation that links β or α to s_0 can be derived:

$$\beta = \frac{4}{(s_0 + 3)} \text{ and } \alpha = \frac{2}{(s_0 + 2)(s_0 + 3)}.$$

Besides, simple expressions relating the correlations of concentration and velocity to the value of the growth parameter can also be obtained.

An alternative characterization of self-similarity can be envisioned. In [14], it was proposed to express α as a function of a the global mixing parameter Θ. The latter quantity is a segregation ratio which gives an indication on the degree of mixing. In this regard, let us precise that the evolution of a turbulent mixing zone is influenced by the level of mixing it experiences: the more mixing there is, the less potential energy is available and the slower the growth of the zone is. This property has long been identified and accounted for in models describing Rayleigh–Taylor turbulence [28]. In particular, the Rapid Acceleration Model (RAM) [14] has been used to derive that:

$$\alpha = \frac{\Lambda^2(1-\Theta)^2}{1 + \Lambda(1-\Theta)},$$

with $\Lambda \approx 0.7$ a parameter characterizing the directional anisotropy of the flow [29]. The prediction made in [14] was checked against numerous experiments and simulations and was found to be in good agreement with them. In particular, it agreed with the simulations described in [30].

In [27, 31], this relation was extended to express all the second order moments of the concentration and velocity fields as a function of Θ. These expressions give access to how mixing influences the repartition of kinetic and potential energies and their anisotropy.

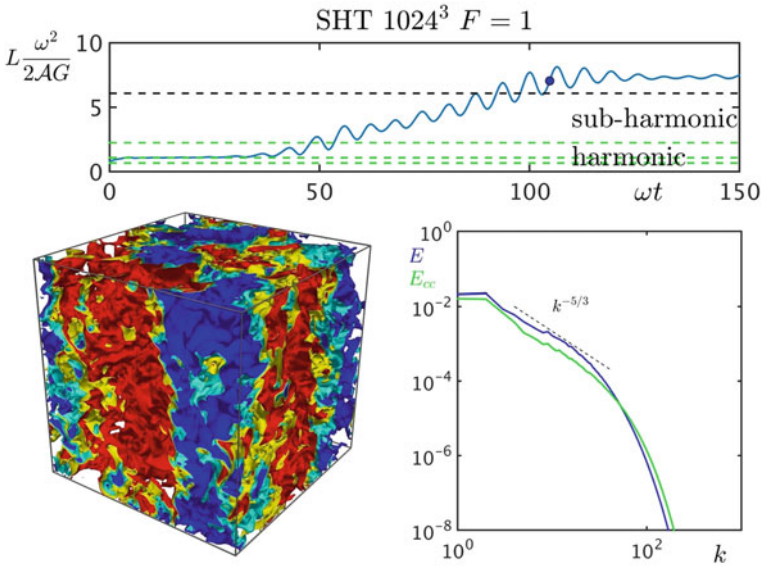

Fig. 4 SHT DNS with periodic acceleration $G(t) = G_0(1 + F\cos\omega t)$ corresponding to the Faraday instability [33]. Top: Time evolution of the mixing zone. Bottom left: Vertically elongated structure of density from DNS at $\omega t = 105$. Bottom right: Kinetic energy E and density E_{cc} spectra at $\omega t = 105$

While the self-similar dynamics of mixing layers has been extensively studied, it occurs scarcely in nature and applications, essentially for two reasons: First, the duration of the transient regime may be long. This explain for instance why the growth rate coefficient α is difficult to measure in many Rayleigh-Taylor experiments and simulations. In addition, if the acceleration is time-varying, then the turbulence time scales cannot adapt instantaneously to the buoyancy forces.

Non self-similar dynamics are more difficult to investigate as they evolve in a larger phase space. This aspect has bitter consequences for one-point turbulence models which, in most case, do not capture correctly the transient while still behaving correctly in the self-similar regimes as shown in [32].

In addition, time-varying accelerations can produce resonances inside the mixing layer and trigger a parametric instability similar to the classical Faraday instability appearing at vibrated interfaces. This leads to the growth and the saturation of the mixing zone, which can be studied and predicted within the SHT framework (see [33] and Fig. 4). This phenomenon explains the complex behaviour of a mixing zone experiencing acceleration decceleration then reacceleration phases [34, 35]. However, the question of how to model mixing zones subjected to such instabilities remains pending.

5 Scaling Laws of Turbulent Spectra

As explained before, the scaling laws of SHT in the inertial range are similar to those in inhomogeneous mixing layers, driven by the Rayleigh–Taylor instability for instance.

Several theories of Rayleigh–Taylor small scales have been expressed in the literature [36–41]. All of them postulate that, for scales much smaller than the integral length scale and much larger than the viscous scale, there exists an "inertial" range where turbulent spectra are scale-similar. However, different scaling laws, stemming from different physical arguments, are predicted in [36–41]. These scaling laws are quantitatively very close to one another. The kinetic energy spectrum is found to have a scaling exponent of -2 in [39], $-7/4$ in [37, 38] and $-5/3$ in [36, 40, 41]. The latter corresponds to the standard Kolmogorov–Obukhov theory. Unfortunately, current simulations [42] and experiments [43] do not allow one to discriminate these values, as they do not reach high enough Reynolds numbers.

From there, two ways can be explored to gain additional knowledge. The first one consists in using theoretical arguments. This course was pursued in [40], where an extension of the Monin–Yaglom relation to Rayleigh–Taylor turbulence, taking into account the inhomogeneous character of the flow and the action of buoyancy forces, was proposed. Among the mentioned theories [36–41], only those corresponding to a classical Kolmogorov–Obukhov scaling were compatible with this Monin–Yaglom relation. As a result, only those theories were fit to describe asymptotically small scales in Rayleigh–Taylor turbulence.

The second way consists in capitalizing on the possibilities offered by USHT [12, 13, 16–18, 27] and its EDQNM modelling [16–18] to explore very large Reynolds numbers. In [16, 18], the properties of USHT at very high Reynolds numbers were scrutinized. One of the main results of these studies was to demonstrate the existence of an inertial range with a scaling exponent compatible with the Kolmogorov–Obukhov theory.

Beyond this aspect, it has been noted that anisotropy has a strong imprint on inertial scales. Following [45, 46], two main physical processes are expected to drive these properties. The first one corresponds to the local action of buoyancy forces and leads to equilibrium spectra. The second one results from the non-local action of transfer terms and is associated with zero-modes, i.e. of modes which nullify the anisotropic part of transfer terms.

The equilibrium mechanism has been studied in [47] and leads to a k^{-3} scaling for the velocity and concentration anisotropic spectra and to a $k^{-7/3}$ scaling for the concentration flux spectrum. The EDQNM model proposed in [16–18] for USHT was used to test these scalings at high Reynolds numbers [16, 18]. A systematic departure from these equilibrium scalings was identified, suggesting the presence of zero-modes.

The properties of zero-modes were then studied in [44]. The zero-mode analysis showed that the velocity and concentration zero-modes display approximate $k^{-7/3}$ scalings. As a result, at very small scales, the velocity and concentration zero-modes

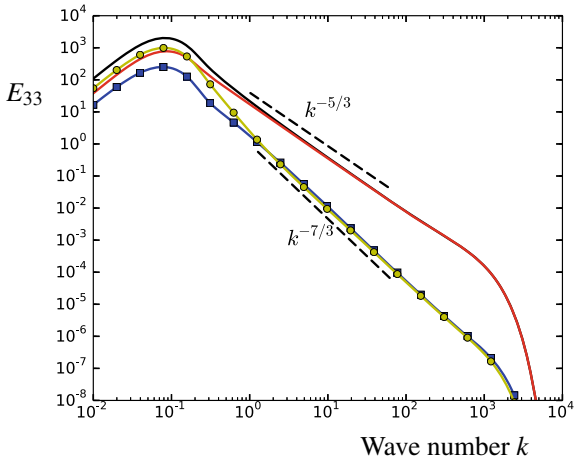

Fig. 5 Vertical velocity spectrum E_{33} and its isotropic and anisotropic contribution from USHT EDQNM simulation at turbulent Reynolds number $= 10^7$ [44]. Black line: total. Red line: isotropic part. Yellow and blue line: Anisotropic polarisation and directional part

become larger than equilibrium spectra, which, we recall, scale as k^{-3}. Therefore, one of the main result of [44] is that the anisotropy of the velocity and concentration spectra is due to the non-local non-linear transfer terms and scales as $k^{-7/3}$ (see Fig. 5). This prediction agrees with the simulations of [16, 18].

As for the concentration flux, the zero-mode analysis also yields an approximate $k^{-7/3}$ scaling. This scaling is close to but different from the equilibrium one. This small variation is such that the the zero-mode contribution will eventually become negligible at high wave numbers. Consequently, the outcome is here the inverse of the one derived for the velocity and concentration spectra: for the smallest scales of the inertial range, the anisotropy of the concentration flux spectrum is linked to the local action of buoyancy forces. Besides, we also derived another noticeable result for the concentration flux spectrum. Indeed, the zero-mode contribution decays only slightly more rapidly than the corresponding equilibrium contribution. When cast in terms of Reynolds numbers, this property implies that the inertial slope of the concentration flux exhibits a slow convergence to $-7/3$. As a result, zero-modes provide a possible explanation for observations on this slow convergence which have already been made in different contexts [48].

6 Conclusion

In this review, it is shown how a combined strategy between theory, numerical simulations and models allows to get insight in the phenomenology of incompressible homogeneous buoyancy-driven turbulence. New results concerning the dynamics and structure of the flow are thus established, listed below:

- The late time dynamics depend on the initial distribution of energy at large scales.
- The mixing zone growth rate and the Reynolds stress tensor in a mixing zone can be derived solely from the global mixing parameter and to a lesser degree to the directional anisotropy.
- The final sizes of mixing zones subjected to parametric instability for time-varying accelerations have been predicted.
- The isotropic part of turbulent spectra in the inertial range obeys the Kolmogorov-Obhukov phenomenology.
- The anisotropic part of velocity spectra seems determined by the non linear transfer through 'mode zero', while the linear buoyancy effects appear sub-dominant.

References

1. Sharp, D.H.: An overview of Rayleigh-Taylor instability. Physica D **12**, 3–18 (1984)
2. Zhou, Y.: Rayleigh-Taylor and Richtmyer-Meshkov instability induced flow, turbulence, and mixing. I. Phys. Rep. (2017)
3. Boffetta, G., Mazzino, A.: Incompressible Rayleigh-Taylor turbulence. Annu. Rev. Fluid Mech. **49**(1), 119–143 (2017)
4. Brouillette, M.: The Richtmyer-Meshkov instability. Annu. Rev. Fluid Mech. **34**(1), 445–468 (2002)
5. Miles, J., Henderson, D.: Parametrically forced surface waves. Annu. Rev. Fluid Mech. **22**(1), 143–165 (1990)
6. Batchelor, G.K.: The Theory of Homogeneous Turbulence. Cambridge Monographs on Mechanics and Applied Mathematics. Cambridge University Press (1953)
7. Sagaut, P., Cambon, C.: Homogeneous Turbulence Dynamics. Cambridge University Press (2008)
8. Vladimirova, N., Chertkov, M.: Self-similarity and universality in Rayleigh-Taylor, Boussinesq turbulence. Phys. Fluids **21**, 015102 (2009)
9. Batchelor, G.K., Canuto, V.M., Chasnov, J.R.: Homogeneous buoyancy-generated turbulence. J. Fluid Mech. **235**, 349–378 (1992)
10. Livescu, D., Ristorcelli, J.R.: Buoyancy-driven variable-density turbulence. J. Fluid Mech. **591**, 43–71 (2007)
11. Chung, D., Pullin, D.I.: Direct numerical simulation and large-eddy simulation of stationary buoyancy-driven turbulence. J. Fluid Mech. **643**, 279–308 (2010)
12. Griffond, J., Gréa, B.-J., Soulard, O.: Unstably stratified homogeneous turbulence as a tool for turbulent mixing modeling. J. Fluids Eng. **136**(9), 091201 (2014)
13. Griffond, J., Gréa, B.-J., Soulard, O.: Numerical investigation of self-similar unstably stratified homogeneous turbulence. J. Turb. **16**(2), 167–183 (2015)
14. Gréa, B.-J.: The rapid acceleration model and growth rate of a turbulent mixing zone induced by Rayleigh-Taylor instability. Phys. Fluids **25**, 015118 (2013)
15. Soulard, O., Griffond, J., Gréa, B.-J.: Large-scale analysis of unconfined self-similar Rayleigh-Taylor turbulence. Phys. Fluids **27**, 095103 (2015)
16. Gréa, B.-J., Burlot, A., Godeferd, F., Griffond, J., Soulard, O., Cambon, C.: Dynamics and structure of unstably stratified homogeneous turbulence. J. Turb. **17**(7), 651–663 (2016)
17. Burlot, A., Gréa, B.-J., Godeferd, F.S., Cambon, C., Griffond, J.: Spectral modelling of high Reynolds number unstably stratified homogeneous turbulence. J. Fluid Mech. **765**, 17–44 (2015)
18. Burlot, A., Gréa, B.-J., Godeferd, F.S., Cambon, C., Soulard, O.: Large Reynolds number self-similar states of unstably stratified homogeneous turbulence. Phys. Fluids **27**, 065114 (2015)

19. Cambon, C., Mons, V., Gra, B.-J., Rubinstein, R.: Anisotropic triadic closures for shear-driven and buoyancy-driven turbulent flows. Comput. Fluids **151**, 73–84 (2017)
20. Canuto, V.M., Dubovikov, M.S., Dienstfrey, A.: A dynamical model for turbulence. IV. Buoyancy-driven flows. Phys. Fluids **9**(7), 2118–2131 (1997)
21. Briard, A., Iyer, M., Gomez, T.: Anisotropic spectral modeling for unstably stratified homogeneous turbulence. Phys. Rev. Fluids **2**, 044604 (2017)
22. Dimonte, G., Youngs, D.L., Dimits, A., Weber, S., Marinak, M., Wunsch, S., Garasi, C., Robinson, A., Andrews, M.J., Ramaprabhu, P., Calder, A.C., Fryxell, B., Biello, J., Dursi, L., MacNeice, P., Olson, K., Ricker, P., Rosner, R., Timmes, F., Tufo, H., Young, Y.-N., Zingale, M.: A comparative study of the turbulent Rayleigh-Taylor instability using high-resolution three-dimensional numerical simulations: the Alpha-Group collaboration. Phys. Fluids **16**(5), 1668–1693 (2004)
23. Batchelor, G.K., Proudman, I.: The large-scale structure of homogeneous turbulence. Philos. Trans. R. Soc. Lond. Ser. A Math. Phys. Sci. **248**(949), 369–405 (1956)
24. George, W.K.: The decay of homogeneous isotropic turbulence. Phys. Fluids A: Fluid Dyn. **4**(7), 1492–1509 (1992)
25. Llor, A.: Langevin equation of big structure dynamics in turbulence. Eur. J. Mech. B **30**(5), 480–504 (2011)
26. Davidson, P.A.: Turbulence: An Introduction for Scientists and Engineers. Oxford University Press, Oxford, UK (2004)
27. Soulard, O., Griffond, J., Gréa, B.-J.: Large-scale analysis of self-similar unstably stratified homogeneous turbulence. Phys. Fluids **26**, 015110 (2014)
28. Dimonte, G.: Dependence of turbulent Rayleigh-Taylor instability on initial perturbations. Phys. Rev. E **69**, 056305 (2004)
29. Cambon, C., Gréa, B.-J.: The role of directionality on the structure and dynamics of strongly anisotropic turbulent flows. J. Turbul. **14**(1), 50–71 (2013)
30. Youngs, D.L.: The density ratio dependence of self-similar Rayleigh-Taylor mixing. Philos. Trans. R. Soc. A **371**, 20120173 (2013)
31. Soulard, O., Griffond, J., Gréa, B.-J.: Influence of the mixing parameter on the second order moments of velocity and concentration in Rayleigh-Taylor turbulence. Phys. Fluids **28**(6), 065107 (2016)
32. Gréa, B.-J., Burlot, A., Griffond, J., Llor, A.: Challenging mix models on transients to self-similarity of unstably stratified homogeneous turbulence. ASME. J. Fluids Eng. **138**, 070904–070904 (2016)
33. Gréa, B.-J., Ebo Adou, A.-H.: What is the final size of a turbulent mixing zone driven by the faraday instability? J. Fluid Mech. (accepted) (2017)
34. Dimonte, G., Ramaprabhu, P., Andrews, M.: Rayleigh-Taylor instability with complex acceleration history. Phys. Rev. E **76**, 046313 (2007)
35. Ramaprabhu, P., Karkhanis, V., Lawrie, A.G.W.: The Rayleigh-Taylor instability driven by an accel-decel-accel profile. Phys. Fluids (1994–present) **25**(11), – (2013)
36. Chertkov, M.: Phenomenology of Rayleigh-Taylor turbulence. Phys. Rev. Lett. **91**(11), 115001 (2003)
37. Mikaelian, K.O.: Turbulent mixing generated by Rayleigh-Taylor and Richtmyer-Meshkov instabilities. Physica D **36**, 343–357 (1989)
38. Zhou, Y.: A scaling analysis of turbulent flows driven by Rayleigh-Taylor and Richtmyer-Meshkov instabilities. Phys. Fluids **13**, 538 (2001)
39. Abarzhi, S.I.: On fundamentals of Rayleigh-Taylor turbulent mixing. Eur. Phys. Lett. **91**, 12867 (2010)
40. Soulard, O.: Implications of the Monin-Yaglom relation for Rayleigh-Taylor turbulence. Phys. Rev. Lett. **109**, 254501 (2012)
41. Verma, M.K., Kumar, A., Pandey, A.: Phenomenology of buoyancy-driven turbulence: recent results. New J. Phys. **19**, 025012 (2017)
42. Cabot, W.H., Cook, A.W.: Reynolds number effects on Rayleigh-Taylor instability with possible implications for type Ia supernovae. Nat. Phys. **2**, 562 (2006)

43. Dalziel, S.B., Linden, P.F., Youngs, D.L.: Self-similarity and internal structure of turbulence induced by Rayleigh-Taylor instability. J. Fluid Mech. **399**, 1–48 (1999)
44. Soulard, O., Gréa, B.-J.: Influence of zero-modes on the inertial-range anisotropy of Rayleigh-Taylor and unstably stratified homogeneous turbulence. Phys. Rev. Fluids **2**, 074603 (2017)
45. Biferale, L., Procaccia, I.: Anisotropy in turbulent flows and in turbulent transport. Phys. Rep. **414**, 43–164 (2005)
46. L'vov, V.S., Procaccia, I., Tiberkevich, V.: Scaling exponents in anisotropic hydrodynamic turbulence. Phys. Rev. E, **67**, 026312 (2003)
47. Soulard, O., Griffond, J.: Inertial-range anisotropy in Rayleigh-Taylor turbulence. Phys. Fluids **24**(2), 025101 (2012)
48. Bos, W.J.T., Touil, H., Bertoglio, J.-P.: Reynolds number dependency of the scalar flux spectrum in isotropic turbulence with a uniform scalar gradient. Phys. Fluids **17**, 125108 (2005)

Small Scale Statistics of Turbulent Fluctuations Close to a Stagnation Point

Peter D. Huck, Nathanael Machicoane and Romain Volk

Abstract Experimental data measured with a 3d Shadow-Particle Tracking Velocimetry (S-PTV) setup in fully developed turbulence ($\mathrm{Re}_\lambda = [175 - 225]$) is presented. The underlying flow is of the von Kármán type and as other similar flows, its mean flow is bistable, the two states having the topology of a stagnation point with one contracting and two dilating directions. Tracer particle trajectories permit the investigation of the inhomogeneity and anisotropy of the smallest scales, namely acceleration statistics. The local variance and time-scale of acceleration components are shown to mimic the large scale properties of the flow, the time-scales being more anisotropic than the variances. We explain the hierarchy of time-scales by investigating the Lagrangian Taylor micro-scale which is related to acceleration and velocity variances, and discuss the very high Reynolds number regime.

1 Introduction

Inhomogeneity in fluid flows is inherent in natural and industrial contexts with examples in the free shear and convection of the planetary boundary layer [1] or rotation in stirred chemical reactors [2] and compression in piston engines [3]. Among the canonical flow types investigated in the literature, strain is an important mechanism that has been used to investigate the link between the imposed mean-field and the resulting anisotropy [4, 5] and theoretical formulation of the role of rapidly applied strain to turbulence succeeded in providing a mechanism to predict anisotropy [6].

Recent experimental [7] and numerical [8] investigations have demonstrated that

P. D. Huck · R. Volk (✉)
Laboratoire de Physique de l'Ecole Normale Supérieure de Lyon, CNRS, Université de Lyon, Lyon, France
e-mail: romain.volk@ens-lyon.fr

P. D. Huck
e-mail: peter.huck@ens-lyon.fr

N. Machicoane
Department of Mechanical Engineering, University of Washington, Seattle, USA
e-mail: nmachico@uw.edu

M. Gorokhovski and F. S. Godeferd (eds.), *Turbulent Cascades II*,
ERCOFTAC Series 26, https://doi.org/10.1007/978-3-030-12547-9_14

accurate prediction is limited to larger scales when applied deformation is not sufficiently rapid to attain the small dissipative regions of the turbulence. Only recently have simulations investigated the implications of strain on the small dissipative scales of turbulence [9] demonstrating stronger root-mean-square (*rms*) acceleration in compressed directions than in divergent directions in asymmetric strain. Interestingly, recent study has not lead to conclusive explanations of the role such flow conditions have on dissipative scale *temporal* dynamics.

In this contribution we build upon these concepts with an experimental Lagrangian investigation of fully developed turbulence ($Re_\lambda = [175 - 225]$). In particular, a highly inhomogeneous and anisotropic von Kármán type flow is studied. Though often thought to belong to the free-shear category [10], recent study has pointed to the fundamental role of the stagnation point at the center of the flow [11]. By way of analogy with the characterization of spatial velocity gradients (Eulerian Taylor scale, λ) [12], the Lagrangian Taylor scale [13] is used to characterize high frequency motions and provides a reasonably accurate estimation of acceleration anisotropy, both in terms of temporal correlation and amplitude.

2 Experimental Set-Up

The device used in this investigation is the so-called von Kármán flow which consists of a square cylindrical enclosure, 15 cm on each side, with two counter-rotating disks of radius $R = 7.1$ cm driven at equal rotation frequencies by constant-current motors that are separated by 20 cm, as depicted in Fig. 1a. Our experiments rely on a Shadow-Particle Tracking Velocimetry [14] where two perpendicular collimated beams permit the tracking of small objects over a large volume [11] approximately $(6\,\text{cm})^3$ (Fig. 1b). Trajectories are reconstructed using typical particle tracking algorithms [15] applied to films obtained with two high speed cameras (Phantom V.12, Vision Research, 1Mpix@7 kHz) with a resolution 800×768 pixels, and a frame rate of $f_s = 12$ kHz.

A vast literature exists on the bistable nature of the von Kármán flow (e.g. [16, 17]) measured primarily in round cylinder geometries. The present square cylinder manifests another type of bistability for which the lifetime of the two states (characterized from LDV measurements, not shown here) is much longer than the duration of each movie. A explained in [14], it is possible to separate S-PTV data into two ensembles, each one corresponding to one of the two states, using the kinetic energy contained in each velocity component averaged over the ensemble of trajectories measured in a single film. Such conditioning allows for a reconstruction of averaged flow properties in 3D for each states such as the mean flow as shown in Fig. 1b for the case of the x-dominant state. The topology of each state have a peculiar topology (see [14] for more details): the x-dominant state, which will be investigated in the following, presents a stagnation point near the origin with one stable direction (x) and two unstable directions (y and z) as depicted in Fig. 1b, c, while x and y directions are exchanged in the y-dominant state (Fig. 1d). We note that the volume over which

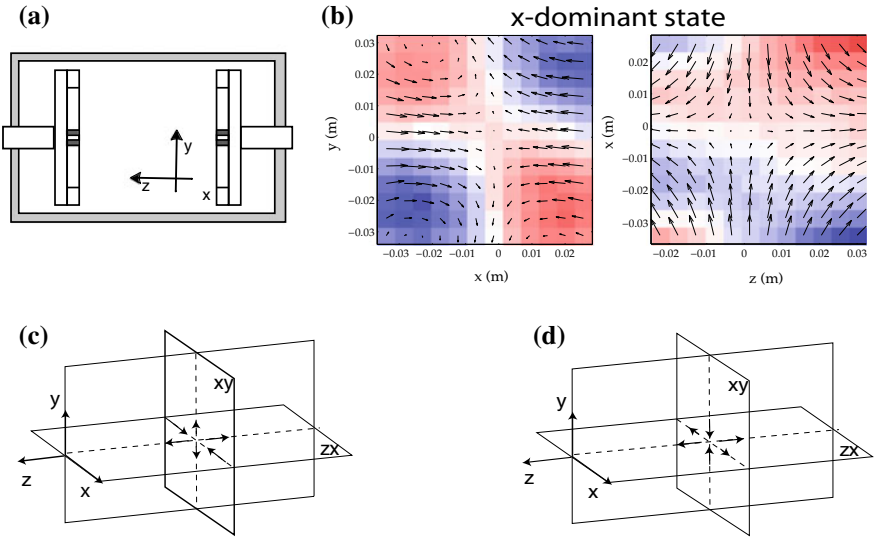

Fig. 1 Experimental apparatus. **a** The square cylindrical enclosure of the von Kármán flow consists of two counter rotating disks driven at equal rotational frequencies. **b** Reconstructed mean flow for the x-dominant state. Left: arrows indicate $(\langle v_x \rangle, \langle v_y \rangle)$ measured in the (xy) plane, the color coding for $\langle v_z \rangle$. Right: arrows indicate $(\langle v_z \rangle, \langle v_x \rangle)$ measured in the (zx) plane, the color coding for $\langle v_y \rangle$. **c** Sketch of the mean flow orientation in the x-dominant state. **d** Sketch of the mean flow orientation in the y-dominant state.

Table 1 Parameters of the flow. Ω, rotation rate of the discs; ε, dissipation rate obtained from the power consumption of the motors. The kinematic viscosity of the water-Ucon^{TM} mixture is $\nu = 8.2 \times 10^{-6}$ m^2 s^{-1} with a density $\rho = 1000$ kg m^{-3}. The dissipative time-scale and length-scale are $\tau_\eta = \sqrt{\nu/\varepsilon}$ and $\eta = (\nu^3/\varepsilon)^{1/4}$, the Taylor-based Reynolds number being estimated as $\mathrm{Re}_\lambda = \sqrt{15 v'^4/\nu\varepsilon}$ with $v' = \sqrt{(\langle v'_x{}^2 \rangle + \langle v'_y{}^2 \rangle + \langle v'_z{}^2 \rangle)/3}$ and $Re = 2\pi R^2 \Omega/\nu$

Ω (Hz)	v' (ms^{-1})	τ_η (ms)	η (μm)	ε_m (W kg^{-1})	Re_λ (–)	Re (–)
4.2	0.34	3.2	162	0.8	175	16,200
5.5	0.45	2.1	131	1.9	200	21,200
6.9	0.56	1.5	111	3.6	225	26,700

the statistics are computed is larger than the Eulerian integral scale $L = v'^3/\varepsilon = 4.8$ cm, where v' is the rms value of the fluctuating velocity, permitting an investigation of their inhomogeneity. Various Eulerian statistics are given at the geometrical center of the flow in Table 1.

2.1 Inhomogeneity in the Acceleration Magnitude

The stagnation point is responsible for a large amplification of fluctuations in the contracting direction (x) while attenuation is observed in the dilating directions [11]. As a consequence the total velocity fluctuations $\langle v'^2 \rangle$ increase as particles approach the stagnation point (Fig. 2a), indicating spatial inhomogeneity, with an anisotropy level $\langle v'^2{}_x \rangle / \langle v'^2{}_z \rangle$ which nearly doubles as the stagnation point is reached (Fig. 2a, inset).

As displayed in Fig. 2b, the acceleration component magnitude (normalized by its maximum value at the center to account its Reynolds number dependence) is also found to increase when approaching the center. Such spatial profile of acceleration fluctuations is reminiscent of the non homogeneity in average dissipation, which was found maximum near the geometrical center [11]. This is because acceleration variance is expected to depend on dissipation following the Heisenberg-Yaglom relation $\langle a_i^2 \rangle = a_{0,i} \varepsilon^{3/2} \nu^{-1/2}$ [18], where $a_{0,i}$ is a non-dimensional function of the Reynolds number. As opposed to the increasing anisotropy of velocity fluctuations, the three components of the fluctuating acceleration increase in equal proportions so that anisotropy is constant over the entire region of Fig. 2b with the hierarchy $\langle a_x{}^2 \rangle > \langle a_y{}^2 \rangle > \langle a_z{}^2 \rangle$. This shows that the anisotropy observed in the large scale quantities propagates down to the very small scales of turbulent fluctuations as was observed in [15].

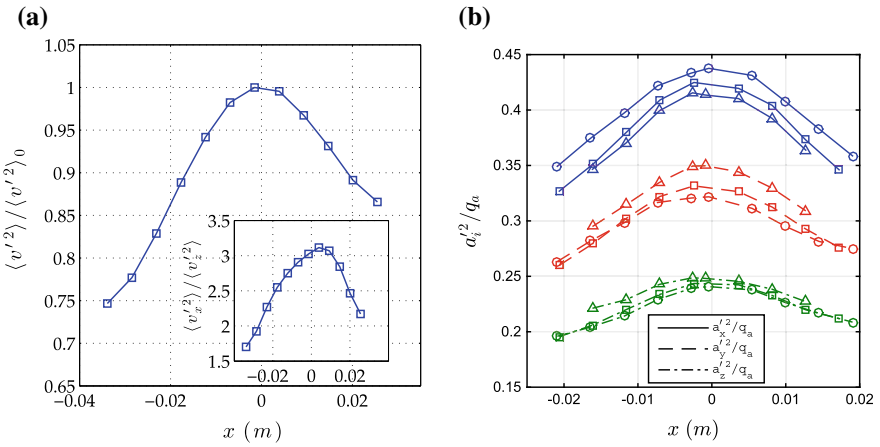

Fig. 2 Velocity fluctuations statistics at $Re_\lambda = 200$. **a** Overall increase in velocity fluctuations ($\langle v'^2 \rangle = (\langle v'_x{}^2 \rangle + \langle v'_y{}^2 \rangle + \langle v'_z{}^2 \rangle)/3$) normalized by its value at the origin. Inset: anisotropy between the converging ($\langle v'^2_x \rangle$) and diverging ($\langle v'^2_z \rangle$) fluctuations. **b** Acceleration magnitude statistics. $\circ$: $Re_\lambda = 175$, $\square$: $Re_\lambda = 200$, $\triangleleft$: $Re_\lambda = 225$. **a** Normalized acceleration variance where $q_a = (\langle a_x{}^2 \rangle + \langle a_y{}^2 \rangle + \langle a_z{}^2 \rangle)$ is evaluated at (0, 0, 0).

2.2 Acceleration Time Scales and Anisotropy

We now investigate the temporal dynamics at small scale and focus on the auto-correlation function of the acceleration components $R_a^i(\tau) = \langle a_i(t)a_i(t+\tau)\rangle/\langle a^2\rangle$. Because the flow is non homogeneous, we restrict to trajectories passing through a ball of 1 cm in diameter whose center is located at the origin (0, 0, 0). Figure 3a plots the auto-correlation function versus normalized time τ/τ_η where $\tau_\eta = (\nu/\varepsilon)^{1/2}$ takes the Reynolds number dependence into account and permits a collapse of the three curves. The plots show that the temporal dynamics is anisotropic since the curves do not have the same zero crossing time t_0. In order to get a robust estimate of the acceleration characteristic time, we measure the integral time $\tau_{a,i} = \int_0^{t_0} R_a^i(\tau)\, \mathrm{d}\tau$ for each component $i = x, y, z$.

The inset of Fig. 3a displays the normalized acceleration integral time obtained for different locations of the ball center along the x axis. As stagnation point is approached, the integral time $\tau_{a,i}$ decreases. This is consistent with an increase of dissipation close to the geometrical center as this time scale is expected to be proportional to $\tau_\eta = \sqrt{\nu/\varepsilon}$ as shown in homogeneous and isotropic turbulence (HIT) [19]. However, we observe $\tau_{a,i}$ become increasingly anisotropic and attain a maximum at the flow geometric center with the hierarchy $\tau_{a,x}/\tau_{a,z} > 1$ whereas $\langle {a_x}^2\rangle > \langle {a_z}^2\rangle$. This observation is somewhat counter-intuitive when considering $\tau_a \simeq \sqrt{\nu/\varepsilon}$ which would suggest a scaling law $\tau_a \propto (\nu/\langle a^2\rangle)^{1/3}$. However, the opposite is observed;

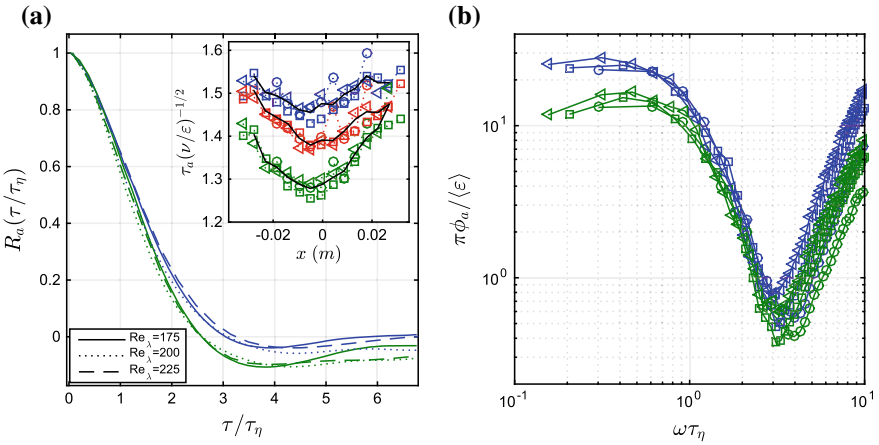

Fig. 3 Acceleration auto-correlation and spectra at the stagnation point. $\circ : Re_\lambda = 175$, $\square : Re_\lambda = 200$, $\triangleleft : Re_\lambda = 225$. **a** Acceleration correlation function (a_x, blue, a_z green) near the stagnation point for all Reynolds numbers. Inset: acceleration integral time normalized by the dissipative time-scale $\tau_\eta = \sqrt{\nu/\varepsilon}$. The black curves are averages of the three Reynolds numbers to serve as a reference. **b** Unfiltered acceleration spectra at the stagnation point normalized using the dissipation (a_x, blue, a_z green).

the strongest component (x) has the largest acceleration time whereas the weakest component (z) has the smallest time-scale.

In order to understand how acceleration variance and time-scale are influenced by the large scales, we display in Fig. 3b the acceleration spectra of a_x and a_z, computed directly from the raw acceleration trajectories. The spectra are related to the auto-correlation functions by the following relationship:

$$\phi_{a,i}(\omega) = \frac{2}{\pi}\int_0^\infty R_a^i(\tau)\cos(\omega\tau)\mathrm{d}\tau. \tag{1}$$

They have been normalized by $\varepsilon\pi^{-1}$ which has been used in the literature to account for Re_λ dependence [20, 21]. This figure shows that anisotropy is contained in the low frequencies below $\omega\tau_\eta \simeq 1$ while higher frequencies in the deep dissipative region ($\omega\tau_\eta > 1$) become isotropic. It is seen from this figure that integral quantities such as acceleration variance $\langle {a_i}^2\rangle = \int_0^\infty \phi_{a,i}(\omega)\mathrm{d}\omega$ and acceleration time-scale have a contribution from low frequencies, *i.e.* from scales larger than the dissipative scales, which are non isotropic.

It is not evident from the acceleration spectrum to estimate the acceleration time-scale, but its hierarchy may be understood by computing the Lagrangian Taylor scale τ_L (not to be confused with the eulerian Taylor microscale λ), which is defined from the short time evolution of the velocity auto-correlation function $1/\tau_L^2 = -1/2\ \mathrm{d}R_L/d\tau^2(0)$. Indeed, this time scale can be linked to the acceleration and velocity variances through the relationship

$$\langle {a_i}^2\rangle R_a^i(\tau) = -\langle {\mathrm{v}'_i}^2\rangle \frac{\mathrm{d}^2}{\mathrm{d}\tau^2} R_L^i(\tau), \tag{2}$$

which is valid for statistically stationary signals. The Lagrangian Taylor time-scale of component i then writes $\tau_{L,i}^2 = 2\langle {\mathrm{v}'_i}^2\rangle/\langle {a_i}^2\rangle$, which shows that this time-scale is influenced both by large and small scales. Although τ_L is not the same as τ_a, the latter is only slightly larger than the former, i.e. in the central region $\tau_{ai} \simeq [1.25 - 1.45]\tau_\eta$ and $\tau_{L,i} \simeq [4 - 6]\tau_\eta$ depending on the component observed. As such, τ_L falls squarely in the region of frequencies most strongly contributing to the anisotropy as seen in the spectra of Fig. 3b. Anisotropy can thus be estimated: $\tau_{a,x}/\tau_{a,z} \simeq 1.13$ as measured by the integral time scales in Fig. 3(a inset) while $\tau_{L,x}/\tau_{L,z} \simeq 1.33$ as estimated from $\tau_{L,i}^2 = 2\langle {\mathrm{v}'_i}^2\rangle/\langle {a_i}^2\rangle$. The Taylor timescale over predicts the anisotropy by roughly 20% and explains why acceleration time-scales are less isotropic than acceleration variances.

In a similar flow velocity anisotropy ratio has been shown to decay slowly to just below $\mathrm{v}'_x/\mathrm{v}'_z \simeq 1.5$ at $Re_\lambda \simeq 1000$ [22] while the ratio of acceleration rms decays to nearly 1.1. However, as shown above, time scales imply interaction of both large (velocity) and small (acceleration) scales. Consequently, the persistent anisotropy in the large scales resulting from the presence of the stagnation point inhibit isotropization of time scales at large Reynolds numbers. Indeed, Lagrangian

measurements spanning $Re_\lambda = [450 - 810]$ indicate very little evolution in τ_{ax}/τ_{az} [23].

3 Conclusion

This article presented an experimental investigation of Lagrangian data in the fully developed turbulence of a von Kármán flow. The flow presents a bistability and each state can be investigated separately by conditioning on the kinetic energy contained in each component. Restricting the data analysis to only one state, the turbulent velocity fluctuations were seen to be strongly inhomogeneous close to the stagnation point. Additionally, anisotropy measured between the converging and weakest diverging direction increased monotonically. The turbulent dissipation rate was observed to be dominated by the converging direction and mirrored the evolution of the turbulent velocity fluctuations. Interestingly, the acceleration variance followed the tendency of the turbulent dissipation and velocity fluctuations to increase, though unlike the latter, acceleration anisotropy remained almost constant.

Although the relationship small scale anisotropy can be linked to the large scales, this relationship is incapable of predicting anisotropy among the acceleration time-scales. The hierarchy of time-scales was explained by investigating the Lagrangian Taylor scale $\tau_{_L} = \sqrt{2\mathrm{v}'^2/a^2}$. The presence of v' in this relationship suggests an influence from lower frequencies, which is confirmed from the inspection of acceleration spectra. Frequencies close to $\omega = 2\pi/\tau_{_L}$ contribute most strongly to anisotropy in the acceleration magnitude whereas the deep dissipative region ($\omega\tau_\eta > 1$) becomes isotropic. Similar behavior is apparent in the acceleration auto-correlation which by consequence lead to anisotropic measurements of its integral scale τ_a.

The literature contains sparse discussion of the anisotropy of small scale statistics and this study proposes a framework in which they may be understood. The derivation of $\tau_{_L}$ follows from the kinematic relationship between velocity and acceleration auto-correlation functions and is expected to not only hold for the fluid particle tracers studied here, but for particles whose dynamics are dominated by their inertia. Further study into the effects of inhomogeneity and anisotropy for these particle classes is of great interest for the atmospheric dispersion of pollutants [18, 24] and the process of rain and ice formation.

Acknowledgements This work is supported by research programs ANR-13-BS09-0009 and PALSE/2013/26. Contribution from the EuHIT—European High-performance Infrastructures in Turbulence—is also acknowledged.

References

1. Sawford, B.L.: Lagrangian statistical simulation of concentration mean and fluctuation fields. J. Clim. Appl Meteorol. **24**, 1152–1166 (1985)
2. Paul, E.L., Atiemo-Obeng, V.A., Kresta, S.M.: Handbook of Industrial Mixing: Science and Practice. Wiley , Inc. (2004)
3. Breuer, S., Oberlack, M., Peters, N.: Non-isotropic length scales during the compression stroke of a motored piston engine. Flow Turbul. Combust. **74**(2), 145–167 (2005)
4. Comte-Bellot, G., Corrsin, S.: The use of a contraction to improve the isotropy of grid-generated turbulence. J. Fluid Mech. **25**(04), 657 (1966)
5. Tucker, H.J., Reynolds, A.J.: The distortion of turbulence by irrotational plane strain. J. Fluid Mech. **32**, 657 (1968)
6. Sagaut, P., Cambon, C.: Homogeneous Turbulence Dynamics. Cambridge University Press (2008)
7. Ayyalasomayajula, S., Warhaft, Z.: Nonlinear interactions in strained axisymmetric high-Reynolds-number turbulence. **566**(2006), 273 (2006)
8. Clay, M.P., Yeung, P.K.: A numerical study of turbulence under temporally evolving axisymmetric contraction and subsequent relaxation. J. Fluid Mech. **805**, 460–493 (2016)
9. Lee, C.-M., Gylfason, Á., Perlekar, P., Toschi, F.: Inertial particle acceleration in strained turbulence. J. Fluid Mech. **785**, 31–53 (2015)
10. Marie, L., Daviaud, L.: Experimental measurement of the scale-by-scale momentum transport budget in a turbulent shear flow. Phys. Fluids **16**(2) (2004)
11. Huck, P.D., Machicoane, N., Volk, R.: Production and dissipation of turbulent fluctuations close to a stagnation point. Phys. Rev. Fluids **2**(8), 084601 (2017)
12. Taylor, G.I.: Statistical theory of turbulence. Proc. Roy. Soc. A **151**(873), 421–478 (1935)
13. Corrsin, S., Uberoi, M.: Diffusion of heat from a line source in isotropic turbulence. Natl. Adv. Comm. Aeronaut. Tech. Rep. **1142**(1142) (1953)
14. Huck, P.D., Machicoane, N., Volk, R.: A cost-efficient shadow particle tracking velocimetry setup suitable for tracking small objects in a large volume. Procedia IUTAM **20**, 175–182 (2017)
15. Ouellette, N.T., Xu, H., Bodenschatz, E.: A quantitative study of three-dimensional Lagrangian particle tracking algorithms. Exper. Fluids **40**(2), 301–313 (2006)
16. De La Torre, A., Burguete, J.: Slow dynamics in a turbulent von Kármán swirling flow. Phys. Rev. Lett. **99**(5), 3–6 (2007)
17. Ravelet, F., Chiffaudel, A., Daviaud, F.: Supercritical transition to turbulence in an inertially driven von Kármán closed flow. J. Fluid Mech. **601**, 339–364 (2008)
18. Sawford, B.L., Pinton, J.F.: A Lagrangian view of turbulent dispersion and mixing. In: Sreenviasan, K.R., Davidson, P.A., Kaneda, Y. (eds.) Ten Chapters in Turbulence, Chapter 4, pp. 132–175. Cambridge University Press, Cambridge (2012)
19. Yeung, P.K., Pope, S.B.: Lagrangian statistics from direct numerical simulations of isotropic turbulence. J. Fluid Mech. **207**, 531 (1989)
20. Sawford, B.L., Yeung, P.K.: Kolmogorov similarity scaling for one-particle Lagrangian statistics. Phys. Fluids **23**(9), 1–5 (2011)
21. Ouellette, N.T., Xu, H., Bourgoin, M., Bodenschatz, E.: Small-scale anisotropy in Lagrangian turbulence. New J. Phys. **8** (2006)
22. Voth Greg, A., La Porta, A., Crawford, A.M., Alexander, J., Bodenschatz, E.: Measurement of particle accelerations in fully developed turbulence. J. Fluid Mech. **469**, 121–160 (2002)
23. Volk, R., Chareyron, D., Pinton, J.: Mesures d'accélération lagrangienne dans un écoulement anisotrope par vélocimétrie laser Doppler étendue. 20ème Congrès Français De Mécanique, pp. 1–6 (2011)
24. Toschi, F., Bodenschatz, E.: Lagrangian properties of particles in turbulence. Ann. Rev. Fluid Mech. **41**, 375–404 (2009)

Anisotropic Turbulent Cascades in Rotating Homogeneous Turbulence

D. Vallefuoco, F. S. Godeferd, A. Naso and A. Delache

Abstract We consider homogeneous turbulence submitted to the effect of an external rotation of the system. The presence of the Coriolis force results in anisotropic dynamics and structure of the flow, due to the presence of propagating inertial waves, and of a modified dynamics. The anisotropic structure of the flow is analyzed by maps of second- and third-order two-point correlation statistics in physical separation space, distinguishing between axial and perpendicular separation. Second-order statistics permit to assess the anisotropy of the flow which develops due to the presence of rotation. However, nonlinear dynamics has to be characterized by examining the third-order correlation term in the Kármán-Howarth-Monin equation, in which the non linear term appears as the divergence of the flux vector **F**. We show that maps of the components of **F** permit to examine the detailed anisotropic interactions, and to discuss the results of our Direct Numerical Simulations to that from Kolmogorov theory, from wave turbulence theory and from experiments.

1 Introduction

Flows submitted to the action of rotation are ubiquitous in nature, for instance large scale motion in geophysical flows. Cyclones and anticyclones in the atmosphere are the result of a complex mix of phenomena related to temperature variations,

D. Vallefuoco · F. S. Godeferd (✉) · A. Naso
Laboratoire de Mécanique des Fluides et d'Acoustique, CNRS/Université de Lyon, ECL/UCBL/INSA, Lyon, France
e-mail: fabien.godeferd@ec-lyon.fr

D. Vallefuoco
e-mail: donato.vallefuoco@ec-lyon.fr

A. Naso
e-mail: aurore.naso@ec-lyon.fr

A. Delache
Laboratoire de Mécanique des Fluides et d'Acoustique, Université Jean-Monnet Saint-Étienne, CNRS/Université de Lyon, ECL/UCBL/INSA, Lyon, France
e-mail: alexandre.delache@univ-st-etienne.fr

M. Gorokhovski and F. S. Godeferd (eds.), *Turbulent Cascades II*,
ERCOFTAC Series 26, https://doi.org/10.1007/978-3-030-12547-9_15

humidity, etc., in which the Earth's rotation does not play the least role. Thus, rotating flows generally exhibit two-dimensionalization tendencies, such that turbulent structures get elongated along the axis of rotation. The corresponding dynamics, or energy exchanges, is rather complex, since it involves a combination of transfers in scale space—associated with a given length scale ℓ or wavenumber $k \sim 1/\ell$—and in direction θ—being that of the two-point vector which is considered when taking the correlation for computing ℓ or being the orientation of the wavector $\mathbf{k}$ where $|\mathbf{k}| = k$. The energy transfer at each scale is therefore a balance between dissipation and non linear transfer modified by the presence of the Coriolis force [1]. If one considers the non linear timescale τ_{NL}—also the eddy turnover time—and the rotation timescale $\tau_\Omega \simeq 1/\Omega$, the ratio between the two is the Rossby number $Ro = \tau_\Omega/\tau_{\mathrm{NL}} = u'\ell/\Omega$, where u' is a characteristic velocity at scale ℓ. Thus, the relative importance of the Coriolis force in the flow dynamics can be evaluated from Ro. If $Ro \gg 1$, rotation has very small effect on the flow structures, and one expects a classical dynamics close to that of isotropic turbulence. If $Ro \ll 1$, inertial waves are rapid and the flow evolution is strongly driven by the Coriolis force. The scale separation corresponding to the two ranges has been discussed in a phenomenological way by Zeman who proposed that the relevant separating length scale be $l_z = (\varepsilon/\Omega^3)^{1/2}$, where ε is the kinetic energy dissipation [2]. In addition to phenomenological arguments, existing experimental [3, 4] and numerical studies [5–9] confirm the existence of a range of scale specifically affected by rotation, and several studies conclude to the relevance of l_Z for providing an estimate of the transition scale between rotation-affected large scales and isotropic smaller scales. This however requires that the Rossby number be not too large—in that case rotation is only a weak perturbation to the flow dynamics—or too small—in that case all scales are strongly affected by rotation, at finite Reynolds number $Re = UL/\nu$, where ν is the kinematic viscosity and U and L macroscopic velocity and length scales.

These results are however based on a local analysis of two-point correlation statistics, but the understanding of the origins of the modified dynamics requires to investigate third-order statistics. Moreover, the strong anisotropy between axial (along the rotation axis) and perpendicular directions also has to be taken into account in the detailed analysis of the flow dynamics. Therefore, we propose to investigate in the present work third-order correlation statistics in physical space, which play an important role in the creation of anisotropy of two-point second-order statistics.

Detailed statistics are thus obtained in terms of the vector $\mathbf{r}$ separating two points in space, so that the two-point velocity correlation is $\mathsf{R}(\mathbf{r})$ and the energy flux is $\Pi(\mathbf{r}, t) = \nabla \cdot \mathbf{F}/4$ where $\mathbf{F}(\mathbf{r}, t) = \langle \delta\mathbf{u}(\delta\mathbf{u})^2 \rangle$ is the flux density and $\delta\mathbf{u}$ the velocity increment between the two points. These quantities are used to characterize the anisotropic energy budget based on the Kármán-Howarth-Monin equation, in terms of separation scale $|\mathbf{r}|$ and polar angle θ.

Let us however recall that there is exact equivalence between physical and spectral space statistics, for both second- and third-order moments of velocity [10]. For instance, in isotropic turbulence, the two-point velocity correlation tensor is related to the kinetic energy spectrum *via*

$$R_{ii}(r) = 2\int_0^\infty sin(kr)/(kr)E(k)\mathrm{d}k \tag{1}$$

and the third-order structure function is related to the kinetic energy transfer spectrum:

$$\langle \delta u_L(\delta \mathbf{u})^2 \rangle = 4r\int_0^\infty g(kr)T(k)\mathrm{d}k$$

where δu_L is the longitudinal projection of the separation vector and $g(k)$ is a simple weighting function as in Eq. (1) (see details in [11]).

Of course, in anisotropic turbulence, as in rotating turbulence, directional θ-dependence of the statistics has to be taken into account, so that the mathematical formalism is more complicated, but, in principle, Fourier-transforming physical- or spectral-space statistics permit to switch identically from one dual space to the other.

We therefore propose in this work to present statistics of the equivalent in physical space of the energy transfer in spectral space, which is the flux divergence $\Pi(\mathbf{r})$, and we will present maps of the flux $\mathbf{F}(\mathbf{r})$ itself. For this we use a database of Direct Numerical Simulations which has been developed for forced rotating homogeneous turbulence [13].

2 Dynamical Equations for Rotating Turbulence

We recall here the dynamical equations for rotating turbulence. The Navier-Stokes equation for the velocity field $\mathbf{u}$ in a rotating frame is

$$\partial_t u_i + u_j \partial_j u_i = -\frac{1}{\rho}\partial_i p + f_i + \nu\nabla^2 u_i + \mathscr{F}_i, \tag{2}$$

where $\mathbf{f} = -2\Omega \times \mathbf{u}$ is the Coriolis force per unit mass, p the pressure field corrected by the centrifugal force. We can consider both the unforced, freely decaying case, where the force $\mathscr{F} = 0$, or a statistically steady flow which results from a forcing at large scales. We can use two kinds of forcing in our simulations, but only results of the second shall be presented in the present proceedings for the sake of conciseness: the ABC-flow forcing which consists of periodic three-dimensional vortices associated with a single wavelength [12], or the forcing by a large-scale flow which evolves according to the truncated Euler equations. Thus, ABC-forcing is permanent in time, whereas turbulent structures in the Euler flow are time-evolving, although their global energy is conserved since the truncated Euler system of equations is conservative. The Navier-Stokes equations are solved in a tri-periodic domain using a classical pseudo-spectral method with 1024 Fourier modes in each direction, a third-order Runge-Kutta time-scheme, and full de-aliasing. The flow is evolved from an initial random distribution of velocity until a statistically converged state is reached. Statistics are then accumulated over the duration required to achieve adequate sampling. (See details of the method in [13, 14].)

The statistics which are computed permit to close the balance equation which is chosen in the form of the Kármán-Howarth-Monin (KHM) equation. This equation describes the evolution of the two-point velocity correlation $R_{ij}(\mathbf{r}, t) = \langle u_i(\mathbf{x}, t)\, u_j(\mathbf{x}+\mathbf{r}, t)\rangle$, where $\langle\rangle$ are in principle spatial or ensemble averages. In the present study, we also take advantage of the possibility of averaging in time. The KHM equation is therefore derived from Eq. (2) by assuming homogeneity, that is the independence of the statistics on the position, but not necessarily isotropy.

Multiplying Eq. (2) by $\mathbf{u}(\mathbf{x}+\mathbf{r})$ and taking the average, one obtains an equation for the two-point correlation $R_{ij}(\mathbf{r})$ whose trace $R \equiv R_{ii}$ is taken to yield the KHM Eq. [10]:

$$\frac{1}{2}\,\partial_t R(\mathbf{r}, t) \;=\; \underbrace{\frac{1}{4}\nabla\cdot\mathbf{F}}_{\Pi(\mathbf{r},t)} \;+\; \underbrace{\nu\nabla^2 R}_{-D(\mathbf{r},t)} \;+\; \phi_{\text{inj}}(\mathbf{r}, t)\;, \tag{3}$$

where $D(\mathbf{r}, t)$ is the dissipation term and $\Pi(\mathbf{r}, t)$ is the energy flux which stems from the flux density vector field

$$\mathbf{F}(\mathbf{r}, t) = \langle \delta\mathbf{u}\,(\delta\mathbf{u})^2\rangle. \tag{4}$$

The last term in Eq. (3) is the contribution due to the forcing, obtained by correlating the velocity with the forcing $\mathscr{F}$. In the stationnary regime we consider, the first term of Eq. (3) vanishes. Note that background rotation is not explictly present in the KHM equation, due to the fact that the Coriolis force does no work. Note also that the KHM equation is formally equivalent to a Lin-type equation for the energy density spectrum

$$\partial_t e(\mathbf{k}, t) = T(\mathbf{k}, t) + 2\nu k^2 e(\mathbf{k}, t) + \hat{\phi}_{\text{inj}}(\mathbf{k}, t)\;,$$

where rotation does not appear explicitly either. It manifests only in a complex way through the $T(\mathbf{k}, t)$ term whose distribution is modified with respect to that of isotropic turbulence.

3 Two-Point Second-Order Statistics

We first illustrate second-order statistics with results of Direct Numerical Simulations of Euler-forced rotating turbulence without helicity forcing at Reynolds number $Re^{\lambda} = 187$ based on the Taylor microscale λ, and moderate Rossby number $Ro^{\omega} = \omega'/\Omega = 2.02$, computed from the *r.m.s.* vorticity ω'.

We compute the trace of the two-point velocity correlation tensor $R(\mathbf{r})$ as a function of the separation vector $\mathbf{r}$. Since the flow is statistically axisymmetric, we only retain the explicit dependence on the perpendicular coordinate $\rho \equiv r_{\perp}$, and on the

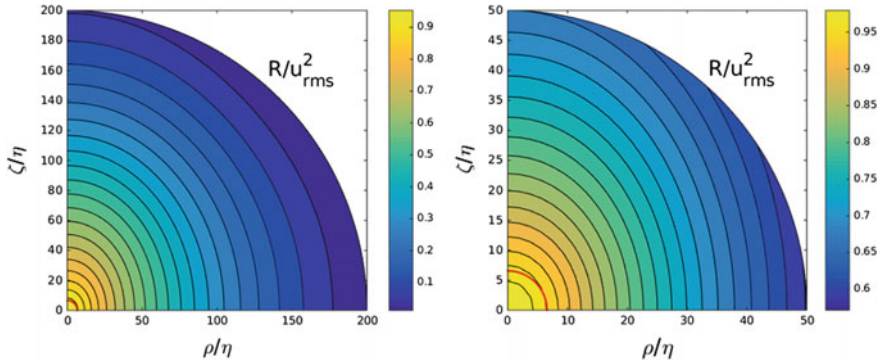

Fig. 1 Maps of the two-point velocity correlation $R(\mathbf{r})$ normalized by u_{rms}^2 for Euler-forced rotating turbulence without helicity forcing at $Re^{\lambda} = 187$ and $Ro^{\omega} = 2.02$. The red circles show the Zeman scale $l_Z = (\varepsilon/(2\Omega)^3)^{1/2}$. Note that the right figure uses a a narrower range of separation scales

axial (along rotation axis) coordinate $\zeta \equiv r_{\parallel}$. In isotropic turbulence, R only depends on the distance $r = |\mathbf{r}|$ and not on its orientation. In rotating turbulence, we observe in Fig. 1 that even at a Rossby number which is not small, of order unity, the isolines of $R(\mathbf{r})$ are clearly elongated along the vertical direction. The trend is more pronounced at decreasing Rossby number. Figure 1 thus shows that two-point correlation at large scales is enhanced along the rotation axis, which is consistent with the fact that turbulent structures are elongated in this direction. A complete two-dimensionalization of rotating turbulence would imply that $R(\mathbf{r})$ be independent of ζ, so that the isolines would become exactly vertical.

However, a careful observation of the isolines of the figure shows that the anisotropy is less in the small scales, and almost recovers isotropy below the Zeman scale which is indicated by a red circle on the plot. This is consistent with the above-mentioned phenomenology stating a reduced relative effect of rotation at scales smaller than l_Z. Similar results were obtained in the rotating experiment by [15].

4 Third-Order Statistics

We now consider the third-order vector moment, for which inertial laws are available from the literature in both the isotropic and the rotating cases. For instance, in isotropic turbulence $F_{\varphi} = F_{\theta} = 0$ and the distribution of F_r is derived from the famous four-thirds Kolmogorov law $\langle \delta u_L^3 \rangle = -(4/5)\varepsilon r$ [16, 17].

Figure 2 shows the distribution of the third-order vector moment radial component F_r non dimensionalized by the isotropic analytical prediction $-(4/3)\varepsilon r$, for two orientations of the separation vector, namely along the axis ($r_{\perp} = 0$, $\theta = 0$) and perpendicular to it ($r_{\parallel} = 0$, $\theta = \pi/2$). Recall that the exact $-4/3$ proportionality constant is obtained in isotropic turbulence only at very large Reynolds number

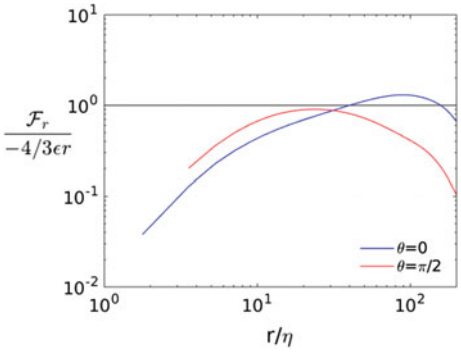

Fig. 2 Third-order vector moment radial component F_r non dimensionalized by $-4\varepsilon r/3$, along the directions $\theta = 0$ ($r_\perp = 0$) and $\pi/2$ ($r_\parallel = 0$). Data from DNS of Euler-forced rotating turbulence without helicity forcing

Re_λ, in excess of ∼2000 [17], and is asymptotically reached by the correlation from below, that is with smaller values than 4/3 (in amplitude, thus dropping the negative sign). Thus, moderate Reynolds number simulations are expected to display values $F_r/(-4\varepsilon r/3) < 1$. In our DNS of rotating turbulence, Fig. 2 shows that the perpendicular component curve is indeed located below the threshold value. However, along the rotation axis, the distribution of F_r overshoots the $-4/3$ value and indicates that fluxes are larger than what they would be in isotropic turbulence. In addition, the maxima of both curves at $\theta = 0$ and $\theta = \pi/2$ are located at different scales. This also indicates a global equilibrium which is achieved at different scales depending on the considered orientation. In other words, one could also say that only the statistics along $\theta = 0$ appear to be mostly affected by rotation.

Figure 3 shows the different terms appearing in the KHM Eq. (3). All the terms are non dimensionalized by kinetic energy dissipation ε. Adding up all the terms shows that the equation is almost exactly balanced, taking into account the sampling which is poor in the very large scales (small wavenumbers where the spectral discretization is coarse with respect to larger wavenumbers). A first observation is that the distribution of all three terms—flux, dissipation, forcing residual—is anisotropic in the large scales. It becomes more and more isotropic at smaller scales, again below the Zeman length scale. As expected, dissipation is maximal at the smallest scales, way below l_Z, but non negligible dissipation is still present in the inertial range. Accordingly, the other two plots of Fig. 3, for Π and residual term Φ, exhibit similarity in the large and inertial scale ranges, since they both contribute most to the balance of the KHM equation at these scales. If one considers the distribution of the flux Π along a circle, that is at uniform separation scales whatever the orientation, one observes that it is more intense along the perpendicular direction than along the axial one. Although we consider here the equation for correlations R, this reminds of the fact that the spectral energy transfer in rotating turbulence is also concentrated towards the equatorial direction, corresponding also to a concentration of energy in this spectral region.

Finally, Fig. 4 shows the streamlines of $\mathbf{F}$ in the ($r_\perp$,$r_\parallel$) plane. In isotropic turbulence, the streamlines are expected to be exactly radial, since energy is flowing

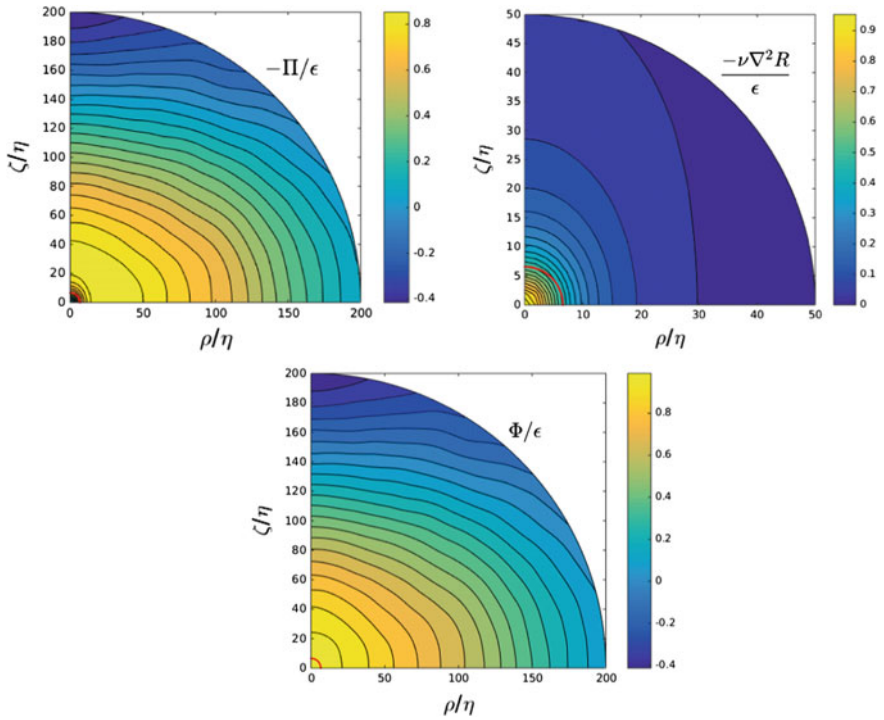

Fig. 3 Maps in the $(\rho = r_\perp, \zeta = r_\parallel)$ plane of the terms appearing in the KHM equation for 1024^3 DNS of rotating Euler-forced turbulence without helicity forcing. From left to right and top to bottom: flux Π/ε normalized by KE dissipation, normalized dissipation term, normalized residual term. Note that a smaller range of scales is considered for the viscous term $\nu\nabla^2 R$. The red circles indicate the Zeman scale $l_Z = (\varepsilon/(2\Omega)^3)^{1/2}$. Separation coordinates are normalized by the Kolmogorov microscale η

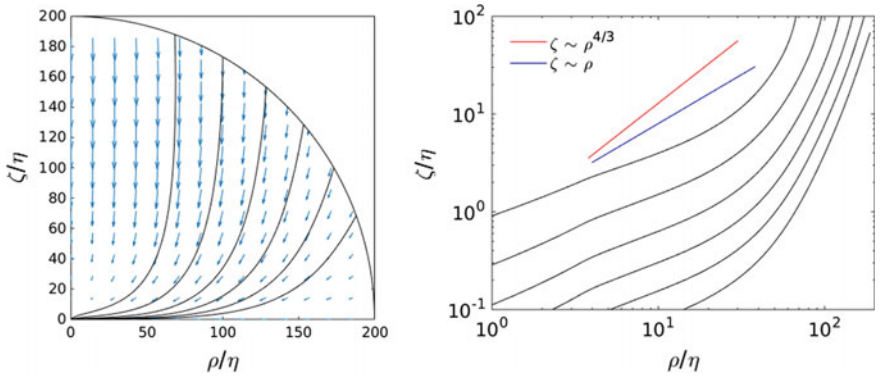

Fig. 4 Vector field (F_r, F_θ) in the $(\rho = r_\perp, \zeta = r_\parallel)$ plane, and corresponding streamlines in linear (left panel) and logarithmic (right panel) scale. 1024^3 DNS of Euler-forced turbulence without helicity forcing, corresponding to moderate Rossby number rotating turbulence. Separation coordinates are normalized by the Kolmogorov microscale η

from scale to scale. In rotating turbulence, this symmetry is broken and anisotropy is expected. Thus the map of $\mathbf{F}$ is informative of the details of the transfers that occur between scales and directions. It provides even more information about the *sources* and *sinks* in scale and orientation space than the spectral transfer term $T(\mathbf{k})$, since the latter is only equivalent to the *divergence* $-\nabla \cdot \mathbf{F}/4$.

The left panel of Fig. 4 shows that the flux vector is clearly oriented along the axial direction at large axial separation $r_\parallel$, and at smallish perpendicular separation $r_\perp$. However, again in the region close to the equator, i.e. for small $r_\parallel$, the direction of the flux vector quickly re-orients towards the origin, so that it becomes more and more horizontal. It therefore seems that two phenomena are at play: (a) at large and inertial vertical scales the flux occurs mostly direction-wise, whereas (b) at small axial scales it becomes more like a downscale flux. Although we consider here forced turbulence, this also reminds of the two regimes which are observed in decaying rotating turbulence starting from isotropic initial conditions, in which anisotropy develops first as a directional transfer of energy towards horizontal motion in the energetic scales, and is later followed by a growth of structural anisotropy linked with the dimensionality of the flow [18].

It is of course rather difficult to come up with analytical predictions for the distribution of the flux in anisotropic turbulence. Nonetheless, a corresponding inertial law for rapidly rotating turbulence has been proposed by Galtier [19]. According to this theory, the streamlines of $\mathbf{F}$ should be proportional to $\zeta = \rho^{4/3}$, the radial flux component $|F_r|$ should slightly decrease with θ and the ortho-radial one F_θ should be positive, i.e. $\mathbf{F}$ should be deflected towards the horizontal axis with respect to the radial direction.

Accordingly, we plot the streamlines $\zeta(\rho)$ in logarithmic scale in the right panel of Fig. 4. The streamlines are basically divided into two parts, one at large scale with a slope larger than one (corresponding to radial $\mathbf{F}$), the other at smaller scale with a slope smaller than one. In the presented DNS, the Rossby number is not low enough for recovering exactly the 4/3 predicted slope, but other DNS runs at lower Rossby number (not presented here, see [13]) do display this 4/3 slope in the inertial range, which is consistent with the assumption of rapid rotation of the inertial theory.

5 Conclusion

We present in this work results on third-order statistical moments of velocity in forced rotating turbulence. These statistics have to be studied in order to evaluate the origin of the anisotropy in the flow in terms of dynamical transfers. The computation of the flux vector moment permits to compare its distribution to Kolmogorov prediction for the third-order velocity increment, the famous $-4/5$–law, for asymptotically high Reynolds number turbulence, but also to the predictions of the theory of inertial wave turbulence for asymptotically small Rossby number. We show that, in our finite-Reynolds, finite-Rossby number Direct Numerical Simulations, statistical features of rotating turbulence are overall not too far from the idealized cases. This is true

for the one case presented in this work, considering Euler-forced turbulence without injection of helicity. Helical forcing modifies significantly the dynamics of the flow, and larger departures from isotropic turbulence or wave turbulence are observed [13]. Assessment of these conclusions ought to be done at larger Reynolds number, in order to get closer to actual flow regimes, such as those observed in geophysics.

Acknowledgements The direct numerical simulations data were obtained thanks to computer time allocated by GENCI on the computing facility of CINES (project number 2206), and thanks to CPU time provided by the FLMSN on the PMCS2I facility in Lyon (France), supported by the Equip@Meso project.

References

1. Zhou, Y.: A phenomenological treatment of rotating turbulence. Phys. Fluids **7**, 2092 (1995)
2. Zeman, O.: A note on the spectra and decay of rotating homogeneous turbulence. Phys. Fluids **6**(10), 3221–3223 (1994)
3. Morize, C., Moisy, F., Rabaud, M.: Decaying grid-generated turbulence in a rotating tank. Phys. Fluids **17**(9), 095105 (2005)
4. Moisy, F., Morize, C., Rabaud, M., Sommeria, J.: Decay laws, anisotropy and cyclone-anticyclone asymmetry in decaying rotating turbulence. J. Fluid Mech. **666**, 5–35 (2011)
5. Staplehurst, P.J., Davidson, P.A., Dalziel, S.B.: Structure formation in homogeneous freely decaying rotating turbulence. J. Fluid Mech. **598**, 81–105 (2008)
6. Bourouiba, L., Bartello, P.: The intermediate Rossby number range and two-dimensional three-dimensional transfers in rotating decaying homogeneous turbulence. J. Fluid Mech. **587**, 139–161 (2007)
7. Yoshimatsu, Y., Midorikawa, M., Kaneda, Y.: Columnar eddy formation in freely-decaying homogeneous rotating turbulence. J. Fluid Mech. **677**, 154–178 (2011)
8. Mininni, P.D., Rosenberg, D., Pouquet, A.: Isotropization at small scales of rotating helically driven turbulence. J. Fluid Mech. **699**, 263–279 (2012)
9. Delache, A., Cambon C., Godeferd, F.S.: Scale by scale anisotropy in freely decaying rotating turbulence. Phys. Fluids. **26**, 025104 (19 pages) (2014)
10. Frisch, U.: Turbulence: The Legacy of A. N. Kolmogorov. Cambridge University Press (2010)
11. Cambon, C., Danaila, L., Godeferd, F.S., Scott, J.: Third-order statistics and the dynamics of strongly anisotropic turbulent flows. J. Turb. **14**(3), 121–160 (2013)
12. Childress, S., Gilbert, A.D.: Stretch, Twist, Fold: The Fast Dynamo. Lecture Notes in Physics Monographs, vol. 37. Berlin, Springer (1995)
13. Vallefuoco, D.: Numerical study of unconfined and confined anisotropic turbulence. Ph.D. Thesis, University of Lyon, École centrale de lyon (2017)
14. Vallefuoco, D., Naso, A., Godeferd, F.S.: Small-scale anisotropy induced by spectral forcing and by rotation in non-helical and helical turbulence. J. Turb. **19**(2), 107–140 (2018)
15. Lamriben, C., Cortet, P.-P., Moisy, F.: Direct measurements of anisotropic energy transfers in a rotating turbulence experiment. Phys. Rev. Lett. **107**, 024503 (2011)
16. Taylor, M.A., Kurien, S., Eyink, G.L.: Recovering isotropic statistics in turbulence simulations: the Kolmogorov 4/5th law. Phys. Rev. E **68**(2 pt 2), 026310 (2003)
17. Antonia, R.A., Burattini, P.: Approach to the 4/5 law in homogeneous isotropic turbulence. J. Fluid Mech. **550**, 175–184 (2006)
18. Cambon, C., Mansour, N.N., Godeferd, F.S.: Energy transfer in rotating turbulence. J. Fluid Mech. **337**, 303–332 (1997)
19. Galtier, S.: Exact vectorial law for homogeneous rotating turbulence. Phys. Rev. E **80**, 046301 (2009)

Part IV
Turbulence ⇔ Scalars

Self-similarity in Slightly Heated Annular Jet with Large Diameter Ratios

A. Bouha, E. Varea, B. Patte-Rouland and L. Danaila




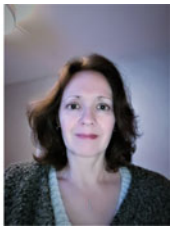

Abstract The study aims at furthering our understanding and quantifying the influence of coherent structures on small-scale turbulence and passive scalar mixing, in an annular jet configuration with large diameter ratios. This 'bluff-body' geometry is close to that widely used in combustion for flame stabilization [1]. A passive contaminant is introduced in the flow, through a slight heating. We report the evolution along the jet axis of the following quantities: mean values of the longitudinal velocity and passive scalar ($\bar{U}$ and $\bar{\Theta}$), as well as the energy and scalar dissipation rates ($\bar{\varepsilon}$ and $\bar{\chi}$). It is shown that these statistics:

- decay as x^{-1} and x^{-4}, where x is the streamwise direction, similarly to the decay in the far-field of classical jets (CJ);
- unlike the CJ, they reach self-similarity faster, a behaviour that may be attributed to the presence of coherent structures.

Keywords Annular jet · Coherent structures · Velocity decay · Scalar decay · Kinetic energy dissipation rate · Scalar variance dissipation rate

A. Bouha · E. Varea · B. Patte-Rouland · L. Danaila (✉)
CNRS UMR 6614 – CORIA, Normandie Université, Rouen, France
e-mail: danaila@coria.fr

M. Gorokhovski and F. S. Godeferd (eds.), *Turbulent Cascades II*,
ERCOFTAC Series 26, https://doi.org/10.1007/978-3-030-12547-9_16

1 Introduction

Annular jets (hereafter AJ) are widely used in industrial processes. They are known for their ability to mix inlet flow with the ambient on relatively short distances compared to standard jets. As far as combustion is concerned, this 'bluff-body'-type geometry allows for a better stabilization of the flame, thus leading to reduction of pollutant emissions [1]. In the case of exhaust fan or chimney, the jet plume is reduced. The dilution of pollutants is enhanced, which decreases the risk of high concentration pollutant pockets transported by wind [2].

Albeit the initial conditions for AJ and classical round jets (CJ) are different, AJ also comprise three regions: (i) the initial, (ii) the intermediate and (iii) the fully developed zones. Unlike the CJ, the mean velocity and turbulence intensity profiles become self-similar over a shorter distance downstream, [3].

Moreover, it is well recognized that in the 'bluff-body'-type geometry of AJ, coherent structures develop in the intermediate zone [3]. It has been shown that coherent structures significantly alter the energy transfer to the small dissipative scales, as already reported e.g. in shear flows [4], grid turbulence configurations [5] or wake flows [6]. To the best of our knowledge, there has been no previous attempt to assess the passive scalar behaviour in AJ flows. The scalar is represented by the temperature which is considered as mixed species and the passive character of the scalar is discussed hereafter in Experimental Conditions sub-section. Therefore, this study aims at evaluating the mean values of velocity $\bar{U}$ and scalar $\bar{\Theta}$ along the AJ axis. Particular attention will be paid to the evolution of the kinetic energy and scalar dissipation rates, respectively $\bar{\varepsilon}$ ($\bar{\varepsilon} = 15\nu\overline{(\partial u/\partial x)^2}$ [7], ν is the kinematic viscosity, u is the longitudinal velocity fluctuation, $\overline{[..]}$ refers to as time average) and $\bar{\chi}$ ($\bar{\chi} = 3\alpha\overline{(\partial\theta/\partial x)^2}$ [7], θ is the temperature fluctuation and α is the thermal diffusivity), respectively. The dissipations of kinetic energy and/or scalar variance act over the small scales and balance the budget of energy and scalar variance.

The paper is organized as follows. In Sect. 2, the experimental configuration, conditions and measurement apparatus are presented. In Sect. 3, the decay rates for the mean velocity and scalar are discussed, as well as the dissipation rates of the kinetic energy and scalar variance. The behaviour of these quantities is critically compared to that already reported in the literature for CJ. Finally, conclusion will be drawn in Sect. 4.

2 Experimental Set-Up

2.1 Experimental Configuration

A schematic of the AJ is shown in Fig. 1. Air enters in the set-up from the bottom, through symmetrical annular inlets. To generate a top-hat velocity profile at the nozzle exit, the fluid passes through fluidized bed of glass balls with a diameter of 2 mm, five

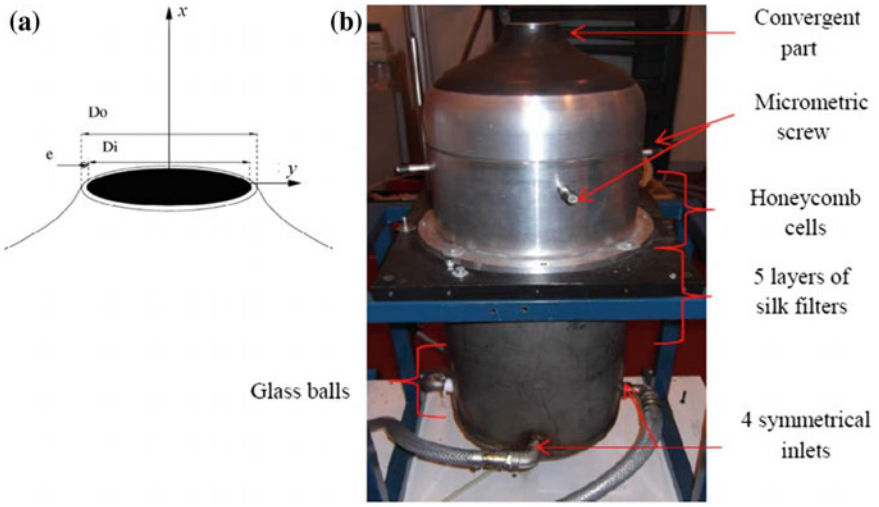

Fig. 1 **a** Schematic of the annular jet (AJ) nozzle of outer diameter D_0 and inner diameter D_i. **b** Image of the AJ set-up

layers of silk filters and finally through honeycomb cells. The convergent part was designed with a specific curvature—see [8]—to avoid boundary layer detachment. The outlet nozzle is characterized by an outer diameter $D_0 = 53.88\,\text{mm}$, and an inner diameter $D_i = 48.75\,\text{mm}$. The inner disk thickness is $e = 2.56\,\text{mm}$. The diameters ratio, $\zeta = \frac{D_i}{D_0} = 0.91$, is significantly higher than that used in Ko and Chan [3] ($\zeta = 0.45$) or than that of Warda et al. [4] ($\zeta = 0.71$). However, our diameter ratio is close to $\zeta = 0.96$ of Aly et al. [9]. As mentioned in [3], large diameters ratio are consistent with reduced reattachment distances.

2.2 Experimental Conditions

The jet exit velocity U_0 is set to 10 m/s which results in a Reynolds number (based on the outside diameter) of $Re_{D_0} = 3.45\,10^4$ ($Re_{D_0} = \frac{U_0 D_0}{\nu}$). The measurements were performed along the AJ axis, between $\frac{x}{D_0} = 2$ and $\frac{x}{D_0} = 9$. The exit temperature Θ_0 was set to 11 °C above the ambient. To evaluate the balance between buoyancy forces due to the air heating and inertial forces, e.g. Antonia and Mi [10], the ratio $\frac{Gr}{R_0^2}$ is estimated, where $Gr \equiv g r_u^3 \overline{\Theta}/\nu^2 \Theta_a$ is the Grashof number, Θ_a is the ambient temperature, r_u is the radius at which the mean velocity reduces by a factor of two, and $R_0 \equiv \overline{U} r_u/\nu$ is the local Reynolds number. The ratio $\frac{Gr}{Re^2}$ is here of 0.002, which is close to the value reported by [10, 11]. Therefore, the temperature is a passive contaminant with no dynamical effect (buoyancy forces are much smaller than the inertial forces) on the fluid motion.

2.3 Measurements

Simultaneous measurements of velocity and temperature were performed. Using X-probe wire operating at a constant temperature (CTA, Constant Temperature Anemometry), we evaluated the axial and radial velocity components u and v, respectively. The probe was made of 5.04 μm diameter Wollaston wires ($Pt - 10\%Rd$). The CTA circuit operated at an overheat ratio of 1.4 (hot wires) and the active length/diameter ratio was of about 200. It was shown that for this specific ratio [12], the errors in $\overline{U}$ and u' (the prime refers to as the root mean square R.M.S) were respectively 1.3 and 1.4%. The X-probe calibration was carried out using the lookup table method (LUT), introduced by Burattini and Antonia [13]. This method was shown to be quite rigorous. We used 374 calibration points. Temperature fluctuations θ were evaluated with a constant current anemometer (CCA), operating at low overheat ratio (cold wire). The latter was made of 0.64 μm diameter Wollaston wire and the active length/diameter ratio was of about 880. Browne and Antonia [14] showed that for active length/diameter ratios lower than 1500, errors due to the heat conduction between prongs could affect the temperature momentum and its time derivative calculation. An increase of the active length/diameter ratio results in a reduced spatial resolution. Therefore, the same strategy in terms of length to diameter ratio as adopted in Lemay and Benassa [11] was chosen. They recommended this ratio to be between 700 and 1000 and it was reported that the errors in $\overline{\chi}$ are smaller than 5%. As suggested by Paranthoën and Lecordier [15], the cold wire was totally etched, which allows for a better time resolution. The spatial arrangement of the X-probe velocity sensors/wires was chosen as indicated by Vukoslavčević and Wallace [16]. More specifically, the X-probe was positioned in the (x, y) plane and the temperature sensor was placed upstream, and perpendicular to the (x, y) plane. This configuration limits possible contamination of the cold wire due to the hot wires. To correct the instantaneous velocity voltage signals for the influence of temperature fluctuations, the following correction procedure was applied [17]:

$$E^2 \frac{\Theta_w - \Theta_a}{\Theta_w - \Theta_i} = E_{corr}^2, \tag{1}$$

where E and E_{corr} are the instantaneous and corrected voltages, respectively. Θ_w and Θ_i are the hot wire temperature of 265 °C and instantaneous temperatures—assessed by the cold wire-, respectively. Θ_a was evaluated through a thermocouple with a resolution of 0,5 °C. The impact on the accuracy of relation (1) is negligible-less than 1%. During the signal conditioning, a Butterworth low pass-filter (cut-off frequency -48 db/dec) was used to avoid aliasing of the frequencies higher than half the sampling frequency, f_s. A number of samples between 10^6 and 8 10^6 were acquired at each spatial location, using a 12 bit A/D converter. Following [11], some parameters should be assessed, as summarized in Table 1 for the experimental conditions at locations $\frac{x}{D_0} = 3$ and 7. This allows us to evaluate the level of error in estimating small-scale quantities. $\overline{U}$ and $\overline{\Theta}$ are the local mean velocity and

Table 1 Experimental conditions at the axial positions $\frac{x}{D_0} = 3, 7$. l_{w1} and l_{w2} refer to as the length of hot and cold wires, respectively

x/D_0	3	7
$\overline{\Theta}$ (°C)	31.04	28.56
R_λ	141	118
$\overline{U}$ (m/s)	4.72	2.36
η (mm)	0.097	0.134
η_θ (mm)	0.116	0.214
l_{w1}/η	10.4	7.5
l_{w2}/η_θ	4.78	2.59
f_s (10^3HZ)	28.05	11.65
f_K (10^3HZ)	7.75	2.81
$f_{K\theta}$ (10^3HZ)	6.48	1.76

temperature, respectively. $R_\lambda = u'\lambda/\nu$ is the Reynolds number based on the Taylor micro-scale, defined as $\lambda = \sqrt{\overline{u^2}/\overline{(\partial u/\partial x)^2}}$. The longitudinal derivatives are determined via the Taylor hypothesis which allows us to assess the spacial increments Δx from the temporal measurements, such as $\Delta x = -\overline{U}\Delta t$. Here, $\eta = (\nu^3/\overline{\varepsilon})^{1/4}$ is the Kolmogorov scale and $\eta_\theta = \eta/Pr^{4/3}$ is the corresponding temperature micro-scale, where $Pr = \nu/\alpha$ is the Prandtl number. $f_K = \overline{U}/2\pi\eta$ is the Kolmogorov frequency and $f_{K\theta} = \overline{U}/2\pi\eta_\theta$ is the Obukhov frequency. The ratios f_s/f_k and l_{w2}/η_θ satisfy the Lemay and Benassa [11] recommendations.

3 Results and Discussion

3.1 Spectral Analysis

Figure 2 shows the velocity and temperature power spectral density PSD—computed through a Fast Fourier transform-, as a function of the dimensionless wave number, $k\eta = \left(2\pi f/\overline{U}\right)\eta$. The error on the spectra calculation is about 8.8%, so that at each wave number we define the error as $error_{u^2} = 2/N$ where N refers to as the number of independent data used to calculate each spectra (in Fig. 2 we present the mean spectra). For low wave numbers, the energy distributions for the longitudinal (u) and radial (v) velocity components are dissimilar, thus reflecting differences in the variances of u and v, and therefore departures from global isotropy. In the intermediate zone, at $\frac{x}{D_0} = 3$, the spike in the radial velocity spectrum reflects the presence of coherent (large scale) structures generated by the central part of the AJ. It is well-known that v is more sensitive to the coherent motion than u, e.g. [18, 19]. The spike in the spectrum of v is absent at $\frac{x}{D_0} = 7$, which reflects the transition to

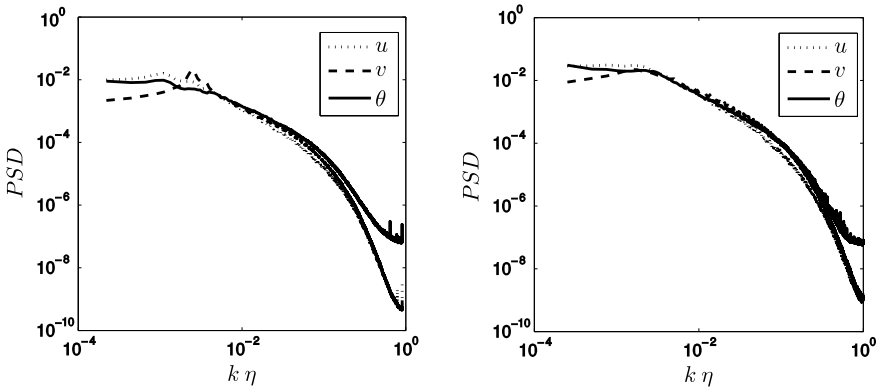

Fig. 2 Power spectral density of fluctuating velocity components (u, v) and temperature (θ). Left: $\frac{x}{D_0} = 3$. Right: $\frac{x}{D_0} = 7$

the developed turbulence. At low wave number, most of the energy is contained in the longitudinal velocity component. Similarly to CJ configurations, the energy is transferred from the mean motion to the longitudinal velocity fluctuations $\overline{u^2}$, and then to the radial velocity fluctuations $\overline{v^2}$, e.g. [20].

3.2 Similarity Along the AJ Centreline

Within the fully developed zone, AJ most likely behave as CJ, with similar decaying exponents for basic turbulence characteristics (mean statistics and dissipation rates), but with some differences that we highlight in the following analysis. We define an equivalent jet with the same outlet velocity U_0, but with an equivalent diameter $D_{eq} = \sqrt{D_0^2 - D_i^2}$ based on the conservation of the mass flow rate. The mean velocity and temperature fields decay in a similar fashion as already reported by e.g. [11, 21, 22],

$$\frac{\overline{U}}{U_0} = A_{\overline{U}} \left(\frac{x - x_0}{D_{eq}} \right)^{-1}, \tag{2}$$

and

$$\frac{\overline{\Theta} - \Theta_a}{\Theta_0 - \Theta_a} = A_{\overline{\Theta}} \left(\frac{x - x_0}{D_{eq}} \right)^{-1}. \tag{3}$$

The prefactors of these power-laws, $A_{\overline{U}}$ and $A_{\overline{\Theta}}$ were evaluated through a fit of the mean normalized velocity and temperature (see Fig. 3). Their values are 4.6 ± 0.2 and 4 ± 0.36, respectively. For CJ, it appears that $5.8 \leq A_{\overline{U}} \leq 6$ [21, 23–25] and

$A_{\overline{\Theta}} = 4.35$ [21]. Pitts [22] established a compendium of $A_{\overline{\Theta}}$ values found in the literature for a variety of measurements methods.

To evaluate the features of small scales, the axial evolution of the mean energy dissipation rates $\overline{\varepsilon}$ and $\overline{\chi}$ are calculated and represented in Fig. 3. Note that mean values of velocity and temperature are also shown in Fig. 3. According to [23, 26], local axisymmetry is a better assumption than local isotropy. Therefore, the expression of $\overline{\varepsilon}_{hom}$ considering local homogeneity becomes

$$\overline{\varepsilon}_{hom} = 3\nu\overline{\left(\left(\frac{\partial u}{\partial x}\right)^2 + 2\left(\frac{\partial v}{\partial x}\right)^2\right)}. \tag{4}$$

Considering relations (2), (3) and given that $\overline{v^2}/\overline{u^2}$ scales whit x, this leads to normalized mean dissipation rates following the power law x^{-4} [27–30], such as

$$\frac{\overline{\varepsilon} D_{eq}}{U_0^3} = A_{\overline{\varepsilon}}\left(\frac{x - x_0}{D_{eq}}\right)^{-4}, \tag{5}$$

and

$$\frac{\overline{\chi} D_{eq}}{U_0\left(\Theta_0 - \Theta_a\right)^2} = A_{\overline{\chi}}\left(\frac{x - x_0}{D_{eq}}\right)^{-4}. \tag{6}$$

The values $A_{\overline{\varepsilon}}$ and $A_{\overline{\chi}}$ are 32 ± 4.8 and 6 ± 0.55 for $Re_{D_{eq}} = 1.47\ 10^4$, respectively. For CJ, the mean dissipation rate of the energy is found to be close to 42.5 for

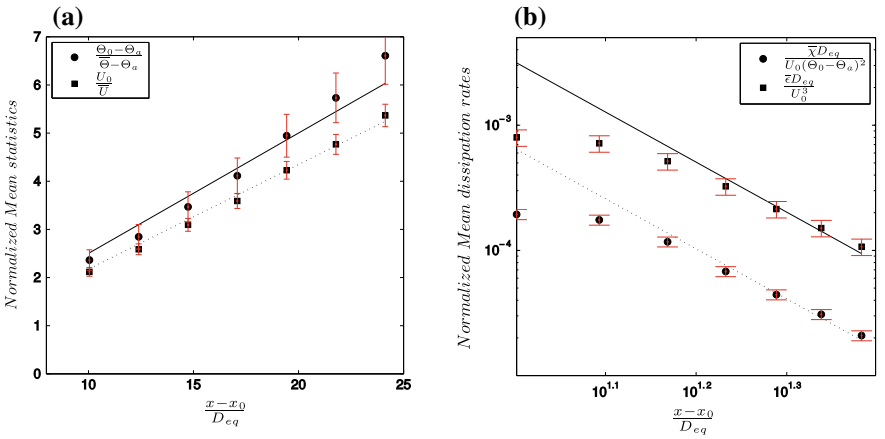

Fig. 3 **a** The streamwise decay of mean statistics. (. . .): fit of relation (2). (——): fit of relation (3). Error bars refer to as $A_{\overline{U}}$ and $A_{\overline{\Theta}}$ confidence intervals. **b**: The streamwise decay of mean dissipation rates. (. . .): fit of relation (5). (——): fit of relation (6). Error bars refer to as $A_{\overline{\varepsilon}}$ and $A_{\overline{\chi}}$ confidence intervals

Table 2 Distances over which either AJ or CJ reach similarity

Similarity of	AJ	CJ
Mean statistics	$4D_{eq}$	$4D$ to $8D$ [4, 21, 31]
R.M.S	$9.5D_{eq}$	$20D$ to $40D$ [4, 20, 21, 24, 29]
Dissipative scales	$14D_{eq}$	$26D$ [29]

$Re_D = 11.3\ 10^4$ and 48 for $Re_D = 12\ 10^4$ [27, 28, 30]. For the scalar it is close to 14.9 for $Re_D = 15\ 10^4$ [29] (D refers to as the round jet diameter).

As far as the similarity is concerned, the mean field becomes self-similar at distances slightly smaller than $x = 7D_{eq}$, as indicated in Fig. 3. The value of the virtual origin, $x_0 = -3D_{eq}$, is provided by the zero-crossing of $U_0/\overline{U}$. Note that the virtual origin should be the same for other statistics [30]. From the first line in Table 2, it appears that the real distance at which self-similarity is achieved, is the same as in CJ. However, when expressing this distance in number of outer diameters, this is far shorter than that necessary in CJ for the similarity to be reasonably applicable. Moreover, self-similarity of mean quantities is not sufficient for the complete similarity (i.e., similarity of all statistics) to be valid [21]. Second-order statistics of both velocity and scalar, as well as small-scale quantities require larger distances to reach similarity. In AJ, self-similarity emerges faster than in CJ. These observations show the effect of initial conditions on self-similarity which is directly related to the flow development. From the applications viewpoint, reaching self-similarity, and thus a fully developed state, over small distances downstream the injection has a positive impact in terms of mixing efficiency.

3.3 Radial Similarity

The radial profiles of mean kinetic energy $\overline{q^2}$ ($\overline{q^2} = \overline{u^2} + 2\overline{v^2}$) and R.M.S. distributions are shown in Fig. 4 following the normalization using the centreline mean velocity $\overline{U}_c$, the velocity half radius $R_{0.5-u}$, the centreline mean temperature $\overline{\Theta}_c$ (relative to ambient) and the mean temperature half radius $R_{0.5-\theta}$. From Fig. 4a, we note that similarity is satisfied in the intermediate ($\frac{x}{D_0} = 1.5-3$) and fully developed zones ($\frac{x}{D_0} = 5-7$). In addition, through those normalizing scales no disparity were raised between the velocity and the scalar fields. However, the radial similarity of R.M.S. quantities—Fig. 4a, b—and the mean energy—Fig. 4c—is only satisfied in fully developed zones, sustaining the sensitivity lack of mean quantities in term of similarity. The large scatter in temperature measurement far from the jet centreline probably results from a contamination of temperature signal due to hot wires.

From Table 2, the longitudinal decay of mean value and dissipation rate is more pronounced for scalar than for the velocity. This result is consistent with the radial transport mechanisms of momentum $\overline{uv}$ and scalar flux $\overline{\theta v}$ which is more enhanced

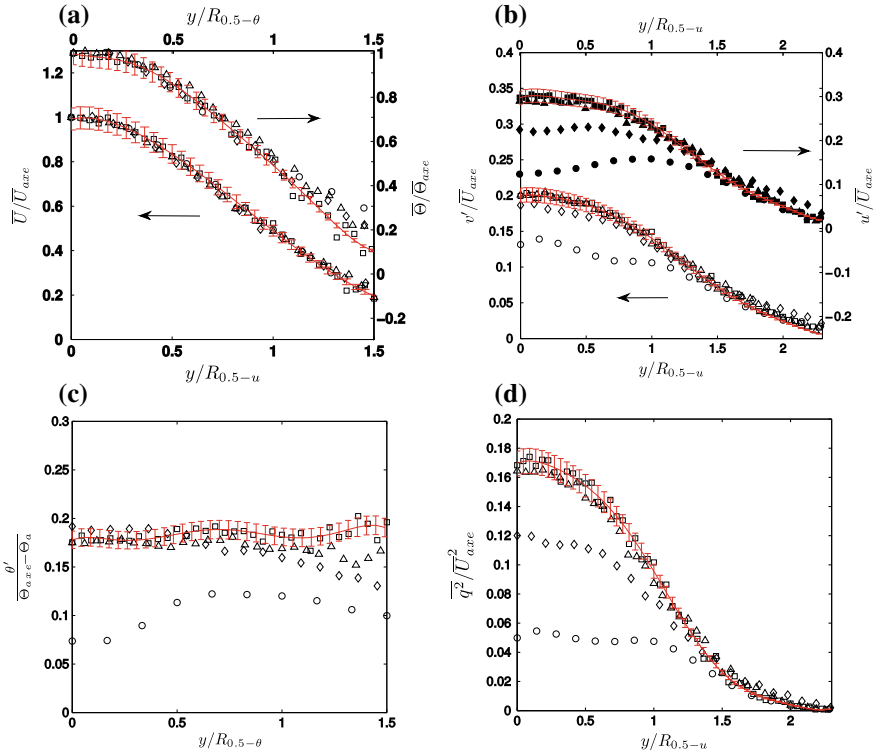

Fig. 4 Similarity over the radial direction, for different quantities. **a** $\overline{U}$ and $\overline{\Theta}$ **b** u' and v', **c** θ', **d** $\overline{q^2} = \overline{u^2} + 2\overline{v^2}$. (□): at $x/D_0 = 7$, (△): at $x/D_0 = 5$, (◇): at $x/D_0 = 3$, (○): at $x/D_0 = 1.5$. Error bars represent 95% confidence intervals

for the scalar, as shown in Fig. 5, evaluated at $\frac{x}{D_0} = 7$. Given that the transport of scalar and momentum is mainly performed by the large scales, Chevray and Tutu [32] argued that small scales are more efficient for the transport of passive scalar than for the momentum. They also expected that the the transport due to pressure forces is achieved at the expense of transport due to convection, thus resulting in a net momentum transport reduction. Recently, Darisse et al. [33] presented budgets of turbulent scalar fluxes $\overline{u_i\theta}$. A noticeable pressure acting far from the jet centerline is highlighted (for scalar as well as momentum), with much radial extend for scalar.

A possible scenario to explain the observed enhanced development of the flow is intimately related to the intermediate zone which is populated by coherent structures. It has been shown for shear flows that the vorticity created after mean field instability initiates other instabilities which are responsible for the energy cascade to smaller scales [6]. For grid turbulence, it has been suggested by [5] that the self-similar state is due to the singular development of vortical structures randomly distributed across the flow. For wake flow [34], one can observe temporal periodicity of coherent structures which affect the turbulent scales thought phase accelerated energy transfer cascades.

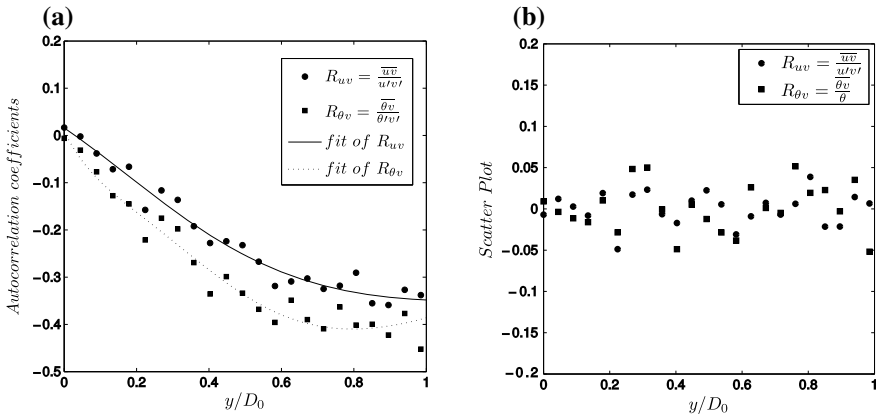

Fig. 5 **a** Radial evolution of autocorrelation coefficients. **b** Scatter plot of the fit

The differences observed between the decay rates of the measured quantities and those of round jet highlight the non-universality of different flows. As mentioned by George and Arndt [6], self-similarity depends on initial conditions. Therefore, in annular jet flows, one can state that due to initial conditions, a multiplicity of scales—large scales and specifically small scales—are generated on relatively short distances.

4 Conclusions

Kinetic energy and scalar variance behaviours were assessed in AJ with large diameter ratio. We have taken great care of measurement implementations and estimation of small-scale quantities. The decay of mean and small-scale statistics has been evaluated, and they scale as x^{-1} and x^{-4} respectively in the fully developed region. This is in full agreement with the CJ. However, the power-law prefactors are quite distinct from those reported for CJ, as they reflect the link between the initial conditions and the way the flow develops step-by-step. The inverse of these prefactors are larger than for CJ, which reflects a stronger decay of mean values and dissipation rates in AJ. This behaviour is mainly related to the strong turbulent activity in the intermediate zone. Thus, this specific geometry generates coherent structures, which:

- influence effectively both the kinetic energy and scalar cascades in the intermediate zone. This behaviour has been investigated for the case of the wake behind different types of obstacles [35, 36];
- lead to an establishment of a self-similar zone over a short distance beyond the injection. This feature emphasizes the particular relevance of AJ for mixing process, particularly given the current issues focused on reducing the geometry of combustion chamber.

References

1. Schefer, R.W., Namazian, M., Kelly, J., Perrin, M.: Effect of confinement on bluff-body burner recirculation zone characteristics and flame stability. Combust. Sci. Technol. **120**(1–6), 185–211 (1996)
2. Brendel, M.: CFD analysis of laboratory exhaust fans and applications. In: Ashrae Winter Annual Meeting, Atlantic City, NJ (2002)
3. Ko, N.W.M., Chan, W.T.: Similarity in the initial region of annular jets: three configurations. J. Fluid Mech. **84**, 641–656, 2 (1978)
4. Warda, H.A., Kassab, S.Z., Elshorbagy, K.A., Elsaadawy, E.A.: An experimental investigation of the near-field region of a free turbulent coaxial jet using LDA. Flow Measurement and Instrumentation **10**(1), 15–26 (1999)
5. George, W.K.: The decay of homogeneous isotropic turbulence. Phys. Fluids A Fluid Dyn. (1989–1993) **4**(7), 1492–1509 (1992)
6. George, W.K., Arndt, R.: Advances in Turbulence. Hemisphere Publishing Corporation (1989)
7. Antonia, R.A., Zhou, T., Danaila, L., Anselmet, F.: Streamwise inhomogeneity of decaying grid turbulence. Phys. Fluids **12**(11), 3086–3089 (2000)
8. Danlos, A.: Dynamique des jets contrôlés: Application à l' étude du mélange dans des écoulements de jets annulaires à très grand rapport de diamètres. Ph.D. thesis, Université de Rouen (2009)
9. Aly, M.S., Rashed, M.I.I.: Experimental investigation of an annular jet. J. Wind Eng. Ind. Aerodyn. **37**(2), 155–166 (1991)
10. Antonia, R.A., Mi, J.: Temperature dissipation in a turbulent round jet. J. Fluid Mech. **250**, 531–551 (1993)
11. Lemay, J., Benaïssa, A.: Improvement of cold-wire response for measurement of temperature dissipation. Exp. Fluids **31**(3), 347–356 (2001)
12. Bruun, H.H.: Hot-Wire Anemometry. Oxford Science (1995)
13. Burattini, P., Antonia, R.A.: The effect of different x-wire calibration schemes on some turbulence statistics. Exp. Fluids **38**(1), 80–89 (2005)
14. Browne, L.W.B., Antonia, R.A.: The effect of wire length on temperature statistics in a turbulent wake. Exp. Fluids **5**(6), 426–428 (1987)
15. Paranthoën, P., Lecordier, J.C.: Mesures de temperature dans les écoulements turbulents. Revue Generale de Thermique **35**(413), 283–308 (1996)
16. Vukoslavčević, P.V., Wallace, J.M.: The simultaneous measurement of velocity and temperature in heated turbulent air flow using thermal anemometry. Meas. Sci. Technol. **13**(10), 1615 (2002)
17. Danaila, L., Anselmet, F., Zhou, T., Antonia, R.A.: A generalization of yaglom's equation which accounts for the large-scale forcing in heated decaying turbulence. J. Fluid Mech. **391**, 359–372 (1999)
18. Papailiou, D.D., Lykoudis, P.S.: Turbulent vortex streets and the entrainment mechanism of the turbulent wake. J. Fluid Mech. **62**(1), 11–31 (1974)
19. Antonia, R.A., Zhou, T., Romano, G.P.: Small-scale turbulence characteristics of two-dimensional bluff body wakes. J. Fluid Mech. **459**, 67–92 (2002)
20. Wygnanski, I., Fiedler, H.: Some measurements in the self-preserving jet. J. Fluid Mech. **38**, 577–612, 9 (1969)
21. Chua, L.P., Antonia, R.A.: The turbulent interaction region of a circular jet. Int. Commun. Heat Mass Transf. **13**(5), 545–558 (1986)
22. Pitts, W.M.: Effects of global density ratio on the centerline mixing behavior of axisymmetric turbulent jets. Exp. Fluids **11**(2–3), 125–134 (1991)
23. Burattini, P., Antonia, R.A., Danaila, L.: Similarity in the far field of a turbulent round jet. Phys. Fluids **17**(2), 025101 (2005)
24. Abdel-Rahman, A.A., Chakroun, W., Al-Fahed, S.F.: LDA measurements in the turbulent round jet. Mech. Res. Commun. **24**(3), 277–288 (1997)
25. Hussein, H.J., Capp, S.P., George, W.K.: Velocity measurements in a high-reynolds-number, momentum-conserving, axisymmetric, turbulent jet. J. Fluid Mech. **258**, 31–75 (1994)

26. George, W.K., Hussein, H.J.: Locally axisymmetric turbulence. J. Fluid Mech. **233**, 1–23 (1991)
27. Friehe, C.A., Van Atta, C.W., Gibson, C.H.: Jet turbulence: Dissipation rate measurements and correlations. In: AGARD-Conference Proceeding on Turbulent Shear Flows, London, U.K, vol. 93, 13–15 September 1971
28. Antonia, R.A., Satyaprakash, B.R., Hussain, A.K.M.F.: Measurements of dissipation rate and some other characteristics of turbulent plane and circular jets. Phys. Fluids **23**(4), 695–700 (1980)
29. Lemay, J., Benaïssa, A., Darisse, A.: Budgets of turbulent kinetic energy and scalar variance in the self-similar region of a round jet. In: The European Turbulence Conference, vol. 14, September 2013
30. Thiesset, F., Antonia, R.A., Djenidi, L.: Consequences of self-preservation on the axis of a turbulent round jet. J. Fluid Mech. **748**, 6 (2014)
31. Bradshaw, P., Ferriss, D.H., Johnson, R.F.: Turbulence in the noise-producing region of a circular jet. J. Fluid Mech. **19**, 591–624 (1964)
32. Chevray, R., Tutu, N.K.: Intermittency and preferential transport of heat in a round jet. J. Fluid Mech. **88**, 133–160, 9 (1978)
33. Darisse, A., Lemay, J., Benassa, A.: Budgets of turbulent kinetic energy, reynolds stresses, variance of temperature fluctuations and turbulent heat fluxes in a round jet. J. Fluid Mech. **774**, 95–142, 7 (2015)
34. Thiesset, F., Danaila, R.A., Antonia, L., Zhou, T.: Scale-by-scale energy budgets which account for the coherent motion. J. Phys. Conf. Ser. **318**(5), 052040 (2011)
35. Thiesset, F., Danaila, L., Antonia, R.A.: Dynamical effect of the total strain induced by the coherent motion on local isotropy in a wake. J. Fluid Mech. **720**, 393–423, 4 (2013)
36. Thiesset, F., Danaila, L., Antonia, R.A.: Dynamical interactions between the coherent motion and small scales in a cylinder wake. J. Fluid Mech. **749**, 201–226, 6 (2014)

Part V
Turbulence Under "Active" Particles

Parametric Instability and Turbulent Cascades in Space Plasmas

Leonardo Primavera, Francesco Malara, Sergio Servidio and Giuseppina Nigro




Abstract Spacecraft observations show the presence, in the polar Solar Wind (SW) plasma, of outward propagating Alfvénic fluctuations with a very broadband spectrum. This is true only up to a certain frequency in the spectrum, after which a consistent amount of energy is present also in the spectra of inward propagating Alfvén and density fluctuations. A mechanism able to explain the production of inward propagating modes and density fluctuations is the parametric instability, in which Alfvén waves can decay and produce back-scattered waves and density perturbations. In this work, we show some recent results obtained with a $(2 + 1/2)$D-MHD pseudo-spectral numerical code in which an attempt is made to reproduce an initial condition similar to that observed in the real SW. The evolution of the instability generates a nonlinear cascade that redistributes the energy towards the small scales in all directions. A striking feature of this evolution is the presence of a few localized, energy containing, coherent pressure-balanced structures.

L. Primavera (✉) · F. Malara · S. Servidio · G. Nigro
Dipartimento di Fisica, Università della Calabria, Cubo 31C, Via P. Bucci, 87036 Rende, CS, Italy
e-mail: leonardo.primavera@unical.it

F. Malara
e-mail: francesco.malara@fis.unical.it

S. Servidio
e-mail: sergio.servidio@fis.unical.it

G. Nigro
e-mail: giusy.nigro@fis.unical.it

M. Gorokhovski and F. S. Godeferd (eds.), *Turbulent Cascades II*,
ERCOFTAC Series 26, https://doi.org/10.1007/978-3-030-12547-9_17

1 Introduction

Spacecraft observations showed that the Solar Wind (SW) is a highly turbulent medium, by revealing in the polar fast streams the presence of a broadband spectrum of outward propagating Alfvénic fluctuations, extending over several decades of frequencies and wave vectors. These oscillations appear to be mostly "arc-polarized", which means that the total intensity of magnetic fluctuations remains spatially constant while propagating into the heliosphere. However, this occurs only up to a certain frequency in the spectrum, after which the observations show an increasing presence of both inward propagating and density fluctuations. Such observations are apparently in contrast with the theoretical argument that prescribes arc-polarized Alfvén waves to be exact solutions of the Magnetohydrodynamic (MHD) equations even in the nonlinear and compressible case. For this reason, these fluctuations, being incompressible, should propagate undistorted along a uniform background magnetic field without undergoing a nonlinear energy cascade and with no production of backward propagating modes and density fluctuations.

A mechanism able to explain this apparent contradiction is the so called "parametric instability". In a compressible plasma, even an infinitesimal perturbation in density or pressure can trigger the instability, in which a circularly polarized Alfvén wave (mother-wave) decays and produces back-scattered (daughter) waves with the two polarizations, along with density perturbations. This can then produce a turbulent energy transfer and a nonlinear cascade of all the quantities involved. This instability has been studied extensively in a variety of situations in past years (see, for instance, [1, 4] for a study of the monochromatic case in 2D and 3D, [5, 6] for a non-monochromatic 1D case, [2] for a 2D case in an expanding box model).

However, in the majority of those studies, the initial condition was chosen either as a single, monochromatic Alfvén wave, or as a broadband spectrum of fluctuations, following only approximately a power-law along a single propagation direction. Moreover, since the instability can lead to large density fluctuations involving production of strong shocks, the codes are often developed in the framework of finite volumes methods. This kind of approach involves the presence in the solution of spurious numerical effects (especially in terms of strong numerical dissipation) which are hard to control and may strongly influence the turbulent development of the instability. The aim of this contribution is to present, for the first time, at the best of our knowledge, a study of the parametric instability in which the initial condition is made of a fully two-dimensional, arc-polarized, Alfvénic perturbation with a Kolmogorov-like power-law spectrum, much closer to the actual SW conditions than those in previous studies.

2 Numerical Code

We carried out several numerical simulations by using a pseudo-spectral, $(2 + 1/2)$D numerical code. The code solves the following set of equations for a compressible, polytropic MHD plasma:

$$\frac{\partial \rho}{\partial t} + (\mathbf{v} \cdot \nabla)\rho = -\rho \nabla \cdot \mathbf{v} \tag{1}$$

$$\frac{\partial \mathbf{v}}{\partial t} + (\mathbf{v} \cdot \nabla)\mathbf{v} = -\beta \rho^{\gamma-2} \nabla \rho + \frac{1}{\rho}(\nabla \times \mathbf{B}) \times \mathbf{B} + \\ + \frac{\nu}{\rho}\left\{\nabla^{2n}\mathbf{v} + \frac{1}{3}\left[\nabla^{2(n-1)}\nabla(\nabla \cdot \mathbf{v})\right]\right\} \tag{2}$$

$$\frac{\partial \mathbf{B}}{\partial t} = \nabla \times (\mathbf{v} \times \mathbf{B}) + \eta \nabla^{2n} \mathbf{B} \tag{3}$$

where ρ is the mass density, $\mathbf{v}$ and $\mathbf{B}$ the velocity and magnetic fields, $\beta = c_s^2/c_A^2$ is the plasma beta and c_s and c_A are the sound and Alfvén speeds, respectively. The coefficients ν and η are the kinetic and magnetic hyperviscosity coefficients, which reduce to the inverse of the ordinary kinetic and magnetic Reynolds numbers for $n = 1$. The equations are dimensionless. The magnetic field is normalized to an arbitrary magnetic field $\mathbf{B}_0$, the density to a background density ρ_0 and, consequently, the velocity field is measured in units of the Alfvén speed: $\mathbf{c}_A = \mathbf{B}_0/\sqrt{4\pi\rho_0}$.

The integration domain is a box of dimensions $2\pi \times 2\pi$ in the $x - y$ plane. We suppose the plasma is homogeneous, therefore we use periodic boundary conditions in both the x and y directions. The code works in $(2 + 1/2)$-dimensions, that is all the vectors retain all the three components, although the quantities depend on the x and y coordinates only.

The numerical code is parallelized and we use in the simulations hyper-viscosity and hyper-resistivity coefficients with $n = 2$. The results presented here are preliminary and obtained with a grid resolution of 512^2 points, to catch the basic dynamical evolution of the turbulence induced by the parametric instability. Further simulations with higher resolutions are planned and will be the subject of a forthcoming paper. The code uses the parallel FFTW library [3] to compute the derivatives in the x and y directions and a second order Runge-Kutta time scheme for the time advancement. Finally, the divergenceless condition for the magnetic field is ensured by projecting, at each time step, the quantities in the spectral space on a subspace in which the solution for a given $\mathbf{k}$-vector is locally orthogonal to the wave-vector itself.

The initial condition setup consists of a background magnetic field with superimposed magnetic fluctuations. The global field must have a constant total intensity, to ensure that the fluctuations are arc-polarized. In order to have real 2D, divergenceless, magnetic fluctuations $\delta B_x(x, y)$ and $\delta B_y(x, y)$ with a power-law spectrum, as observed in SW, we built up the initial conditions as the derivatives of a vector potential field in the spectral space, whose components follow a power-law spectrum with random phases. The third component B_z of the magnetic

field is built as $B_z = \sqrt{C^2 - B_x^2 - B_y^2}$, where C is a suitable constant such that $C \geq \max(\sqrt{B_x^2 + B_y^2})$. Note that, the resulting mean magnetic field will have components along both x and z directions. The velocity field of the Alfvénic fluctuations has a negative correlation with the magnetic field: $\delta\mathbf{v} = -\delta\mathbf{B}/\sqrt{\rho_0}$, where ρ_0 is the background density. Finally, we add a noise on the density to trigger the parametric instability: $\rho = \rho_0 + \delta\rho$, where $\delta\rho$ is built up in the spectral space with a power-law spectrum and random phases.

3 Numerical Results

We carried out numerical simulations for different values of the plasma β. In the monochromatic case and low-beta approximation [7], it is known that the growth rate of the instability decreases with increasing values of β. Other important parameters are: the amplitude and (in the monochromatic case) the wavelength of the initial Alfvénic perturbation that triggers the instability. In this work we can only quickly explore the dependence on β. Further investigations of the relevant space of parameters will be the subject of a forthcoming paper.

The plasma β in the SW is not constant, but it changes with the distance from the Sun and it ranges between about 0.5 and 1.5. For this reason, we run two different simulations, one with $\beta = 0.5$ and the other with $\beta = 1.5$. Please, note that since we use an explicit time scheme in the code, larger values of β mean higher values for the sound speed, which in turn implies smaller time steps in the simulation.

A convenient description of an Alfvén wave propagating along a specific direction can be given in terms of the so called Elsässer variables $\mathbf{Z}^{\pm}$ defined as:

$$\mathbf{Z}^{\pm} = \delta\mathbf{v} \pm \delta\mathbf{B}/\sqrt{\rho} \tag{4}$$

Notice that in the initial conditions we use a negative correlation between velocity and magnetic field fluctuations, that is the mother-wave corresponds to a $\mathbf{Z}^-$ Elsässer variable, whilst $\mathbf{Z}^+ = 0$.

3.1 Results for $\beta = 0.5$

In Fig. 1, we show the temporal evolution of the following parameters:

$$r(t) = \sqrt{< \left(\frac{\delta\rho}{\rho_0}\right)^2 >}; \qquad m(t) = \sqrt{< \left(\frac{\delta|b|}{|b_0|}\right)^2 >}; \qquad e^{\pm}(t) = \frac{1}{2} < \left(\delta\mathbf{Z}^{\pm}\right)^2 > \tag{5}$$

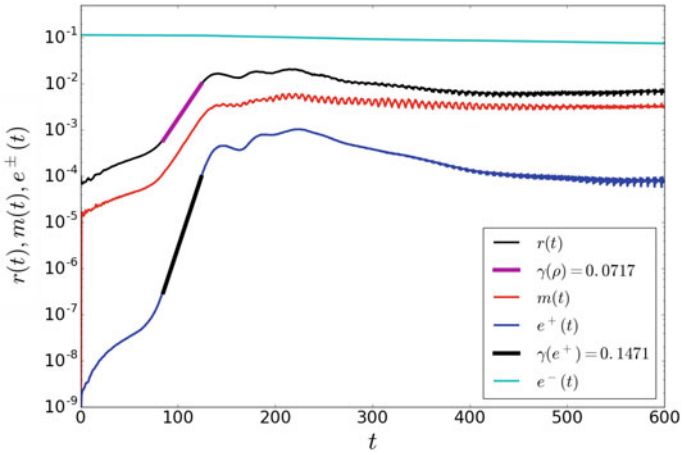

Fig. 1 Time evolution of the parameters $r(t)$, $m(t)$, $e^{\pm}(t)$ as given by Eq. 5 for the $\beta = 0.5$ case

which represent the root mean square of the density fluctuations, the magnetic field intensity fluctuations (both normalized to the average value) and energies of the Elsässer variables $\mathbf{Z}^{\pm}$, respectively, averaged on the whole simulation domain, as a function of time. The plot shows that, after an initial adjustment of the solution, the noise superposed on the background density triggers the parametric instability and one observes, during times $t = 30 \div 200$ an exponential increase for the density fluctuations (r parameter), magnetic field intensity fluctuations (m parameter) and energy of the Elsässer variable $\mathbf{Z}^+$ (e^+ parameter). The growth rate of the instability is $\gamma \sim 0.072$ for r and m parameters, the double in the case of e^+, being a quadratic quantity. Correspondingly, the energy of the mother-wave $\mathbf{Z}^-$ slightly decreases in time. After $t \sim 250$ the instability saturates.

The saturation levels for all the parameters are considerably small, which means that the amount of energy transferred from the mother $\mathbf{Z}^-$ wave to the density and backscattered Alfvénic fluctuations is actually only a few percent. However, we will see shortly that large amplitude density and $\mathbf{Z}^+$ fluctuations are indeed present in the computational domain, though in very localized, energy containing, coherent structures.

In Fig. 2, we represent a contour plot of the density fluctuations in the simulation domain. It is visible that at the beginning of the simulation, the noise on the density is equally distributed over the whole computational domain. After the instability triggers ($t \sim 50$), fluctuations are observed mainly in the y direction, meaning that an anisotropic spectrum is initially formed mainly along this direction, which is the direction perpendicular to the main magnetic field (that has x-z components only). However, this situation changes at subsequent times ($t \sim 200$), where the fluctuations seem to focus mainly in very specific points of the domain, in particular in a horizontal narrow band near the axis $y = 0$. In the final fully-nonlinear stage of the evolution, the fluctuations start to spread everywhere in the computational domain, due to the

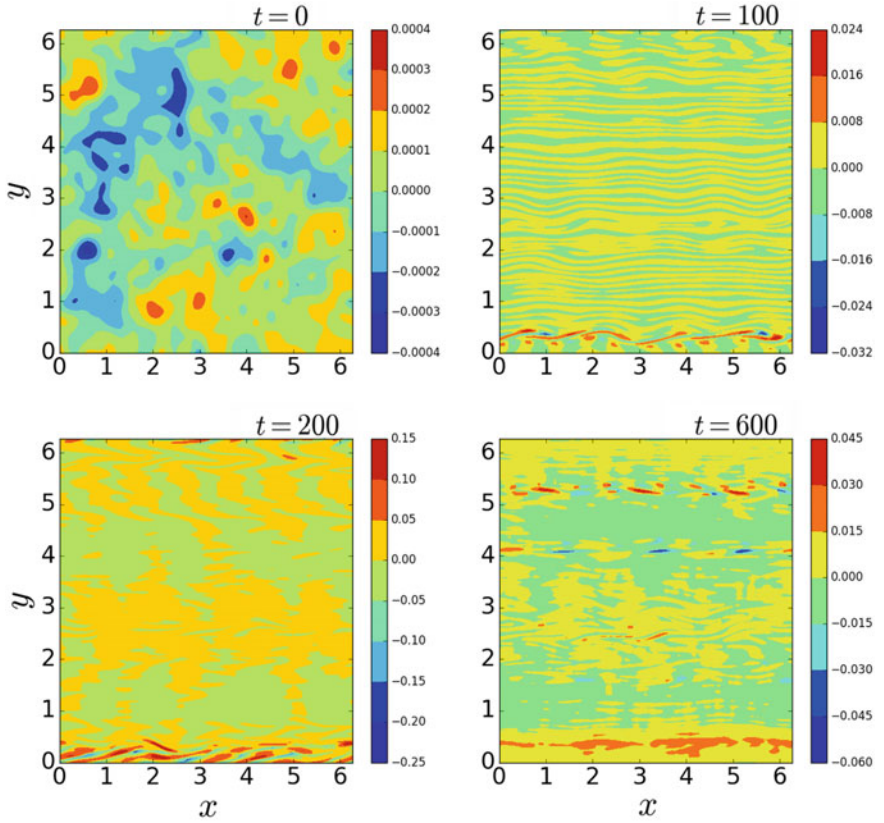

Fig. 2 Density fluctuations at different times for the $\beta = 0.5$ case

nonlinear interactions. By looking at the color scale of the contour plots we actually notice that at $t = 200$ the density fluctuations are considerably high (the values are between $\delta\rho/\rho_0 \sim -0.25 \div 0.15$), but mainly concentrated in structures at small scales. A very similar behaviour is observed on the contour plots of the Elsässer variable $\mathbf{Z}^+$ (the backscattered wave, not shown here).

To understand the nature of the density fluctuations concentrated near $y = 0$, we plot the profiles of the density and magnetic field intensity for two cuts made along the x direction at $y = 0.5$, the first, and along the y direction at $x = 1.3$, the second. The plots are shown in Fig. 3. We see that in both plots the density fluctuations are strictly anti-correlated with the magnetic field intensity fluctuations. In the framework of MHD waves, this anti-correlation of the two quantities corresponds to slow magnetosonic waves with wavevectors nearly perpendicular to the magnetic field. Such waves, which have a group velocity essentially directed along the magnetic field (x-z direction, in our case), would be driven by pressure variations generated by the superposition of $\mathbf{Z}^+$ and $\mathbf{Z}^-$ modes. Moreover, the plot shows also that density

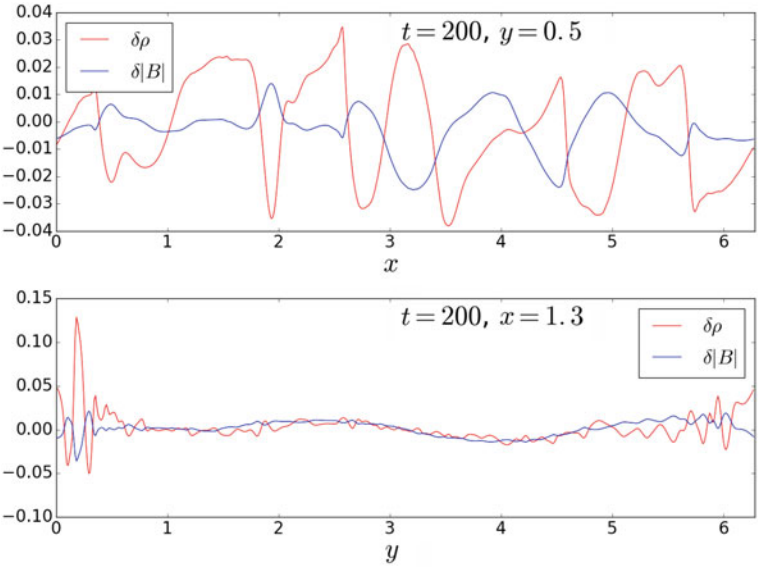

Fig. 3 Cuts of $\delta\rho$ and $\delta|\mathbf{B}|$ in the y and x directions at $t = 200$ for the $\beta = 0.5$ case

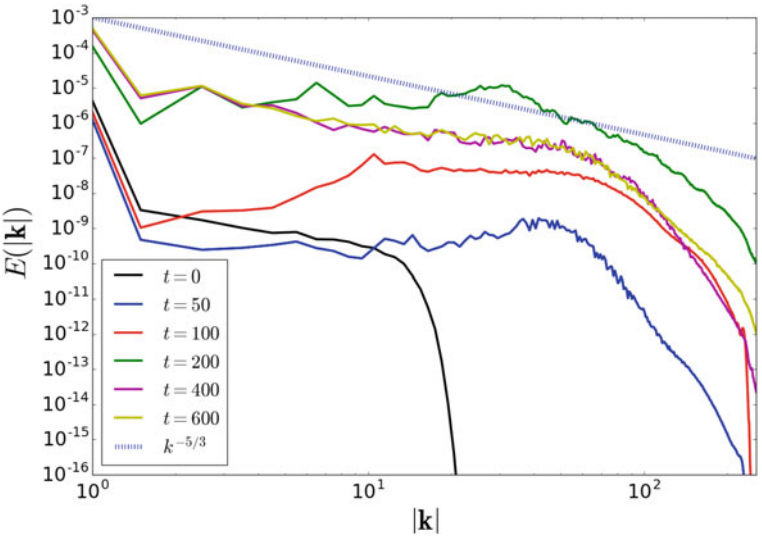

Fig. 4 Integrated spectra of density fluctuations at different times for the $\beta = 0.5$ case

fluctuations are actually present in every part of the domain, although most of their energy is focused near the $y = 0$ axis.

In Fig. 4, we plot the time evolution of the spectra of the density fluctuations, integrated in shells in the Fourier $k_x - k_y$ plane, as a function of $|k|$. At the beginning

($t = 0$) only the power-law due to the noise on the density is present. At subsequent times ($t = 50$ and $t = 100$) the nonlinear interactions start to transfer energy towards smaller and smaller scales, although the energy in the spectra seems to increase only on specific ranges of wave-numbers, probably due to the initial anisotropic behaviour of the energy transfers. At later times, in the fully nonlinear phase of the evolution, the energy is spread more isotropically in the Fourier space and the final form of the spectrum approaches more and more a power-law with spectral indices not very far from a Kolmogorov $k^{-5/3}$ law (plotted along for comparison). Of course, the spectra are quite noisy, therefore it does not make any sense to measure directly the slopes of the spectra.

3.2 *Results for* $\beta = 1.5$

We ran a simulation with the identical initial condition as in the previous case, but with a higher value for the β parameter, that is now equal to 1.5.

In Fig. 5 we show the behaviour of the quantities defined in Eq. 5 for this value of β. It is evident that the instability evolves on time scales faster than before. In particular, the growth rate of the density fluctuations (and, correspondingly, of m and e^+, as well) $\gamma \sim 0.101$ is larger for higher values of β and the instability saturates at earlier times $t \sim 100$ and on slightly larger saturation values.

By plotting the contour plots of the density fluctuations (not shown here) at the beginning of the instability ($t = 50$), at the saturation ($t = 100$), and in the fully nonlinear case ($t = 150,\ 250$), we find an analogous behaviour as in the low β case, with a prevalence of small scale fluctuations along the y direction at the beginning of the instability growth, after which the spectrum tends to become more isotropic but,

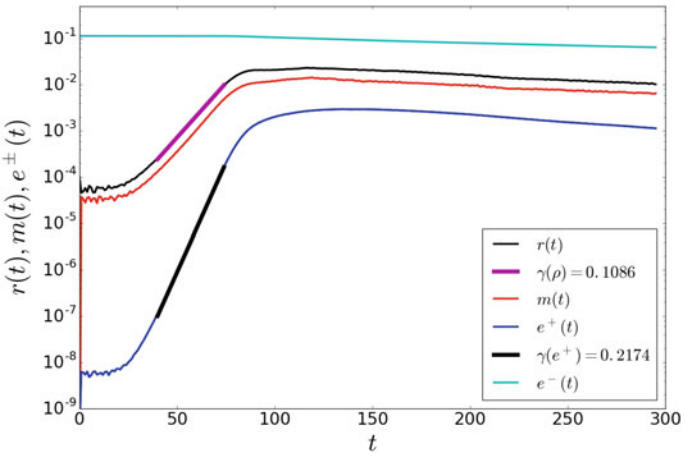

Fig. 5 Time evolution of the parameters $r(t)$, $m(t)$, $e^{\pm}(t)$ as given by Eq. 5 for the $\beta = 1.5$ case

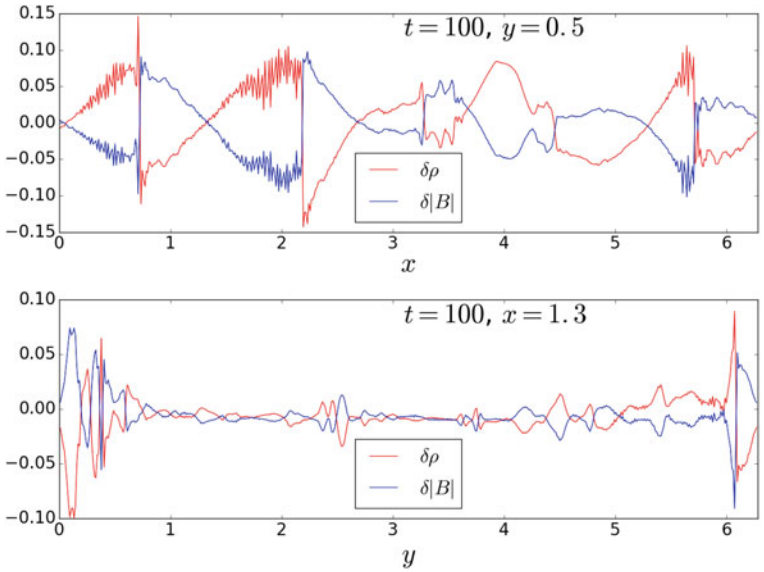

Fig. 6 Cuts of $\delta\rho$ and $\delta|\mathbf{B}|$ in the y and x directions at $t = 100$ for the $\beta = 1.5$ case

at the same time, localized structures appear close to the axis $y = 0$. At later times, in the fully non-linear case, those structures tend to spread in the whole simulation domain.

Again, in order to understand the nature of the density fluctuations, we plot some cuts along the x and y directions in proximity of the localized density structures (Fig. 6). As in the low-β case, again the fluctuations of density and magnetic field intensity are strictly anti-correlated each to the other. Moreover, it is remarkable that, in spite of the fact that density fluctuations do not reach very high values, shock fronts are clearly present, which indicate the presence of strongly local nonlinear interactions.

4 Conclusions

In this work we study the evolution of the parametric instability by starting from an initial condition which tries to mimic the situation of the actual Solar Wind. The main result of our investigation is that the instability (that can take place only in presence of compressibility) not only survives at high plasma β values, but it seems to be even more efficient than at low β-s. The fluctuations produced by the instability tend to localize in specific parts of the domain forming pressure-balanced structures with properties similar to the slow MHD waves in propagation perpendicular to the

magnetic field. The spectra of the quantities evolve towards a power-law distribution of energy, although a clear identification of the spectral slope is difficult.

References

1. Del Zanna, L., Velli, M., Londrillo, P.: Parametric decay of circularly polarized Alfvén waves: multidimensional simulations in periodic and open domains. Astron. Astrophys. **367**, 705–718 (2001)
2. Del Zanna, L., Matteini, L., Landi, S., Verdini, A., Velli, M.: Parametric decay of parallel and oblique Alfvén waves in the expanding solar wind. J. Plasma Phys. (2015). https://doi.org/10.1017/S0022377814000579
3. Frigo, M., Johnson, S.G.: The design and implementation of FFTW3. Proc. IEEE **93**, 216231 (2005)
4. Ghosh, S., Viñas, A.F., Goldstein, M.L.: Parametric instabilities of a large-amplitude circularly polarized Alfvén wave: linear growth in two-dimensional geometries. J. Geophys. Res. **98**(A9), 15561–15570 (1993)
5. Malara, F., Primavera, L., Veltri, P.: Nonlinear evolution of parametric instability of a large-amplitude nonmonochromatic Alfvén wave. Phys. Plasmas **7**, 2866–2877 (2000)
6. Malara, F., Primavera, L., Veltri, P.: Nonlinear evolution of the parametric instability: numerical predictions versus observations in the heliosphere. Nonlinear Proc. Geophys. **8**, 159–166 (2001)
7. Sagdeev, R.Z., Galeev, A.A.: Nonlinear Plasma Theory. W.A. Benjamin Inc., New York (1969)

Large-Scale Structures in a Turbulent Fluid with Solid Particles and with Gas Bubbles

Arakel Petrosyan

Abstract The properties of helical turbulence in heterogeneous media are studied. It is shown that the amplification of large-scale eddy perturbations by initially homogeneous isotropic spiral turbulence is possible in an incompressible fluid with solid particles. The motion of solid particles provides non-zero divergence on a pulsating scale and thus provides non-zero values of Reynolds stresses in averaged equations. Eddy instability of helical turbulence against large-scale perturbations in an incompressible fluid with oscillating gas bubbles is found. It is shown that bubble oscillations provide an asymmetry of the Reynolds stresses in the averaged equations and the appearance of generation terms.

1 Introduction

Recently, a lot of attention has been given to the problem of structure appearance in nonequilibrium media. Of particular interest are the large-scale eddies, arising in a turbulent fluid, coherent structures. Such structures are observed experimentally.

A. Petrosyan (✉)
Space Research Institute of the Russian Academy of Sciences, 84/32 Profsoyuznaya Str, Moscow 117997, Russia
e-mail: apetrosy@iki.rssi.ru

M. Gorokhovski and F. S. Godeferd (eds.), *Turbulent Cascades II*,
ERCOFTAC Series 26, https://doi.org/10.1007/978-3-030-12547-9_18

Coherent structures are also observed in natural conditions: Rossby eddies in the Earth and Jupiter atmospheres, tropical cyclones. In the study of the turbulence phenomenon an important role is played by the model of homogeneous isotropic and stationary turbulence. Thus, the question whether such turbulence can enhance large-scale perturbations arises. It is shown in magnetohydrodynamics that initially homogeneous isotropic and reflectional symmetrical turbulence cannot enhance large-scale magnetic fields. However, if the reflectional symmetry of turbulence is disturbed such a medium can enhance large-scale magnetic field. This phenomenon is called magnetic dynamo. The simplest example of reflectional symmetry disturbance is a velocity field where the value of the average helicity is nonzero. Such a turbulence velocity field is characterized by the fact that right-handed and left-handed eddies are observed with a different probability, i.e. there are more eddies of the one sign than the other sign.

2 Helical Turbulence with Solid Particles

Properties of helical homogeneous turbulence are also considered as a possible mechanism of large-scale vortical flows amplification [1]. In this work we study the properties of helical turbulence in an incompressible fluid filled with solid particles. Confining ourselves to cases where the solid particle sizes are many times larger than the molecular-kinetic ones and the scales of considered perturbations are such that solid particles form a continuous medium, we use the equations of two-phase hydrodynamics. In deriving the averaged equations we make substantial use of the fact that the relative volume of particles is small, which allows us to neglect the collisions of the particles with each other. The motion of a viscous incompressible fluid with solid particles is described by the following set of equations by Nigmatulin [2]:

$$\frac{\partial n}{\partial t} + \operatorname{div}(n\mathbf{V}_S) = 0 \tag{1}$$

$$\operatorname{div}(\mathbf{V}) = -\frac{4}{3}\pi a^3 \operatorname{div}(n(\mathbf{V}_S - \mathbf{V})) \tag{2}$$

$$\frac{\partial \mathbf{V}_S}{\partial t} + \beta(\mathbf{V}_S - \mathbf{V}) + (\mathbf{V}_S \cdot \nabla)\mathbf{V}_S + \frac{1}{\rho_S}\nabla P = 0 \tag{3}$$

$$\frac{\partial \mathbf{V}}{\partial t} + \gamma n(\mathbf{V}_S - \mathbf{V}) + (\mathbf{V} \cdot \nabla)\mathbf{V} + \frac{1}{\rho}\nabla P = \nu \Delta \mathbf{V} \tag{4}$$

Here $\mathbf{V}_S$ and $\mathbf{V}$ are hydrodynamic velocities of liquid and solid phase respectively, ρ_S and ρ are densities of phases, n is concentration of solid particles with radius a, ν is kinematic viscosity, P is pressure in the medium. In the model (1)–(4) solid phase particles are assumed to be identical. Coefficients

$$\gamma = \frac{4}{3}\pi a^3 \beta \frac{\rho_S}{\rho}, \quad \beta = \frac{9}{2}\frac{\nu}{a^2}\frac{\rho}{\rho_S} \tag{5}$$

describe the Stokes friction between components of each phase.

Let us represent variables in the initial system as following:

$$\begin{aligned}\mathbf{V} &= \langle \mathbf{V} \rangle + \mathbf{V}' \\ \mathbf{V}_S &= \langle \mathbf{V}_S \rangle + \mathbf{V}'_S \\ n &= \langle n \rangle + n' \\ P &= \langle P \rangle + P',\end{aligned}$$

where $\langle\rangle$ denotes the ensemble averaged turbulent pulsations and prime denotes turbulent components. Equations of mean motion

$$\frac{\partial \langle n \rangle}{\partial t} + \mathrm{div}(\langle n \rangle \langle \mathbf{V_s} \rangle) + \mathrm{div}(n' \mathbf{V}'_s) = 0 \quad (6)$$

$$\mathrm{div}(\langle \mathbf{V} \rangle) = \frac{4}{3}\pi a^3 \frac{\partial \langle n \rangle}{\partial t} + \frac{4}{3}\pi a^3 \mathrm{div}(\langle \mathbf{V} \rangle)\langle n \rangle + \frac{4}{3}\pi a^3 \mathrm{div}(\langle \mathbf{V}' n' \rangle) \quad (7)$$

$$\frac{\partial \langle \mathbf{V}_s \rangle}{\partial t} + \beta(\langle \mathbf{V}_s \rangle - \langle \mathbf{V} \rangle) + (\langle \mathbf{V}_s \rangle \cdot \nabla)\langle \mathbf{V}_s \rangle + \langle (\mathbf{V}'_s \cdot \nabla)\mathbf{V}'_s \rangle + \frac{1}{\rho_0}\nabla \langle P \rangle = 0 \quad (8)$$

$$\frac{\partial \langle \mathbf{V} \rangle}{\partial t} + \gamma \langle n \rangle (\langle \mathbf{V}_s \rangle - \langle \mathbf{V} \rangle) + \gamma \langle n' (\mathbf{V}' - \mathbf{V}'_s) \rangle + $$
$$+ (\langle \mathbf{V} \rangle \cdot \nabla)\langle \mathbf{V} \rangle + \langle (\mathbf{V}' \cdot \nabla)\mathbf{V}' \rangle + \frac{1}{\rho}\nabla \langle P \rangle = \nu \Delta \langle \mathbf{V} \rangle \quad (9)$$

contain unknown Reynolds stresses and are supplemented by corresponding equations of pulsation components:

$$\frac{\partial n'}{\partial t} + div(n' \langle \mathbf{V}_s \rangle + \langle n \rangle \mathbf{V}'_s) + div(n' \mathbf{V}'_s - \langle n' \mathbf{V}'_s \rangle) = 0 \quad (10)$$

$$div(\mathbf{V}') = \frac{4}{3}\pi a^3 \frac{\partial n'}{\partial t} + \frac{4}{3}\pi a^3 div(\mathbf{V}' n' - \langle \mathbf{V}' n' \rangle) + $$
$$+ \frac{4}{3}\pi a^3 div(\langle \mathbf{V} \rangle n' + \mathbf{V}' \langle n \rangle) \quad (11)$$

$$\frac{\partial \mathbf{V}'_s}{\partial t} + \beta(\mathbf{V}'_s - \mathbf{V}') + (\langle \mathbf{V}_s \rangle \cdot \nabla)\mathbf{V}'_s + (\mathbf{V}'_s \cdot \nabla)\langle \mathbf{V}_s \rangle + $$
$$+ \left\{ (\mathbf{V}'_s \cdot \nabla)\mathbf{V}'_s - \langle (\mathbf{V}'_s \cdot \nabla)\mathbf{V}'_s \rangle \right\} + \frac{1}{\rho_s}\nabla P' = 0 \quad (12)$$

$$\frac{\partial \mathbf{V}'}{\partial t} + \gamma \langle n \rangle (\mathbf{V}'_s - \mathbf{V}') + \gamma n' (\langle \mathbf{V}_s \rangle - \langle \mathbf{V} \rangle) + (\langle \mathbf{V} \rangle \cdot \nabla)\mathbf{V}' + (\mathbf{V}' \nabla)\langle \mathbf{V} \rangle +$$
$$+ \left\{ (\mathbf{V}' \cdot \nabla)\mathbf{V}' - \langle (\mathbf{V}' \cdot \nabla)\mathbf{V}' \rangle \right\} + \left\{ \gamma n' (\mathbf{V}' - \mathbf{V}'_s) - \gamma \langle n' (\mathbf{V}' - \mathbf{V}'_s) \rangle \right\} +$$
$$+ \frac{1}{\rho}\nabla P' = \nu \Delta \mathbf{V}' \quad (13)$$

Equations (10)–(13) are used further to obtain closed equations for mean motion.

Using the second order correlation approximation and the two-scale hypothesis, we obtain complete Reynolds set of equations in a linear approximation in average velocity:

$$\frac{\partial \langle n \rangle}{\partial t} + n_0 \mathrm{div}\,(\langle \mathbf{V}_s \rangle) = 0 \tag{14}$$

$$\mathrm{div}\,(\langle \mathbf{V} \rangle) = \frac{4}{3}\pi a^3 \frac{\partial}{\partial t}\langle n \rangle \tag{15}$$

$$\frac{\partial \langle \mathbf{V}_s \rangle}{\partial t} + \beta\,(\langle \mathbf{V}_s \rangle - \langle \mathbf{V} \rangle) + \frac{1}{\rho_s}\nabla \langle P \rangle = 0 \tag{16}$$

$$\frac{\partial \langle \mathbf{V} \rangle}{\partial t} - \gamma n_0 (\langle \mathbf{V} \rangle - \langle \mathbf{V}_s \rangle) + \alpha \mathrm{rot}\,(\langle \mathbf{V} \rangle) + \frac{1}{\rho}\nabla P = \nu \Delta \langle \mathbf{V} \rangle \tag{17}$$

We have obtained a system of equations describing the average perturbations of helical turbulence. These equations contain terms that can lead to instability. It is easy to see that for potential motions these new terms disappear from the equations and thus the potential motion decays.

Being interested in the evolution of vortex perturbations, we pass from (14)–(17) to the corresponding equations for vorticity $\boldsymbol{\Omega} = \mathrm{rot}\,(\langle \mathbf{V} \rangle)$, $\boldsymbol{\Omega}_S = \mathrm{rot}\,(\langle \mathbf{V}_S \rangle)$

$$\frac{\partial \boldsymbol{\Omega}_s}{\partial t} + \beta\,(\boldsymbol{\Omega}_s - \boldsymbol{\Omega}) = 0 \tag{18}$$

$$\frac{\partial \boldsymbol{\Omega}}{\partial t} + \gamma n_0\,(\boldsymbol{\Omega}_s - \boldsymbol{\Omega}) + \alpha \mathrm{rot}\,(\langle \mathbf{V} \rangle) = \nu \Delta \boldsymbol{\Omega} \tag{19}$$

The obtained equations contain a term that describes the generation of vortices as a result of instability. The dispersion equation for small perturbations

$$-\frac{1}{\beta}(-\mathrm{i}\omega)^2 - \omega\left(\frac{\gamma n_0 + \nu k^2 \pm \alpha k}{\beta}\right) + \left(\nu k^2 \pm \alpha k\right) = 0 \tag{20}$$

has a solution describing an instability with the following increment:

$$-\mathrm{i}\omega = -\frac{1}{2}\left(\gamma n_0 + \nu k^2 - \alpha k + \beta\right) \pm \sqrt{\left(\gamma n_0 + \nu k^2 - \alpha k + \beta\right)^2 - 4\beta\left(\nu k^2 - \alpha k\right)} \tag{21}$$

Let us consider a limit of single-phase medium in (20). To do this we set the particle radius to zero. Therefore, coefficients α, γ and $\frac{1}{\beta}$ also approach zero. In this limit we get

$$-\mathrm{i}\omega = -\nu k^2 \tag{22}$$

which corresponds to perturbations decay in incompressible viscous fluid.

It is shown that in complete set of equations a generation term arises due to nonzero divergence as a result of fluid flow around the solid particles. In essence, such a two-phase medium acts like compressible one. The analysis shows that helical

turbulence in an incompressible fluid with solid particles is unstable with respect to vortex perturbations.

3 Helical Turbulence with Gas Bubbles

A similar eddy structures generation mechanism is investigated for the case of a liquid with distributed gas bubbles. We study the physical processes in a fluid with distributed bubbles. We neglect the collapse of the bubbles, assuming a constant number of bubbles in the fluid that perform radial oscillations is maintained. To study the turbulent motions in such a mixture, we use the following system of hydrodynamic equations for a mixture of fluid with bubbles:

$$\frac{\partial \rho}{\partial t} + \frac{\partial}{\partial x_i}(\rho V_i) = 0 \tag{23}$$

$$\frac{\partial}{\partial t} V_i + (V_k \nabla_k) V_i = -\frac{\nabla p}{\rho} + \frac{\nu}{\rho} \Delta^2 V_i \tag{24}$$

complemented with Rayleigh equation for a solitary bubble:

$$R\ddot{R} + \frac{3}{2}\dot{R}^2 = \frac{1}{\rho_0}(p_r - p) \tag{25}$$

In Eqs. (23)–(25) ρ is gas-liquid mixture density, p , V_i are fluid pressure and velocity, R is bubble radius, ρ_0 is fluid density, p_r is gas pressure in a bubble.

Equation (25) is equivalent to the following equation for bubble volume $U = \frac{4}{3}\pi R^3$

$$\alpha U^{-\frac{1}{3}} \ddot{U} - \frac{\alpha}{6} U^{-\frac{4}{3}} \dot{U}^2 + \frac{3}{2}\dot{R}^2 = p_r - p \tag{26}$$

where $\alpha = \rho_0 / 3^{\frac{1}{3}} (4\pi)^{\frac{2}{3}}$.

For our purposes it is more convenient to consider the deviation of pressure from the equilibrium value and corresponding deviations of small bubble pulsations:

$$p = p_0 + p^1, \quad U = U_0 + U^1$$

Under the condition $\frac{p^1}{p_0} < 1$, $\frac{U^1}{U_0} < 1$ of adiabatic equation of state for a bubble

$$p_r = p_0 \left(\frac{V_0}{V}\right)^{\gamma}$$

we will further use an equation for bubble oscillations, obtained by Zabolotskaya [3] (primes omitted)

$$\ddot{U} + w_0^2 U - \alpha U^2 - \beta\left(2\ddot{U}U + \dot{U}^2\right) + \mu U^2 + \nu\left(\ddot{U}U^2 + \dot{U}^2 U\right) = -\varepsilon p \tag{27}$$

$$w_0 = \frac{3\gamma p_0}{\rho_0 R_0^2}, \quad \varepsilon = \frac{4\pi R_0}{\rho_0}, \quad f = \frac{w_0}{Q}, \quad \alpha = \frac{(\gamma+1)\, w_0^2}{2U_0},$$

$$\beta = \frac{1}{6}U_0, \quad \nu = \frac{2}{9U_0^2}, \quad \mu = \frac{(\gamma+2)\,(\gamma+1)\, w_0^2}{6U_0^2}$$

To close the set of Eqs. (23)–(25) we use an expression for mixture density

$$\rho = \frac{\rho_0}{1 - \chi p + nU}, \tag{28}$$

where n is bubble concentration and $\chi = -\frac{1}{U}\frac{\partial U}{\partial p}$ characterizes compressibility from changes in bubbles volume.

Let us simplify the set of Eqs. (23)–(28) further. We consider sufficiently slow motions that are not resonant with bubble oscillations therefore, to simplify further calculations, we neglect the nonlinear terms in the bubble oscillation equation and assume that the determining nonlinearity is the hydrodynamic nonlinearity. This essentially means neglecting sound motions in the main phase of the fluid, that is, neglecting the intrinsic compressibility of fluid. We also neglect nonlinearity in Eq. (28), describing the gas-liquid mixture density, which imposes restrictions on bubble concentration.

Thus in subsequent analysis of perturbations evolution in a turbulent medium we use the following set of equations:

$$\rho = \rho_0\,(1 - nU + \chi p) \tag{29}$$

$$\frac{\partial \rho}{\partial t} + \frac{\partial}{\partial x_i}\left(\rho_0 V_i\right) = 0 \tag{30}$$

$$\frac{\partial}{\partial t} V_i + \left(V_k \nabla_k\right) V_i = -\frac{\nabla p}{\rho_0} + \frac{\nu}{\rho_0}\Delta V_i \tag{31}$$

$$\ddot{U} + w_0^2 U = -\varepsilon p \tag{32}$$

The simplified equations of a gas-liquid medium written in the form (29)–(32) is especially interesting for our study, since it is possible to consider a random vortex velocity field with as a basic unperturbed state.

Let us employ Eqs. (29)–(32) to study the perturbations evolution against a small-scale turbulence background. In order to do this, we represent the problem variables in the following form:

$$V_i = \bar{V}_i + V_i' \tag{33}$$

$$\rho_i = \bar{\rho}_i + \rho_i' \tag{34}$$

$$p_i = \bar{p}_i + p_i' \tag{35}$$

$$U_i = \bar{U}_i + U_i' \tag{36}$$

where overline denotes Reynolds averaging and primed variables denote pulsing components with zero mean. Substituting (33)–(36) in (29)–(32) and taking an average the following set of equations describing mean motions is obtained:

$$\bar{\rho} = \rho_0 \left(1 - n\bar{U} + \chi \bar{p}\right) \tag{37}$$

$$\frac{\partial \bar{\rho}}{\partial t} + \frac{\partial}{\partial x_i}\left(\rho_0 \bar{V}_i\right) = 0 \tag{38}$$

$$\frac{\partial}{\partial t}\bar{V}_i + \overline{\left(V_k' \nabla_k\right) V_i'} = -\frac{\nabla p}{\rho_0} + \frac{\nu}{\rho_0}\Delta \bar{V}_i \tag{39}$$

$$\ddot{\bar{U}} + w_0^2 \bar{U} = -\varepsilon \bar{p} \tag{40}$$

Subtracting (37)–(40) from Eqs. (29)–(32), averaging and employing (33)–(36) we get the following set of equations, describing pulsation components:

$$\rho' = \rho_0 \left(1 - nU' + \chi p'\right) \tag{41}$$

$$\frac{\partial \rho'}{\partial t} + \frac{\partial}{\partial x_i}\left(\rho_0 V_i'\right) = 0 \tag{42}$$

$$\begin{aligned} &\frac{\partial}{\partial t}\bar{V}_i + \left(V_k' \nabla_k\right) V_i' - \overline{\left(V_k' \nabla_k\right) V_i'} + \\ &+ \left(V_k' \nabla_k\right) \bar{V}_i' + \left(\bar{V}_k' \nabla_k\right) V_i' = -\frac{\nabla p'}{\rho_0} + \frac{\nu}{\rho_0}\Delta V' \end{aligned} \tag{43}$$

$$\ddot{U}' + w_0^2 U' = -\varepsilon p' \tag{44}$$

We study the mean perturbations evolution against a small-scale helical turbulence. To do this let us represent problem variables in the following form: $V_i' = V_i^t + V_i^1$, $p' = p^t + p^1$, $\rho' = \rho^t + \rho^1$, $U' = U^t + U^1$. Using the second-order correlation approximation and the two-scale hypothesis, we obtain an equation system that describes the evolution of mean motions against a background of small-scale helical turbulence in a fluid with pulsating gas bubbles in a linear approximation:

$$\frac{\partial \bar{V}_i}{\partial t} = \alpha \left(\mathrm{rot}\bar{\mathbf{V}}\right)_i - \frac{\nabla_i \bar{p}}{\rho_0} + \frac{\nu}{\rho_0}\Delta \bar{V}_i \tag{45}$$

$$\frac{\partial \rho}{\partial t} + \frac{\partial}{\partial x_i}\left(\bar{V}_i \rho_0\right) = 0 \tag{46}$$

$$\bar{\rho} = \rho_0 \left(1 - n\bar{U} + \chi \bar{p}\right) \tag{47}$$

$$\frac{d^2 \bar{U}}{dt^2} + w_0^2 \bar{U} = -\varepsilon \bar{p} \tag{48}$$

Note that a new term vanishes for potential perturbations, therefore potential motion decays in such system. For vortical motions, the vorticity equation separates from (45)–(48) and becomes

$$\frac{\partial}{\partial t}\bar{\Omega} + \alpha \mathrm{rot}\bar{\Omega} = \nu' \Delta \Omega \tag{49}$$

where ν' is summed kinematic and turbulent viscosity.

Equation (49) is known in α^2-dynamo theory of magnetic field. We note that in the absence of bubbles the coefficient α vanishes, which corresponds to the damping of the eddy perturbations in incompressible fluid. We also note that in the absence of helicity in the correlator of small scale velocity field, large scale structures also damp.

Let us seek a solution of (49) in the form $\boldsymbol{\Omega} = \boldsymbol{\Omega}_k \mathrm{e}^{\mathrm{i}wt - \mathrm{i}\mathbf{Kr}}$. In the usual way we get the dispersion relation

$$\left(w - \mathrm{i}\nu' K^2\right)^2 = -\alpha^2 K^2 \tag{50}$$

and instability increment

$$\gamma = \mathrm{i}w, \quad \gamma = -\nu' K^2 + \alpha K \tag{51}$$

reaches the maximum

$$\gamma_m = \frac{\alpha^2}{4\nu'}, \quad K_m = \frac{|\alpha|}{2\nu'} \tag{52}$$

The characteristic size of the forming structure is K_m.

4 Conclusion

The properties of helical turbulence in heterogeneous media are studied. It is shown that the amplification of large-scale eddy perturbations by initially homogeneous isotropic spiral turbulence is possible in an incompressible fluid with solid particles. The motion of solid particles provides non-zero divergence on a pulsating scale and thus provides non-zero values of Reynolds stresses in averaged equations. Eddy instability of helical turbulence against large-scale perturbations in an incompressible fluid with oscillating gas bubbles is found. It is shown that bubble oscillations provide an asymmetry of the Reynolds stresses in the averaged equations and the appearance of generation terms. Note that that the resulting structures have a helical nature, i.e. $\langle \mathbf{V} \cdot \mathrm{rot}\mathbf{V} \rangle \neq 0$.

References

1. Branover, H., Moiseev, S., Golbraikh, E., Eidelman, A.: Turbulence and Structures: Chaos, Fluctuations, and Helical Self-Organization in Nature and Laboratory, 1st edn. Academic Press, San Diego (1999)
2. Nigmatulin, R.I.: Dynamics of Multiphase Media, vol. 1, 1st edn. CRC Press, Boca Raton (1990)
3. Zabolotskaya, E.A.: Nonlinear waves in fluid with gas bubbles. Trans. Prokhorov Gen. Phys. Inst. Russ. Acad. Sci. **18**, 121–155 (1989)

Cloud Turbulence and Droplets

Izumi Saito, Toshiyuki Gotoh and Takeshi Watanabe



Abstract Evolution of droplets and turbulence in a small box which is ascending inside the maritime cumulus cloud has seamlessly been simulated for about 10 min from the view point of the microscopic dynamics. It is found that the kinetic energy spectrum obeys the Kolmogorov spectrum $k^{-5/3}$ at low to moderate wavenumbers, while the spectra of the temperature and the water vapor mixing ratio are modified, close to $k^{-1/3}$ at low wavenumbers and roll off more slowly than the exponential in the diffusive range. This modification of the spectra arises from the condensation-evaporation and the liquid water mass loading to the flow. It is also found that the spectra related to the cloud droplets consist of two contributions, one is from the spatially correlated part and the other is from the uncorrelated part which originates from the discreteness of droplets. The former dominates the spectrum at low to moderate wavenumbers and the latter at high wavenumbers. We argue the effects of the two contributions on the turbulence spectra.

I. Saito · T. Gotoh (✉) · T. Watanabe
Nagoya Institute of Technology, Gokiso, Nagoya 466-8555, Japan
e-mail: gotoh.toshiyuki@nitech.ac.jp

I. Saito
e-mail: izumi@gfd-dennou.org

T. Watanabe
e-mail: watanabe@nitech.ac.jp

M. Gorokhovski and F. S. Godeferd (eds.), *Turbulent Cascades II*,
ERCOFTAC Series 26, https://doi.org/10.1007/978-3-030-12547-9_19

1 Introduction

Turbulence and clouds are most uncertain factors in weather forecasting and prediction of the future climate. In most numerical simulations of the atmosphere, the clouds are treated as continuum accompanied with models for the microphysical processes like nucleation, condensation growth and collision-coalescence which occur at scales much smaller than the computational grid size. Turbulence is also simulated by Large Eddy Simulation (LES) in which the fluid motion below the grid scale is represented by the subgrid scale model. Although there have been many efforts to improve the models, still the accurate prediction of the atmospheric motion is difficult because of limited knowledge of the cloud microphysical processes and because the turbulence is not well understood [5, 12, 18]. Recent progress in the high performance computers allows us to directly simulate dynamics of cloud droplets convected by turbulent flow from the view point of first principle, an approach to numerically follow the evolution of all the degrees of freedom as faithfully to their fundamental physics as possible. There have been many studies in this direction of research [2, 11, 16, 17]. Central issues are the growth of cloud droplets, droplet spectrum (size distribution), and various effects such as turbulence and hydrodynamic interaction on the droplet collision rate [1, 3, 4, 8, 9, 13, 14]. But less attention has been paid on the effects of the cloud droplets on the turbulence and/or their interaction with the turbulent flow. Recently we have seamlessly simulated the evolution of the cloud droplets from about 10 to 500 micron meters over 10 min which required about 2.4 million time steps [10]. The long time simulation have found the modification of the spectra of the turbulence, the temperature and the water vapor mixing ratio. This modification arises from the interaction between the cloud droplets and the turbulent field. Droplets in the present study are smaller than the Kolmogorov scale but they affect the evolution of the turbulent flow though the water mass loading ratio, water vapor and temperature through the condensation process at all scales. In this paper we examine the effects of the droplets on the turbulent spectra.

2 Fundamental Equations

Since the system under consideration is the same as that used in Ref. [10], we describe the essential parts necessary for the arguments. We consider a small air parcel ascending inside the core region of maritime cumulus cloud. The parcel is a cubic box with lengths of L_{box} per side, and is assumed to be much smaller than the size of the entire cloud so that statistical properties of fluctuating quantities inside the box can be regarded as homogeneous and periodic boundary conditions in three directions are imposed on the flow field. The updraft velocity of the parcel is self-consistently determined by the mean buoyancy force inside the parcel, and a local coordinate moving in tandem with the box is introduced. The fluid inside the box is assumed to be incompressible under the Boussinesq approximation. The temperature

T and the water vapor mixing ratio Q_v are expressed as the sum of the mean and fluctuation as $T = \overline{T} + \theta, \quad Q_\mathrm{v} = \overline{Q}_\mathrm{v} + q$ respectively, where the over bar denotes the volume overage over the box. The fluctuating turbulent velocity $\boldsymbol{u} = (u_1, u_2, u_3)$, temperature θ, and water vapor mixing ratio q are assumed to obey

$$\frac{\partial \boldsymbol{u}}{\partial t} + \boldsymbol{u} \cdot \nabla \boldsymbol{u} = -\frac{1}{\rho_\mathrm{a}} \nabla p + \nu_a \nabla^2 \boldsymbol{u} + (B - \overline{B}) \boldsymbol{e}_3 + \boldsymbol{f}, \quad \nabla \cdot \boldsymbol{u} = 0, \tag{1}$$

$$\frac{\partial \theta}{\partial t} + \boldsymbol{u} \cdot \nabla \theta = \kappa_T \nabla^2 \theta + \frac{L_\mathrm{v}}{c_\mathrm{p}} \left(C_\mathrm{d} - \overline{C}_\mathrm{d} \right) - \Gamma(t) u_3, \tag{2}$$

$$\frac{\partial q}{\partial t} + \boldsymbol{u} \cdot \nabla q = \kappa_\mathrm{v} \nabla^2 q - \left(C_\mathrm{d} - \overline{C}_\mathrm{d} \right), \tag{3}$$

in the local coordinate system of the box, respectively, where p is the pressure, and $\boldsymbol{f}$ is the external force applied at low wavenumbers $k L_\mathrm{box} \leq 4$. The kinematic viscosity of dry air ν_a, as well as the diffusivity of temperature and water vapor κ_T and κ_v, are the same as those in [10]. The buoyancy force B is given by

$$B(\boldsymbol{x}, t) = g \left\{ \frac{T(\boldsymbol{x}, t) - T_\mathrm{e}(\overline{H}(t))}{T_\mathrm{e}(\overline{H}(t))} + \alpha \left[Q_\mathrm{v}(\boldsymbol{x}, t) - Q_\mathrm{ve}(\overline{H}(t)) \right] - q_\mathrm{l}(\boldsymbol{x}, t) \right\}, \tag{4}$$

where q_l is the liquid water mixing ratio, $\alpha = R_\mathrm{d}/R_\mathrm{v} = 0.61$, and R_d and R_v are the gas constants for dry air and water vapor, respectively. T_e and Q_{ve} are the mean temperature and water vapor mixing ratio as function of altitude which are taken from the observation data at Hawaii [15]. The term with $\Gamma(t)$ in (2) denotes the cooling effect imposed by the ascending motion.

Droplets affect the evolution of fluid through the term C_d in (2) and (3) (representing latent heat release and mass exchange through condensation, respectively), and the term q_l in (4) (representing drag force due to the weight of the condensed water). These terms are assumed to be given by

$$C_\mathrm{d}(\boldsymbol{x}, t) = \frac{4\pi \rho_\mathrm{l} K_\mathrm{s}}{\rho_\mathrm{a} (\Delta x)^3} \sum_{j=1}^{N_\Delta} R_j(t) S\left(\boldsymbol{X}_j(t), t \right), \tag{5}$$

$$q_\mathrm{l}(\boldsymbol{x}, t) = \frac{4\pi \rho_\mathrm{l}}{3\rho_\mathrm{a} (\Delta x)^3} \sum_{j=1}^{N_\Delta} R_j(t)^3, \tag{6}$$

respectively, where $R_j(t)$ and $\boldsymbol{X}_j(t)$ are the radius and the position for the jth droplet, respectively, $N_\Delta(\boldsymbol{x}, t)$ is the number of droplets in the grid cell $(\Delta x)^3$, S is the supersaturation, and K_s is a temperature-dependent diffusion coefficient that is assumed to be constant because its dependence on temperature is very weak [4]. The droplet undergoes the Reynolds number dependent drag and the gravity force with modification due to the time dependent Galilean transformation, and its radius evolves

Table 1 Numerical and mean turbulence parameters. R_λ is the Taylor microscale Reynolds number, E is the kinetic energy, ε is the mean energy dissipation rate per unit mass, $\mathcal{L}$ is the integral scale, λ is the Taylor microscale, η is the Kolmogorov length, $k_{\max}\eta$ is the cut off wavenumber normalized by the Kolmogorov length, Δt is the time increment

Run No.	R_λ	E ($\mathrm{cm^2 s^{-2}}$)	ε ($\mathrm{cm^2 s^{-3}}$)	$\mathcal{L}$ (cm)	λ (cm)	η (mm)	$k_{\max}\eta$	Δt (ms)	CPU time hours
Run 1	59	11.2	1.75	3.30	2.18	1.06	6.31	0.5	50
Run 2	104	80.6	26.8	8.25	2.13	1.06	3.08	0.5	50
Run 3	131	197	101	8.16	1.72	0.763	2.21	0.4	63
Run 4	167	501	400	8.13	1.38	0.541	1.57	0.25	100

according to the supersaturation. Also the droplets collide and coalesce according to the Hall table which describes the hydrodynamic interaction between droplets [6].

The equations of turbulent flow are computed by using the pseudo spectral method and the time integration is made by the second order Runge Kutta method. The fluid velocity, the temperature and the water vapor mixing ratio at the droplet position are computed by the linear interpolation and the condensation rate and the liquid water mixing ratio are redistributed on the grid by the particle in cell (PIC) method with the same weight as the linear interpolation. The four Runs were made. Typical parameters are the box size is $L_{\mathrm{box}} = 51.2\,(\mathrm{cm})$, the numbers of the grid points and the droplets at the initial time are $N = 512^3$ and $N_p = 16$ millions, respectively. The code is written by using MPI and OpenMP and the typical number of the computational nodes is 1024 (8192 cores). The computation was made on K at RIKEN, FX100 at Nagoya University, and FX100 at National Institute for Fusion Science at Toki site. For the details of the computation, refer to [10] (Table 1).

3 Results

The spectra of the kinetic energy and the water vapor mixing ratio are shown in Fig. 1 [10]. The kinetic energy spectrum evolves quickly and has already attained a steady state at 10 s, where it remains unchanged except in the far dissipation range. The spectral slope at low wavenumbers ($2 \le kL_{\mathrm{box}} \le 20$) is close to $-5/3$, which matches the Kolmogorov spectrum in the inertial range and is consistent with a previous turbulence DNS. However, the spectral tail in the far dissipation range gradually increases at latter times. The spectrum of the water vapor mixing ratio evolves into the usual spectral form like $k^{-5/3}$ at low wavenumbers and exponential in the far diffusive range by 10 s, but develops in a different way for the latter period of evolution. The increase of amplitudes begins at high wavenumbers and gradually propagates toward low wavenumber band, and ceases to grow at the end of computation. The propagation of the excitation in the negative direction in the wavenumber space is opposed to the idea of forward cascade in Kolmogorov–Obukhov–Corrsin's theory. The slope of the

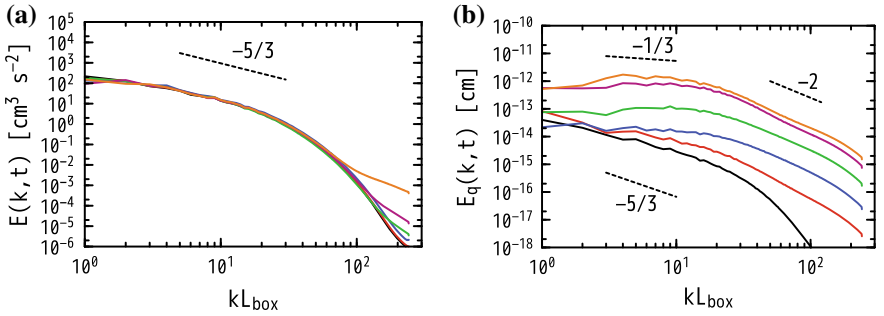

Fig. 1 Time evolution of turbulence spectra for Run 2. **a**: $E(k,t)$, **b**: $E_q(k,t)$. $t = 10$ s (black), 120 s (red), 240 s (blue), 360 s (green), 480 s (magenta), 600 s (orange). Dashed lines show the slope $-5/3$, $-1/3$ and -2

curve $E_q(k,t)$ for $3 < kL_{\rm box} < 10$ is close to $-1/3$ and -2 for $40 < kL_{\rm box} < 100$, at 600 s, respectively.

In order to explore the physical explanation of the spectral modification, we first consider the correlation function of the droplet number density n [10]. The two point correlation function with separation $\boldsymbol{r}$ is given by

$$\langle \tilde{n}(\boldsymbol{x}+\boldsymbol{r},t)\tilde{n}(\boldsymbol{x},t)\rangle = \langle n(\boldsymbol{x}+\boldsymbol{r},t)n(\boldsymbol{x},t)\rangle - \overline{n}^2 = \overline{n}^2(t)w(\boldsymbol{r}) + \overline{n}(t)\delta(\boldsymbol{r}), \quad (7)$$

where $\tilde{n} = n - \overline{n}$, the first term on the right-hand side is related to the probability of finding a droplet within a small volume $\mathrm{d}V$ at $\boldsymbol{r}$ conditioned on one droplet within $\mathrm{d}V$ at the origin, and the second term is related to the probability that two droplets will reside within the same volume [7]. The first term (*correlated term*) describes the spatial coherency of two droplets at nonzero separation, and $w(\boldsymbol{r}) \to 0$ as $r \to \infty$, and is related to the radial distribution function $w(\boldsymbol{r}) = g(r) - 1$ for isotropic case. The second term arises from the discreteness of the droplets and corresponds to spatially uncorrelated distribution. The spectrum of the number density which is defined by $\langle \tilde{n}^2 \rangle = \int E_n(k)dk$ is given by the sum of two terms as

$$E_n(k,t) = E_n^{\rm c}(k,t) + E_n^{\rm uc}(k,t), \qquad E_n^{\rm uc}(k,t) = 4\pi\overline{n}(t)k^2/(2\pi)^3. \quad (8)$$

The second term $E_n^{\rm uc}(k,t)$ is the equipartition spectrum. This equipartition spectrum is numerically filtered near the wavenumber cut off at $k_{\rm max}$. For example, the condensation rate computed at the droplet position is distributed on the surrounding grid points with the linear weight in the PIC method, so that the droplet position spatial accuracy is lost for scales smaller than the grid spacing $\Delta x = 2\pi/(K_{\rm max}L_{\rm box})$. Figure 2a shows $4\pi k^2/L_{\rm box}^3$ (black) and the ensemble-average of $E_n(k,0)/\overline{n}(0)$ (cyan) computed from the continuum number density after distributing the droplets on the grid points using the PIC method, where ensembles are calculated by changing the random droplet positions. The ratio of the black to cyan curve provides the filter

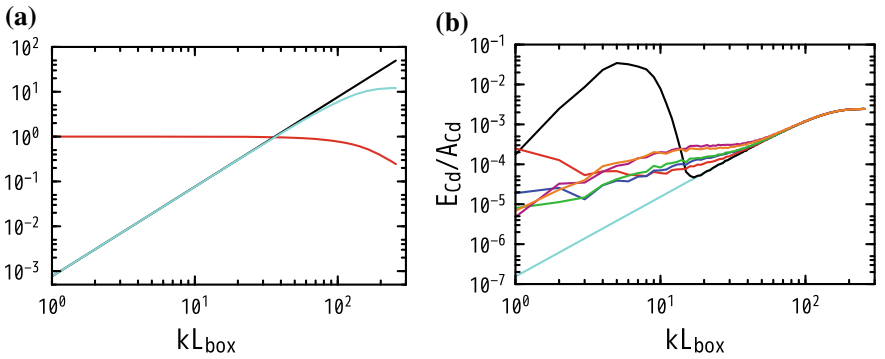

Fig. 2 Spectra related to the droplets and the filter function. **a**: $4\pi k^2/L_{\rm box}^3$ (black), the ensemble average of $E_n(k,0)/\overline{n}(t)$ (cyan), and $F_{\rm filter}(k)$ (red), which is the ratio of the cyan to black curve. **b**: Normalized spectrum $E_{C_d}(k,t)/A_{C_d}(t)$

function $F_{\rm filter}(k)$ due to the PIC method. $F_{\rm filter}(k)$ is close to unity for $kL_{\rm box} < 70$ and decreases for high wavenumbers $kL_{\rm box} > 100$. This filter applies to all spectra related to the droplets, $E_{C_d}(k,t)$ and $E_{q_l}(k,t)$.

Similarly, the spectrum of the fluctuating condensation term which is defined by $\left\langle \tilde{C}_d^2 \right\rangle = \int E_{C_d}(k)dk$ and $\tilde{C} = C_d - \overline{C_d}$ also has two contributions $E_{C_d}(k,t) = E_{C_d}^{\rm c}(k,t) + E_{C_d}^{\rm uc}(k,t)$ and the second term is also of the form of k^2. Figure 2b shows the time evolution of the normalized spectrum $E_{C_d}(k,t)/A_{C_d}(t)$, where $A_{C_{\rm d}}(t) = \left(4\pi\rho_{\rm l}K_{\rm s} \,/\, \rho_{\rm a}\right)^2 \times \overline{n}(t)\left\langle \left[R_j(t)S\left(\boldsymbol{X}_j(t),t\right)\right]^2 \right\rangle$ [10]. Initially the spectrum is of the form of the initial condition like $E_{D_d}(k,0) \propto k^4 \exp(-2(k/k_0)^2)$ for low k and k^2 for high k. The spectrum evolves to be like k for $3 < kL_{\rm box} < 10$, k^2 for $30 < kL_{\rm box} < 100$ and k^0 near the wavenumber cut off.

With this knowledge of the condensation spectrum, we proceed to analyze the spectrum of the water vapor mixing ratio. The equation for $E_q(k,t)$ is given by

$$\frac{\partial E_q(k,t)}{\partial t} + 2\kappa_{\rm v}k^2 E_q(k,t) = T_q(k,t) + F_q(k,t), \tag{9}$$

$$F_q(k,t) = -\sum_{k<|\boldsymbol{k}|<k+\Delta k}\left[\left\langle \tilde{C}_{\rm d}(\boldsymbol{k},t)q(-\boldsymbol{k},t)\right\rangle + \left\langle q(\boldsymbol{k},t)\tilde{C}_{\rm d}(-\boldsymbol{k},t)\right\rangle\right], \tag{10}$$

where $T_q(k,t)$ represents the scalar variance transfer function due to the convective term. The function $F_q(k,t)$ provides the input rate by the condensation and is estimated as $F_q(k,t) = 4\pi k^2 \int^t \left\langle G^L(k,t,s)C_d(\boldsymbol{k},s)C_d(-\boldsymbol{k},t)\right\rangle ds \approx \tau_q(k)E_{C_d}(k,t)$ on the dimensional ground where $G^L(k,t,s)$ is the response function of the water vapor mixing ratio and $\tau_q(k)$ is the characteristic time of the response function at the wavenumber k. Then the time integration of (9) yields

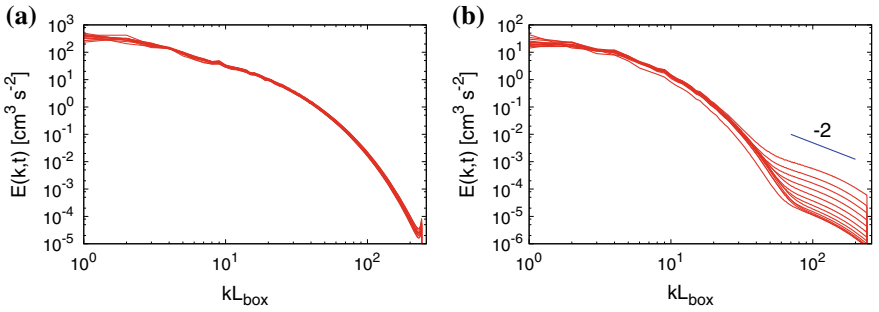

Fig. 3 Time evolution of the kinetic energy spectrum. **a**: $E(k,t)$ without q_l term for $R_\lambda = 101$, $\varepsilon = 26.8\,(\mathrm{cm}^2\mathrm{s}^{-3})$. **b**: $E(k,t)$ with q_l term for $R_\lambda = 59$, $\varepsilon = 1.75\,(\mathrm{cm}^2\mathrm{s}^{-3})$ (Run 1). Curves are plotted at $t = 10 + 50\,\mathrm{ns}$, $n = 0, 1, \cdots 10$

$$E_q(k,t) \approx [\tau_q(k)]^2 E_{C_d}(k,t) \tag{11}$$

again by the dimensional argument. The spectral slope of $E_q(k)$ in Fig. 1b is argued as follows. For $5 < kL_{\mathrm{box}} < 20$, we observe $E(k,t) \propto k^{-5/3}$ in Fig. 1a meaning that $\tau_q(k) \propto \varepsilon^{-1/3}k^{-2/3}$, so that we obtain $E_q(k) \propto k^{-1/3}$ which is close to the slope of $E_q(k,t)$ curve at the final time. For $50 < kL_{\mathrm{box}} < 150$, we observe that $E(k,t)$ rolls off exponentially in Fig. 1a and $Sc = 0.72$ we substitute $\tau_q(k) \approx (\kappa_v k^2)^{-1}$ and $E_{C_d}(k,t) \approx k^2$ into (11) to obtain $E_q(k) \propto k^{-2}$ which is close to the $E_q(k,t)$ curve. For $150 < kL_{\mathrm{box}}$, since $E_{C_d}(k,t) \approx k^0$ due to the filtering effect, we predict $E_q(k,t) \approx k^{-4}$ which is consistent with the faster decay of $E_q(k,t)$ observed near the wavenumber cut off.

The above consideration implies that the spectral modification by the droplets is determined by the relative amplitudes of the correlated and uncorrelated spectra. In order to see this point, we consider the contributions due to the q_l term of the buoyancy term. For this purpose, we computed two cases. The first computation is to do the same simulation without q_l term and the second one is to simulate with q_l term but with lower turbulent intensity at $R_\lambda = 59$ and $\varepsilon = 1.75\,(\mathrm{cm}^2\mathrm{s}^{-3})$ (Run 1). Figure 3a shows the time evolution of $E(k,t)$ without q_l term. There is no rise of the spectrum in the far dissipation range, as expected, meaning that the rise of the kinetic energy spectrum tail is due to the contributions of the droplets. On the other hand, when the turbulent intensity is weak, it is seen from Fig. 3b that the effects of q_l term becomes stronger, the length and the excitation level of the spectral tail in the dissipation range increases in time and the slope of the curve is close to -2. This slope can be explained in the same way as in the case of the water vapor mixing ratio.

4 Summary

We have successfully simulated the evolution of the cloud droplets and turbulence in the cumulus cloud. The long time simulation reveals the modification of the turbulent spectra due to the cloud droplets. The condensation process is responsible for the modification of the scalar variance spectra of the temperature and water vapor mixing ratio at all wavenumbers. It is found that the spectra related to the cloud droplets consists of two contributions, the spatially correlated part and the uncorrelated part. The latter spectrum is of the form of the low pass filtered equipartition. It is not unclear to what extent these scalar, especially, the spectrum of the water vapor mixing ratio is modified at very large Reynolds numbers. The further studies at larger Reynolds number are certainly necessary.

Acknowledgements This research used the computational resources of the K computer provided by the RIKEN Advanced Institute for Computational Science, through the High Performance Computing Infrastructure (HPCI) System Research Project (hp160085, hp170189). The computational supports provided by Japan High Performance Computing and Networking, Large-scale Data Analyzing and Information Systems (JHPCN) (jh160012, jh170013), by High Performance Computing (HPC 2016) at Nagoya University and by "Plasma Simulator" under the auspices of the NIFS Collaboration Research program (NIFS16KNSS076) are also gratefully acknowledged. Development of some numerical codes used in this work was supported in part by the "Code development support program" of Numerical Simulation Reactor research Project (NSRP), NIFS. I. S. and T. G. and T. W. are supported by Grants-in-Aid for Scientific Research Nos. 15H02218, 26420106, respectively, from the Ministry of Education, Culture, Sports, Science, and Technology (MEXT) of Japan.

References

1. Ayala, O., Rosa, B., Wang, L.-P., Grabowski, W.W.: Effects of turbulence on the geometric collision rate of sedimenting droplets: Part 1. Results from direct numerical simulation. New J. Phys. **10**, 075015 (2008)
2. Devenish, B.J., Bartello, P., Brenguier, J.-L., Collins, L.R., Grabowski, W.W., IJzermans, R.H.A., Malinowski, S.P., Reeks, M.W., Vassilicos, J.C., Wang, L.-P., Warhaft. Z.: Droplet growth in warm turbulent clouds. Q. J. R. Meteorol. Soc. **138**, 1401–1429 (2012)
3. Falkovich, G., Fouxon, A., Stepanov, M.G.: Acceleration of rain initiation by cloud turbulence. Nature **419**, 151–154 (2004)
4. Gotoh, T., Suehiro, T., Saito, I.: Continuous growth of cloud droplets in cumulus cloud. New J. Phys. **18**, 043042 (2016)
5. Grabowski, W.W., Wang, L.-P.: Growth of cloud droplets in a turbulent environment. Annu. Rev. Fluid Mech. **45**, 293–324 (2013)
6. Hall, W.D.: A detailed microphysical model within a two-dimensional dynamic framework: model description and preliminary results. J. Atmos. Sci **37**, 2486–2507 (1980)
7. Landau, L.D., Lifshitz, E.M.: Statistical Physics. Third edition, Part 1, volume 5. Pergamon, Oxford, 1980
8. Onishi, R., Matsuda, K., Takahashi, K.: Lagrangian tracking simulation of droplet growth in turbulence? Turbulence enhancement of autoconversion rate. J. Atmos. Sci. **72**, 2591–2607 (2015)

9. Rosa, B., Parishani, H., Ayala, O., Grabowski, W.W., Wang, L.-P.: Kinematic and dynamic collision statistics of cloud droplets from high-resolution simulations. New J. Phys. **15**, 045032 (2013)
10. Saito, I., Gotoh, T.: Turbulence and cloud droplets in cumulus clouds. New J. Phys. **20**, 023001 (2018)
11. Sardina, G., Picano, F., Brandt, L., Caballero, R.: Continuous growth of droplet size variance due to condensation in turbulent clouds. Phys. Rev. Lett. **115**, 1–5 (2015)
12. Shaw, R.A.: Particle-turbulence interactions in atmospheric clouds. Annu. Rev. Fluid Mech. **35**, 183–227 (2003)
13. Sundaram, S., Collins, L.R.: Collision statistics in an isotropic particle-laden turbulent suspension. Part 1. Direct numerical simulations. J. Fluid Mech. **335**, 75–109 (1997)
14. Sundaram, S., Collins, L.R.: A numerical study of the modulation of isotropic turbulence by suspended particles. J. Fluid Mech. **379**, 105–143 (1999)
15. Takahashi, T.: Warm rain development in a three-dimensional cloud model. J. Atmos. Sci. **71**, 1991–2013 (1981)
16. Vaillancourt, P.A., Yau, M.K., Grabowski, W.W.: Microscopic approach to cloud droplet growth by condensation. Part 1: model description and results without turbulence. J. Atmos. Sci. **58**, 1945–1964 (2001)
17. Vaillancourt, P.A., Yau, M.K., Bartello, P., Grabowski, W.W.: Microscopic approach to cloud droplet growth by condensation. Part II: turbulence, clustering, and condensational growth. J. Atmos. Sci. **59**, 3421–3435 (2002)
18. Wang, P.K.: Physics and Dynamics of Clouds and Precipitation. Cambridge University Press, Cambridge (2013)

Bubble-Induced Turbulence

Frédéric Risso

Abstract A homogenous swarm of bubbles rising through a liquid generates anisotropic homogeneous random velocity fluctuations. The statistical properties of bubble-induced fluctuations differ from the classical shear-induced turbulence. The probability density functions are non Gaussian and show a succession of exponential evolutions. The power spectral densities exhibit a k^{-3} subrange for wavelengths around the bubble size. The understanding of these properties requires to consider that bubble-induced agitation involves two contributions of a different nature. The first one is not related to any flow instability and results from the anisotropic flow disturbances generated near the bubbles, principally in the vertical direction. The second one is the almost isotropic turbulence induced by the instability of the flow through a population of bubbles, which turns out to be the main cause of horizontal fluctuations. Even if the two contributions are coupled, only the second one deserves to be called bubble-induced turbulence.

F. Risso (✉)
Institut de Mécanique des Fluides de Toulouse, IMFT, Université de Toulouse, CNRS, Toulouse, France
e-mail: frisso@imft.fr

M. Gorokhovski and F. S. Godeferd (eds.), *Turbulent Cascades II*,
ERCOFTAC Series 26, https://doi.org/10.1007/978-3-030-12547-9_20

1 Agitation in a Homogeneous Bubble Column

Bubbles rising through a liquid otherwise at rest generate random fluctuations. When the bubbles are uniformly distributed over space, the agitation of the liquid is homogeneous. Here, we consider situations where the Reynolds number $Re = \langle V \rangle d/\nu$ (based on bubble average velocity $\langle V \rangle$, bubble diameter d and kinematic viscosity of the liquid) is larger than 200. Since the pioneering work of Lance and Bataille [2], many authors have investigated homogeneous bubble columns (left side of Fig. 1), in which the average liquid velocity is everywhere zero. These works have been extensively reviewed in a recent state-of-the-art paper [8] and we recall here the salient features of bubble-induced agitation.

The variance of the fluctuations $\langle \mathbf{u}^2 \rangle$ is roughly proportional to the product of the gaz volume fraction α and the square of the average bubble velocity. However, the fluctuations are anisotropic since the variance of the vertical velocity $\langle u_z^2 \rangle$ is larger than that of the horizontal velocity $\langle u_x^2 \rangle$. The probability density functions of both the horizontal and the vertical velocity fluctuations (PDFs) are non Gaussian. Moreover, the vertical PDFs are asymmetric with a long exponential tail for positive (upward) fluctuations, which becomes more and more important as α increases (right side of Fig. 1).

The spectrum of the velocity fluctuations shows a subrange where the power density evolves as the power -3 of the wavenumber k. As shown in Fig. 2, the k^{-3}

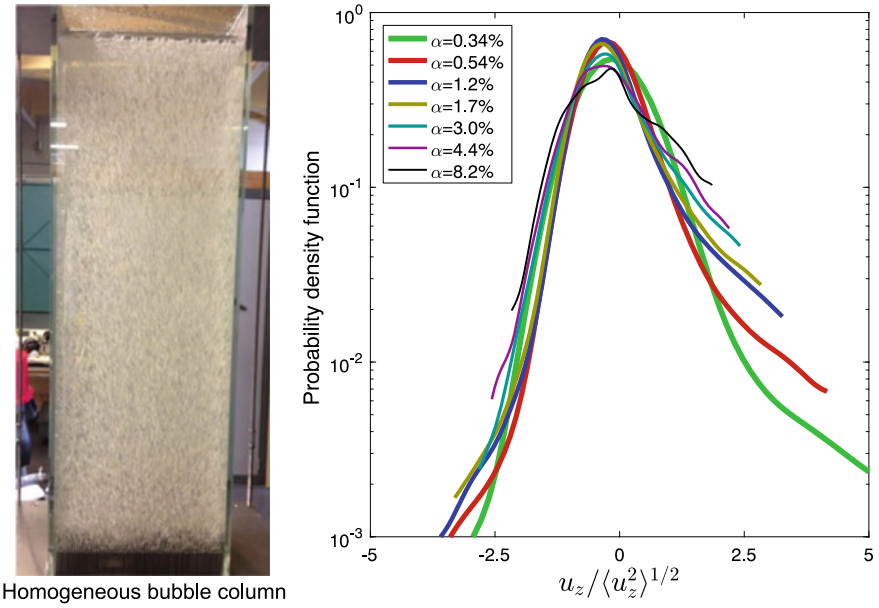

Fig. 1 Homogeneous bubble column. To the right: picture. To the left: probability density function of the vertical liquid velocity fluctuations for various gas volume fractions α from [4]

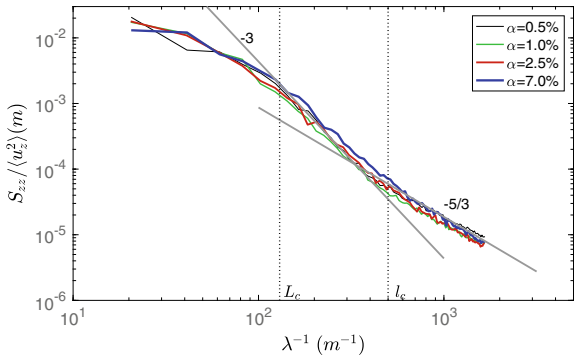

Fig. 2 Power spectra of liquid vertical velocity fluctuations measured in a bubble column by [4] ($d = 2.5\,\text{mm}$, $\alpha = 1.7\%$, $Re = 760$). The wavelengths limiting the k^{-3} subrange are $l_c = 2\,\text{mm}$ and $L_c = 7.7\,\text{mm}$

subrange is observed for wavelengths, $\lambda = 2\pi/k$, around the bubble diameter. Surprisingly, when normalised by the variance of the fluctuations, the spectra measured for various values of α collapse onto a single curve. This means that the integral length scale Λ of the velocity fluctuations is independent of the gas volume fraction. The value of Λ is related to the length of the wake that develops behind each bubble. The wake of a bubble that belongs to a swarm of rising bubbles is considerably shorter than the wake of an isolated rising bubble because of the interactions with neighbouring wakes. It decreases exponentially with the distance to the bubble on a length scale $L_w \approx 5d$, which is observed to be independent to the gas volume fraction provided $\alpha \gtrsim 0.5\%$.

2 Distinction Between Turbulent Fluctuations and Average Bubble Disturbances

The temporal velocity fluctuations which are measured in a given point located within a swarm of rising bubbles combine two contributions of a different nature. The first contribution corresponds to the average disturbance generated in the vicinity of each bubble. Even if the flow around each bubble would be steady in a frame that follows the bubble, temporal fluctuations would be observed in the laboratory frame as the bubble passes close to the measurement point. Since the bubbles are randomly distributed over space, random temporal fluctuations would be measured. It is clear that these fluctuations are not related to any kind of flow instability and must not be confused with turbulence. The second contribution is the real turbulence that develops provided the Reynolds number is large enough.

It is easy to make the distinction between these two kinds of fluctuations in the idealized situation where the bubbles are not moving relatively to each other [5]. In this case, we can consider the liquid velocity in the frame where all the bubbles are at rest. Let us denote spatial averaging by angle brackets and time averaging by an overbar. After having removed the uniform average velocity, the liquid velocity $\mathbf{u}(\mathbf{x}, t)$ can be decomposed as

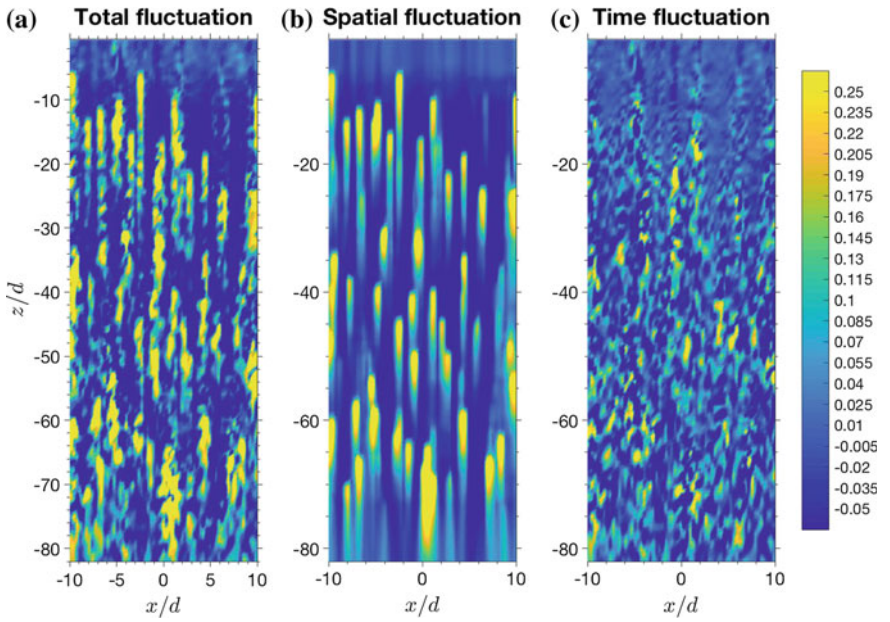

Fig. 3 Vertical velocity in a vertical plane computed by large-eddy simulation from [3]. Decomposition of velocity fluctuations by Eq. 1: **a** total fluctuation $u_z(\mathbf{x}, t)$; **b** spatial fluctuation $\overline{u}_z(\mathbf{x})$; **c** time fluctuation $u'_z(\mathbf{x}, t)$

$$\mathbf{u}(\mathbf{x}, t) = \overline{\mathbf{u}}(\mathbf{x}) + \mathbf{u}'(\mathbf{x}, t)\,. \tag{1}$$

The spatial fluctuation $\overline{\mathbf{u}}(\mathbf{x})$ only depends on the spatial coordinate $\mathbf{x}$ and described the contribution of the individual bubble disturbances. The time fluctuation $\mathbf{u}'(\mathbf{x}, t)$ depends on both the time t and the location $\mathbf{x}$ and accounts for the turbulence. The variance of the total fluctuation $\mathbf{u}(\mathbf{x}, t)$ is the sum of the variances of these two contributions:

$$\langle \mathbf{u}^2 \rangle = \langle \overline{\mathbf{u}}^2 \rangle + \langle \mathbf{u}'^2 \rangle. \tag{2}$$

Such a decomposition has been applied to results of an experimental investigation of the flow through a random array of fixed spheres [1] and to results of large-eddy simulations (LES) of the flow through a fixed swarm of bubbles [3]. Figure 3 presents the fields of total, spatial and time vertical velocity fluctuations obtained by LES. The spatial fluctuations clearly exhibits the bubble wakes whereas the time fluctuations are almost the same everywhere and therefore not strongly correlated to the bubble locations. From these investigations of flows through random array of obstacles, the following conclusions are obtained. The fluctuations due to individual bubble disturbances are strongly anisotropic and constitute the dominant contributions to the total fluctuations in the vertical direction. The turbulent fluctuations are almost isotropic, predominant in the horizontal direction, and their PDFs are exponential.

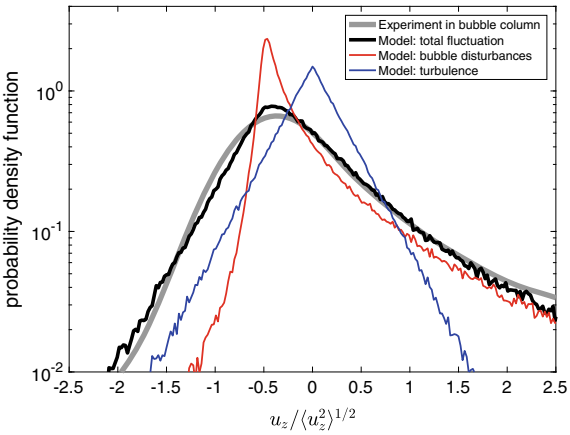

Fig. 4 Probability density function of vertical liquid velocity fluctuations: Comparison between experimental results measured in a bubble column by [4] ($\alpha = 1.7\%$, $Re = 760$) and model by [7]

Regarding the spectrum, the bubble disturbances are dominant at larger scales while the turbulence is preponderant at smaller scales. However, both contributions show a k^{-3} spectral subrange.

Having regard to the results obtained in idealized flows, a model for the fluctuations in a real bubble swarm was proposed by [7]; it is shortly summarized below.

The bubble disturbances are described by considering that the flow around a given bubble is the sum of the potential flow around the bubble and an exponential decaying wake, which is characterized by a length scale L_w. The locations of a large number of bubbles are randomly chosen independently of each other. The disturbances generated by all these bubbles at a given point are linearly superimposed. A sample of velocity fluctuation is thus obtained. This operation is repeated a great number of times in order to obtain a statistically significant ensemble of samples, from which a PDF is computed. Figure 4 compares the model PDF of the vertical fluctuations due to bubble disturbances (red curve) to an experimental PDF (grey curve) measured in a homogeneous bubble column. Note that the value of L_w has been adjusted to fit the experimental tail of positive fluctuations. We see that if the model is able to reproduce well the tail of positive fluctuations, which is dominated by the wakes, it fails to reproduce the negative fluctuations.

Assuming that turbulence is isotropic, the three components of the turbulent fluctuations are model by the same exponential PDF:

$$f_t(u') = \frac{\sqrt{2}}{2\sigma_t} \exp\left(-\frac{\sqrt{2} \mid u' \mid}{\sigma_t}\right), \tag{3}$$

where the value of σ_t is chosen to fit the central part of the experimental PDF of the horizontal fluctuations (not shown here). The blue curve in Fig. 4 shows the model PDF of the vertical fluctuations due to bubble-induced turbulence.

The model for the total fluctuations is obtained by assuming that the turbulent fluctuations are independent of the bubble locations, which implies that fluctuations induced by bubble disturbances and turbulence are statistically independent. A sample of the total fluctuations is thus obtained as the sum of a sample of each contribution. The model PDF for the total vertical fluctuations is represented by a black curve in Fig. 4. It matches well the experimental results.

This model has been satisfactorily compared to experimental results obtained for various gas volume fractions and several bubble diameters. In agreement with results obtained from investigations of flows through arrays of fixed obstacles, this confirms that the turbulent contribution to bubble-induced agitation in a real bubble column is almost isotropic and well described by an exponential PDF.

3 Discussion of the Spectrum of the Bubble-Induced Turbulence

The bubble-induced turbulence has two important features that may help to shed light on its spectral behaviour: (1) It exhibits a k^{-3} power law within a range of scales around the bubble size where the motions of the bubble supply energy to the liquid; (2) The wavenumber spectrum is invariant with α when normalized by the variance $\langle u'^2 \rangle$ and the integral length scale Λ of the fluctuations.

Let us start analysing property (1) by considering the energy balance in the spectral domain. In a statistically steady and homogeneous state, the power spectral density E of the turbulent fluctuations u' is related to the energy production Π and to the energy transfer T between the wavenumbers by

$$2\nu k^2 E = T + \Pi \,. \tag{4}$$

Lance and Bataille [2] proposed that the turbulent fluctuations were localized within the bubble wakes where there were both produced and dissipated. Assuming that the production only depends on the dissipation rate ε and on the wavenumber k, dimensional considerations leads to $\Pi \propto \varepsilon k^{-1}$. Inserting this expression in Eq. 4 and neglecting T, they obtained a spectrum in k^{-3}:

$$E \propto \frac{\varepsilon k^{-3}}{2\nu} \,. \tag{5}$$

Owing to the results of LES in which the scales smaller than the wakes are not resolved [3] and the fact that a k^{-3} subrange has been observed in experiments for scales larger than d [4], the assumption that turbulence is localized within the wakes is invalided. However, the assumption that Π and T depend only upon ε and k is a less restrictive assumption that still leads to Eq. 5.

Then, property (2) implies the following relation for the k^{-3} subrange:

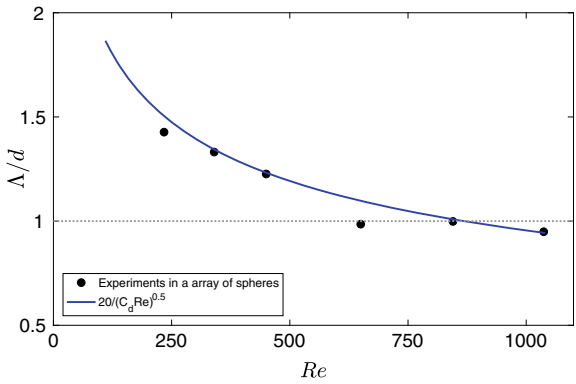

Fig. 5 Evolution of the Eulerian integral length scale as a function of the Reynolds number in an experimental random array of spheres by [1] ($\alpha = 2\%$)

$$\frac{E}{\langle u'^2 \rangle \Lambda} \propto (\Lambda k)^{-3} . \tag{6}$$

Equating Eqs. 5 and 6 yields

$$\varepsilon \propto \nu \frac{\langle u'^2 \rangle}{\Lambda^2} , \tag{7}$$

where Λ appears as sort of Taylor scale for the k^{-3} subrange. Taking into account that $\varepsilon = \alpha g \langle V \rangle$ and $\langle u'^2 \rangle \propto \alpha \langle V \rangle^2$ finally leads to the following scaling for Λ:

$$\Lambda \propto \sqrt{\frac{\nu \langle V \rangle}{g}} \propto \frac{d}{\sqrt{C_d Re}} . \tag{8}$$

The interest of this relation is that it can be tested in experiments or simulations to assess the validity of the assumptions leading to Eq. 5. For the experiments of [4], taking the values of Re and C_d corresponding to an isolated bubble, Eq. 8 leads to the same value of Λ for the three investigated bubble diameters, which is in agreement with the observations. In Fig. 5, the various scalings for Λ have been compared to the results obtained by [1] in an random array of fixed spheres for various Re by estimating C_d by the Schiller and Naumann relation for an isolated solid sphere. It turns out that Eq. 8 gives the correct evolution of Λ. Comparisons with other investigations covering a broader range of parameters are nevertheless required to reach a definitive conclusion regarding the validity of Eqs. 5 and 8.

4 Conclusion

Bubble-induced agitation combines two contributions: the fluctuations generated by the disturbances localized around each bubble and real bubble-induced turbulence. The major statistical properties of both contributions have been determined by many

authors and are now well known. On the one hand, the role of the localized bubble disturbances is now well understood since their PDFs have been satisfactorily described by considering the summation of individual disturbances [7] and their spectral behaviour reproduced by considering a succession of random bursts [6]. On the other hand, the exponential PDFs and the k^{-3} spectral subrange of the bubble-induced turbulence are still not understood. They are probably the consequences of the instability of the flow through a random array of obstacles.

References

1. Amoura, Z., Besnaci, C., Risso, F., Roig, V.: The flow through a random array of spheres as a model of bubble-induced agitation. J. Fluid Mech. **823**, 592–616 (2017)
2. Lance, M., Bataille, J.: Turbulence in the liquid-phase of a uniform bubbly air water-flow. J. Fluid Mech. **222**, 95–118 (1991)
3. Riboux, G., Legendre, D., Risso, F.: A model of bubble-induced turbulence based on large-scale wake interactions. J. Fluid Mech. **719**, 362–387 (2013)
4. Riboux, G., Risso, F., Legendre, D.: Experimental characterization of the agitation generated by bubbles rising at high Reynolds number. J. Fluid Mech. **643**, 509–539 (2010)
5. Risso, F., Roig, V., Amoura, Z., Riboux, G., Billet, A.-M.: Wake attenuation in large Reynolds number dispersed two-phase flows. Phil. Trans. R. Soc. A **366**, 2177–2190 (2008)
6. Risso, F.: Theoretical model for k^{-3} spectra in dispersed multiphase flows. Phys Fluids. **23**, 011701 (2011)
7. Risso, F.: Physical interpretation of probability density functions of bubble-induced agitation. J. Fluid Mech. **809**, 240–263 (2016)
8. Risso, F.: Agitation, mixing, and transfers induced by bubbles. Annu Rev. Fluid Mech. **50**, 25–48 (2018)

Non Spherical and Inertial Particles in Couette Turbulent Large Scale Structures

Guiquan Wang, Micheline Abbas, Annaïg Pedrono and Eric Climent

Abstract We are studying dispersion of finite-size particles in a turbulent plane Couette flow by numerical simulations. The effect of particle non-sphericity was discussed (particles are neutrally buoyant and shape varies from oblate to prolate, aspect ratio is ranging from 0.5 to 2). Particle dispersion is analyzed also when inertia is considered for different particle densities for spherical particles (while keeping comparable Stokes number). This work yields evidences that the particle distribution in turbulent flow coherent structures is in general correlated to the cycle of regeneration of turbulence in Couette flow (the strongest correlation being for massless bubbles), and that the particle residence time in large scale vortices is equal to the characteristic time scale of the flow regeneration cycle.

G. Wang · A. Pedrono · E. Climent (✉)
Institut de Mécanique des Fluides de Toulouse, IMFT, Université de Toulouse, CNRS, Toulouse, France
e-mail: ecliment@imft.fr

A. Pedrono
e-mail: annaig.pedrono@imft.fr

G. Wang
FERMAT, Université de Toulouse, CNRS, INPT, INSA, UPS, Toulouse, France
e-mail: gwang4academy@gmail.com

M. Abbas
Laboratoire de Génie Chimique, Université de Toulouse, CNRS, INPT, UPS, Toulouse, France
e-mail: Micheline.Abbas@ensiacet.fr

M. Gorokhovski and F. S. Godeferd (eds.), *Turbulent Cascades II*,
ERCOFTAC Series 26, https://doi.org/10.1007/978-3-030-12547-9_21

1 Introduction

Shear driven turbulent flows near walls are composed of coherent flow structures which result in enhancing heat and mass transfer [1]. Kaftori et al. [2] found that neutrally-buoyant particles can form particle streaks near the wall where the vortical flow structures create suitable conditions for particle preferential accumulation. Among the coherent structures, sweep and ejection events (regions of negative shear stress pushing the fluid toward or away from the wall denoted as Q2 and Q4 respectively in quadrant representation) are driving pointwise inertial particles toward the wall or the bulk flow region respectively [3]. In a previous work [4], we have considered modulation of turbulent plane Couette flow by particles which size was comparable to the smallest flow structures (flow inertia is finite at the particle scale) and which particle-to-fluid density ratio was varied from 0 to 5 (without considering settling under gravity). In that paper, we showed that the flow features were not significantly modified when the particle volumetric concentration was less or equal to 10%. In the present communication, we address the effect of the deviation from sphericity on the particle transport in turbulent plane Couette flow configuration. We analyze the particle spatial dispersion, their residence time in flow structures and their transport from the streaks to the large scale vortical flow structures.

2 Two-Phase Flow Simulations

The plane Couette flow is driven by two walls moving with opposite velocities of the same magnitude. We chose the dimensions of the numerical domain to be adapted to the minimal flow unit [4]. Table 1 gives a summary of all numerical parameters. The length and velocity are scaled by wall units $y^+ \equiv yu_\tau/\nu$, and $u^+ \equiv u/u_\tau$ where $u_\tau = \sqrt{\tau_w/\rho_f}$, τ_w being the wall shear stress. All the cases of Table 1 are adapted to the range of validity of the Force Coupling Method. This method is suitable to couple the flow momentum equations with the particle dynamics and more specifically particle response to flow fluctuations has been validated in [4]. Results with neutrally buoyant non-spherical particles are compared to that obtained for various particle-to-fluid density ratios. The size ratio between the Couette gap and the radius of smallest spherical particles r_p used for this study is $L_y/r_p = 40$. The particle Reynolds number $Re_p \equiv \Gamma(V_r^{1/3}r_p)^2/\nu$ is based on local shear rate $\Gamma = |d\overline{u}/dy|$ and the effective radius evaluated from the particle volume $r_{eff} \equiv (V_r)^{1/3}r_p$. V_r is the ratio of the spheroid volume to the reference sphere volume (see Table 1). The Stokes number $St \equiv (2\rho_p/9\rho_f)Re_p$ is based both on an increase of inertia due to particle size or to density ratio $\rho_r \equiv \rho_p/\rho_f$. The Stokes number is defined in accordance with the relaxation time of spheroidal particles (summarized in [5]). For example for $A_r = 2$ (resp $A_r = 0.5$), the Stokes number is 1.52 (resp 2.42) larger than the reference particle Stokes number when calculated from [5] while the increase is 1.59 (resp 2.51) times in the current work.

Table 1 Configuration of the numerical simulations. The Reynolds number of the singe-phase flow is $Re_b \equiv U_w h/\nu = 500$ where $U_w = 0.5$ is half of the relative wall velocity and $h = L_y/2$ is half of the Couette gap. $r_p = L_y/40$ is the radius of the reference sphere and A_r is the aspect ratio of spheroids. The Stokes number is low near the Couette center (because the shear rate is weak) and maximum near the walls. The statistics are formed over ∼500 time units (h/U_w) at steady state

Domain size: $L_x \times L_y \times L_z = 0.88\pi \times 1.0 \times 0.6\pi$									
Case	$\overline{\Phi}(\%)$	A_r	ρ_r	V_r	L_y^+	Re_τ	$Re_p(max)$	$St(max)$	line type
$N_x \times N_y \times N_z = 30 \times 86 \times 32$									
Single-phase	–	–	–	–	81	40.2	–	–	+
Shape effect $N_x \times N_y \times N_z = 182 \times 66 \times 128$									
C500-5-1-1(l)	5	1	1	8	80.6	40.3	12.5	2.78	- - - - -
$N_x \times N_y \times N_z = 280 \times 100 \times 256$									
C500-5-1-1(s)	5	1	1	1	80.6	40.3	3.75	0.83	——
C500-5-05-1	5	0.5	1	4	80.1	40.0	6.9	1.53	– – –
C500-5-2-1	5	2	1	2	81.4	40.2	3.5	0.78	- - -
Inertia effect $N_x \times N_y \times N_z = 382 \times 134 \times 256$									
C500-10-1-0	10	1	$1.25\,10^{-3}$	1	84.7	42.4	3.75	$1.1\,10^{-3}$	- - - - -
C500-10-1-1	10	1	1	1	84.1	42.1	3.75	0.83	——
C500-10-1-2	10	1	2	1	85.1	42.5	3.75	1.67	– – –
C500-10-1-5	10	1	5	1	87.6	43.9	3.75	4.15	- - -

3 Results

3.1 Particle Dispersion

Figure 1a, b show a projection in the $y-z$ plane, of the positions of oblate and prolate spheroids, overlaid by the flow velocity isocontours. The spheroids, like spheres, tend to be rather located in the center of the vortices, whereas the strong ejection regions are almost free from particles. The concentration profiles in the wall-normal direction are shown in Fig. 1c. It can be noted that at moderate inertia the particle distribution is not influenced by particle inertia or shape (the Stokes numbers of tests $C500-5-05-1$ and $C500-10-1-2$ are close). In Fig. 1d, we plot the orientation angle of the symmetry axis. For oblate spheroids, both θ and φ are relatively high, meaning that oblate spheroids move more likely with the symmetry axis parallel to the wall-normal direction especially in the near wall region. This indicates that oblate particles are tumbling more frequently than spinning motion.

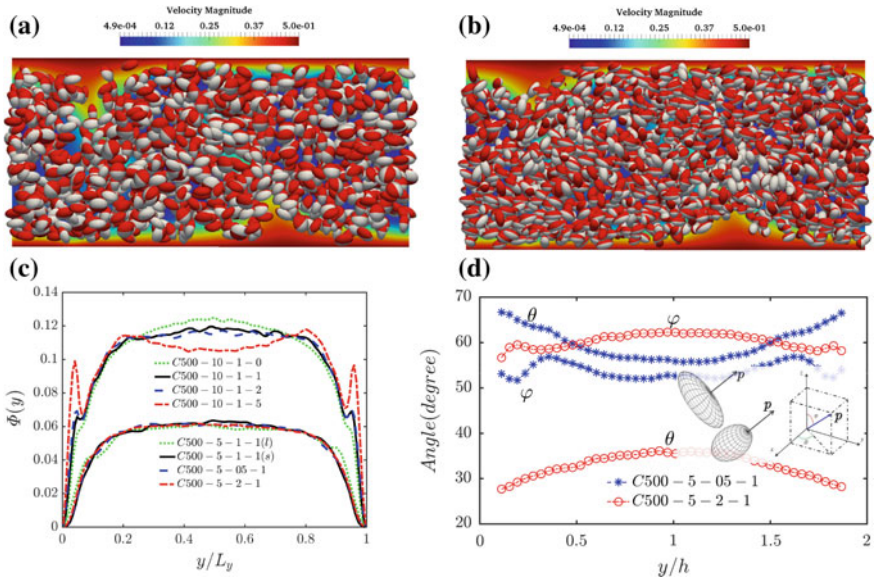

Fig. 1 **a** and **b** show the particle distribution and orientation viewed from streamwise direction of C500-5-05-1 (oblate) and C500-5-2-1 (prolate particles), respectively. The figures are chosen when the intensity of large scale streaks is the strongest. The isocontours represent the instantaneous velocity magnitude in $y-z$ slice. **c** Particle concentration profiles for different particle shapes and density ratios. **d** shows wall-normal profiles of the particle orientation angles θ and φ (projections of the **p** vector). The angle between the symmetry axis (**p** or $-$**p**) with the positive axis ($+x$ or $+z$) is used. $*$ and $\circ$ stand for oblate and prolate particles respectively

However, prolate spheroids are more likely orientated with their major axis parallel to the flow direction especially close to the wall and then tumble (φ is large and θ is small on average).

3.2 *Characterization of Particle Accumulation in Large Scale Vortices*

Inertial particles spend slightly less time than tracers in vortical regions in 3D turbulent flows, for Stokes numbers ranging between 0 and 3 [6]. The most energetic structures of a turbulent plane Couette flow in the limit of low turbulence, consist in pairs of contra-rotating Large Scale Vortices (LSVs) which size is comparable to the Couette gap and large scale streaks [7]. The Large Scale Vortices (LSVs) carry significant fraction of turbulent kinetic energy [8]. In [4], we observed that light particles are accumulating in the LSVs while heavier particles are moving outwards. The centrifugal motion of particles from the vortical coherent structures drives particle spatial distribution, yielding preferential accumulation or not [9].

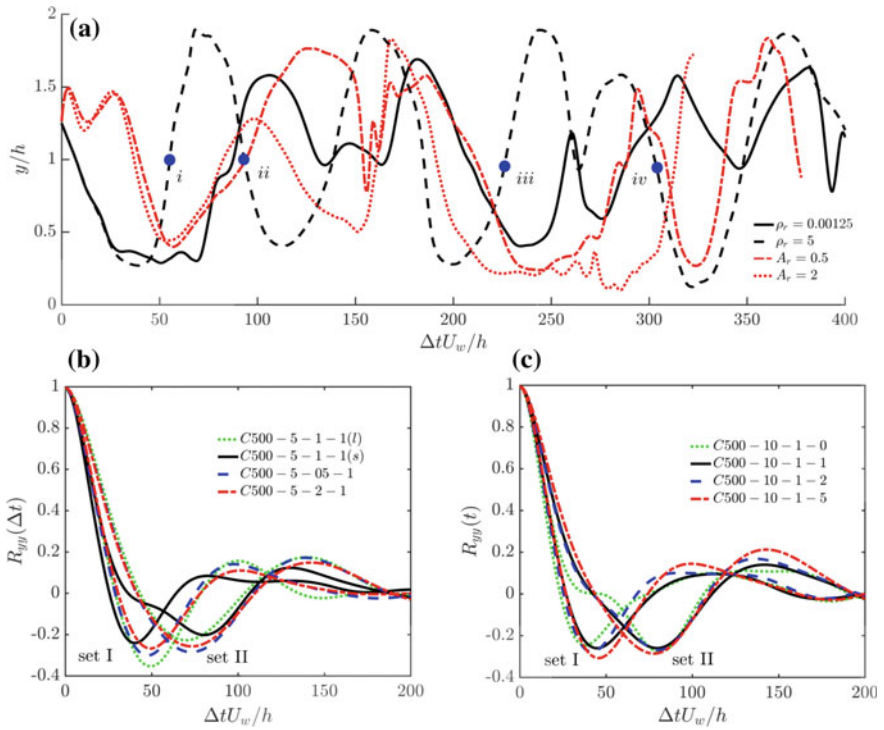

Fig. 2 **a** Time series of the wall-normal distance of a particle at Reynolds number 500 for different aspect ratios and particle densities: —— $\rho_r = 1.25\ 10^{-3}$; – – – $\rho_r = 5$ and -·-·- $A_r = 0.5$; ····· $A_r = 2$. **b** and **c** are temporal auto-correlation functions of the wall-normal particle position fluctuation. The line style of **b** and **c** is shown in Table 1. Set I in these figures contains the statistics of particles trapped in one large scale vortex and set II contains particles transferred from one LSV to the other. Particles are attributed to set I, set II or neither of the two sets, depending on the value of Δt_{min} at which the minimum of R_{yy} corresponding to each particle occurs: if $\Delta t_{min} U_w/h < 60$, particle is attributed to set I; if $60 < \Delta t_{min} U_w/h < 100$, particle is counted in set II. Typically, 10–20% of the total number particles is attributed to each set

Particle residence time in a vortex has been measured based on temporal evolution of the wall-normal distance. In Fig. 2a, the temporal evolutions of wall-normal distance of oblate and prolate spheroids are shown. The spheroids response is similar to neutrally-buoyant spherical particles (periodic oscillations between the two walls). Two distinct trajectories can be observed: a rotation in a single LSV from i to ii (dashed line of Fig. 2a), and a rotation in a LSV followed by its transfer to the other counter-rotating vortex from iii to iv.

Quantitative measure of the residence time in LSV can be calculated from temporal auto-correlation function of the particle distance from the wall (which on average corresponds to h because particles move equally through all the domain). The auto-correlation functions (Fig. 2b, c) characterize the fluctuating motion of particles. It is negative when the particle passes from one half of the Couette gap to the other. It

is zero when the particle escape from the LSVs. Figure 2b, c correspond to two sets of statistics: particles captured in a unique LSV and particles moving from one LSV to another in the second set.

The average residence time of particles in one vortex (set I) is $\sim 100\ U_w/h$ and $\sim 150\ U_w/h$ for particles that are moving from one LSV to another LSV (set II). The smaller and lighter spherical particles have shorter periods whereas they have longer periods when they move from one LSV to the other. The typical time of particle residence in one vortex is approximately equal to the period of the regeneration cycle (see Hamilton et al. [10]). This means that there is a strong correlation between particle dispersion of finite-size particles and intermediate stages of the regeneration cycle in turbulent pCf.

3.3 Particle Spatial Distribution in Turbulent Flow Structures

With a lower level of energy than the LSVs, the x-independent streaks contain the mode corresponding to most of turbulent kinetic energy. The x-independent streaks predominantly consist in Q2 and Q4 regions (ejection and sweep respectively). The energy of this mode decreases during its breakdown to x-dependent streaks (wavy streaks). We show here that the accumulation of particles in the sweep and ejection regions is correlated, in time, to the evolution of the streaks and therefore to the regeneration cycle. For the temporal evolution of the streaky motion, it is represented by the modal analysis of the flow fluctuating energy. The Fourier decomposition of the energy over streamwise and spanwise directions, as introduced by Hamilton et al. [10], is written as follows:

$$M(k_x = m\alpha, k_z = n\beta) \equiv \{\int_{Y_1}^{Y_2} [\widehat{u_i'}\widehat{u_i'}(m\alpha, y, n\beta)]dy\}^{1/2} \tag{1}$$

where Y_1 and Y_2 stand for the integration over the distance from the wall, (α, β) are fundamental wavenumbers in streamwise and spanwise directions defined as $(2\pi/L_x, 2\pi/L_z)$, where m and n are integers. Any flow structure can be represented by one mode $(m\alpha, n\beta)$. As an example, mode $(0, n\beta)$ with $n \neq 0$ corresponds to x-independent flow structure while mode $(m\alpha, n\beta)$ with $m \neq 0$ correspond to x-dependent structure. The time series of the x-independent structures (mode $(0, \beta)$) is plot in Fig. 3a–f, for two-phase flows with different particle shapes and densities. However, Fig. 3 shows time series of the percentage of particles located near the walls at $10 < y^+ < 40$ inside the streaky regions Q2 and Q4 (this is where sweeps and ejections are strong in the buffer layer). We observed that half of particles are located in the sweep and ejection regions. The temporal fluctuations of particle concentration are in-phase with the fluctuation of energy of x-independent streaks in these regions. This observation is more obvious at low Stokes numbers (C500-5-2-1 and C500-10-1-0). Similarly, we observed that the percentage of particles located in

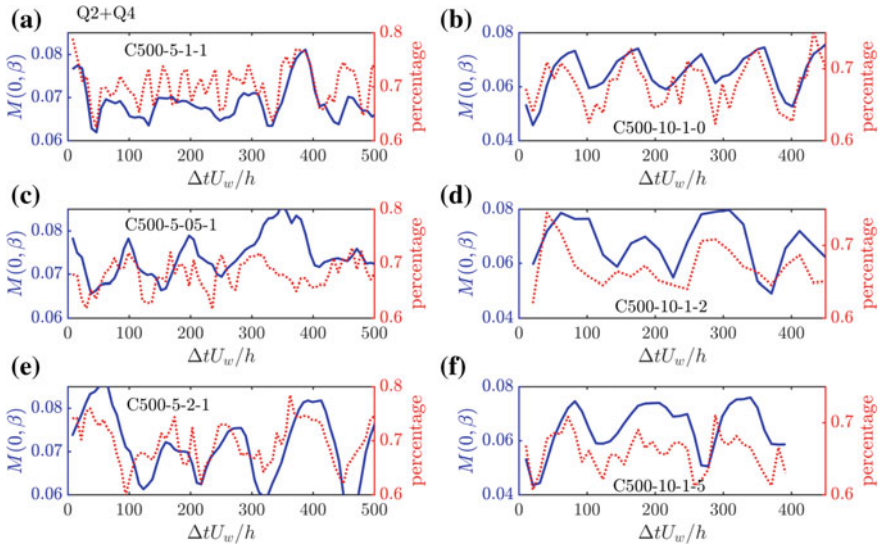

Fig. 3 Time series of mode $(0, n\beta)$ corresponding to turbulent kinetic energy contained in the x-independent streaks (blue lines), and of the local particle percentage (ratio of particles in Q2 and Q4 to the total number of particles) in both ejection and sweep event regions (red dash lines). **a**, **c**, **e** emphasize the effect of particle non-sphericity—cases from top to bottom: C500-5-1-1, C500-5-05-1 and C500-5-2-1. **b**, **d**, **f** emphasize the effect of particle density—from top to bottom: C500-10-1-0, C500-10-1-2 and C500-10-1-5

Q1 and Q3 events is strongly related to the flow circulation, which is out-of-phase from the temporal evolution of x-independent streak energy (figure not shown).

4 Conclusion

We have shown that, in turbulent plane Couette flow, the motion of finite-size particles is strongly related to the fluid motion regardless their shape or density, up to Stokes numbers ($St \approx 5$). The residence time of a single particle in a large scale vortex is equal to the characteristic time scale of the turbulence regeneration cycle. At equivalent volume fraction, the particle distribution of spheroids in the flow is not significantly altered by their shape. Particles are on average more present inside the large scale streamwise vortices, compared to the x-independent streaks. However instantaneous particle distribution depends on the sequence of sub-processes along the turbulence regeneration cycle. The ejection regions are seeded by more particles during the streak formation stage (when the x-independent structures are energetic) and they loose particles during the streak breakdown stage (when the energy of x-independent structures decreases). During streak formation (resp. breakdown), the

flow circulation decreases (resp. increases), and the Q1 region mainly located inside large scale vortices looses (resp. gains) particles, leaving toward (resp. coming from) large scale streaks.

References

1. Robinson, S.K.: Coherent motions in the turbulent boundary layer. Annu. Rev. Fluid. Mech. **23**(1), 601–639 (1991)
2. Kaftori, D., Hetsroni, G., Banerjee, S.: Particle behavior in the turbulent boundary layer. I. motion, deposition, and entrainment. Phys. Fluids **7**(5), 1095–1106 (1995)
3. Marchioli, C., Soldati, A.: Mechanisms for particle transfer and segregation in a turbulent boundary layer. J. Fluid Mech. **468**, 283–315 (2002)
4. Wang, G., Abbas, M., Climent, E.: Modulation of large-scale structures by neutrally buoyant and inertial finite-size particles in turbulent couette flow. Phys. Rev. Fluids **2**(8), 084,302 (2017)
5. Voth, G.A., Soldati, A.: Anisotropic particles in turbulence. Annu. Rev. Fluid. Mech. **49**, 249–276 (2017)
6. Bhatnagar, A., Gupta, A., Mitra, D., Pandit, R., Perlekar, P.: How long do particles spend in vortical regions in turbulent flows? Phys. Rev. E **94**(5), 053,119 (2016)
7. Komminaho, J., Lundbladh, A., Johansson, A.V.: Very large structures in plane turbulent couette flow. J. Fluid Mech. **320**, 259–285 (1996)
8. Pirozzoli, S., Bernardini, M., Orlandi, P.: Turbulence statistics in couette flow at high reynolds number. J. Fluid Mech. **758**, 327–343 (2014)
9. Marshall, J.: A model of heavy particle dispersion by organized vortex structures wrapped around a columnar vortex core. Phys. Fluids **10**(12), 3236–3238 (1998)
10. Hamilton, J.M., Kim, J., Waleffe, F.: Regeneration mechanisms of near-wall turbulence structures. J. Fluid Mech. **287**, 317–348 (1995)

Part VI
Particles Under the Turbulence

Preferential Concentration of Finite Solid Particles in a Swirling von Kármán Flow of Water

Martin Obligado, Romain Volk, Nicolas Mordant and Mickael Bourgoin

Abstract We present a study of preferential concentration with Voronoï diagrams of finite size solid particles in a von Kármán flow. This flow is an interesting case of strongly inhomogeneous turbulence with high Re_λ. We investigate preferential concentration of PMMA particles with density $\rho_p = 1400\,\mathrm{kg/m^3}$ and diameter $2.8 < d_p/\eta < 6.3$ for $340 < Re_\lambda < 810$. We conclusively find that particles form clusters and voids. The geometry of these structures is therefore studied, and results compared with previous works in other flows.

1 Introduction

Turbulent flows laden with inertial particles are widely encountered in nature (particles dispersion in the atmosphere, rain formation, marine snow sedimentation …) and in industry (fuel or coal combustion, fluidized beds reactors, separation techniques …). In all these configurations, inertial particles interacting with turbulence form high and low concentration regions leading to non-trivial spatial organization of particles: this so-called preferential concentration. This phenomenon involves many ingredients such as particle inertia, turbulence characteristics, gravitational settling, disperse phase volume fraction, and many others. The specific role of each parameter remains to be clarified (a review on this topic can be found on [7]). It is in this context

M. Obligado (✉) · N. Mordant
Université Grenoble Alpes, CNRS, Grenoble INP, LEGI, 38000 Grenoble, France
e-mail: martin.obligado@univ-grenoble-alpes.fr

N. Mordant
e-mail: nicolas.mordant@univ-grenoble-alpes.fr

R. Volk · M. Bourgoin
Laboratoire de Physique de l'École Normale Supérieure de Lyon,
CNRS & Université de Lyon, 46 allée dItalie, 69364 Lyon Cedex 07, France
e-mail: romain.volk@ens-lyon.fr

M. Bourgoin
e-mail: mickael.bourgoin@ens-lyon.fr

M. Gorokhovski and F. S. Godeferd (eds.), *Turbulent Cascades II*,
ERCOFTAC Series 26, https://doi.org/10.1007/978-3-030-12547-9_22

that the study of preferential concentration of particles in different types of flows is important, as it allows to isolate the role of each parameter.

Most numerical studies of preferential concentration have considered the case of high density ratios of particles using purely stokesian point particle models in direct numerical simulations of turbulence. In such conditions particles inertia is primarily quantified by the Stokes number, $St = \tau_p/\tau_\eta$ (with τ_p the particles relaxation time and τ_η the turbulent dissipation scale). Experimental counter-part studies have investigated for instance the preferential concentration of small (sub-kolmogorov) water droplets in grid-generated turbulence in wind-tunnels (see for instance [11]). These studies show qualitative agreements between experiments and numerics, for instance with a maximum of clustering around Stokes numbers of order unity. However a quantitative systematic comparison remains to be performed accounting in particular for the role of gravity (not always included in numerical studies) and for trends with Reynolds number (which were found to be quite dramatic in experiments [11]), in order to clarify the exact mechanism at play and leading to preferential concentration (for instance in terms of centrifugation [15] or sweep-stick [4]).

The case of moderate density ratios remains less investigated, particularly in experiments. Fiabane and collaborators characterized the clustering properties of finite size neutrally buoyant particles and glass particles in water and homogeneous isotropic turbulence [2] at Reynolds number up to $R_\lambda \approx 400$ (based on Taylor microscale). Their study shows in particular that in this case the Stokes is not any longer a relevant indicator of clustering.

Here we present a study of preferential concentration with Voronoï diagrams of solid particles at moderate density ration in a von Kármán flow of water at a Reynolds number up to $R_\lambda \approx 810$. We investigate preferential concentration of PMMA particles with density $\rho_p = 1400\ \mathrm{kg/m^3}$ and diameter $2.8 < d_p/\eta < 6.3$ for $340 < Re_\lambda < 810$. Therefore, with high Re_λ and heavy particles in the a range of diameters close to the limit classically considered for point particle dynamics, *i.e.* around $d_p/\eta \sim 5\eta$ [2].

2 Experimental Setup

The flow is a turbulent von Kármán swirling flow, described in references [12, 13]. Water fills a cylindrical container of internal diameter $D = 15$ cm and a length of 25 cm. It is driven by two disks of diameter 14 cm, fitted with blades. Three different rotation rates were studied: 2.8, 5.6 and 8.3 Hz (Fig. 1a). The distance between the disks is 20 cm while the rotation frequency is imposed by two calibrated constant current engines. The angular velocity is measured with two dynamos with a precision in the order of 2% and is adjusted in a way that the disks have the same velocity but opposite direction (Fig. 1b). This setup allows us to obtain developed turbulence with Re_λ up to $\sim$800 in a compact region of space. This type of flow has been extensively used for studying the properties of turbulence, Lagrangian ([5, 8, 14]) or Eulerian ([16]).

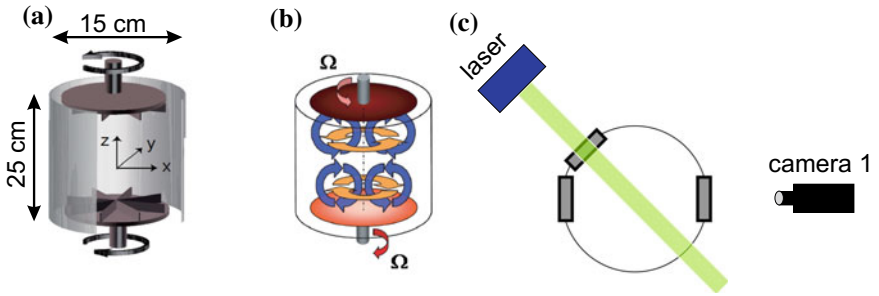

Fig. 1 **a** Schema of the experimental setup. **b** Inhomogeneous flow generated in the container. **c** Schema of the imaging system

Table 1 Turbulence parameters of the flow for the three velocities studied. The values are obtained using the results in [13]

Ω (Hz)	u_x (m/s)	u_z (m/s)	η (μm)	τ_η (ms)	ε (W kg^{-1})	Re_λ
2.8	0.38	0.19	28.5	3.55	3.1	340
5.6	0.76	0.41	21.2	7.11	7.2	570
8.3	1.14	0.62	16.4	20.7	20.7	810

The von Kármán flow generated has a large scale non-homogeneous, non-isotropic 3D mean structure (Fig. 1b). As the disks counter-rotate, the mean flow has a strong azimuthal velocity component (in the order of $\pi D\Omega$ close to the disks) and vanishes in the middle plane of the cylinder. Furthermore, the impeller disks work as centrifugal pumps ejecting the flow in the radial direction near the disks, creating a poloidal re-circulation with a stagnation point at the center of the cylinder.

The turbulence generated is locally homogeneous in the center of the cylinder but conserves the anisotropy for big and small scales ([14]). In the limit $Re_\lambda \gg 1$ the usual local isotropy hypothesis is generally assumed for the small scales of the flow (although the validity of this assumption has been recently questioned [10]). For the measurements reported here, the Taylor-based Reynolds number reaches values up to 810 and the dissipation rate ε values up to 25 W/kg (Table 1). We study PMMA particles with density ratio 1.4 and two different radii: 80 and 100 μm (Table 2). The water temperature was maintained constant during all measurements at $T = 30$ °C. As the flow is anisotropic, the Reynolds number based in the Taylor scale is estimated as $Re_\lambda = \sqrt{\frac{15u^4}{\varepsilon\nu}}$, where $u = \sqrt{\frac{2u_x^2+u_z^2}{3}}$, is obtained using the rms value of velocity fluctuations.

The cylindrical container is equipped with three windows that allow a proper visualization of the flow. The flow passes through a laser sheet (inclined 45°, as shown in Fig. 1c), where a high-speed camera Phantom-Miro M310 was placed in the horizontal direction. The laser produces a continuous beam with a wavelength

Table 2 Particles considered and their Stokes number for each velocity

Particle	d_p (μm)	$St_{\Omega 1}$	$St_{\Omega 2}$	$St_{\Omega 3}$
1	80	0.83	1.50	2.50
2	100	1.30	2.30	4.0

of 532 nm working at 5.2 W. The camera is connected to a Scheimpflug system in order to have a proper focus of the measurement section.

10 films are recorded for each configuration (i.e. for each given particle class and rotation rate of the impellers) with a sample rate of 3200 fps at a resolution of 1280×800 at 12 bits (which considering camera's available internal memory gives 8309 images per film, being ∼2.60 s). Therefore, ∼26 s were recorded for granting proper statistical accuracy. The real size of the window measured in the real world is $\sim 4 \times 2$ cm^2. A calibration mask was used for performing pixel to real world transformation.

3 Results

Once the films are recorded, particles centers can be identified with sub-pixel accuracy, by using standard tracking techniques. Then, Voronoï tessellations can be obtained, following [6]. Figure 2 shows the probability density functions (PDF) of

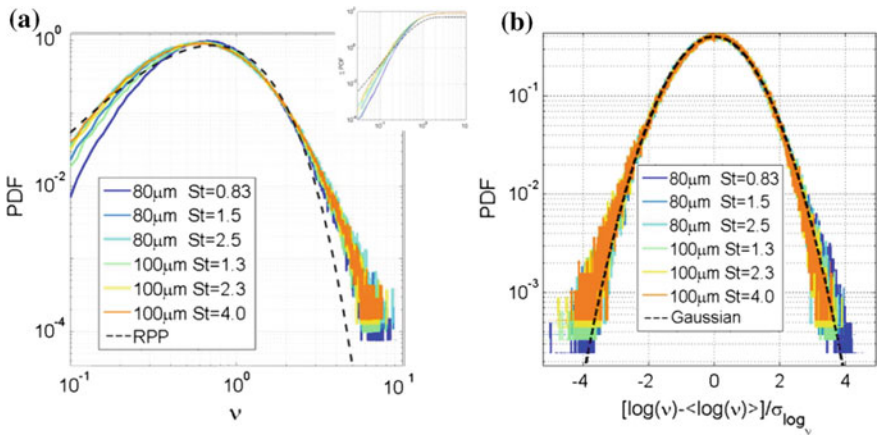

Fig. 2 **a** PDF of normalized Voronoï areas $\mathscr{V}$ for experiments at different Reynolds number and Stokes number. The black dashed line represents a random Poisson process (RPP) distribution. **b** PDF, centered and reduced, of $\log(\mathscr{V})$. The black dashed line represents a Gaussian distribution

the normalised Voronoï area $\mathscr{V} = A/\bar{A}$ (with A the area of a Voronoï cell and $\bar{A}$ their average) and of $\log(\mathscr{V})$ centered and reduced.

It can be clearly seen that the measured distributions are not that of a uniform random process (Fig. 2a). Large Voronoï areas are significantly over-represented compared to the RPP case, indicating the existence of large depleted regions. Similarly, normalized areas between a few tenth (depending on the particle class) and about $\mathscr{V} \sim 0.5$ are over-represented in the experiment compared to a RPP, indicating the preferential concentration phenomenon. Besides, the most probable value for the normalized Voronoï area is smaller for the particles than for a RPP, which indicates the predominance of over-concentrated areas. Much smaller areas are on the contrary under-represented. However, the log-log representation misleadingly exacerbates this under-representation. As shown in the inset in Fig. 2a, showing the cumulative PDF, normalized areas above 0.15–0.3 are already cumulatively more represented with the inertial particles compared to a RPP.

Big Voronoï areas (or depleted regions) are robust when changing particle and flow parameters, while small areas (or concentrated regions) are affected by these changes. This has been already observed in the previous study by Monchaux and collaborators [6] at moderate Reynolds number. In that work it was also observed that the Voronoï area PDFs for inertial particles in turbulence were well approximated by a lognormal distribution. This is confirmed as a robust characteristic also preserved in the higher Reynolds number regime explored in the present study, as it can be seen in Fig. 2b: the PDF of $\log(\mathscr{V})$ is approximately Gaussian, at least within the range $\pm 3\sigma_{\log(\mathscr{V})}$. Deviation from lognormality is only observed for small values of $\log(\mathscr{V})$ which are slightly over-estimated. Therefore, the overall statistical distribution of Voronoï areas is almost characterized entirely by one single parameter, which we choose to be the standard deviation $\sigma_{\mathscr{V}}$ and whose dependency with experimental parameters can be used to quantify the evolution of particles clustering.

Figure 3a shows the standard deviation of normalized Voronoï areas $\sigma_{\mathscr{V}}$ as a function of Stokes number. It can be observed that it is clearly larger than $\sigma_{\mathscr{V}} = 0.53$, that corresponds to a RPP. This is a strong evidence of the formation of clusters and voids in our system, while the amount of clustering tends to grow when St is increased with possibly a saturation or even a reduction for the largest explored Stokes number. This may suggest a maximum of clustering for $St \sim 3$–4, as also observed by Monchaux et al., although the available data here does not allow to be conclusive on this point.

3.1 Clusters

In the present section, we will focus on the identification and characterisation of clusters and voids formed by the particles. One important aspect concerns the analysis of the geometry of the clusters. Do they have a fractal structure? Do they have a characteristic size? As voids present similar properties, we will only present results

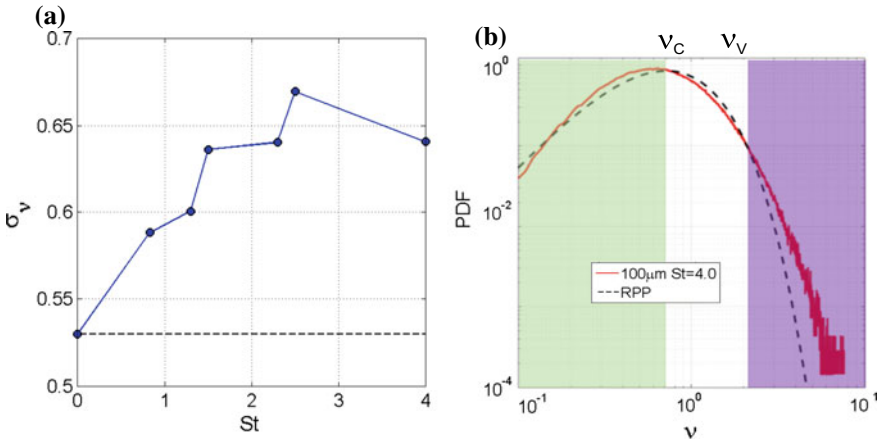

Fig. 3 **a** Standard deviation of normalized Voronoï areas $\sigma_{\mathscr{V}}$ as a function of the Stokes number. The point for $St = 0$ has been artificially added while the black dashed line represents the value $\sigma_{\mathscr{V}} = 0.53$, that correspond to a RPP phenomenon. **b** Schema of clusters and voids detection

from the clusters study (a similar analysis for the voids on this experiment can be found in [9]).

To define a cluster and a void, we follow the idea proposed by Monchaux et al. [6, 7]. Clusters and voids are easily identified by choosing an appropriate threshold for particles local concentration (defined as the inverse of Voronoï cell area) as can be seen in Fig. 3b (where the distribution for higher St of Fig. 2 is shown). The two intersections of the experimental PDF with the RPP closer to the maximum of the distribution are used as thresholds. The values that satisfy $\mathscr{V} < \mathscr{V}_C$ are defined as clusters while the values where $\mathscr{V} > \mathscr{V}_V$ as voids. The values in between are not considered clusters nor voids. The referred work shows the validity of $\mathscr{V}_C$ and $\mathscr{V}_V$ as such thresholds. These two parameters are robust when varying St and Re_λ, as it can be observed in Fig. 2a. The resulting process for obtaining clusters and voids from the centers in real world is shown in Fig. 4.

Once clusters have been identified, their geometry can be analysed. Figure 5a shows the clusters area PDFs, normalised by the mean area value. Surprisingly, all curves collapse and show a clear peak at $\frac{A_V^{max}}{<A_C>} \sim 0.15$. This is a strong experimental evidence of a system with a typical cluster area. We also observe a power law behaviour of area PDF for large events, with an exponent of the order of $-5/3$, slightly less steep than the -2 exponent reported by Monchaux et al., but in good agreement with [11] and the predictions from [3]. Figure 5b shows how the mean value of clusters area varies with St. This value tends to grow with St, and it seems to reach an asymptotic value of the order of 3.5 mm^2 (corresponding to $\sim 100\eta^2$) for $St \sim 4$, although more values would be required to confirm this asymptotic trend.

Aliseda and collaborators [1], working with grid turbulence in a wind tunnel with $Re_\lambda = 75$, using qualitative inspection found that poly-dispersed water droplets

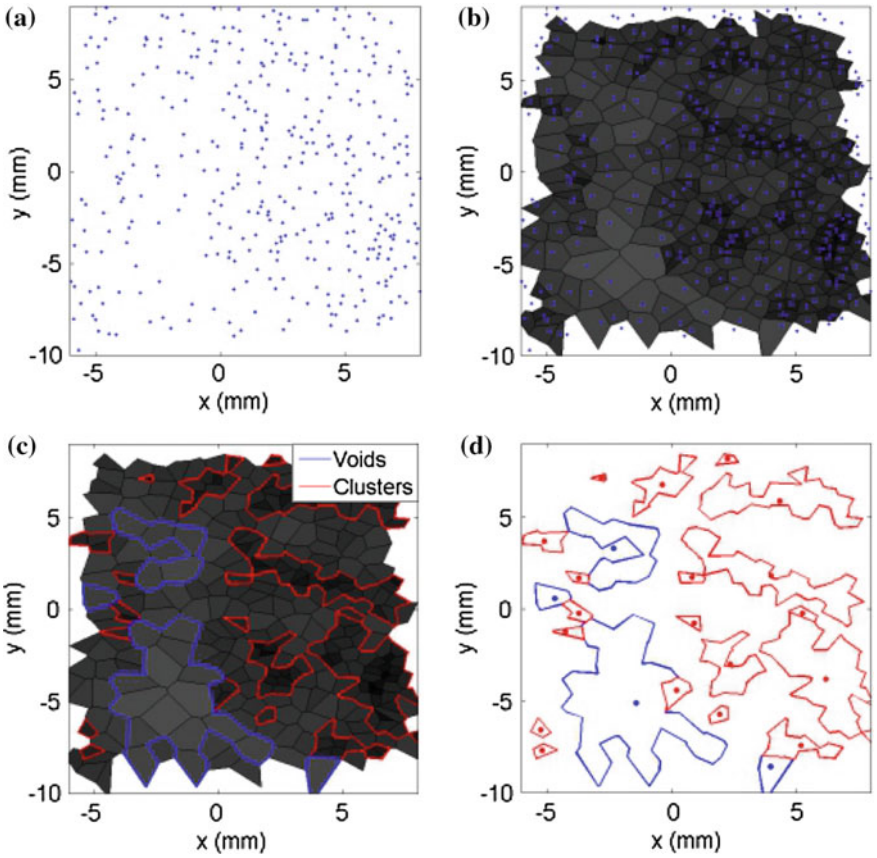

Fig. 4 Schema of clusters and voids detection. Starting from particle's centers in real space (**a**), the Voronoï diagrams are obtained (**b**). With the method explained above, clusters and voids are identified (**c**). In a final step, centers of mass of clusters and voids are calculated (**d**)

form clusters with a typical area of 10η. In order to compare results, Fig. 6a shows $\sqrt{<A_C>}/\eta$ as a function of Re_λ and St. Figure 6b shows the same relationship but considering the most probable cluster area A_C^{max} instead of the average area $<A_C>$ (i.e. the peak of the PDFs of areas in Fig. 5a). The fact that the PDF of clusters area collapses, means that the mean area and the most probable area are simply related by a proportionality relation: $A_C^{max} = C<A_C>$ with $C = 0.15$. Therefore, both curves in Fig. 6 show a similar trend.

Interestingly, the characteristic areas reported here are always bigger than the results reported in [1], the minimum value reaches $\sqrt{A_C^{max}}/\eta = 20$, while the maximum goes up to 50η (Fig. 6c). Such typical dimensions of clusters are larger than previously reported values in experiments with small droplets at larger density ratios (such as [11]) at similar St and Reynolds numbers. The trends are however qualitatively consistent. In particular, Sumbekova et al. reported a strong dependency of

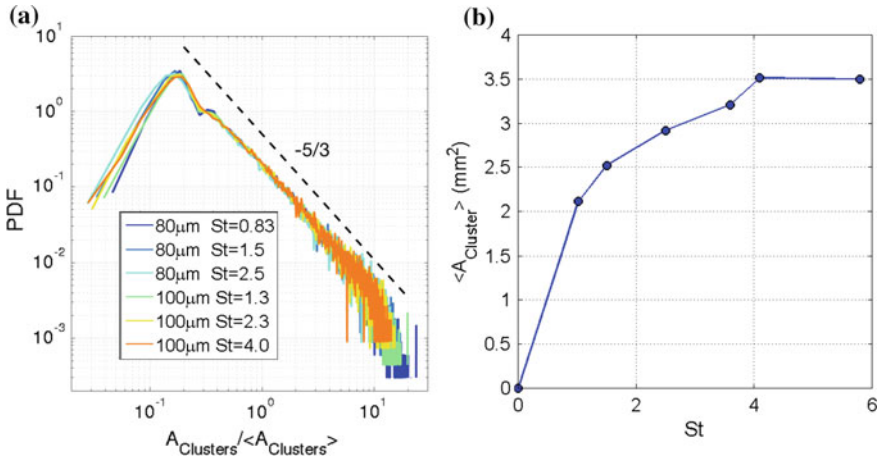

Fig. 5 **a** Clusters area PDFs, normalized by the mean area value. **b** Mean value of clusters area as a function of Stokes number

cluster size with Reynolds number, in agreement with the present observations. Note that in our experiment it is difficult though to clearly disentangle Stokes and Reynolds number dependencies (what would require to systematically vary the actual particle diameters).

Finally, Fig. 6d shows cluster perimeters as a function of the square root of its area. The figure shows many different tendencies but the fractional behavior of the exponent evidences the fractal nature of clusters with the presence of several different populations. Moreover, the almost continuum range for this exponent (ranging from ∼1.4 to ∼3.5) and the differences with previous works evidence the extreme complexity of these structures, and the necessity of further studies for better understanding this phenomenon.

4 Conclusions

Preferential concentration of inertial particles with $\Gamma = 1.4$ in the range $2.8 < d_p/\eta < 6.3$ for $340 < Re_\lambda < 810$ and $0.8 < St < 4$ has been studied. This is an interesting case as it represents particles in the limit between point and finite size particles.

Clear evidence of clustering was observed. The Voronoï analysis in this case allowed us to easily identify clusters and voids and analyse their structure. Clusters PDFs collapse when they are normalised with their mean value and show a maximum for $A_C/<A_C> \sim 0.15$. The typical size of clusters, given for instance by the most probable area of clusters, is found to increase from about 20η up to 50η when the stokes number increases from 1 to 4. The fractal nature of these structures have been

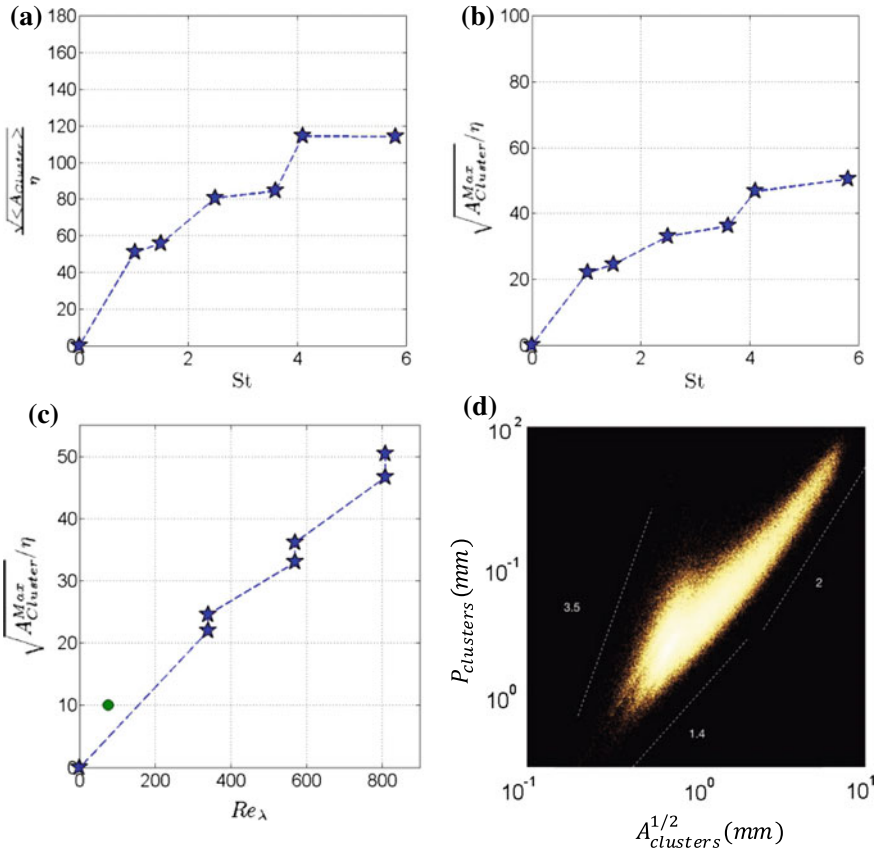

Fig. 6 **a** Square root of the mean value of clusters area, normalized with the Kolmogorov length scale η as a function of Stokes number. **b** Same figure as before but for the peak of cluster area distribution. **c** Value of the peak of cluster area distribution as a function of Re_λ. The green point corresponds to the measurements by Aliseda an collaborators [1]. **d** Clusters perimeters as a function of the squared root of its area

verified, with a complex behaviour that involves many different populations. The cluster properties seems to be qualitatively consistent with the results from [11], studying sub-kolmogorov water droplets in active-grid generated turbulence in a wind tunnel.

Future studies shall aim at systematically varying St and Re_λ independently, to clearly disentangle the specific role of both parameters in clustering properties of inertial particles at moderate density ratio. Comparison with point particle models, including the added mass term, would also be of primary interest to further explore the relevance of those parameters as indicators of clustering.

References

1. Aliseda, A., Cartellier, A., Hainaux, F., Lasheras, J.C.: Effect of preferential concentration on the settling velocity of heavy particles in homogeneous isotropic turbulence. J. Fluid Mech. **468**(1), 77–105 (2002)
2. Fiabane, L., Zimmermann, R., Volk, R., Pinton, J.-F., Bourgoin, M.: Clustering of finite-size particles in turbulence. Phys. Rev. E **86**(3), 035301 (2012)
3. Goto, S., Vassilicos, J.C.: Self-similar clustering of inertial particles and zero-acceleration points in fully developed two-dimensional turbulence. Phys. Fluids **18**, 115103 (2006)
4. Goto, S., Vassilicos, J.C.: Sweep-stick mechanism of heavy particle clustering in fluid turbulence. Phys. Rev. Lett. **100**(5), 054503 (2008)
5. La Porta, A., Voth, G.A., Crawford, A.M., Alexander, J., Bodenschatz, E.: Fluid particle accelerations in fully developed turbulence. Nature **409**(6823), 1017–1109 (2001)
6. Monchaux, R., Bourgoin, M., Cartellier, A.: Preferential concentration of heavy particles: a voronoï analysis. Phys. Fluids **22**, 103304 (2010)
7. Monchaux, R., Bourgoin, M., Cartellier, A.: Analyzing preferential concentration and clustering of inertial particles in turbulence. Int. J. Multiph. Flow **40**, 1–18 (2012)
8. Mordant, N., Metz, P., Michel, O., Pinton, J.-F.: Measurement of Lagrangian velocity in fully developed turbulence. Phys. Rev. Lett. **87**(21), 214501 (2001)
9. Obligado, M.: Fluid-particle interactions: from the simple pendulum to collective effects in turbulence. Ph.D. thesis, Université de Grenoble (2013)
10. Ouellette, N.T., Xu, H., Bourgoin, M., Bodenschatz, E.: Small-scale anisotropy in Lagrangian turbulence. New J. Phys. **8**(6), 102 (2006)
11. Sumbekova, S., Cartellier, A., Aliseda, A., Bourgoin, M.: Preferential concentration of inertial sub-kolmogorov particles: the roles of mass loading of particles, stokes numbers, and reynolds numbers. Phys. Rev. Fluids **2**(2), 024302 (2017)
12. Volk, R., Mordant, N., Verhille, G., Pinton, J.-F.: Laser doppler measurement of inertial particle and bubble accelerations in turbulence. Europhys. Lett. **81**(3), 34002 (2008)
13. Volk, R., Chareyron, D., Pinton, J.-F.: Mesures d'accélération lagrangienne dans un écoulement anisotrope par vélocimétrie laser doppler étendue. 20ème Congrès Français de Mécanique, 28 août/2 sept. 2011-25044 Besançon, France (FR) (2011)
14. Voth, G.A., la Porta, A., Crawford, A.M., Alexander, J., Bodenschatz, E.: Measurement of particle accelerations in fully developed turbulence. J. Fluid Mech. **469**(1), 121–160 (2002)
15. Wang, L.-P., Maxey, M.R.: Settling velocity and concentration distribution of heavy particles in homogeneous isotropic turbulence. J. Fluid Mech. **256**, 27–68 (1993)
16. Zocchi, G., Tabeling, P., Maurer, J., Willaime, H.: Measurement of the scaling of the dissipation at high Reynolds numbers. Phys. Rev. E **50**(5), 3693 (1994)

Relative Dispersion in Direct Cascades of Generalized Two-Dimensional Turbulence

Alexis Foussard, Stefano Berti, Xavier Perrot and Guillaume Lapeyre

Abstract The statistical features of turbulent flows depend on the locality properties of energy transfers among scales. The latter, in turn, may have consequences for the relative dispersion of passive particles. We consider a class of two-dimensional flows of geophysical interest, namely α-turbulence models, possessing different locality properties. We numerically study relative dispersion in such flows using both fixed-time and fixed-scale indicators. The results are compared with predictions based on phenomenological arguments to explore the relation between the locality of the turbulent cascade and that of relative dispersion. We find that dispersion behaviors agree with expectations from local theories, for small enough values of the parameter α (dynamics close to surface quasi geostrophy) and for sufficiently small initial pair separations. Non-local dispersion is instead observed for the largest α considered (quasi-geostrophic model).

A. Foussard · X. Perrot · G. Lapeyre
LMD/IPSL, CNRS/ENS, 24 rue Lhomond, 75005 Paris, France
e-mail: afoussard@lmd.ens.fr

X. Perrot
e-mail: xperrot@lmd.ens.fr

G. Lapeyre
e-mail: glapeyre@lmd.ens.fr

S. Berti (✉)
Université de Lille, Unité de Mécanique de Lille, UML EA 7512, Lille, France
e-mail: stefano.berti@polytech-lille.fr

M. Gorokhovski and F. S. Godeferd (eds.), *Turbulent Cascades II*,
ERCOFTAC Series 26, https://doi.org/10.1007/978-3-030-12547-9_23

1 Introduction

Particle pair dispersion in turbulent flows is a subject of interest for both fundamental studies and applications, e.g. in atmospheric and oceanic sciences. Due to the generally complex relations between particle spreading behaviors and turbulence cascade processes, statistical properties of relative dispersion can be difficult to predict. In two-dimensional (2D) turbulence, enstrophy is transferred towards small scales through a (marginally) nonlocal turbulent cascade for which straining processes at small scales are driven by large-scale eddies [1, 2]. On the contrary, kinetic energy is transferred towards large scales through a local turbulent cascade [1, 2]. The dynamics of pair separation distances are essentially controlled by the strain rate field. It is then reasonable to expect that dispersion properties will be mainly determined by the large-scale strain in the direct enstrophy cascade range of scales, while they will be affected by velocity gradients at scales comparable to the separation distance in the inverse cascade range. For more general turbulent flows, using self-similarity arguments, a relation between the slope of the kinetic energy spectrum and the laws of relative dispersion was proposed [3, 4] separating two different regimes. A first "local" one corresponds to dispersion at a particular lengthscale l only depending on flow features at that lengthscale. This is the case for kinetic energy spectra shallower than k^{-3} (k being the horizontal wavenumber). In this regime pair separation grows as a power-law in time. In a second "nonlocal" regime, corresponding to kinetic energy spectra steeper than k^{-3}, the dispersion law depends on the largest scales of the flow, and separation exponentially grows in time [4].

Several studies investigated the correspondence between relative dispersion laws and energy spectra through the analysis of pair separations data from oceanic [5, 6] and atmospheric [3, 7, 8] field observations, laboratory experiments [9, 10] and numerical simulations [11–13], but the results are still not completely conclusive. Many of these studies reported difficulties to observe a clear relation between the kinetic energy spectral slope and relative dispersion. A commonly stressed reason is the dependence of scaling laws on the initial particle pair separation [11–13].

In this paper we study a class of 2D flows, α-turbulence models [14], all exhibiting double cascades of an active tracer. Kinetic energy spectral slopes depend on the parameter α; energy fluxes are supposed to be ruled by local and nonlocal scale interactions for small and large α, respectively [14]. Our goal is to numerically explore the relation between cascade locality and dispersion behaviors. Two geophysically interesting models belong to this class: the barotropic quasi-geostrophic (QG) and the surface quasi-geostrophic (SQG) model [15]. Both are relevant, in particular, for oceanic dynamics, as the SQG model resembles what occurs at the ocean surface while the QG model resembles what occurs in the interior [16].

2 Theoretical Expectations for Relative Dispersion

We recall here the main properties of relative dispersion in turbulent flows (see, e.g., [17] for a review). Let us consider N particles whose positions at time t, denoted $\mathbf{x}_i(t)$ with $i = 1, \ldots, N$, evolve according to $\dot{\mathbf{x}}_i = \mathbf{u}(\mathbf{x}_i(t), t)$ where $\mathbf{u}$ is a given velocity field. Relative dispersion is defined as

$$\langle y^2(t) \rangle = \langle |\mathbf{x}_i(t) - \mathbf{x}_j(t)|^2 \rangle \tag{1}$$

where $\mathbf{y}(t) = \mathbf{x}_i(t) - \mathbf{x}_j(t)$ is the separation vector between particles i and j and $\langle\ \rangle$ is the average over all particle pairs satisfying $|\mathbf{x}_i(0) - \mathbf{x}_j(0)| = \mathbf{y}_0$. From this, relative diffusivity can be computed as

$$K_{rel}(t) = \frac{1}{2} \frac{d\langle y^2(t) \rangle}{dt} = \langle \delta\mathbf{v}(t) \cdot \mathbf{y}(t) \rangle \tag{2}$$

with the relative velocity defined by $\delta\mathbf{v}(t) = d\mathbf{x}_i/dt - d\mathbf{x}_j/dt = \mathbf{v}(x_i(t), t) - \mathbf{v}(x_j(t), t)$. Assuming that relative velocity is independent of the particle pair separation, i.e. $\langle\, \boldsymbol{\delta}\mathbf{v}(t) \cdot \mathbf{y}_0 \,\rangle = 0$, and posing $\boldsymbol{\delta}\mathbf{v}_0 = \boldsymbol{\delta}\mathbf{v}(t = 0)$, at small enough times one has [18, 19]:

$$\langle y^2(t) \rangle \approx y_0^2 + \langle \delta\mathbf{v}_0 \cdot \delta\mathbf{v}_0 \rangle\ t^2. \tag{3}$$

In the long time limit, one expects that particles are separated by a distance larger than the largest eddies. Relative diffusivity then converges to twice the (constant) absolute diffusivity, due to uncorrelated particle velocities.

At intermediate times for which particle separations are in the inertial range of the turbulent cascade, following [3], it is possible to derive the behavior of relative diffusivity from a dimensional argument. One can apply a local cascade hypothesis using $(kE(k))^{1/2}/k$ as a diffusivity scale, where $E(k)$ is the kinetic energy spectrum. By self-similarity and for a spectrum $E(k) \propto k^{-\beta}$, one expects that

$$\frac{1}{2} \frac{d\langle y^2 \rangle}{dt} \propto \langle y^2 \rangle^{\frac{\beta+1}{4}}; \tag{4}$$

relative dispersion then scales as

$$\langle y^2 \rangle \propto t^{4/(3-\beta)}. \tag{5}$$

For Kolmogorov scaling ($\beta = 5/3$) one obtains Richardson's law $\langle y^2 \rangle \propto t^3$. Previous studies observed finite scale effects in the scaling relations due to the initial separation value (see e.g. [11, 13]). In the sequel we will assess the relevance of such effects in our numerical study of α-turbulence.

A different situation occurs for nonlocal cascades and sufficiently steep ($\beta \geq 3$) spectra. In this case the flow is smooth and relative dispersion grows exponentially in time as

$$\langle y^2 \rangle \propto e^{at}, \tag{6}$$

where a is related to the maximum Lagrangian Lyapunov exponent of the flow or, equivalently, to the square root of enstrophy. Accordingly, one obtains

$$\frac{1}{2}\frac{d\langle y^2 \rangle}{dt} \propto \langle y^2 \rangle \tag{7}$$

for relative diffusivity. The exponential growth of $\langle y^2 \rangle$ is essentially driven by the largest eddies and it does not depend on the slope of the spectrum. From a Lagrangian point of view this corresponds to a regime of "nonlocal dispersion".

Equations (4) and (7) suggest that flows with nonlocal (local) spectral transfers would imply nonlocal (local) dispersion. However, such correspondence could cease to hold if either the spectral transfers receive both local and nonlocal contributions, or the energy spectra are steeper than predicted by the theory.

3 Relative Dispersion in α Turbulence

3.1 Generalized 2D Turbulence

By analogy with usual 2D turbulence, we consider the dynamics of a conserved active tracer q:

$$\frac{\partial q}{\partial t} + \mathbf{u} \cdot \nabla q = 0, \tag{8}$$

where $\mathbf{u} = (-\partial_y \psi, \partial_x \psi)$ is an incompressible flow defined by a streamfunction ψ. The relation between q and ψ is expressed in Fourier space as

$$\widehat{q} = -k^{\alpha}\, \widehat{\psi}, \tag{9}$$

with α a fixed parameter [14]. The case $\alpha = 2$ corresponds to the QG model where q is relative vorticity. For $\alpha = 1$ one has the SQG model with q being temperature.

Such models possess generalized energies and enstrophies that are quadratic invariants. Our interest will be focused on the cascade to small scales of the generalized enstrophy (expressing the variance of the scalar field q). Heuristic arguments based on the locality of the strain rate indicate that the (shell-averaged) kinetic energy spectrum is

$$E(k) \propto k^{-(4\alpha+1)/3} \tag{10}$$

for $\alpha < 2$ [14]. For these models the spectral exponent then is $\beta = (4\alpha + 1)/3$. As the scaling law is obtained taking only into account local quantities (at scale k), this regime is associated with local transfers. For $\alpha \geq 2$ one has, instead, a regime that is associated with nonlocal generalized enstrophy transfers [14], with spectrum

$$E(k) \propto k^{1-2\alpha}. \tag{11}$$

One important consequence of Eq. (10) is that the strain rate between $1/k$ and $2/k$ behaves as $k^{2(2-\alpha)/3}$ for $\alpha < 2$. For these values of α, the dispersion of particles separated by a given distance should then be "local", namely controlled by eddies of comparable size. On the contrary for $\alpha \geq 2$, dispersion will be "nonlocal", i.e. governed by the largest scale eddies. However it has to be reminded that the presence of nonlinear vortices generally tends to steepen the spectra, so that such phenomenological scalings are only an indication on what could be observed.

To explore how local is relative dispersion in α-turbulence, we perform simulations with different values of α (= 1, 1.25, 1.5, 1.75, 2). Equations (8–9) are integrated in a doubly-periodic square box of side 2π in free decay using a pseudo-spectral code at a spatial resolution of 1024^2; an exponential filter provides numerical dissipation at small scales [20]. In order to ease the comparison of runs at different α, we choose to fix the initial generalized energy to a common value in all cases, which gives initial streamfunctions only differing by a constant prefactor. The particle trajectories are integrated using a standard Lagrangian approach with the velocity at particle positions obtained by bicubic interpolation.

After a transient, the statistical properties of the flow evolve more slowly with the continuous decay of the total energy and the system attains a quasi-steady turbulent regime. Figure 1 presents the active tracer fields for $\alpha = 1, 1.5, 2$ in this regime. For $\alpha = 1$ we observe intensified coherent structures from the largest to the smallest scales (Fig. 1a). This is clearly also the case for $\alpha = 1.5$. For greater values of α small-scale eddies tend to be replaced by long, thin and quasi-passive filaments (see Fig. 1c for $\alpha = 2$) as also observed in forced simulations [14].

Figure 2 shows the kinetic energy spectra for different α averaged over several realizations in the quasi-steady regime. From $k = 20$ to $k = 200$, to a good extent, we observe a constant spectral slope in each simulation. For values of $\alpha < 2$, the actual slopes are close to the predictions based on local transfer arguments. For $\alpha = 2$ the observed spectrum is steeper than k^{-3}, probably due to numerical dissipation effects [2]. The positivity of the tracer variance flux for $8 < k < 300$ for all α (not shown) confirms the existence of a direct cascade of q from large to small scales [20].

3.2 Relative Dispersion Statistics

Relative dispersion statistics were computed from up to 2×10^6 particle pairs evolving in each turbulent flow, starting from a uniform particle distribution. The main features of the turbulent dynamics persisted almost unaltered during the particle tracking experiments. Relative dispersion depends on the initial pair separation $y(t = 0) = y_0$ (see also [11–13, 19]), where here and in the following $t = 0$ denotes the instant of particle release. We then choose y_0 such that, for all α, $k_0 = 2\pi/y_0$ is larger than the wavenumber at which the energy spectrum rapidly drops to zero ($k_\nu \approx 350$), and typically $k_0 = 512$. We also performed a computation with $k_0 = 1024$ but for

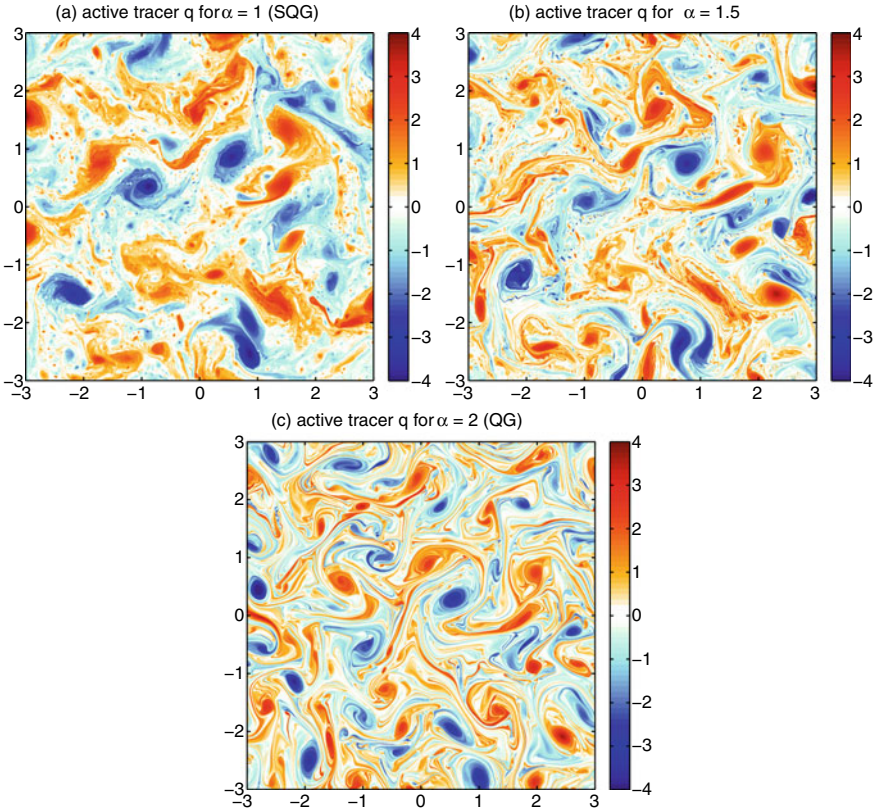

Fig. 1 Active tracer q in the quasi-steady turbulent regime for **a** $\alpha = 1$, **b** $\alpha = 1.5$ and **c** $\alpha = 2$, normalized by $< q^2 >^{1/2}$. The space domain is $[-\pi, \pi]^2$

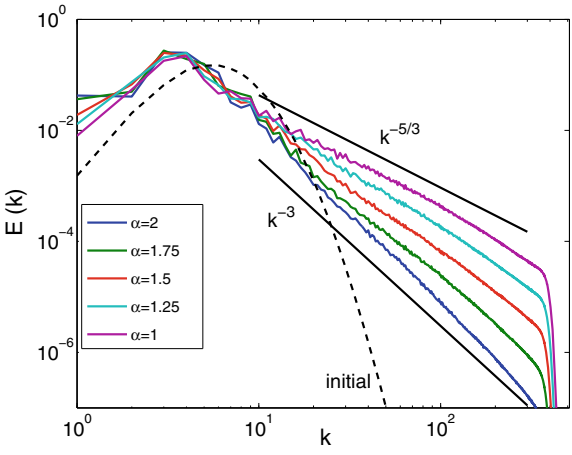

Fig. 2 Kinetic energy spectra normalized by total energy in the quasi-steady turbulent regime

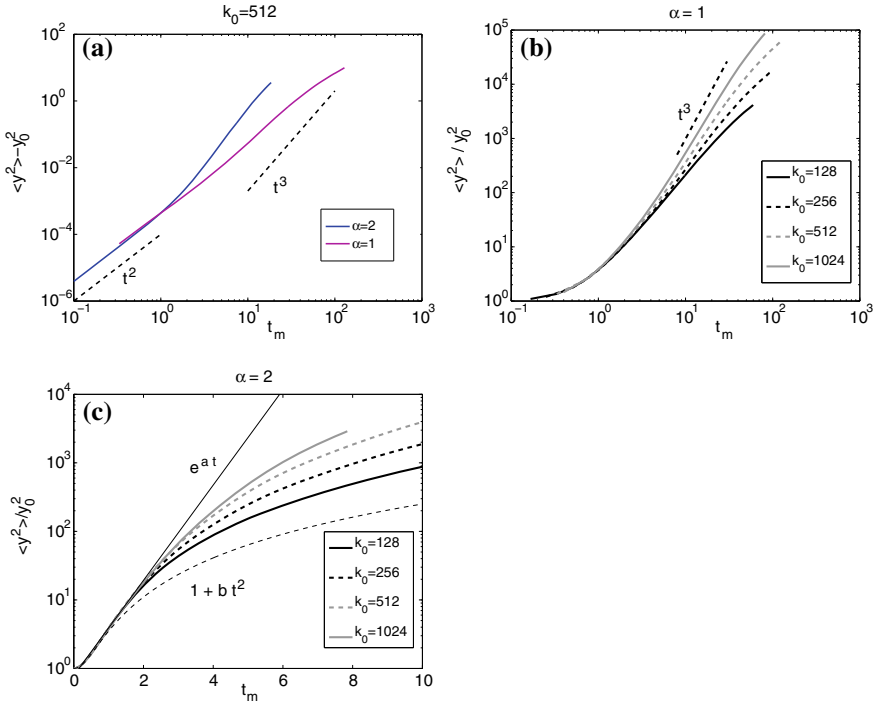

Fig. 3 Relative dispersion (after subtraction of the initial value) as a function of time t_m for fixed $k_0 = 2\pi/y_0$ and $\alpha = 1, 2$ (**a**). Relative dispersion versus t_m for different initial separations (i.e. k_0) for $\alpha = 1$ (**b**) and $\alpha = 2$ (**c**). Here a and b are constant prefactors (see Eqs. (3) and (6))

shorter particle tracking. Simulations revealed that particle pairs lose "memory" of their initial separation, i.e. the early behavior (Eq. (3)), in a common manner during a time interval τ_m that was estimated from the separation autocorrelation function. Note that such memory effects tend to delay the onset of scaling relations. In the following we will then rescale time as $t_m = t/\tau_m$ to facilitate comparisons.

Let us start discussing the results returned by time-dependent statistics. Here we mainly focus on the two limiting cases $\alpha = 1$ and $\alpha = 2$. In agreement with other studies [13, 19], Fig. 3a clearly indicates that the early regime (3) is observed up to a time $t_m \approx 1$, after which the dispersion scale is in the inertial range. At later times, relative dispersion grows in time more slowly than predicted (Eqs. (5–6)). Figure 3b and c display $\langle y^2 \rangle / y_0^2$ as a function of time for different k_0, for $\alpha = 1$ and $\alpha = 2$, respectively. We see that the asymptotic dispersion regime is better realized when increasing k_0. For $\alpha = 1$, relative dispersion tends to approach the theoretical expectation $\langle y^2 \rangle \sim t^3$. For $\alpha = 2$, Fig. 3c suggests that, after the ballistic growth up to $t_m \approx 1$, relative dispersion could grow exponentially, but only for smaller and smaller y_0 and $t_m \leq 2$. Such difficulties to detect clear scalings were noted by other authors [3, 9, 12, 13]. Here two reasons can be invoked. Relative dispersion is a

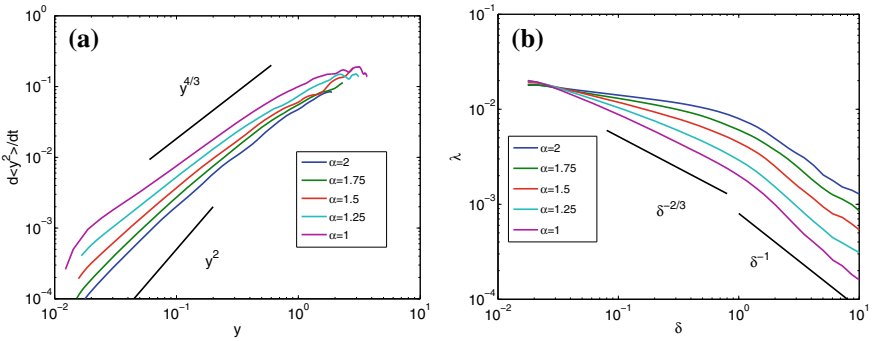

Fig. 4 **a** Diffusivity $d\langle y^2\rangle/dt$ as a function of $y = \langle y^2\rangle^{1/2}$. **b** FSLE (rescaled by Okubo-Weiss parameter, as in [22]) computed from original pairs and with scale separation factor $r = 1.2$. Regimes $\lambda \propto \delta^{-2/3}$ (Richardson dispersion) and $\lambda \propto \delta^{-1}$ are indicated for comparison. In each case, the initial separation corresponds to $k_0 = 512$

fixed-time average and this can lead to spurious behaviors due to averaging together, at fixed time, potentially very different pair separations [21]. Furthermore, due to the weakly non-stationary character of the flow, relative enstrophy slowly decreases in time, causing a temporal variation of the exponential growth rate of $\langle y^2\rangle$ for $\alpha = 2$.

Figure 4a reports relative diffusivity $d\langle y^2\rangle/dt$ as a function of $y = \langle y^2\rangle^{1/2}$. Only data for which the particle pairs have forgotten their initial separation (i.e. $t > \tau_m$) are plotted. Power-law regimes are somehow more evident using this indicator. However, for $\alpha = 2$, the expected y^2 scaling is difficult to observe, even for small y_0 [20]. A better way to disentangle contributions from different flow scales and to diagnose local/nonlocal dispersion is to resort to genuine fixed-scale indicators. To this end one can, e.g., measure the time $\tau(\delta)$ needed for separation to grow from scale δ to scale $r\delta$ (with $r > 1$). The Finite Size Lyapunov Exponent (FSLE) [21] is then defined as

$$\lambda(\delta) = \frac{\log(r)}{\langle \tau(\delta)\rangle} \tag{12}$$

where the brackets indicate an average over all particle pairs. If the kinetic energy spectrum scales as $k^{-\beta}$ the FSLE is expected to be given by

$$\lambda(\delta) \propto \delta^{(\beta-3)/2} \tag{13}$$

for $\beta < 3$ (i.e. $\alpha < 2$). For spectra steeper than k^{-3} ($\alpha \geq 2$), $\lambda(\delta)$ should reach a constant value, implying that dispersion is controlled by nonlocal processes. The behavior of the FSLE is shown in Fig. 4b. For $0.03 < \delta < 0.3$, approximately corresponding to $20 < k < 200$ (for which constant spectral slopes were detected, Fig. 2) we observe a power law $\lambda(\delta) \propto \delta^{-\gamma}$ with an exponent γ that decreases, as β increases, in fair agreement with the theory. The case $\alpha = 2$ displays a considerably weaker scale dependence, with almost constant FSLE up to scales $\delta \approx 0.5$, pointing to an

essentially nonlocal dispersion regime. Finally, independently of the value of α, for $\delta > 1$ $\lambda(\delta)$ decreases faster with δ but note that the behavior at scales $\delta > \pi$ may be affected by the periodicity of the velocity field. The computation of relative displacement probability distributions further confirms the dispersion regimes identified by the FSLE [20].

4 Conclusions

We examined a class of 2D turbulent flows (α-turbulence models), encompassing the QG and SQG models as limiting cases. All these models exhibit a direct cascade of tracer variance to small scales. As expected, the numerically computed kinetic energy spectral slopes are close to phenomenological predictions for $1 \leq \alpha < 2$ while the spectrum was found to be quite steep in our simulations for $\alpha = 2$ (probably due to numerical dissipation effects).

We then analysed relative dispersion by means of both time-dependent and scale-dependent statistics to see to what extent the laws predicted by local self-similarity arguments are verified. As in previous studies, we found that the determination of relative dispersion temporal scaling behaviors is challenging, due to the strong dependence on initial pair separations. In particular, for $\alpha = 2$, exponential growth was possibly observed only for a limited range of time, even for initial separations much smaller than the inertial range scales. On the other hand, fixed-scale statistical indicators were able to reveal it. For $1 \leq \alpha < 2$, relative dispersion was found to grow in agreement with the power-law predictions from local cascade theories. The agreement improves as α approaches 1 and for small initial pair separation.

Acknowledgements This work was supported by TOSCA/CNES as a contribution to the SWOT project. Figures are adapted from [20] (reproduced with permission).

References

1. Kraichnan, R.H.: Phys. Fluids **10**, 1417 (1967)
2. Boffetta, G., Ecke, R.E.: Annu. Rev. Fluid Mech. **44**, 427 (2012)
3. Morel, P., Larcheveque, M.: J. Atmos. Sci. **31**, 2189 (1974)
4. Bennett, A.F.: J. Atmos. Sci. **41**, 1881 (1984)
5. LaCasce, J.H.: Prog. Oceanogr. **77**, 1 (2008)
6. Berti, S., dos Santos, F., Lacorata, G., Vulpiani, A.: J. Phys. Oceanogr. **41**, 1659 (2011)
7. Er-El, J., Peskin, R.L.: J. Atmos. Sci. **38**, 2264 (1981)
8. Lacorata, G., Aurell, E., Legras, B., Vulpiani, A.: J. Atmos. Sci. **61**, 2936 (2004)
9. Jullien, M.-C.: Phys. Fluids **15**, 2228 (2003)
10. Rivera, M.K., Ecke, R.E.: Phys. Rev. Lett. **95**, 194503 (2005)
11. Babiano, A., Basdevant, C., Le Roy, P., Sadourny, R.: J. Fluid Mech. **214**, 535 (1990)
12. Boffetta, G., Sokolov, I.: Phys. Fluids **14**, 3224 (2002)
13. Nicolleau, F., Yu, G.: Phys. Fluids **16**, 2309 (2004)
14. Pierrehumbert, R.T., Held, I.M., Swanson, K.L.: Chaos. Solitons and Fractals **4**, 1111 (1994)

15. Lapeyre, G.: Fluids **2**, 7 (2017)
16. Klein, P., Lapeyre, G., Roullet, G., Le Gentil, S., Sasaki, H.: Geophys. Astrophys. Fluid Dyn. **105**, 421 (2011)
17. Salazar, J.P.L.C., Collins, L.R.: Annu. Rev. Fluid Mech. **41**, 405 (2009)
18. Batchelor, G.K., Meteorol, Q.J.R.: Soc. **551**, 133 (1950)
19. Bourgoin, M., Ouellette, N.T., Xu, H., Berg, J., Bodenschatz, E.: Science **311**, 835 (2006)
20. Foussard, A., Berti, S., Perrot, X., Lapeyre, G.: J. Fluid Mech. **821**, 358 (2017)
21. Aurell, E., Boffetta, G., Crisanti, A., Paladin, G., Vulpiani, A.: J. Rev. A **30**, 1 (1997)
22. Özgökmen, T.M., Poje, A.C., Fischer, P.F., Childs, H., Krishnan, H., Garth, C., Haza, A.C., Ryan, E.: Ocean Model. **52**, 16 (2012)

Thermally Responsive Particles in Rayleigh-Bénard Convection

Kim M. J. Alards, Rudie P. J. Kunnen, Herman J. H. Clercx and Federico Toschi

Abstract The effect of thermal inertia on the dynamics of particles with a thermal expansion coefficient larger than that of the fluid is investigated in Rayleigh-Bénard convection (RBC) using direct numerical simulations. A simple point-particles approach is used, where thermal expansion of both particles and fluid is included. These thermally responsive particles move towards the hot (bottom) or cold (top) plates, where they become lighter or heavier than the fluid to eventually escape this region of the flow. When the thermal response time of particles is large, this process is slow and particles spend more time at the walls than in the bulk. It is indeed shown that in this regime the number of particles at the plates is enhanced, com-

K. M. J. Alards · R. P. J. Kunnen · H. J. H. Clercx · F. Toschi (✉)
Fluid Dynamics Laboratory, Department of Applied Physics, Eindhoven University of Technology, P.O. Box 513, 5600 Eindhoven, MB, The Netherlands
e-mail: f.toschi@tue.nl

F. Toschi
Centre of Analysis, Scientific Computing, and Applications W&I, Department of Mathematics and Computer Science, Eindhoven University of Technology, P.O. Box 513, 5600, MB Eindhoven, The Netherlands

F. Toschi
Istituto per le Applicazioni del Calcolo, Consiglio Nazionale delle Ricerche, Via dei Taurini 19, 00185 Rome, Italy

M. Gorokhovski and F. S. Godeferd (eds.), *Turbulent Cascades II*,
ERCOFTAC Series 26, https://doi.org/10.1007/978-3-030-12547-9_24

pared to the uniform distribution found for tracer particles in RBC. A more complex point-particle approach, including non-linear effects on the drag forces, shows that non-linear thermal effects influence both the temperature and velocity statistics of the thermally responsive particles and cannot be ignored.

1 Introduction

Non-isothermal particle-laden flows know many applications in nature, e.g. pollution by aerosols in the atmosphere [1], and in industry, e.g. food processing. To understand the dynamics of these particles in non-isothermal turbulence, it is important to understand the interaction between particles and fluid, such as the heat transfer. When the heat transfer between particles and fluid is not instantaneous, thermal inertia of particles has to be taken into account. The time-scale of thermal inertia is characterized by the thermal response time, that depends on the specific heat of the particle material and the surrounding fluid. When the size of particles is temperature-dependent, such as, for example, in the case of bubbles [4, 7], this thermal inertia can significantly change the motion of particles. In this study, the temperature dependency of particle and fluid properties is included as a linear volumetric expansion of particles and fluid with temperature. Like this, we can model dispersed systems with two different materials based on their thermal expansion coefficients; from fluid-fluid systems to the motion of gel-like particles in a turbulent flow.

The behavior of such thermally responsive particles is studied in a turbulent Rayleigh–Bénard convection flow; a confined fluid heated from below and cooled from above. We use a simple point-particle approach to study the dynamics of the inertial particles and compare it to the behavior of passive tracers that perfectly follow the flow. In particular, we model particles with a thermal expansion coefficient larger than that of the fluid, such that particles become lighter than the fluid, close to the hot plate, and heavier than the fluid, close to the cold plate. This is expected to induce an upwards motion on the particles at the bottom plate and vice-versa at the top plate. We investigate the effect of this dynamics on the distribution of particles within the RBC cell.

While the point-particle approach can be extended, e.g. to include the effect of non-linear flow and temperature gradients around the particles [2, 3], it is not clear how this will effect the velocity and temperature statistics of the thermally responsive particles. Here we discuss the influence of the non-linear drag terms to understand the importance of including such effects in the point-particle model.

2 Numerical Method

The RBC flow is described by the incompressible Navier–Stokes equations in the Boussinesq approximation:

$$\nabla \cdot \mathbf{u}_f = 0, \tag{1}$$

$$\frac{\partial \mathbf{u}_f}{\partial t} + (\mathbf{u}_f \cdot \nabla)\mathbf{u}_f = -\nabla p + \sqrt{\frac{Pr}{Ra}}\nabla^2 \mathbf{u}_f + T_f \hat{\mathbf{z}}, \tag{2}$$

$$\frac{\partial T_f}{\partial t} + (\mathbf{u}_f \cdot \nabla)T_f = \frac{1}{\sqrt{PrRa}}\nabla^2 T_f, \tag{3}$$

where $\mathbf{u}_f$ and T_f are the fluid velocity and temperature, respectively. The control parameters for the RBC flow are the Rayleigh number, $Ra = g\alpha_f \Delta T H^3/(\nu\kappa)$ and the Prandtl number, $Pr = \nu/\kappa$, where ν is the kinematic viscosity, κ is the thermal diffusivity, α_f is the thermal expansion coefficient of the fluid and g is the gravitational acceleration. Equations are non-dimensionalized using the cell height, H, for length, the temperature difference between the plates, ΔT, for temperature and $t_c = H/U$ for time, based on the free-fall velocity $U = \sqrt{g\alpha_f \Delta T H}$. In the horizontal directions periodic boundary conditions (BCs) are applied, while at $z = 0$ and $z = 1$ no-slip BCs are applied and the temperature is fixed as $T_f(z = 0) = 1$ and $T_f(z = 1) = 0$. The domain is discretized into $128 \times 128 \times 128$ grid points with at least ten grid points in the viscous and thermal boundary layers (BLs). A finite difference scheme is applied to discretize Eqs. (2)–(3) and time integration is performed using a third order Runge–Kutta scheme (a detailed description of this method is given in [9, 10]). The RBC flow studied here is characterized by $Ra = 2 \cdot 10^7$ and $Pr = 6.7$.

In this RBC flow $1.6 \cdot 10^5$ tracer particles are evolved and a tri-linear interpolation scheme is used to interpolate the fluid velocity and temperature at the position of the passive tracers. On top of the tracer particles, $1.6 \cdot 10^5$ thermally inertial particles are inserted, that are modeled using the approach proposed by Maxey and Riley [5] for the mechanical inertia and by Michaelides and Feng [6] for the thermal inertia, where for the moment we leave out the non-linear contributions in the drag terms. The equations for the velocity of particles, $\mathbf{u}_p$, and the temperature of particles, T_p, are

$$\left(1 + \frac{1}{2\beta}\right)\frac{d\mathbf{u}_p}{dt} = \frac{1}{\tau_p}\left(\mathbf{u}_f - \mathbf{u}_p\right) + \frac{1}{2\beta}\frac{D\mathbf{u}_f}{Dt} - \left(1 - \frac{1}{\beta}\right)g\hat{\mathbf{z}} \tag{4}$$

$$\frac{dT_p}{dt} = \frac{1}{\tau_T}\left(T_f - T_p\right), \tag{5}$$

where β is the ratio between the density of particles and the density of the fluid, $\beta = \rho_p/\rho_f$, and $\tau_p = 2\beta r_p^2/(9\nu)$ and $\tau_T = \beta\gamma r_p^2/(3\kappa)$ are the viscous and thermal response times, respectively, with r_p the particle radius and $\gamma = c_p/c_f$ the ratio between the specific heat of the particle material and the specific heat of the fluid. The terms on the right-hand-side (rhs) of Eq. (4) represent Stokes drag, added mass and gravity, respectively.

We take into account that both particles and fluid can expand or shrink as a result of temperature fluctuations, by including linear thermal expansion of both particles and fluid. This means that the radius of particles is a function of $T_p' = T_p - \langle T_p \rangle$, with $\langle ... \rangle$ the average over time and space, as

$$r_p = r_0 \left(1 + \frac{1}{3}\alpha_p T_p'\right), \tag{6}$$

where a Taylor expansion is used in the limit of small temperature fluctuations, neglecting higher order terms, α_p is the thermal expansion coefficient of particles and r_0 is the radius of particles at the average temperature. Now also the density of particles depends on temperature fluctuation and the density ratio β becomes,

$$\beta = \frac{1 - \alpha_p T_p'}{1 - \alpha_f T_f'}, \tag{7}$$

where $T_f' = T_f - \langle T_f \rangle$ and we assumed that both $\rho_p = \rho_f = 1$ at the average temperature. Note that the viscous and thermal response times, that both depend on β and r_p, now depend on temperature fluctuations as well. In this study we fix the properties of the thermally inertial particles at the average temperature as $\tau_p = 0.038$, $\tau_T = 1$ and $r_0 = 0.01$. The ratio between the thermal expansion coefficient of the particles and that of the fluid is set to $K = \alpha_p/\alpha_f = 2$.

3 Results

Thermally inertial particles are transported to the horizontal plates in the RBC cell, due to the large scale circulation of rising hot fluid and descending cold fluid and due to their mechanical inertia. Particles deposited at the plates are expected to move back towards the bulk after some characteristic time due to thermal expansion, where the thermal expansion coefficient of particles is larger than that of the fluid. First, we visualize the particles at the hot bottom plate for both tracers and thermally inertial particles in Fig. 1. While tracers have a temperature equal to that of the fluid (Fig. 1a),

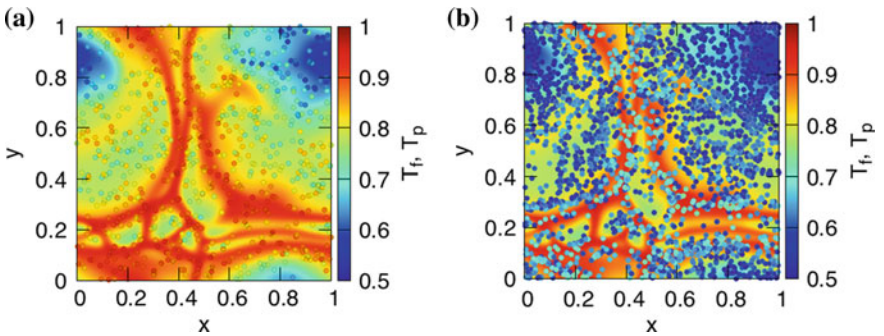

Fig. 1 The temperature field of the fluid in a horizontal slab at $z = 0.009H$ in Rayleigh–Bénard convection (with H the height of the cell), together with **a** tracer particles and **b** thermally inertial particles. All particles with $z < 0.012H$ are shown and particles are colored with their (non-dimensional) temperature, T_p. Length scales are non-dimensionalized by the cell height H

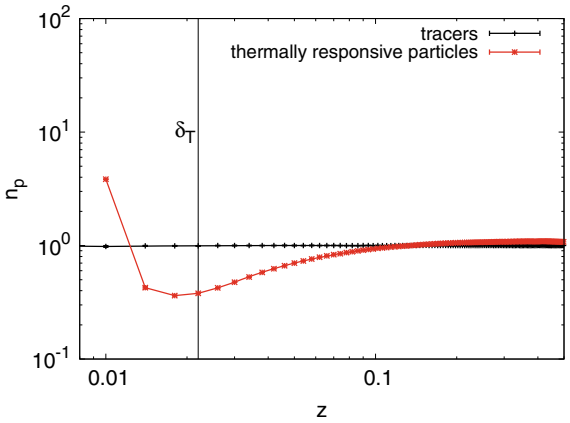

Fig. 2 The vertical distribution of tracer particles (black) and thermally responsive particles (red) in Rayleigh-Bénard convection. n_p represents the number density of particles, averaged over the horizontal directions and over time and z is non-dimensionalized with the cell height H. The vertical line corresponds to the thermal boundary layer length, $\delta_T \approx 0.022H$. Error bars fall within the symbols

the temperature of thermally inertial particles differs from the fluid temperature, as visible in Fig. 1b. In this figure particles are clearly colder than the surrounding fluid. Warmer particles, that are lighter than the fluid, immediately escape the hot bottom plate, while colder heavier particles stay in this region of the flow for a longer time. This also explains why the number of particles at the plate has increased in Fig. 1b when including thermal inertia with $\tau_T = 1$, compared to tracer particles in Fig. 1a.

Thermal expansion of thermally inertial particles is expected to lead to a non-uniform distribution of particles in the vertical direction of the RBC cell. An enhanced number of particles inside the thermal BL (for large enough thermal response time) is expected, and indeed confirmed in Fig. 2, where the vertical distribution of tracer particles and thermally response particles is shown. This vertical distribution is quantified by counting particles in horizontal slabs of thickness $\Delta z = 0.004H$ and average this number over time and in the horizontal directions. Furthermore, only the bottom half of the domain is shown, which is sufficient due to symmetry. Apart from an enhanced number of thermally responsive particles at the plate, a depletion is observed at a distance of approximately the thermal boundary layer length, δ_T, from the plate, related to the larger upwards velocity gained by particles at the hot plate.

So, a simple version of the point-particle approach, where only Stokes drag, added mass and gravity are included (Eq. (4)), captures the effect of thermal expansion qualitatively; particles move towards the plates, expand or shrink due to the heat exchange with the surrounding fluid and then escape the BL region to move back towards the bulk.

However, since we are studying particles with a particle Reynolds number of $Re_p = 2r_p|\mathbf{u}_f - \mathbf{u}_p|/\nu \approx 10$, effects of a non-linear velocity and temperature gradient can become important. This effect is included in the point-particle model by

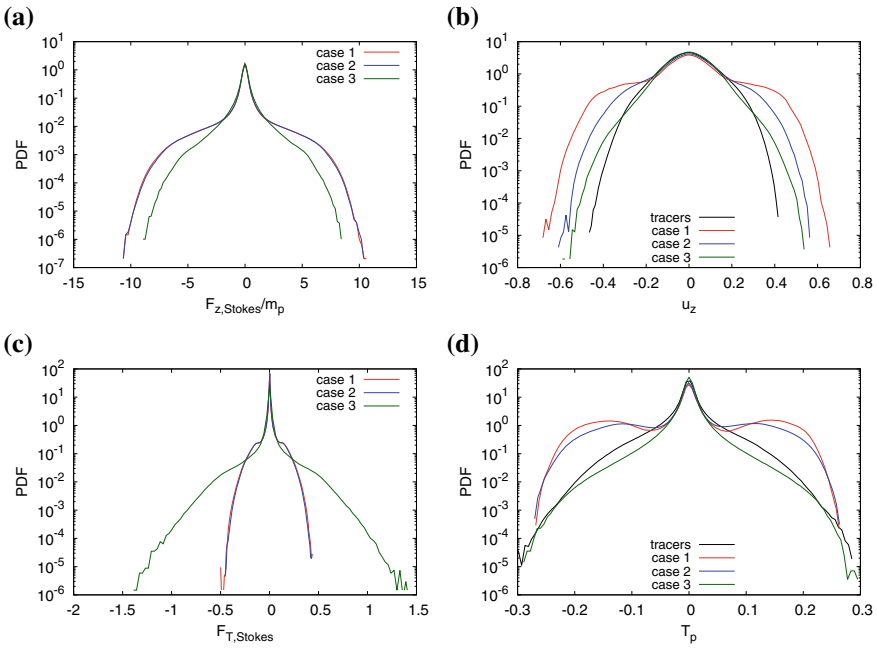

Fig. 3 **a** PDFs of the contribution of the Stokes drag in the vertical direction, $F_{z,Stokes}/m_p$, with m_p the mass of a particle, for three different types of thermally responsive particles in Rayleigh-Bénard convection; case 1 (linear Stokes drag and linear thermal drag, red), case 2 (non-linear Stokes drag and linear thermal drag, blue) and case 3 (non-linear Stokes and non-linear thermal drag, green). $F_{z,Stokes}$ is non-dimensionalized by U^2/H. **b** PDFs of the vertical velocity for the three cases of thermally inertial particles, together with tracer particles (black). **c** PDFs of the contribution of the thermal drag, $F_{T,Stokes}$, for the three different cases of thermally inertial particles, where $F_{T,Stokes}$ is non-dimensionlized by $\Delta TU/H$. **d** PDFs of the particle temperature, T_p, for the three different cases of thermally inertial particles, together with tracer particles (black), where the temperature is non-dimensionalized by the temperature difference ΔT

replacing the first terms on the rhs of Eq. (4) and Eq. (5), representing the drag forces, by $1/\tau_p(\mathbf{u}_f - \mathbf{u}_p)(1 + 0.15Re_p^{0.687})$ and $1/\tau_T(T_f - T_p)(1 + 0.3Re_p^{1/2}Pr^{1/3})$, respectively [2, 8]. Here we try to understand the influence of non-linear drag, in both the mechanical and thermal inertia of particles, by comparing statistics of three types of thermally inertial particles; one without non-linear effects, one with only non-linear mechanical Stokes drag and one with both non-linear mechanical and non-linear thermal drag. We will refer to these three types of particles as case 1, case 2 and case 3.

First, we focus on the contribution of the non-linear Stokes drag in Eq. (4), computing PDFs of the Stokes drag in Fig. 3. The PDFs for case 1 and case 2 are very similar and indeed for the low viscous response time used here, $\tau_p = 0.038$, non-linear effects in the mechanical inertia are expected to have very little effect. When including also non-linear effects in the thermal drag, the contribution of mechanical Stokes drag has decreased in the tails of the PDFs. This means that the fluctuations

in the velocity difference between particles and fluid have decreased, as indeed confirmed by the velocity statistics shown in Fig. 3b. Since the temperature of particles only influences the motion through the buoyancy term in Eq. (4) this indicates that the contribution of this buoyancy terms has decreased as well.

A decrease of the buoyancy term can be a result of lower temperature differences between particle and fluid. We can quantify this effect by computing the statistics of the contribution of the thermal drag term in Eq. (5). In Fig. 3c it is shown that the thermal drag is enhanced when non-linear effects are included. The effect on the temperature statistics is shown in Fig. 3d, where non-linear thermal drag is shown to push the temperature of thermally responsive particles closer to that of tracers and therefore to that of the fluid. The increase in the contribution of the thermal drag is thus a result of the non-linear term and can be seen as an effective decrease in the thermal response time, considering that the thermal drag force is inverse proportional to τ_T (Eq. 5). Consequently, particles need less time to adjust their temperature to that of the surrounding fluid, explaining why the temperature of particles is closer to that of the fluid when non-linear thermal drag is included. Due to the thermal expansion, which is coupling the motion of particles to the temperature fluctuations, also the velocity statistics is closer to that of tracer in this case.

Including non-linear drag, affects the temperature statistics and is therefore also expected to affect the vertical distribution of particles within the RBC cell. This distribution is shown in Fig. 4, for all three cases of thermally responsive particles and tracer particles. Again the behavior is closer to that of tracers when including non-linear thermal drag. However, also when using this extended version of the

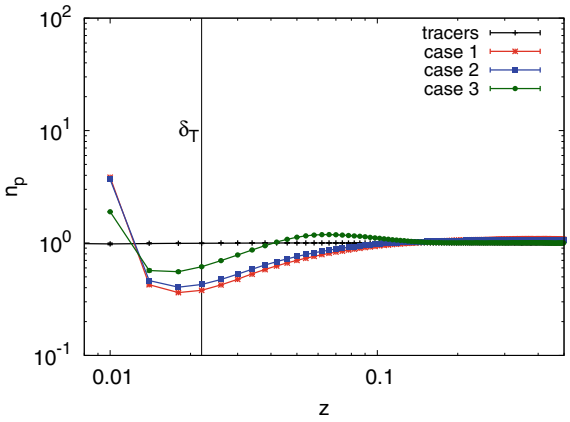

Fig. 4 The vertical distribution of tracer particles (black) and three different types of thermally responsive particles in Rayleigh-Bénard convection; case 1 (linear Stokes drag and linear thermal drag, red), case 2 (non-linear Stokes drag and linear thermal drag, blue) and case 3 (non-linear Stokes and non-linear thermal drag, green). n_p represents the number density of particles, averaged over the horizontal directions and over time and z is non-dimensionalized with the cell height H. The vertical line corresponds to the thermal boundary layer length, $\delta_T \approx 0.022H$. Error bars fall within the symbols

point-particle approach, the effect of thermal expansion is again observed as an enhancement in the number of particles at the plates and a depletion at a distance of about δ_T from the plate.

4 Conclusions

The influence of thermal inertia on the dynamics of thermally responsive particles, with a thermal expansion coefficient larger than that of the surrounding fluid, is investigated. It was shown that these thermally responsive particles are deposited at the plates and cluster there, before moving back towards the bulk when becoming lighter (at the bottom plate) or heavier (at the top plate) than the surrounding fluid. On average this results in a non-uniform distribution of particles in the vertical direction of the RBC cell, with an enhanced number of particles at the plates.

Although the simple point-particle model captures the dynamics of these thermally expanding particles with a particle Reynolds number of about $Re_p \sim 10$ qualitatively, non-linear thermal drag is shown to be of importance. In particular, including the non-linear temperature field around the particle, results in particle temperatures being closer tot hat of the fluid due to a lower effective thermal response time. Due to the temperature dependent density ratio in the buoyancy term, not only the temperature statistics is influenced by these non-linear thermal effects but also the velocity statistics are pushed towards that of tracers when including non-linear thermal drag. When investigating the behavior of these thermally inertial particles and the effect of thermal inertia on this dynamics in more detail, it is recommended to use a more complex version of the point-particle approach, including non-linear effects of the temperature field in the thermal drag.

Acknowledgements This work is supported by the Nederlandse Organisatie voor Wetenschappelijk Onderzoek (NWO), the Netherlands. The authors gratefully acknowledge the support of the NWO for the use of supercomputer facilities (Cartesius) under Grant No. 16289. EU-COST action MP1305 'Flowing matter' is kindly acknowledged.

References

1. Ackerman, A.S., Kirkpatrick, M.P., Stevens, D.E., Toon, O.B.: The impact of humidity above stratiform clouds on indirect aerosol climate forcing. Nature **432**(7020), 1014–1017 (2004)
2. Armenio, V., Fiorotto, V.: The importance of the forces acting on particles in turbulent flows. Phys. Fluids **13**(8), 2437–2440 (2001)
3. Clift, R., Grace, J.R., Weber, M.E.: Bubbles, Drops, and Particles. Academic, New York (1978)
4. Lakkaraju, R., Schmidt, L.E., Oresta, P., Toschi, F., Verzicco, R., Lohse, D., Prosperetti, A.: Effect of vapor bubbles on velocity fluctuations and dissipation rates in bubbly Rayleigh-Bénard convection. Phys. Rev. E **84**, 036,312 (2011)
5. Maxey, M.R., Riley, J.J.: Equation of motion for a small rigid sphere in a nonuniform flow. Phys. Fluids **26**(4), 883–889 (1983)

6. Michaelides, E.E., Feng, Z.: Heat transfer from a rigid sphere in a nonuniform flow and temperature field. Int. J. Heat Mass Transf. **37**(14), 2069–2076 (1994)
7. Oresta, P., Verzicco, R., Lohse, D., Prosperetti, A.: Heat transfer mechanisms in bubbly Rayleigh–Bénard convection. Phys. Rev. E **80**, 026,304 (2009)
8. Ranz, W.E., Marshall, W.R.: Evaporation from droplets, parts i and ii. Chem. Eng. Prog. **48**(4), 173–180 (1952)
9. van der Poel, E.P., Ostilla-Mónico, R., Donners, J., Verzicco, R.: A pencil distributed finite difference code for strongly turbulent wall-bounded flows. Comput. Fluids **116**, 10–16 (2015)
10. Verzicco, R., Camussi, R.: Numerical experiments on strongly turbulent thermal convection in a slender cylindrical cell. J. Fluid Mech. **477**, 19–49 (2003)

Part VII
Interplay of Waves and Turbulence

The Energy Cascade of Surface Wave Turbulence: Toward Identifying the Active Wave Coupling

Antoine Campagne, Roumaissa Hassaini, Ivan Redor, Joel Sommeria and Nicolas Mordant

Abstract We investigate experimentally turbulence of surface gravity waves in the Coriolis facility in Grenoble by using both high sensitivity local probes and a time and space resolved stereoscopic reconstruction of the water surface. We show that the water deformation is made of the superposition of weakly nonlinear waves following the linear dispersion relation and of bound waves resulting from non resonant triadic interaction. Although the theory predicts a 4-wave resonant coupling supporting the presence of an inverse cascade of wave action, we do not observe such inverse cascade. We investigate 4-wave coupling by computing the tricoherence i.e. 4-wave correlations. We observed very weak values of the tricoherence at the frequencies excited on the linear dispersion relation that are consistent with the hypothesis of weak coupling underlying the weak turbulence theory.

1 Introduction

Wave Turbulence is a general framework that aims at describing the statistical properties of a large ensemble of waves. Although no general theory exists, the Weak Turbulence Theory (WTT) focusses on the case of vanishing non linearity in very large systems [1–3]. It predicts an energy cascade in scale space between the large scale of forcing down to small scales at which dissipation dominates. Due to weak nonlinearity energy transfer occurs among resonant waves. Oceanic waves is the

A. Campagne · R. Hassaini · I. Redor · J. Sommeria · N. Mordant (✉)
LEGI, Grenoble, France
e-mail: nicolas.mordant@univ-grenoble-alpes.fr

A. Campagne
e-mail: antoine.campagne@univ-grenoble-alpes.fr

R. Hassaini
e-mail: roumaissa.hassaini@univ-grenoble-alpes.fr

I. Redor
e-mail: ivan.redor@univ-grenoble-alpes.fr

J. Sommeria
e-mail: joel.sommeria@legi.cnrs.fr

M. Gorokhovski and F. S. Godeferd (eds.), *Turbulent Cascades II*,
ERCOFTAC Series 26, https://doi.org/10.1007/978-3-030-12547-9_25

natural field of application of the theory following the work of Hasselman [4] that assumes transfer among 4 resonant waves. A major result of the WTT is that analytic solutions of the wave Fourier spectrum can be exhibited in many cases, the so-called Kolmogorov-Zakharov spectra. For gravity surface waves the prediction of the wave elevation spectrum is [2]:

$$E^{\eta}(k) \propto g^{1/2} P^{1/3} k^{-5/2} \tag{1}$$

$$\text{or } E^{\eta}(\omega) \propto g P^{1/3} \omega^{-4} \tag{2}$$

where g is the gravity acceleration, P is the energy flux, k is the wave number and ω the angular frequency. Although some field measurements of the spectra appear compatible with this prediction, laboratory experiments fail to reproduce this prediction. The observed spectral exponents of the frequency spectrum are significantly steeper than the -4 theoretical value [5–7]. Our goal is to investigate further the statistical properties of the wave field recorded experimentally to obtain some insight on the reasons for the discrepancy between theory, observations and laboratory data. For surface gravity wave, due to the 4-wave coupling, the theory predicts also an inverse cascade of wave action [2] that maybe responsible for the long wave generation by the wind.

2 Experimental Setup

Waves are generated by two wedge wavemakers in a circular tank of 13 m diameter and 0.9 m depth (the Coriolis facility located in Grenoble, France). Wave elevation is recorded by a set of 10 capacitive wave gauges that provide a local measurement and a stereoscopic system that provides a space and time resolved measurement of the wave elevation over a surface $2 \times 2.6\ \text{m}^2$ (Fig. 1).

Three datasets are acquired with distinct generation and called *weak*, *strong* and *short* (see Table 1). The waves are generated by oscillating the wavemakers with a random modulation of amplitude ± 0.15 Hz around a central frequency f_p with a vertical amplitude of 2 cm. The *weak* dataset corresponds to the lowest peak frequency and a moderate wave steepness $\varepsilon_p = 0.11$. In the *strong* dataset the wavemakers are operated at a slightly higher frequency at which they are more efficient and thus the steepness is larger $\varepsilon_p = 0.16$. The *short* datasets corresponds to smaller wavemakers that are operated at a higher frequency (1.5 Hz) so that to generate shorter waves and investigate the possible generation of an inverse cascade. The stepness is very large in this case.

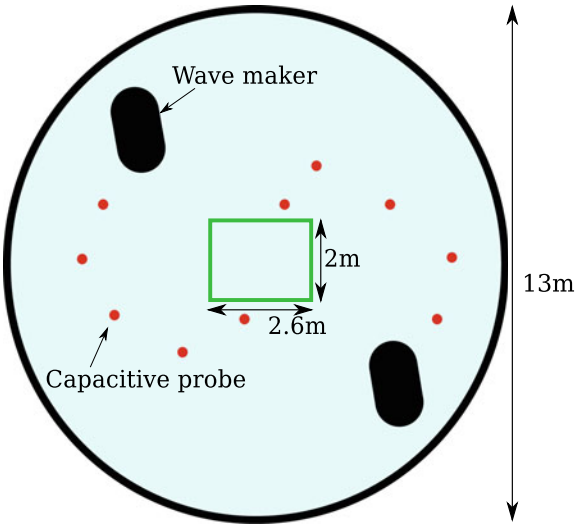

Fig. 1 Schematics of the setup in the Coriolis facility. The tank is 13 m in diameter and the water is 0.9 m deep. The position of the two wavemakers is shown as black ovals and that of the 10 capacitive probes is shown as red dots. The field of view of the stereoscopic reconstruction is the green rectangle at the center

Table 1 Parameters of the three datasets. f_p is the frequency of the peak of the spectrum. k_p is the wavenumber corresponding to f_p following the linear dispersion relation. σ_η is the elevation variance. ε_p is the wave steepness computed as $\varepsilon_p = 2k_p\sigma_\eta$ (see [7])

Dataset	f_p (Hz)	k_p (m^{-1})	σ_η (m)	ε_p
Weak	0.65	1.83	0.0294	0.11
Strong	0.76	2.4	0.0339	0.16
Short	1.5	9.05	0.0131	0.24

3 Fourier Spectra

Frequency Fourier spectra are shown in Fig. 2 for all three datasets. A turbulent spectrum is generated at frequencies higher that the peak frequency. At change of slope is observed at 14 Hz that corresponds to the gravity-capillary crossover. At frequencies lower than the peak frequency, the wave spectrum is two orders of magnitude lower than at the peak frequency meaning that no inverse cascade is observed even for the *short* dataset. This observation raises the question of the relevance of the 4-wave coupling in our experiment.

Figure 3 displays the full frequency-wavenumber spectrum $E^\eta(\omega, k)$ corresponding to the *weak* case. A strong concentration of the energy is observed on the linear dispersion relation (LDR, red curve) that follows:

$$\omega_{LDR} = \sqrt{gk + \frac{\gamma k^3}{\rho}}, \tag{3}$$

where ω_{LDR} is the angular frequency, k is the wavenumber, g is the gravity acceleration, γ is the surface tension and ρ is the density of water. This shows that most of

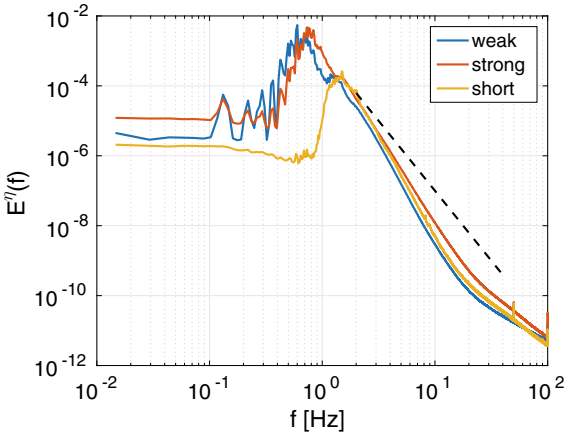

Fig. 2 Frequency spectrum $E^{\eta}(f)$ of the surface elevation for the three datasets

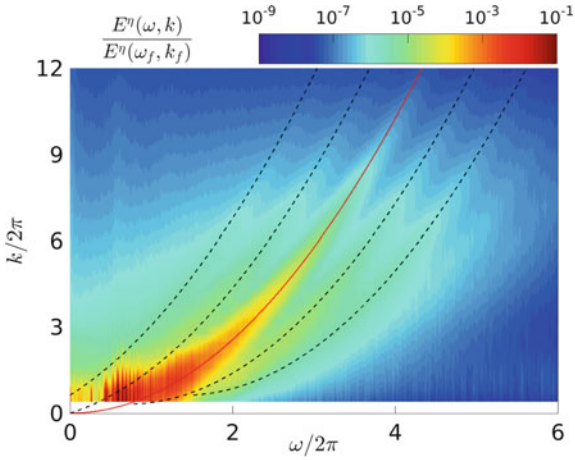

Fig. 3 $k-\omega$ spectrum $E^{\eta}(\omega,k)$ for $\varepsilon = 0.11$ ("weak" case). The spectrum has been normalized by its value at the forcing and is displayed in $\log_{10}$ scale. The red line is the linear dispersion relation (3) and the dashed lines corresponds to bound waves (4) (see text)

the energy is made of freely propagating waves. Nevertheless a significant amount of the energy lies out of the linear dispersion relation. In particular several lines can be distinguished that are highlighted by the black dashed lines. These lines where constructed by translating the dispersion relation by multiples of the forcing peak so that the equations of the dashed lines are

$$\omega^{(\pm n)} = \omega_{LDR}(k \mp nk_p) \pm n\omega_p \,, \tag{4}$$

with n being an integer either positive or negative. For instance for $n = \pm 1$, energy can be transferred on the first dashed line (on the left or right of the LDR) by triadic interactions between a free wave that lies on the peak of the spectrum at position (ω_p, k_p) and another wave on the LDR $(\omega_{LDR}(k), k)$. Energy is thus transferred to position $(\omega_{LDR}(k) \pm \omega_p, k \pm k_p)$. For $|n| > 1$, the same process implies successive harmonics of the forcing peak. These waves are not free to propagate and are known

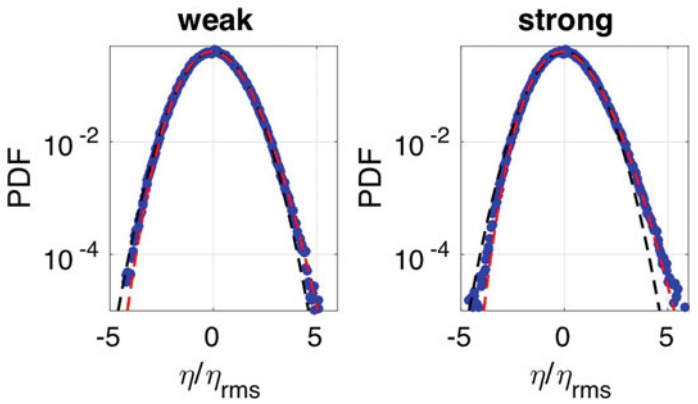

Fig. 4 Distribution of the wave elevation for the *weak* (left) and *strong* (right) case. The black dashed line is a Gaussian distribution and the red dashed line is the Tayfun distribution that corresponds to the parameter of each case

as bound waves. A first effect of the bound waves is that the statistics of the wave elevation are not Gaussian. Indeed as seen in Fig. 4, the distribution of the wave elevation is positively skewed and follows the Tayfun distribution which is known to incorporate second order effects [8]. The asymmetry is more pronounced for the *strong* dataset for which the slope is higher than for the *weak* case.

4 Occurrence of 4-Wave Correlations

In the WTT for gravity waves, 3-wave coupling is not resonant as the bound wave is not a true free wave and thus it is not expected to contribute directly to the energy cascade [4]. Indeed for deep water the resonance equations

$$\omega_{LDR1} + \omega_{LDR2} = \omega_{LDR3}, \quad \mathbf{k}_1 + \mathbf{k}_2 = \mathbf{k}_3 \tag{5}$$

do not have non trivial solutions in the gravity range due to the curvature of the LDR. Thus the resonant transfers of the WTT occur through 4-wave resonant coupling.

$$\omega_{LDR1} + \omega_{LDR2} = \omega_{LDR3} + \omega_{LDR4}, \quad \mathbf{k}_1 + \mathbf{k}_2 = \mathbf{k}_3 + \mathbf{k}_4 \tag{6}$$

In order to fully express this 4-wave coupling in the theory, the 3-wave non resonant contributions are summed through a canonical change of variables [9]. In this framework, part of the 4-wave coupling is actually due to the interplay of two non resonant triads. Unfortunately the change of variable is quite involved and is very hard to implement on experimental data. Nevertheless one can probe the occurrence of the 4-wave coupling through calculation of 4-wave tricoherence defined as

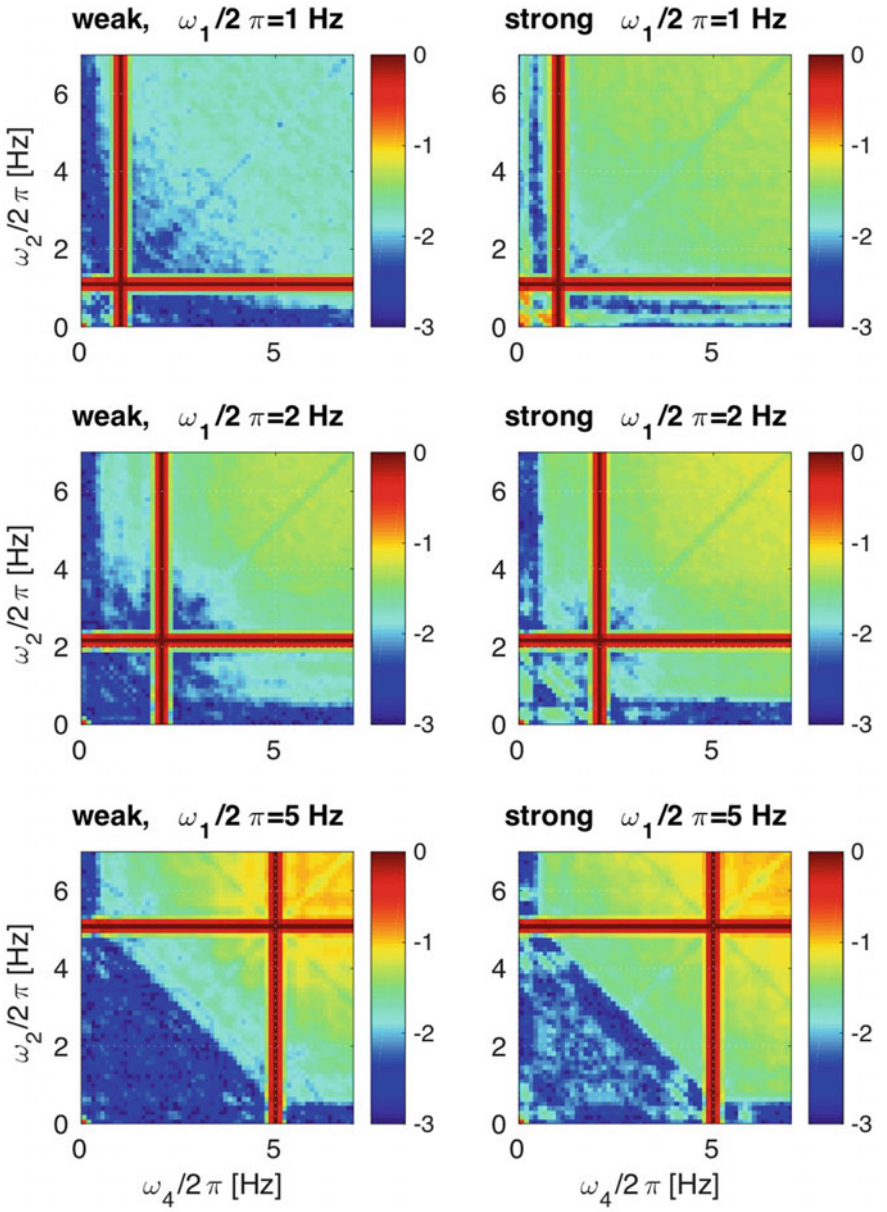

Fig. 5 Maps of the tricoherence computed on the local probe data following (7) for 3 given values $\omega_1/2\pi = 1$, 2 and 5 Hz from top to bottom. The left column corresponds to the *weak* dataset and the right column to the *strong* one. Colors correspond to $\log_{10} C$. See text for details

$$C(\omega_1, \omega_2, \omega_3, \omega_4) = \frac{\langle \tilde{\eta}(\omega_1)\tilde{\eta}^\star(\omega_2)\tilde{\eta}(\omega_3)\tilde{\eta}^\star(\omega_4)\rangle}{\sqrt{\langle|\tilde{\eta}(\omega_1)\tilde{\eta}(\omega_3)|^2\rangle\langle|\tilde{\eta}(\omega_2)\tilde{\eta}(\omega_4)|^2\rangle}} \quad (7)$$

$$\text{with} \qquad \omega_1 + \omega_3 = \omega_2 + \omega_4\,.$$

$\tilde{\eta}(\omega)$ is the Fourier transform in time of the elevation field at a given point over a temporal window of finite duration (chosen to 8.5 s). $\langle\ \rangle$ is an average over successive temporal windows and over the local probes. The four frequencies are imposed to be resonant so that the tricoherence $C(\omega_1, \omega_2, \omega_3, \omega_4)$ is actually depending only on three of the frequencies. The denominator is chosen to impose $|C| \leq 1$ and that C is nondimensional. Examples of the values of the tricoherence are shown in Fig. 5 for the case *weak* and *strong*. The tricoherence being a 3D object we impose given values of ω_1 (here $\omega_1/2\pi$ is 1, 2 or 5 Hz) chosen in the gravity range of frequencies. The statistical convergence level is estimated to be $3\ 10^{-3}$ which corresponds to dark blue colors. The red cross corresponding to values of tricoherence equal to one are due to trivial combinations of the frequencies such as $\omega_1 = \omega_2$ and $\omega_3 = \omega_4$. Out of this special cases converged values of tricoherence can be observed.

Note that small scale singular events can be also observed (see example in Fig. 6). These events can be related to small whitecapping events of the waves due to the fact that nonlinearity is not vanishingly small. These events are quite rare and occur at relatively small scale as compared to the large scales associated to gravity waves that are discussed in the following. Thus, we detect them by thresholding the vertical velocity and do not take them into account in the computation of the tricoherence.

For $\omega_1/2\pi = 1$ Hz, the coherence is very weak (about 10^{-2} for the *weak* case) and seems to be almost zero (at our level of convergence) when either ω_2 or ω_4 is less than ω_1. This appears consistent with the lack of observation of an inverse cascade. The coherence is increasing with ω_2 and ω_4. For $\omega_1/2\pi = 5$ Hz it can even reach strong values close to 10^{-1} when $\omega_2/2\pi \approx \omega_4/2\pi \approx 7$ Hz. The frequencies get close to the gravity-capillary crossover (14 Hz) at which a specific 3-wave resonant process has been observed that involves one gravity wave and two capillary waves [10]. Such very strong values of the tricoherence may be related to this process rather than to resonance between four gravity waves. For $\omega_1/2\pi = 1$ Hz and 1 Hz $< \omega_2/2\pi, \omega_4/2\pi < 4$ Hz the observed non zero coherence maybe a trace of genuine

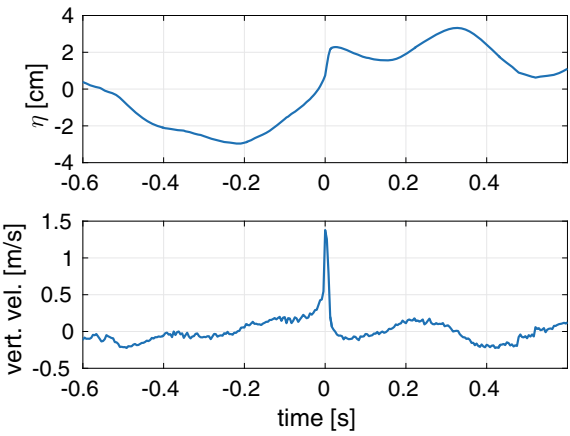

Fig. 6 Example of a singularity in the elevation due to a whitecapping at small scale. Top is the elevation and bottom is the vertical velocity

4-wave coupling that may be responsible for the direct transfert of energy along the dispersion relation as observed in Fig. 3 at frequencies up to 4 Hz.

5 Concluding Remarks

The analysis of the tricoherence suggests that a 4-wave resonant process maybe indeed operating at low frequencies between the forcing peak and 4 Hz and be responsible for the energy flux that provides energy along the dispersion relation as observed on the (k, ω) spectrum. At the lowest frequency the lack of coherence is consistent with the lack of inverse cascade. At the highest frequencies the very large values of the tricoherence are most likely due to a distinct 3-wave resonant process reported previously by Aubourg and Mordant [10] near the gravity-capillary crossover. As this process should be always operating, the condition for a clearer evidence of the 4-wave resonant process among gravity waves would require the use of a much larger wave facility.

Acknowledgements This project has received funding from the European Research Council (ERC) under the European Union's Horizon 2020 research and innovation programme (grant agreement No 647018-WATU).

References

1. Zakharov, V.E., L'vov, V.S., Falkovich, G.: Kolmogorov Spectra of Turbulence. Springer, Berlin (1992)
2. Nazarenko, S.: Wave Turbulence. Springer, Berlin (2011)
3. Newell, A.C., Rumpf, B.: Ann. Rev. Fluid Mech. **43** (2011)
4. Hasselmann, K.: J. Fluid Mech. **12** (1962)
5. Nazarenko, S.V., Lukaschuk, S.: Annu. Rev. Condens. Matter Phys. **7** (2016)
6. Deike, L., Miquel, B., Gutierrez, P., Jamin, T., Semin, B., Berhanu, M., Falcon, E., Bonnefoy, F.: J. Fluid Mech. **781** (2015)
7. Aubourg, Q., Campagne A., Peureux, C., Ardhuin, F., Sommeria, J., Viboud, S., Mordant, N.: Phys. Rev. Fluids **2** (2017)
8. Socquet-Juglard, H., Dysthe, K.B., Trulsen, K., Krogstad, H.E., Liu, J.: J. Fluid Mech. **542** (2005)
9. Krasitskii, V.P.: J. Fluid Mech. **272** (1994)
10. Aubourg, Q., Mordant, N.: Phys. Rev. Lett. **114** (2015)

Part VIII
Presence of Free Gas/Liquid Interface

Interactions Between Turbulence and Interfaces with Surface Tension

R. Chiodi, Jeremy McCaslin and O. Desjardins



Abstract Turbulence is a complex, multi-scale fluid process that can be strongly modified by the presence of multiple phases. In this work, we will discuss various aspects of the interaction between turbulence and interfaces with surface tension, as commonly encountered in liquid-gas flows. This study is based on a series of direct numerical simulations of homogeneous and isotropic turbulence in the presence of an initially flat interface that separates two fluids of equal densities and viscosities. This highly simplified flow configuration is selected as it isolates a critical aspect of turbulent liquid-gas flows and allows for deeper analysis. A second order numerical discretization that conserves mass, momentum, and kinetic energy is employed for all simulations. The scales of interface corrugation are presented, identifying the presence of a critical cutoff length scale below which surface tension suppresses interface deformation.

R. Chiodi · O. Desjardins (✉)
Cornell University, Ithaca, USA
e-mail: olivier.desjardins@cornell.edu

R. Chiodi
e-mail: rmc298@cornell.edu

J. McCaslin
ANSYS Inc., Canonsburg, USA
e-mail: jom48@cornell.edu

M. Gorokhovski and F. S. Godeferd (eds.), *Turbulent Cascades II*,
ERCOFTAC Series 26, https://doi.org/10.1007/978-3-030-12547-9_26

1 Introduction

Turbulent liquid-gas flows are ubiquitous in nature and engineered systems. These flows are highly complex, characterized by many different length and time scales resulting from the turbulence itself and the presence of multiple phases. Given their ubiquity, it is critical to be able to simulate multiphase flows, allowing a detailed and quantitative look into their physics. Even using current state of the art techniques, however, simulating complete systems remains out of reach, requiring an intractable amount of computational resources.

To remedy this, sub-grid scale (SGS) models are required to include the effect of the small scales without the need to resolve them. In single phase flows, large-eddy simulation (LES) has achieved this, enabling simulation of a plethora of complicated flows. These LES models are possible due to well developed theory for single phase turbulence. The knowledge of the turbulent cascade and isotropic inertial range allows accurate modeling of SGS turbulent effects while remaining general enough to be valid for many turbulent flows, leading to their significant impact.

The surface tension force and discontinuity of fluid properties in liquid-gas flows require new developments in multiphase turbulence theory before similarly effective SGS models can be created. In 2003, Fulgosi et al. [1] used direct numerical simulations (DNS) to study the effect of an air-water interface on a turbulent shear layer. For this, they mainly focused on comparing the dissipation and anisotropy of gas phase turbulence at the liquid-gas interface to that of a wall-bounded shear flow. In 2006, Reboux et al. [2] revisited the configuration of Fulgosi et al. [1], performing LES with the variational multi-scale approach (VMS) and comparing the results to both DNS and a modified Smagorinsky model LES. The VMS LES is seen to perform significantly better than the modified Smagorinsky model but, as noted by the authors, is highly dependent on the user-selected filter scale.

Both of these studies attempt to incorporate all of the complexities of liquid-gas flows at once, making it difficult to determine the effect of each individual component. Additionally, due to the numerical method used to represent the liquid-gas interface, their simulations were limited to low Weber number cases with limited interface deformation. This significantly limits its impact through excluding cases with complex topology changes. Trontin et al. [3] instead focused squarely on the effect of surface tension on decaying turbulence, representing the interface using a level-set method [4, 5] to allow large-scale interface deformation. Their configuration consisted of a sheet of one phase placed in a domain of another phase, with each phase having an identical density and viscosity. With the velocity field initialized as homogeneous isotropic turbulence (HIT), this then isolated the effect of surface tension on turbulence. The simulation configuration, however, contained a potentially important free parameter, the thickness of the initial sheet, that can affect the likelihood of forming droplets and the eventual droplet size distribution.

This work focuses on how surface tension affects decaying HIT using a single interface in order to avoid introducing a free parameter. First, Sect. 2 will detail the case configuration and range of parameters simulated. Section 3 then describes the

governing equations and numerical methods used to perform the DNS. In Sect. 4, initial results on the modification of interface topology by surface tension are presented. Lastly, conclusions drawn from the results are discussed in Sect. 5.

2 Case Configuration

All DNS performed as part of this work will use a cubic domain with side lengths of 2π resolved with 512 uniformly spaced cells in each direction. At the start of a simulation, an HIT velocity field from a separate simulation will be initialized on this mesh, along with an interface dividing the domain equally into two $2\pi \times \pi \times 2\pi$ sections. The two phases creating the interface are given identical densities and kinematic viscosities, isolating the effect of surface tension. In order to maintain the homogeneous and isotropic nature of the turbulence, periodic boundary conditions are used for the velocity. Penetration of one phase into the other through the top or bottom boundary condition is prevented with a Dirichlet boundary condition on the liquid volume fraction, forcing the boundary to remain its initial phase. At no point during the simulation does the initial interface undergo large enough deformation to approach the top or bottom boundary.

The field of HIT used as the initial velocity in the simulation is generated using linear forcing [6, 7] on an identical mesh. The DNS used to generate the HIT is run until statistically stationarity, where the velocity field is then saved to be used as the initial condition. On this mesh, the maximum resolvable Reynolds number, $Re_\lambda = u_{\text{rms}}\lambda_g/\nu$, is 160, where u_{rms} is the root-mean-square velocity, λ_g is the Taylor microscale, and ν is the kinematic viscosity. For this Reynolds number, a small inertial range exists, as shown by the $-5/3$ slope in the normalized E_{11} energy spectrum plotted in Fig. 1.

To study the effect of surface tension, we will vary the turbulent Weber number, $We_\lambda = \rho u_{\text{rms}}^2 \lambda_g/\sigma$, with ρ being the fluid density and σ the surface tension coefficient. This Weber number will be calculated using the initial HIT properties. With

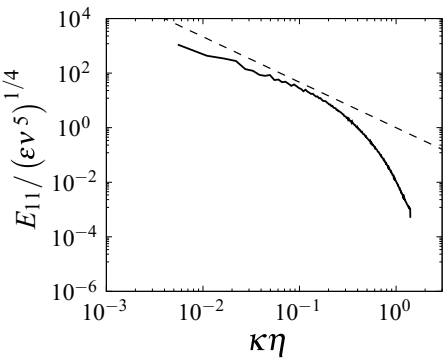

Fig. 1 Normalized E_{11} energy spectrum for the initial HIT field (——) along with a reference $-5/3$ slope (- - -)

Table 1 Table of different test cases and the case number used to reference them

Case	0	1	2	3	4
We_λ	∞	21.06	8.47	1.36	0.22

the same initial HIT field being used for each simulation, We_λ is directly controlled by σ. A total of five different Weber numbers will be simulated and are listed in Table 1 along with a reference case number.

3 Governing Equations and Numerical Methods

All simulations are performed using NGA [8, 9]. NGA solves the incompressible Navier-Stokes equation,

$$\frac{\partial \mathbf{u}}{\partial t} + \mathbf{u} \cdot \nabla \mathbf{u} = -\frac{1}{\rho} \nabla p + \nu \nabla \cdot \left(\nabla \mathbf{u} + \nabla \mathbf{u}^{\mathsf{T}} \right) + \frac{\sigma \kappa \delta_\Gamma(\phi) \mathbf{n}}{\rho} \tag{1}$$

on a staggered mesh using a second order finite-volume spatial discretization and a second order semi-implicit Crank-Nicolson time advancement. Uniform density and viscosity has been assumed due to the unity density and viscosity ratios between the two phases. The last term on the right, $\sigma \kappa \delta_\Gamma(\phi) \mathbf{n}/\rho$, represents the surface tension force, where $\mathbf{n}$ is the interface normal, κ the interface curvature, and $\delta_\Gamma(\phi)$ is a Dirac delta function localizing the surface tension force to the interface. In its discrete form, this term is represented as a jump in pressure, p, as

$$[p]_\Gamma = \sigma \kappa. \tag{2}$$

The phase volume fractions are advected using an unsplit, discretely conservative, geometric algorithm based on the Volume of Fluid (VOF) method [10]. The interface is represented in each cell by a plane using PLIC. The plane is defined by a normal vector from the ELVIRA algorithm [11] and a normal distance to it, computed using an analytic relation [12] to conserve the phase volume fraction in each cell. The jump in pressure due to surface tension, Eq. 2, is imposed in the pressure Poisson equation using the ghost fluid method (GFM) [13], with the interface curvature calculated using a least-squares fit to a reconstructed distance level-set field [14]. This provides a discretely conservative and spatially second order tracking of the interface.

4 Results

The primary focus of this work is the transformation of turbulent kinetic energy into surface energy. Figure 2 shows the turbulent kinetic energy, dissipated energy, and surface energy after the initial startup period for the $We_\lambda = 8.47$ simulation. It can be seen that even at this moderately high Weber number, surface tension extracts a non-negligible amount of energy from the turbulence during the creation of additional surface area.

To better understand the scales at which surface tension extracts this energy, the effect of surface tension on interface topology must be studied. It is expected that surface tension will oppose high wavenumber corrugations of the interface that would result in high curvatures. The interface shapes at $t/\tau_{\text{init}} = 0.5$ for Cases 1–4 shown in Fig. 3 support this. As the Weber number decreases, i.e. σ increases, small interface features are prevented. At the lowest Weber number, $We_\lambda = 0.22$, the surface tension becomes dominant enough to prevent any overturning of the interface.

Quantitatively, the length scales of surface corrugation can be studied using a spectrum of the liquid volume fraction variance, $\alpha'(\mathbf{x}) = \alpha(\mathbf{x}) - \langle \alpha(\mathbf{x}) \rangle_{x,z}$, where α is the liquid volume fraction, $'$ represents a fluctuating quantity, and $\langle\ \rangle_{x,z}$ the averaging in the x and z directions (tangential to the initial interface plane). This liquid volume fraction variance spectrum is calculated at the domain mid-plane and is shown in Fig. 4.

To observe the effect of surface tension, first we will consider the variance for a passive scalar, such as the material interface in Case 0. For a passive scalar in isotropic turbulence, a range of κ^{-1} scaling is expected, followed by a $\kappa^{-5/3}$ scaling [15]. This κ^{-1} scaling appears in Fig. 4 as the horizontal line due to the multiplication

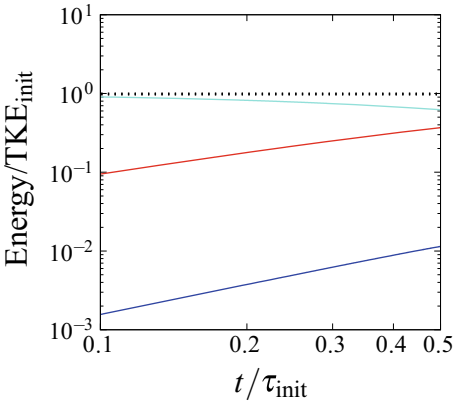

Fig. 2 Turbulent kinetic energy (———), dissipated energy (———), and surface energy (———) as a function of time for the $We_\lambda = 8.47$ simulation. All energies are normalized by the initial turbulent kinetic energy at $t/\tau_{\text{init}} = 0$ and the total (.....) is plotted for reference

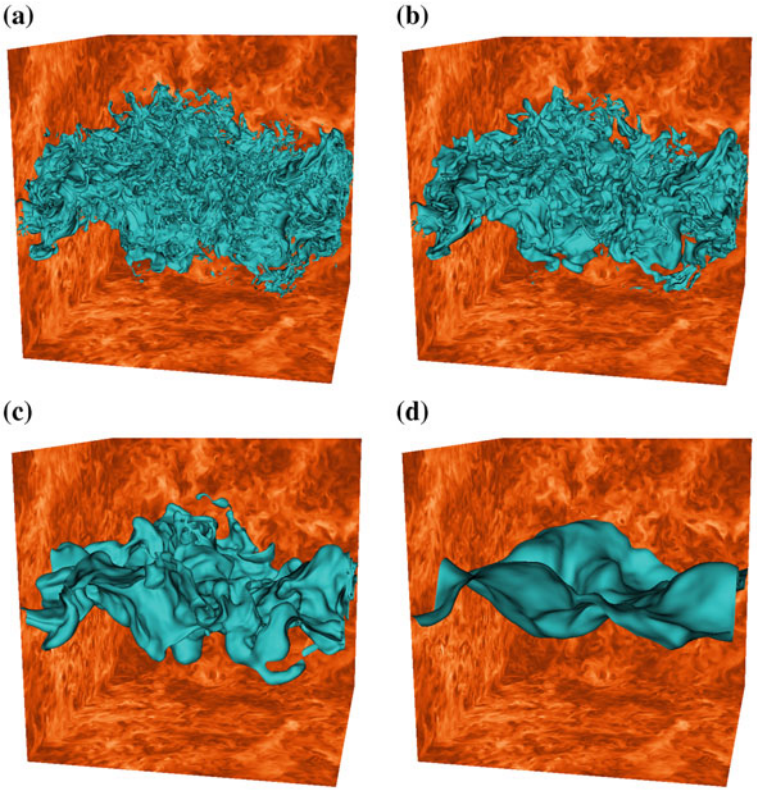

Fig. 3 Interface shape at $t/\tau_{\text{init}} = 0.5$ with velocity magnitude color map (lighter colors are greater values). Case 1 (**a**); Case 2 (**b**); Case 3 (**c**); Case 4 (**d**)

Fig. 4 Liquid volume fraction variance spectrum.
Case 0 (———);
Case 1 (———);
Case 2 (———);
Case 3 (———);
Case 4 (———);
κ^{-1} (.....)

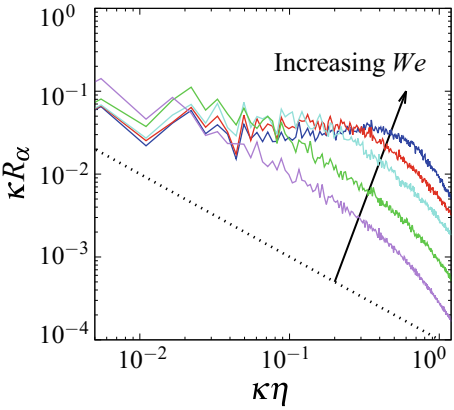

of the variance by κ. At a certain wavenumber, κ_σ, the variance spectrum begins scaling with κ^{-2}, providing an indication that surface tension is prohibiting high wavenumber corrugations. With increasing Weber number, surface tension prevents larger wavelength corrugations, indicated by κ_σ moving to smaller wavenumbers. As a separate note, the change in scaling for Case 0 ($We_\lambda = \infty$) is unphysical and represents the presence of a "numerical surface tension" that is a consequence of the interface reconstruction. Since all other cases display a κ_σ at a lower wavenumber than Case 0, it can be assumed that the "numerical surface tension" does not play a significant role in the other cases and is superseded by the true surface tension force.

5 Conclusions

A suite of DNS have been performed for a canonical flow configuration created to study the interplay between decaying HIT and surface tension. While keeping the Reynolds number constant, five separate Weber numbers have been simulated. Through this, the suppression of small interface corrugations due to surface tension has been seen visually in Fig. 3 and quantitatively in the liquid volume fraction variance spectrum. From this, a critical scale below which the surface tension force will prevent turbulence corrugations can be extracted. This is an important first step in understanding the transformation of kinetic energy in HIT to stored surface energy.

References

1. Fulgosi, M., Lakehal, D., Banerjee, S., De Angelis, V.: Direct numerical simulation of turbulence in a sheared airwater flow with a deformable interface. J. Fluid Mech. **482**, 319–345 (2003)
2. Reboux, S., Sagaut, P., Lakehal, D.: Large-eddy simulation of sheared interfacial flow. Phys. Fluids **18** (2006)
3. Trontin, P., Vincent, S., Estivalezes, J.L., Caltagirone, J.P.: Direct numerical simulation of a freely decaying turbulent interfacial flow. Int. J. Multiphase Flow **36** (2010)
4. Osher, S., Sethian, J.: Front propagating with curvature dependent speed: algorithms based on Hamilton-Jacobi formulations. J. Comput. Phys. **79**, 12–49 (1988)
5. Sussman, M., Smereka, P., Osher, S.: A level set approach for computing solutions to incompressible two-phase flow. J. Comput. Phys. **114** (1994)
6. Lundgren, T.S.: Linear forcing in numerical simulations of isotropic turbulence: physical space implementations and convergence properties. In: Center for Turbulence Research Annual Research Briefs, pp. 461–473 (2003)
7. Rosales, C., Meneveau, C.: Linear forcing in numerical simulations of isotropic turbulence: physical space implementations and convergence properties. Phys. Fluids **17** (2005)
8. Desjardins, O., Blanquart, G., Balarac, G., Pitsch, H.: High order conservative finite difference scheme for variable density low Mach number turbulent flows. J. Comput. Phys. **227**(15), 7125–7159 (2008)
9. Desjardins, O., McCaslin, J., Owkes, M., Brady, P.: Direct numerical and large-Eddy simulation of primary atomization in complex geometries. Atom. Sprays **23**(11), 1001–1048 (2013)

10. Owkes, M., Desjardins, O.: A computational framework for conservative, three-dimensional, unsplit, geometric transport with application to the volume-of-fluid (VOF) method. J. Comput. Phys. **270**, 587–612 (2014)
11. Pilliod, J.E., Puckett, E.G.: Second-order accurate volume-of-fluid algorithms for tracking material interfaces. J. Comput. Phys. **199**(2), 465–502 (2004)
12. Scardovelli, R., Zaleski, S.: Analytical relations connecting linear interfaces and volume fractions in rectangular grids. J. Comput. Phys. **164**(1), 228–237 (2000)
13. Fedkiw, R., Aslam, T., Merriman, B., Osher, S.: A non-oscillatory eulerian approach to interfaces in multimaterial flows (the ghost fluid method). J. Comput. Phys. **152**(2), 457–492 (1999)
14. Marchandise, E., Geuzaine, P., Chevaugeon, N., Remacle, J.-F.: A stabilized finite element method using a discontinuous level set approach for the computation of bubble dynamics. J. Comput. Phys. **225**(1), 949–974 (2007)
15. Lesieur, M., Rogallo, R.: Large-eddy simulation of passive scalar diffusion in isotropic turbulence. Phys. Fluids A Fluid Dyn. **1**, 718–722 (1989)

A Dual-Scale Approach for Modeling Turbulent Liquid/Gas Phase Interfaces

Dominic Kedelty, James Uglietta and Marcus Herrmann



Abstract Advances to a dual-scale modeling approach [1] are presented to describe turbulent phase interface dynamics in a large-eddy-simulation-type spatial filtering context. Spatial filtering of the governing equations introduces several sub-filter terms that require modeling. Instead of developing individual closure-models for the terms associated with the interface, the dual-scale approach uses an exact closure by explicitly filtering a fully resolved realization of the phase interface. This resolved realization is maintained on a high-resolution over-set mesh. The advection equation for the phase interface on this DNS scale requires a model for the fully resolved interface advection velocity. This velocity is the sum of the filter scale LES velocity, available from the LES flow solver, and the sub-filter velocity fluctuation. The sub-filter velocity fluctuation is due to sub-filter turbulent eddies, reconstructed using a local fractal interpolation technique [2]. Results of the dual-scale model are compared to recent DNS of unit density and viscosity contrast interfaces in homogeneous isotropic turbulence without surface tension [3].

D. Kedelty · J. Uglietta · M. Herrmann (✉)
Arizona State University, Tempe, AZ 85287-6106, USA
e-mail: marcus.herrmann@asu.edu

D. Kedelty
e-mail: dkedelty@asu.edu

J. Uglietta
e-mail: juglietta@asu.edu

M. Gorokhovski and F. S. Godeferd (eds.), *Turbulent Cascades II*,
ERCOFTAC Series 26, https://doi.org/10.1007/978-3-030-12547-9_27

1 Introduction

Atomization in turbulent environments involves a vast range of length and time scales. Predictive simulations aiming to resolve all relevant scales thus require enormous computational resources, taxing even the most powerful computers available today [4]. Since primary atomization is governed by the dynamics of the interface, a need therefore exists for appropriate interface models that make the computational cost of predicting the atomization outcome more tractable.

A wide range of phenomenological models aiming to represent statistically the essential features of atomization have been proposed in the past. Although these aim to introduce the dominant mechanisms for breakup, they often use round blobs injected from the nozzle exit and hence neglect all details of the interface dynamics.

Other modeling approaches to atomization include stochastic models [5, 6] representing the interface by constituent stochastic particles and the mean interface density transport equation model for Reynolds-Averaged Navier-Stokes (RANS) approaches [7, 8]. The former treats the interface dynamics in a stochastic sense but requires the a priori knowledge of the breakup mechanism, whereas the latter is affected by the drawbacks of the RANS approach: the transport of the mean interface density is modeled by a diffusion-like hypothesis, thereby neglecting the spatial grouping effects of liquid elements [4].

In the context of Large Eddy Simulations (LES), [9–12] have proposed models to close the unclosed terms arising from the introduction of spatial filtering into the governing equations. However, these models typically neglect the contribution of the sub-filter surface tension term and are based on a cascade process hypothesis that may be questionable in the context of surface tension-driven atomization.

In [13, 14], a dual-scale approach for LES of interface dynamics was proposed and a model for the sub-filter surface tension induced motion of phase interfaces was developed. The purpose of this contribution is to develop a model for the sub-filter phase interface motion induced by sub-filter turbulent velocity fluctuations. Combining such a model with the surface tension model proposed in [13, 14] will result in a LES model applicable to atomizing flows.

2 Governing Equations

The equations governing the fully resolved motion of an unsteady, incompressible, immiscible, two-fluid system in the absence of surface tension are the Navier-Stokes equations,

$$\frac{\partial \rho \mathbf{u}}{\partial t} + \nabla \cdot (\rho \mathbf{u} \otimes \mathbf{u}) = -\nabla p + \nabla \cdot \left(\mu \left(\nabla \mathbf{u} + \nabla^{\mathrm{T}} \mathbf{u} \right) \right) , \tag{1}$$

where $\mathbf{u}$ is the velocity, ρ the density, p the pressure, and μ the dynamic viscosity. Here, we neglect surface tension to solely focus on the turbulence induced dynamics

of phase interfaces. Furthermore, the continuity equation results in a divergence-free constraint on the velocity field

$$\nabla \cdot \mathbf{u} = 0\,. \tag{2}$$

Assuming ρ and μ are constant within each fluid, density and viscosity can be calculated from

$$\rho = \psi\rho_l + (1-\psi)\rho_g, \qquad \mu = \psi\mu_l + (1-\psi)\mu_g\,, \tag{3}$$

where indices l and g denote values in liquid and gas, respectively, and ψ is a volume-of-fluid scalar that is $\psi = 0$ in the gas and $\psi = 1$ in the liquid with

$$\frac{\partial\psi}{\partial t} = -\mathbf{u}\cdot\nabla\psi = -\nabla\cdot(\mathbf{u}\psi) + \psi\nabla\cdot\mathbf{u}\,. \tag{4}$$

Here, the last term on the right-hand side is zero for incompressible flows.

2.1 Filtered Governing Equations

Introducing spatial filtering into Eqs. (1) and (2) and assuming that the filter commutes with both the time and spatial derivatives, the filtered governing equations can be derived [10],

$$\frac{\partial\overline{\rho}\,\overline{\mathbf{u}}}{\partial t} + \nabla\cdot(\overline{\rho}\bar{\mathbf{u}}\otimes\overline{\mathbf{u}}) = -\nabla\bar{p} + \nabla\cdot(\overline{\mu}(\nabla\overline{\mathbf{u}} + \nabla^{\mathrm{T}}\overline{\mathbf{u}})) + \boldsymbol{\tau}_1 + \nabla\cdot(\boldsymbol{\tau}_2 + \boldsymbol{\tau}_3)\,, \tag{5}$$

$$\nabla\cdot\bar{\mathbf{u}} = 0\,, \tag{6}$$

where $\bar{}$ indicates spatial filtering, and

$$\boldsymbol{\tau}_1 = \frac{\partial\overline{\rho}\,\overline{\mathbf{u}}}{\partial t} - \frac{\partial\overline{\rho\mathbf{u}}}{\partial t} \tag{7}$$

$$\boldsymbol{\tau}_2 = \overline{\rho}\,\overline{\mathbf{u}}\otimes\overline{\mathbf{u}} - \overline{\rho\mathbf{u}\otimes\mathbf{u}} \tag{8}$$

$$\boldsymbol{\tau}_3 = \overline{\mu(\nabla\mathbf{u} + \nabla^T\mathbf{u})} - \overline{\mu}(\nabla\overline{\mathbf{u}} + \nabla^T\overline{\mathbf{u}})\,, \tag{9}$$

where $\boldsymbol{\tau}_1$, $\boldsymbol{\tau}_2$, and $\boldsymbol{\tau}_3$ are associated, respectively, with acceleration, advection, and viscous effects [10]. Using Eq. (3), the filtered density and viscosity in Eq. (5) are

$$\overline{\rho} = \rho_l\overline{\psi} + \rho_g(1-\overline{\psi}), \qquad \overline{\mu} = \mu_l\overline{\psi} + \mu_g(1-\overline{\psi})\,, \tag{10}$$

where

$$\overline{\psi} = \int \mathscr{G}(\mathbf{x})\psi\, d\mathbf{x}\,, \tag{11}$$

and $\mathscr{G}$ is a normalized spatial filter function.

3 The Dual-Scale Model for Sub-filter Interface Dynamics

Instead of relying on a cascade process for the interface by which dynamics on the sub-filter scale can be inferred from the dynamics on the resolved scale, the dual-scale approach proposed in [14] aims to maintain a fully resolved realization of the interface geometry at all times, expressed, for example, in terms of a volume-of-fluid scalar ψ. Then $\overline{\psi}$ can be calculated exactly by explicit filtering using Eq. (11).

Although this is an exact closure, the problem of modeling is of course simply shifted to the problem of maintaining a fully resolved realization of the interface geometry, i.e., describing the fully resolved motion of the interface, Eq. (4). Since the fully resolved velocity is the sum of the filtered velocity and the sub-grid velocity, $\mathbf{u} = \overline{\mathbf{u}} + \mathbf{u}_{sg}$, this results in

$$\frac{\partial \psi}{\partial t} = -\nabla \cdot \left(\left(\overline{\mathbf{u}} + \mathbf{u}_{sg} \right) \psi \right) + \psi \nabla \cdot \left(\overline{\mathbf{u}} + \mathbf{u}_{sg} \right) , \tag{12}$$

where the only term requiring modeling is $\mathbf{u}_{sg}$.

In [14], a model for $\mathbf{u}_{sg}$ is proposed consisting of three contributions,

$$\mathbf{u}_{sg} = \mathbf{u}' + \delta\mathbf{u} + \mathbf{u}_{\sigma} , \tag{13}$$

where $\mathbf{u}'$ is due to sub-filter turbulent eddies, $\delta\mathbf{u}$ is attributed to the interface velocity increment due to relative sub-filter motion between the two immiscible fluids, and $\mathbf{u}_{\sigma}$ is due to sub-filter velocities induced by sub-filter surface tension forces. The focus of the current contribution is on the first term; a modeling outline of the second term is discussed in [1, 14], and the last term is modeled in [13].

3.1 Sub-filter Turbulent Fluctuation Velocity Models

We propose to reconstruct the sub-filter turbulent fluctuation velocity $\mathbf{u}'$ using fractal interpolation [2]. To demonstrate fractal interpolation in one dimension, consider 3 adjacent LES scale nodes x_0, x_1, and x_2 with velocities $\overline{u}_0$, $\overline{u}_1$, and $\overline{u}_2$. Following [2, 15] the fractal interpolation operator $\mathscr{W}_{FI}$ can be written as

$$\mathscr{W}_{FI}(x) = \overline{u}_0 + \frac{\overline{u}_1 - \overline{u}_0}{x_1 - x_0}(x - x_0) + d_1 \left(u(2x - x_0) - \overline{u}_0 - \frac{\overline{u}_2 - \overline{u}_0}{x_2 - x_0}(2x - x_0) \right) \text{ if } x \in [x_0, x_1] \tag{14}$$

$$\mathscr{W}_{FI}(x) = \overline{u}_1 + \frac{\overline{u}_2 - \overline{u}_1}{x_2 - x_1}(x - x_1) + d_2 \left(u(2x - x_0) - \overline{u}_0 - \frac{\overline{u}_2 - \overline{u}_0}{x_2 - x_0}(2x - x_0) \right) \text{ if } x \in [x_1, x_2] \tag{15}$$

Here $|d_1| < 1$ and $|d_2| < 1$ are stretching factors making $\mathscr{W}_{FI}$ a contractive mapping [2]. Successively applying the fractal interpolation operator $\mathscr{W}_{FI}$ starting with the LES filter velocities, generates the fully resolved turbulent fluctuation velocity.

Two different approaches are pursued to extend the above formulation to three dimensions. In the first, fractal interpolation is first performed in one spatial direction only, followed by separate 1D fractal interpolations in the other two directions [2]. The second approach replaces the 1D linear interpolation operators in Eqs. (14) and (15) with 3D trilinear interpolation operators and performs the fractal interpolation directly in three dimensions [16].

Furthermore, two different approaches are used to determine the values of the stretching factors d_1 and d_2. The first follows the so-called ZE1 model [2], using $d_1 = -d_2 = \pm 2^{-1/3}$ with the sign chosen randomly with equal probability. This choice of d_i generates a velocity signal that satisfies the $-5/3$ kinetic energy spectrum of turbulence.

The second approach chooses d_i with random sign and absolute value determined from a log-Poisson distribution [15, 16],

$$P\left(|d_i| = \left(\frac{1}{2}\right)^{\gamma} \beta^n\right) = e^{-\lambda} \frac{\lambda^n}{n!}, \; n = 0, 1, \ldots \quad \text{with} \quad \lambda = \frac{1 - 3\gamma}{1 - \beta^3} \ln 2 \tag{16}$$

and $\gamma = 1/9$ and $\beta = (2/3)^{1/3}$ [16].

Finally, two different approaches are analyzed concerning the spatial location of the LES velocities $\overline{u}_0$, $\overline{u}_1$, and $\overline{u}_2$. If the LES flow solver utilizes a staggered mesh layout, face normal velocities are not co-located and hence the fractal interpolation has to be performed for different locations depending on the spatial component of the velocity vector. However, if one first interpolates the staggered face velocities to cell corners (nodes), then the velocity components are co-located and fractal interpolation for all components can be performed at the same location. However, this interpolation step is in essence an additional spatial filter of the LES velocity before fractal interpolation is performed.

4 Numerical Methods

Equation (12) is solved using an unsplit geometric transport scheme for volume-of-fluid scalars that ensures both discrete volume conservation of each fluid and boundedness of ψ [17]. Geometric reconstruction of the interface is done using PLIC employing analytical formulas [18] with ELVIRA estimated normals [19].

To efficiently solve Eq. (12) for the fully resolved interface, the RLSG method [20] is employed. By design, it solves Eq. (12) on a separate, highly resolved Cartesian overset grid of mesh spacing h_G, independent of the underlying LES flow solver grid of mesh spacing h. In the dual scale LES approach, h_G needs to be chosen sufficiently small to maintain a fully resolved realization of the phase interface.

The unsplit, geometric advection scheme of [17] requires face-centered velocities that are discretely divergence-free to ensure both conservation and boundedness. While discretely divergence free filtered velocities $\overline{\mathbf{u}}$ are available on the flow solver

mesh due to the application of a projection step of the velocities in a standard fractional step method, such velocities $\mathbf{u}$ are not directly available on the fine overset mesh. Since $\mathbf{u} = \overline{\mathbf{u}} + \mathbf{u}'$, both $\overline{\mathbf{u}}$ and $\mathbf{u}'$ need to be discretely divergence free on the fine overset mesh. To ensure $\nabla_{h_G} \cdot \overline{\mathbf{u}} = 0$ if $\nabla_h \cdot \overline{\mathbf{u}} = 0$, we employ the optimal constrained approach for divergence-free velocity interpolation [21], recursively applying the interpolation technique for nested staggered meshes up to the refinement level of the overset mesh.

The sub-filter fluctuation velocity $\mathbf{u}'$ is calculated from

$$\mathbf{u}' = \mathscr{W}_{FI}^{k} \overline{\mathbf{u}} - \overline{\mathbf{u}}, \tag{17}$$

where the superscript k indicates k-times application of the fractal interpolation operator $\mathscr{W}_{FI}$, with $k = \log\left(\frac{h}{h_G}\right) / \log(2)$. Next $\mathbf{u}'$ is projected into the subspace of solenoidal velocity fields using the projection/correction step of a fractional step method. Although the fractal interpolation could be applied to the temporally evolving LES velocity $\overline{\mathbf{u}}$ to obtain a time dependent $\mathbf{u}'$, here, we use a single snapshot of the LES field only (the initial velocity field), and thus $\mathbf{u}'$ is frozen in time.

To calculate $\overline{\psi}$, Eq. (11) is evaluated by setting the filter size to the flow solver mesh size h and evaluating the integral by explicitly summing ψ of those overset-mesh cells that are contained within a given LES flow solver cell.

5 Results

An initially flat interface is placed inside a box of fully developed isotropic turbulence. Both density and viscosity ratio are unity, and no surface tension forces are present with a Reynolds number of $Re_\lambda = 313$ and $We_\lambda = \infty$. Direct numerical simulation results using a 1024^3 mesh for this case are reported in [3]. Here, we present LES results using the dual-scale approach employing a LES mesh resolution of 32^3 and an overset mesh resolution of 256^3 and 512^3. The sub-filter velocity $\mathbf{u}'$ is obtained from fractal interpolation using the combination of approaches summarized in Table 1.

We define $\alpha(x, z, t)$ as the liquid volume fraction that is contained within a square column normal to the planar interface and with cross sectional area equal to h_G^2. The corresponding quantity on the LES mesh, $\overline{\alpha}(x, z, t)$, can be calculated using a column

Table 1 Fractal interpolation methods used

Method	Interpolation	Scaling factors	Velocity location
3D-ZE1-N	3D	ZE1	Node
3D-P-N	3D	Poisson	Node
3D-P-F	3D	Poisson	Face
1D-P-F	1D	Poisson	Face

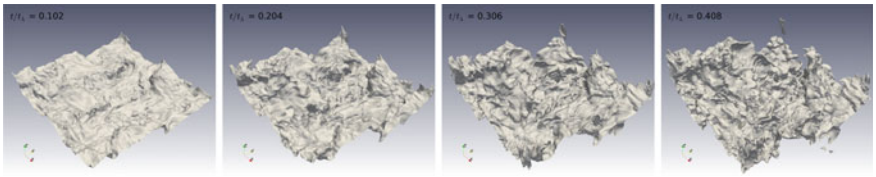

Fig. 1 Interface geometry at different times using fractal interpolation velocity method 3D-ZE1-N

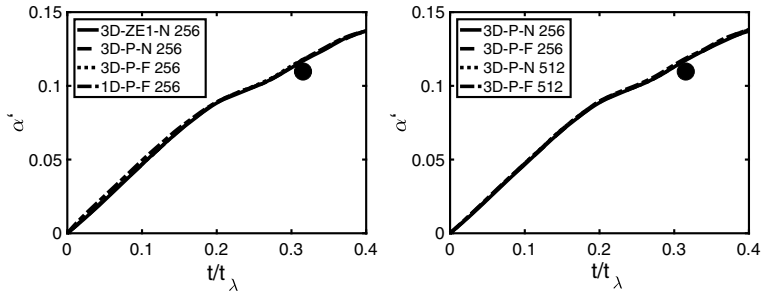

Fig. 2 Comparison of sub-filter liquid column height RMS α'. Left: 3D-ZE1-N-256, 3D-P-N-256, 3D-P-F-256, 1D-P-F-256, and DNS-1024 (symbol). Right: impact of overset mesh resolution with 3D-P-N-256, 3D-P-F-256, 3D-P-N-512, 3D-P-F-512, and DNS (symbol)

with cross sectional area h^2. Then, the sub-filter liquid column height RMS can be defined as

$$\alpha'(t) = \sqrt{\frac{1}{L^2}\int_L \int_L ((\alpha(x,z,t) - \overline{\alpha}(x,z,t))^2\, dx dz}. \tag{18}$$

Note that without a dual scale model, both α' remains zero for all time.

Figure 1 shows realizations of the phase interface geometry at different times using fractal interpolation 3D-ZE1-N. Significant small scale surface corrugations on the overset mesh are visible, i.e., significant sub-filter surface fluctuations exist.

Figure 2 shows the sub-filter liquid column height RMS α' using the four methods listed in Table 1 compared to the result of the 1024^3 DNS [3]. No significant difference between the four fractal interpolation methods can be discerned. Compared to the DNS, the dual scale LES slightly over-predicts α'. This is due to the fact that the dual scale model uses a frozen fluctuation velocity field, whereas the DNS is simulated in decaying turbulence. Interactive coupling of the dual scale approach to the time evolving LES field, to be done in future work, should eliminate this discrepancy. On the right, Fig. 2 analyzes the impact of the overset mesh resolution, comparing results obtained using a 256^3 overset mesh to a 512^3 mesh. No significant differences are present, indicating that in this metric, the phase interface is well resolved even on the 256^3 overset mesh.

6 Conclusions

A dual-scale modeling approach for phase interface dynamics in turbulent flows is presented. The method uses overset high-resolution meshes for a resolved realization of the interface geometry that can be explicitly filtered to close the terms that require modeling in the filtered Navier-Stokes equations. This contribution focuses on different fractal interpolation techniques to generate sub-filter velocity fluctuations that have a significant impact on interface metrics as compared to the case of no dual-scale model, where these metrics remain zero for all time. Results show that no differences between the different fractal interpolation methods can be discerned using the metric of sub-filter column height RMS. Necessary future work includes more detailed comparisons to DNS data as well as on-the-fly reconstruction of the sub-filter turbulent eddy velocity u' to capture the temporal evolution of the sub-filter velocity.

Acknowledgements The support of NASA TTT grant NNX16AB07A is gratefully acknowledged.

References

1. Herrmann, M., Gorokhovski, M.: Proceedings of the 2008 CTR Summer Program, pp. 171–181. Stanford University, Stanford, CA, Center for Turbulence Research (2008)
2. Scotti, A., Meneveau, C.: Phys. D Nonlinear Phenom. **127**(3–4), 198 (1999)
3. McCaslin, J., Desjardins, O.: Proceedings of the 2014 CTR Summer Program. Stanford University, Stanford, CA, Center for Turbulence Research (2014)
4. Gorokhovski, M., Herrmann, M.: Annu. Rev. Fluid Mech. **40**(1), 343 (2008)
5. Gorokhovski, M., Jouanguy, J., Chtab, A.: Proceedings of International Conference on Liquid Atomization and Spray Systems (2006)
6. Gorokhovski, M., Jouanguy, J., Chtab, A.: International Conference on Multiphase, Flow, Leipzig, Germany (2007)
7. Vallet, A., Borghi, R.: Proceedings of International Conference on Multiphase Flow, Lyon, France (1998)
8. Vallet, A., Burluka, A., Borghi, R.: Atom. Sprays **11**, 619 (2001)
9. Labourasse, E., Lacanette, D., Toutant, A., Lubin, P., Vincent, S., Lebaigue, O., Caltagirone, J.P., Sagaut, P.: Int. J. Multiphase Flow **33**(1), 1 (2007)
10. Toutant, A., Labourasse, E., Lebaigue, O., Simonin, O.: Comput. Fluids **37**(7), 877 (2008)
11. Toutant, A., Chandesris, M., Jamet, D., Lebaigue, O.: Int. J. Multiphase Flow **35**(12), 1119 (2009)
12. Toutant, A., Chandesris, M., Jamet, D., Lebaigue, O.: Int. J. Multiphase Flow **35**(12), 1100 (2009)
13. Herrmann, M.: Comput. Fluids **87**, 92 (2013)
14. Herrmann, M., Gorokhovski, M.: ICLASS 2009, 11th Triennial International Annual Conference on Liquid Atomization and Spray Systems. Vail, CO (2009)
15. Ding, K.Q., Zhang, Z.X., Shi, Y.P., She, Z.S.: Phys. Rev. E **82**(3), 036311 (2010)
16. Zhang, Z.X., Ding, K.Q., Shi, Y.P., She, Z.S.: Phys. Rev. E (2011)
17. Owkes, M., Desjardins, O.: J. Comput. Phys. **270**, 587 (2014)
18. Scardovelli, R., Zaleski, S.: J. Comput. Phys. **164**(1), 228 (2000)
19. Pilliod Jr., J.E., Puckett, E.G.: J. Comput. Phys. **199**(2), 465 (2004)
20. Herrmann, M.: J. Comput. Phys. **227**(4), 2674 (2008)
21. Cervone, A., Manservisi, S., Scardovelli, R.: Comput. Fluids **47**(1), 101 (2011)

Part IX
Posters

Precession of Plumes in the Presence of Background Rotation

Iresha Atthanayake, Petr Denissenko, Yongmann M. Chung and Peter J. Thomas




Abstract We present results of a particle image velocimetry (PIV) study conducted on forced plumes in a rotating system. The measurements were carried out for nine different background rotations and it was found that the plume precesses anticyclonically around the axis of background rotation. The data analysis has revealed that the precession rate increases linearly with the rate of background rotation.

1 Introduction

Turbulent jets, plumes and thermals are prevalent in nature and technology. Jets and plumes are continuous streams of, respectively, non-buoyant or buoyant fluid forced out of a small opening. The instantaneous release of a parcel of buoyant liquid from such a source is referred to as a thermal. Technological examples for jets and plumes

I. Atthanayake · P. Denissenko (✉) · Y. M. Chung · P. J. Thomas
School of Engineering, University of Warwick, Coventry, UK
e-mail: P.Denissenko@warwick.ac.uk

I. Atthanayake
e-mail: I.U.Atthanayake@warwick.ac.uk

Y. M. Chung
e-mail: lY.M.Chung@warwick.ac.uk

P. J. Thomas
e-mail: P.J.Thomas@warwick.ac.uk

M. Gorokhovski and F. S. Godeferd (eds.), *Turbulent Cascades II*,
ERCOFTAC Series 26, https://doi.org/10.1007/978-3-030-12547-9_28

include ventilation and heating, smoke release from chimney stacks and waste-water disposal outfalls. Jet- and plume-like behaviour can be found in natural settings such as volcanic eruptions and sea floor hydrothermal vents. The length scales and velocity scales of most of the jets and plumes in technological or industrial category are small enough not to be affected by the earth's rotation while naturally occurring flows can can be associated with parameter ranges where effects of the earth's rotation need to be taken into consideration. The influence of the Earth's rotation on the dynamics of turbulent plumes and jets is also problem of interest in a wide variety of geophysical problems, including deep ocean mixing induced by either surface cooling in the open ocean or freezing events in the Earth's atmosphere [2, 4, 5]. On the other hand there do also exist a variety of industrial applications where jets and plumes are emerging into rotating environments such as combustion chambers, chemical mixing processes and cooling towers.

Plumes in rotating fluids have recently attracted attention. Bruno et al. [1] numerically investigated the effects of background rotation on convective plumes. They concluded that the rotation strongly affects classical convection patterns of the plumes, that the plume is confined at the intrusion level by the establishment of a geostrophic balance, and that non-trivial swirl speed develops in and around the plume. Tomas et al. [6] also carried out a numerical study to investigate the effects of rotation on the turbulent dynamics of thermally driven buoyant plumes in stratified environments at large Rossby numbers. Their simulations revealed that the primary response to the adverse pressure gradient is an off-axis deflection of the plume that evolves into a robust, organized anticyclonic radial precession about the buoyancy source. Frank et al. [3] recently conducted an experimental study on plumes in rotating systems. They conducted a series of dye-visualisation experiments and concluded that after approximately one rotation period, the plume tilts laterally and starts to precess anticyclonically. The experiments of Frank et al. [3] motivated us to conduct the current short study where we revisit the observed precession described in their paper but by means of more quantitative Particle-Image-Velocimetry (PIV) measurements.

2 Experimental Facility and Methodology

The experiments were conducted inside a large tank mounted on a computer controlled turntable. A schematic diagram of the experimental set up is shown in Fig. 1. The plumes studied were released vertically upwards from an exit nozzle embedded flush within the top surface of an acrylic ejector box as illustrated in the figure. The ejector box had a diameter of 500 mm and it was placed at the bottom of the rotating tank. The center of the exit nozzle was aligned to coincide with the rotational axis of the turntable. The diameter of the exit nozzle, from which the plumes were ejected, was $d = 6$ mm. Thus, the ratio of tank width to source diameter was approximately 167. This ensured that effects from the surrounding walls of the tank, induced on the flow during the experiments, can be assumed to be negligible. The density difference between the plume and the surrounding environment was maintained by increasing

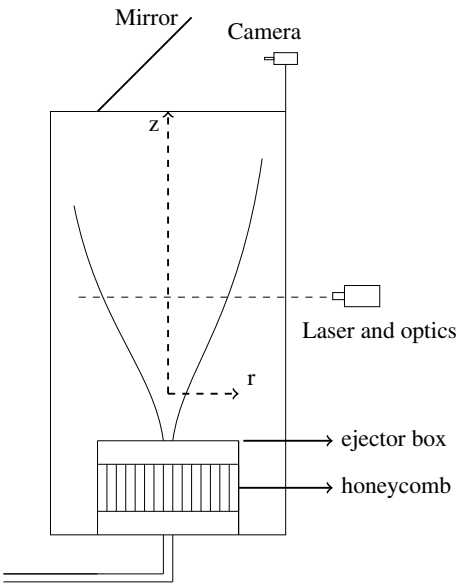

Fig. 1 Schematic diagram of the experimental set up

the salinity of the ambient water in the tank. In preparation for each experiment that the turntable was accelerated to the required rotation rate and the fluid inside the tank was allowed to reach solid-body rotation. Then the plume was released with a flow rate 0.5×10^{-3} m^3/min. The Reynolds number based on the diameter of the nozzle and the mean ejection velocity is $Re_0 = 1800$. The plume Richardson number (Γ) is approximately 0.03. Therefore the plume considered in the study is a forced plume not a pure plume.

The velocity-field measurements were conducted at a non-dimensional height $z/d = 10$, where z is the axial height and d is the diameter of the source. The data were analysed by means of Proper Orthogonal Decomposition(POD). The time characteristics of the first energetic POD mode was used to calculate the precession frequency of the plume. Moreover, since these time characteristics show non stationary behaviour, they were analysed using the Hilbert-Huang transformation to find the frequency of precession (ω_p).

3 Results

Figure 2a–o show a series of vector fields of the plume in the horizontal plane, at height $z/d = 10$ above the source. The figures represent the time development of the plume in the horizontal plane between 20 s after ejection of liquid had commenced and 104 s. Due to the entrainment velocity affected by the Coriolis force a cyclonic vortex is formed. The background rotation associated with the figures is 0.52 rad s^{-1}.

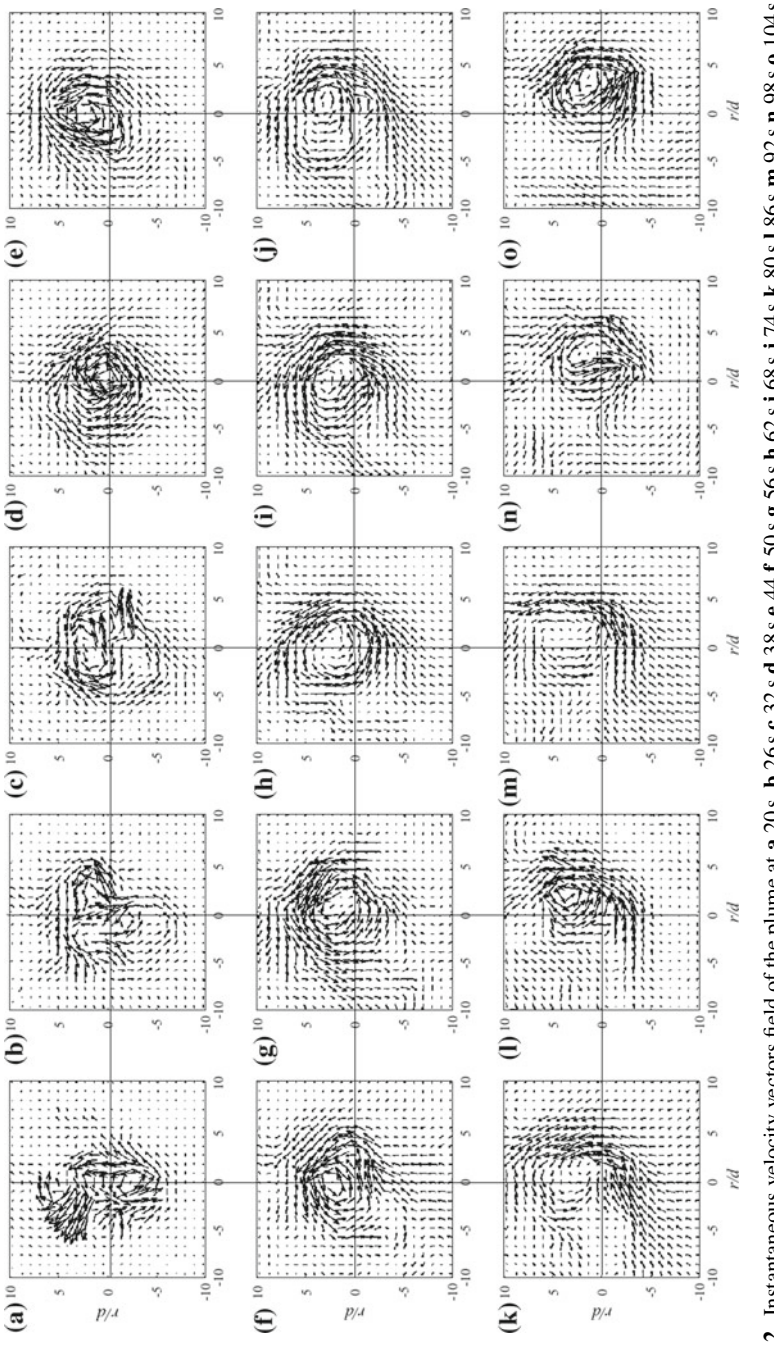

Fig. 2 Instantaneous velocity vectors field of the plume at **a** 20 s, **b** 26 s **c** 32 s **d** 38 s **e** 44 **f** 50 s **g** 56 s **h** 62 s **i** 68 s **j** 74 s **k** 80 s **l** 86 s **m** 92 s **n** 98 s **o** 104 s for a plume with $Re_0 = 1800$, at $\Omega_0 = 0.52\,\mathrm{rad\,s^{-1}}$, for $z/d = 10$

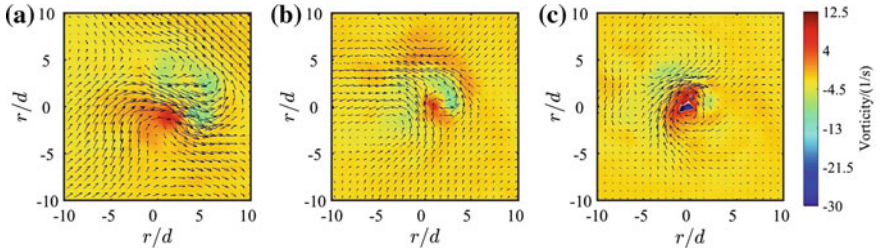

Fig. 3 Velocity vectors and vorticity field of **a** first, **b** second and **c** third POD mode for a plume with $Re_0 = 1800$, at $\Omega = 0.21\,\text{rad s}^{-1}$, for $z/d = 10$

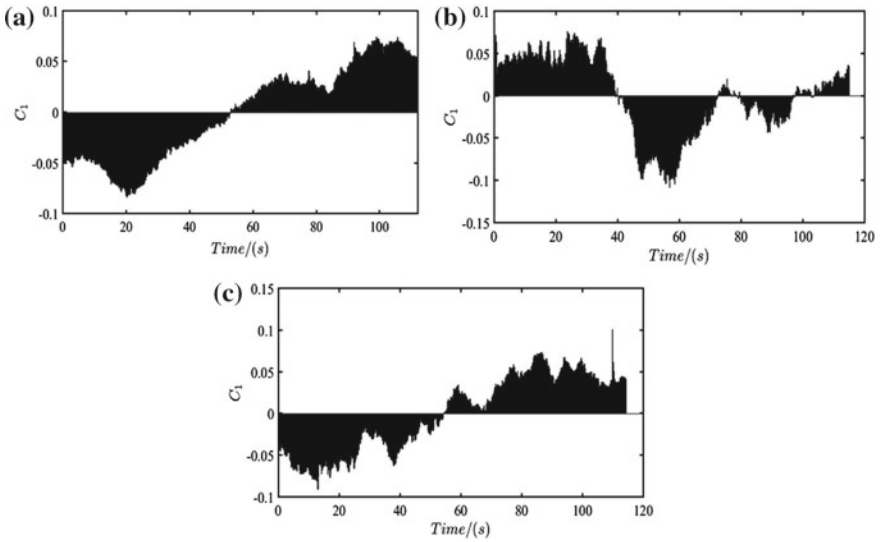

Fig. 4 The time characteristics of the first POD mode: **a** $\Omega = 0.21\,\text{rad s}^{-1}$, **b** $\Omega_0 = 0.31\,\text{rad s}^{-1}$ and **c** $\Omega = 0.42\,\text{rad s}^{-1}$ POD mode for a plume with $Re_0 = 1800$, at $z/d = 10$

In each one of Fig. 2a–o the superposed crosshair-style lines identify the center of the source at distance $z/d = 10$ below the measurement location. These lines serve to provide a clear visualisation of the movement of the centre of the vortex with respect to the centre of the source. An inspection of the series of figures reveals that the centre of the vortex, that is the centre of the plume, precesses anticyclonically around the centre of the source.

Figure 3a, b show the first three POD modes of a plume subject to background rotation of $\Omega = 0.21\,\text{rad s}^{-1}$. The velocity vector arrangement of the three POD modes represent two counter rotating vortices. The background of the three figures shows the corresponding vorticity. Moreover Fig. 4 shows the time characteristics associate with the first POD mode for three different rotation rates as identified in the caption. The temporal variation of the time coefficient(C_1) of the first POD mode

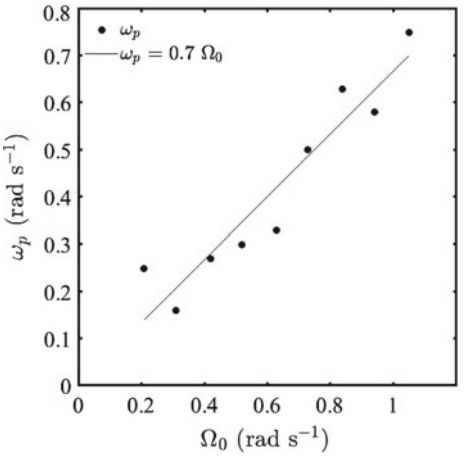

Fig. 5 Variation of plume precession frequency(ω_p) with the rotational velocity of the turntable (Ω_0)

displays a non-stationary behaviour for each one of the three rotation rates. Therefore the Fourier transform was not used for analysing these data. The time characteristics were subjected to Hilbert-Huang transformation and instantaneous frequencies were obtained. Then the mean frequency was calculated and identified as the precession frequency at the respective background rotation rate.
Figure 5 displays the dependence of the precession rate of the plume as a function of the rotational velocity Ω_0 of the turntable. A linear least-squares fit to the measured data yields $\omega_p \approx 0.7\Omega_0$ and is identified in Fig. 5 by the solid line interpolating the data points.

4 Summary and Conclusions

Results from series of PIV experiments investigating plumes subject to different levels of background rotation rates were presented. The PIV measurements were conducted at the cross section of the plume at height $z/d = 10$ above the source for nine different background rotation rates. The velocity fields obtained from the PIV measurements were subjected to POD analysis. It was found that the first POD mode, for all background rotation rates, displays two counter rotating vortices. The time characteristics of the first POD mode was further subjected to a Hilbert-Huang transformation which yielded the precession frequency of the plume around axis of rotation. This frequency was found to increase with the background rotation. Figure 6 shows the variation of the precession rate with the background rotation for plumes for nine different experimental data sets by Frank et al. [3]. The nine different data series shown in the figure are for nine different Rossby number ranges. The least square fit shown by green line suggests $\omega_p \approx 0.4\Omega_0$. Further Frank et al. [3] considered pure

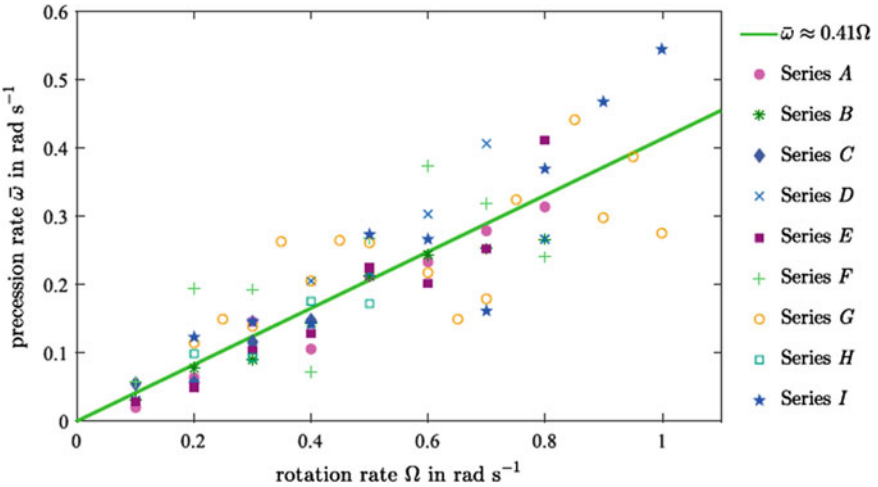

Fig. 6 Mean plume precession frequency $\overline{\omega}$ as a function of the rotation rate of the environment Ω by Frank et al. [3]

plumes($\Gamma \approx 1$). But the plume that we considered in our study is a forced plume for which $\Gamma \approx 0.03$. Therefore in summary it can be concluded that even with a initial momentum at the source plumes do precess around the axis of background rotation.

References

1. Deremble, B.: Convective plumes in rotating systems. J. Fluid Mech. **799**, 27–55 (2016)
2. Fernando, H.J.S., Chen, R.R., Ayotte, B.A.: Development of a point plume in the presence of background rotation. Phys. Fluids **10**, 2369–2383 (1998)
3. Frank, D., Landel, J., Dalziel, S., Linden, P.: Anticyclonic precession of a plume in a rotating environment. Geophys. Res. Lett. **44**(18), 9400–9407 (2017)
4. John, W.M.B., Andrew, W.W.: Experiments on buoyant plumes in a rotating channel. Geophys. Astrophys. Fluid Dyn. **89**(1–2), 1–22 (1998)
5. Lavelle, J.W., Smith, D.C.: Effects of rotation on convective plumes from line segment sources. J. Phys. Oceanogr. **26**, 863–872 (1996)
6. Tomàs, A.F., Poje, A.C., Özgökmen, T.M., Devar, W.K.: Effects of rotation on turbulent buoyant plumes in stratified environments. J. Geophys. Res. **121**, 5397–5417 (2016)

Flow Structures and Scale Interactions in Stable Atmospheric Boundary Layer Turbulence

Nikki Vercauteren and Danijel Belušić

Abstract Atmospheric boundary layer turbulence in stably stratified conditions is characterised by an intermittent, unsteady behaviour. The intermittency can result from localised flow acceleration due to non-turbulent motions, which can exhibit structures such as ramp-cliff convective patterns, waves or microfronts. Based on a timeseries clustering method, we characterise interactions between scales of motion in a dataset of near-surface stable boundary layer turbulence. Individual flow structures are investigated in two weak-wind flow regimes exhibiting distinct scale interaction properties. The signature of flow structures differs despite comparable wind and stability properties.

1 Introduction

Turbulent flows can become globally intermittent in cases of strongly stable density stratification. In this context, turbulence is observed to cease partially and localized turbulent patches on scales that are large compared to the main eddy size occur within otherwise quiet flow [8]. Within such a globally intermittent flow, the spatio-temporal patterns of mixing events are modulated by increased shear due to larger scale flow structures which lack the universal character of the inertial range [1, 2]. In the case of atmospheric turbulence, the increased shear can be the result of external perturbations due to nonstationary wind accelerations on the so-called submeso-scales (scales between the largest turbulent eddies and the smallest mesoscale motions traditionally specified at 2 km). These submeso motions have been shown to exhibit structures such as ramp-cliff convective patterns, waves or microfronts but are generally

N. Vercauteren (✉)
Department of Mathematics and Computer Sciences, Freie Universität Berlin, Arnimallee 6, 14195 Berlin, Germany
e-mail: nikki.vercauteren@fu-berlin.de

D. Belušić
Swedish Meteorological and Hydrological Institute (SMHI), 601 76 Norrkping, Sweden
e-mail: danijel.belusic@smhi.se

M. Gorokhovski and F. S. Godeferd (eds.), *Turbulent Cascades II*,
ERCOFTAC Series 26, https://doi.org/10.1007/978-3-030-12547-9_29

unknown [7]. There are ongoing challenges to represent strongly stable conditions in atmospheric models; progress in the characterisation of submeso motions, along with a characterisation of their effect on turbulence, can be a step to inform model improvement.

The goal of our study is to apply a combination of methods originating from non-stationary timeseries analysis in order to gain insights on the non-stationary enhancement mechanism of intermittent turbulence in the stable atmospheric boundary layer (SBL). We want to extract ubiquitous flow structures, or events, in the SnoHATS dataset of near-surface atmospheric turbulence [3]. The SnoHATS dataset was collected over the Plaine Morte glacier in Switzerland and includes long periods of stable stratification, with several periods of very stable stratification. Several methods were previously applied to this dataset in order to analyse flow regimes, and the activity of different scales of motion in the different regimes [12, 13]. In [9], a statistical indicator that quantifies the dynamical (in)stability of timeseries, provided evidence that flow regimes under the influence of submeso motions are dynamically unstable and require higher order closure models to reflect non-local scale interactions.

In the present contribution, we relate two flow regimes characterised by very stable stratification but different scales activity to a signature of flow structures thought to be submeso motions.

2 Scale Interactions

Periods of influence of non-turbulent scales of motion on the time evolution of the turbulent vertical velocity variance are detected based on a statistical clustering methodology. The procedure is based on a finite element, bounded variation, vector autoregressive factor method (FEM-BV-VARX) introduced by Horenko [5] which allows to cluster timeseries according to dynamical properties and to detect regime modulation by external variables. The turbulent timeseries analysed here are the vertical velocity fluctuations on scales faster than 1 min, which is fast enough to minimise contamination by non-turbulent motions [13]. The influence of the horizontal wind velocity, filtered to extract contributions on scales ranging from 1 to 30 minutes, is considered by defining it as the external factor in the statistical VARX models. Those scales are denoted as sub-mesoscales and correspond in large part to non-turbulent fluctuations [13]. Vercauteren and Klein [12] showed that modulation of the turbulence by sub-mesoscale motions differs in different flow regimes corresponding to weakly and strongly stable, and that the algorithmic procedure was able to separate the flow regimes automatically. The reader is referred to [12] for further details on the clustering of the turbulent flow regimes.

The multiple resolution decomposition (MRD, [14]) is a wavelet filtering method that allows to analyse the dynamical activity of different scales of motion. MRD cospectra can be used to assess the amount of flux that is due to eddies of a certain size, thereby providing a method to identify a cospectral gap scale. The gap is usually identified as the scale at which the flux crosses the zero-line and indicates the

appropriate averaging period needed to separate contributions of non-turbulent sub-mesoscales of motion from turbulent flux. In an extended MRD methodology [10], the relative contributions to the flux variability of the horizontal and vertical wind velocity fluctuations on different pairs of scales can be quantified. Detailed analyses of the scale dependent dynamical activity in distinct flow regimes of the SnoHATS dataset are presented in [13]. In the present work we focus on two different regimes of very stable flows, which were found to be influenced by submeso motions in [12]. Those will be denoted as regime 2 and regime 4 in order to follow numbering used in [12]. Our goal in this study is to identify flow structures in each regime to analyse if the differences in scales and turbulence dynamics relates to different signatures of submeso motions. The results on the dynamics activity of different scales of motion, which were presented in [13], are summarised here for the two strongly stable flow regimes under investigation.

The scales activity is shown in Fig. 1 for regime 2, and in Fig. 2 for regime 4, based on MRD analyses. MRD cospectra and extended cospectra are calculated on periods of 30 minutes, and results are shown for the median (heat flux cospectra) resp. average (extended cospectra) over all periods within the given flow regime. In both regimes, the variability of larger horizontal scales relates to smaller vertical scales (middle panels, Figs. 1 and 2). The right panels show the joint variability of the scale-wise horizontal velocity fluctuations and of the vertical velocity variance. The strongest joint variability appears for large horizontal scales and simultaneous small vertical scales, in agreement with the hypothesis that sub-mesoscales motions modulate turbulent fluxes. The submeso-influenced regimes 2 and 4 however differ in their scale characteristics. Indeed, regime 2 (Fig. 1) shows very little turbulent fluctuations while showing more fluctuations in the submeso scales, suggesting the presence of a scale gap between turbulence and submeso scales. In regime 4 (Fig. 2), the variability is continuously spread between turbulent and larger scales.

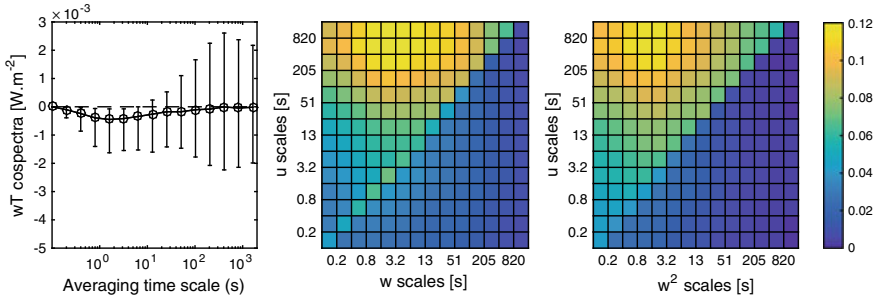

Fig. 1 Heat flux MRD cospectra (left panel) and extended MRD showing the standard deviations (std) of the streamwise u and vertical w wind velocity components (middle panel), resp. w^2 (right panel) on all pairs of scales, normalized by the total std of $u'w'$. Left panel: median over all 30-min periods within flow regime 2, with 0.1 and 0.9 quantiles as errorbars. Middle and right panels: average over all 30-min periods in regime 2. Adapted from [13]

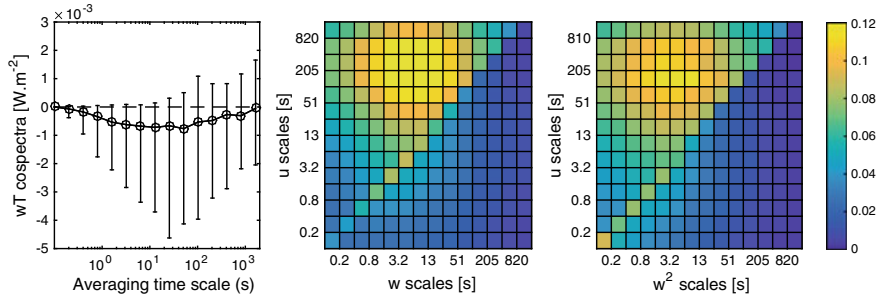

Fig. 2 Heat flux MRD cospectra (left panel) and extended MRD showing the standard deviations (std) of the streamwise u and vertical w wind velocity components (middle panel), resp. w^2 (right panel) on all pairs of scales, normalized by the total std of $u'w'$. Left panel: median over all 30-min periods within flow regime 2, with 0.1 and 0.9 quantiles as errorbars. Middle and right panels: average over all 30-min periods in regime 2. Adapted from [13]

3 Turbulent Event Detection

The present contribution aims at characterizing submeso motions which are present in the two introduced very stable flow regimes. The timeseries analysis methodology for turbulent event detection (TED) derived by Kang et al. [6] aims at identifying non-stationary events or flow patterns in noisy timeseries. Instead of detecting signatures of known flow patterns in timeseries, the TED method detects flow structures as events that are significantly different from noise, assuming that the typical duration of events is know a priori. In the context of timeseries resulting from turbulent quantities, the noise is taken as white and red noise. Indeed, statistical descriptions of turbulence lead to the formulation of stochastic models for the turbulent observables such that in the inertial subrange, Lagrangian velocities can be modeled by a Langevin equation (or Ornstein–Uhlenbeck process) with suitable drift and noise terms [11]:

$$du = -\frac{u}{T_L}dt + \sqrt{C_0\varepsilon}dW, \tag{1}$$

where u is the velocity (or a turbulent observable), T_L is the Lagrangian decorrelation timescale, C_0 is a universal constant and ε is the the mean dissipation; dW are increments of a Wiener process. As shown in Faranda et al. [4], this model is in fact equivalent to an autoregressive process of order one or AR(1) process (also known as red noise):

$$u_t = \phi u_{t-1} + \psi_t, \tag{2}$$

where t is a discrete time label, and $\phi = \left(1 - \frac{\Delta t}{T_L}\right)$ and ψ_t are independent variables being normally distributed. In the SBL, gravity waves, transient drainage flows and other flow structures on submeso scales will typically superimpose on the turbulence or affect its intensity, thereby inducing non-stationarity and hence departures from

the idealized inertial subrange Langevin model Eq. 1 or AR(1) model Eq. 2. This is the core idea of the TED method: sequential subsequences of the timeseries $x(t)$ of turbulent observables are analysed using a sliding window of predefined length-scale l. Events are defined as subsequences that are significantly different from white noise or from an AR(1) process. In practice, an AR(1) model is fitted to each detrended subsequence $x_q(t) = \left[x(t_q), \ldots, x(t_{q+l-1})\right]$ and a test is performed on the model residuals to see whether they are uncorrelated. If this is not the case (i.e. if the residuals are not white noise), then $x_q(t)$ is defined as a potential event. Additionally, non-stationary subsequences that exhibit a structural break are considered as potential events.

The TED method is applied to 6 s averaged temperature measurements from both flow regimes. The choice of scale for the block averages of the turbulent observables will define the time increments of the AR(1) model in Eq. 2. Hence the averaging scale should be chosen such that the increments fall within the range of scales of inertial turbulence. As shown by the extended MRD analyses, scales faster than approximately 5–10 s exhibit fluctuations characteristic of isotropic turbulence and block averaging within this time range represents an appropriate choice. An example of temperature timeseries detected as an event is shown in Fig. 3. The trajectories are shown for the corresponding event, where the temperature is shown in colour. We observe a clear structure in the event. Comparison with periods not detected as event by the TED method showed absence of structures (not shown).

Statistics of the main physical characteristics of the identified events are shown in Fig. 4, conditionally on the flow regime affiliation (i.e. for regime 2 and regime 4 separately). The median and quartiles of the mean wind speed and bulk Richardson number are shown as an indicator of the wind and stability conditions during the

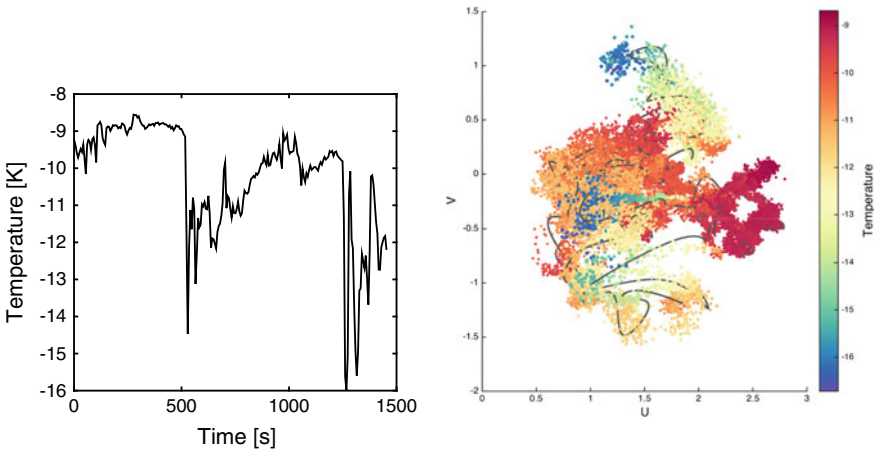

Fig. 3 Timeseries of temperature detected as an event (left) and corresponding phase space visualisation of the event (right), where the axis show the streamwise and cross-stream wind coordinates, and the temperature is shown in colour

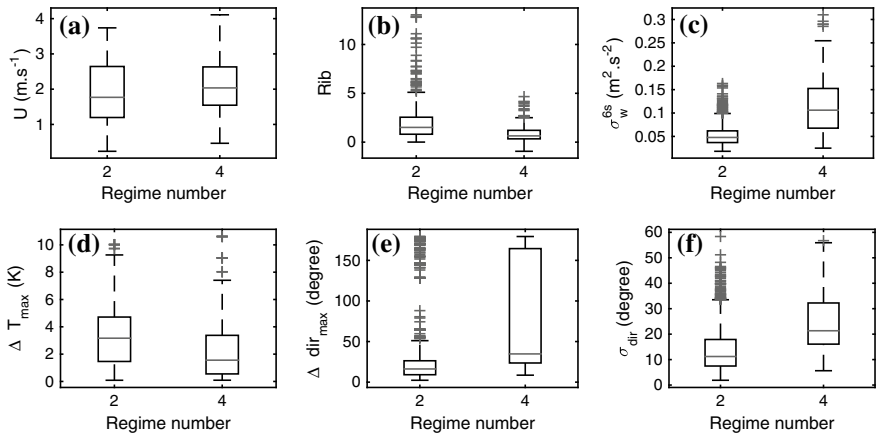

Fig. 4 Boxplots of main physical characteristics for events in the two different flow regimes. **a** Wind speed, **b** bulk Ri number, **c** vertical velocity variance $\left(\overline{(w'w')}_{6s}\right)$, **d** largest temperature change, **e** largest wind direction change and **f** standard deviation of the wind direction

events. Events in regime 2 occur with slightly lower wind speed, and slightly higher bulk Ri number. The vertical velocity variance (based on the 6 s averaging windows), the largest temperature change within one event, the maximal wind direction change, and the standard deviation of the wind direction, highlight that events occurring in regime 2 and in regime 4 have a different signature.

The largest difference appears in the wind direction behaviour during events: events in regime 2 have very little wind direction variability while those in regime 4 have a very large wind direction variability. On the contrary, events in regime 2 have larger temperature changes than in regime 4. Note that the events are detected based solely on the temperature timeseries, without considering information on the wind direction. Events in regime 2 are associated with very little vertical velocity fluctuations, while those in regime 4 have larger vertical velocity fluctuations.

4 Conclusions

The submeso-influenced flow regimes analysed here differ in their scale characteristics. Indeed, regime 2 exhibits a scale gap, whereas turbulent and submeso scales overlap in regime 4. The results in Fig. 4 show that non-stationary events in regime 2, where the scale of events is significantly larger than the turbulent scales do not appear to trigger much turbulent mixing. From the observed signature of the type of events in this regime (temperature changes with little wind direction variability), we hypothesise that advected air masses or density currents that tend to take a microfront structure, while enhancing shear locally, may only trigger little turbulence on small

scales. On the contrary, the wind-direction variability characteristics of events in regime 4, with its scale overlap, lead us to hypothesise that this regime encompasses wave-like phenomena that may break down to turbulence through a cascade of scales.

Acknowledgements This research has been supported by Deutsche Forschungsgemeinschaft (DFG) through grant number VE 933/2-1, and through the CRC1114 "Scaling Cascades in Complex Systems", project B07.

References

1. Ansorge, C., Mellado, J.P.: Global intermittency and collapsing turbulence in the stratified planetary boundary layer. Bound.-Layer Meteorol. **153**(1), 89–116 (2014)
2. Ansorge, C., Mellado, J.P.: Analyses of external and global intermittency in the logarithmic layer of Ekman flow. J. Fluid Mech. **805**, 611–635 (2016)
3. Bou-Zeid, E., Higgins, C.W., Huwald, H., Meneveau, C., Parlange, M.: Field study of the dynamics and modelling of subgrid-scale turbulence in a stable atmospheric surface layer over a glacier. J. Fluid Mech. **665**, 480–515 (2010)
4. Faranda, D., Pons, F.M.E., Dubrulle, B., Daviaud, F., Saint-Michel, B., Herbert, É., Cortet, P.-P.: Modelling and analysis of turbulent datasets using ARMA processes. Phys. Fluids (1994-present) **26**(10), 105101 (2014)
5. Horenko, I.: On the identification of nonstationary factor models and their application to atmospheric data analysis. J. Atmos. Sci. **67**(5), 1559–1574 (2010)
6. Kang, Y., Belušić, D., Smith-Miles, K.: Detecting and classifying events in noisy time series. J. Atmos. Sci. **71**(3), 1090–1104 (2014)
7. Kang, Y., Belušić, D., Smith-Miles, K.: Classes of structures in the stable atmospheric boundary layer. Q. J. R. Meteorol. Soc. **141**(691), 2057–2069 (2015)
8. Mahrt, L.: Stably stratified atmospheric boundary layers. Annu. Rev. Fluid Mech. **46**, 23–45 (2014)
9. Nevo, G., Vercauteren, N., Kaiser, A., Dubrulle, B., Faranda, D.: Statistical-mechanical approach to study the hydrodynamic stability of the stably stratified atmospheric boundary layer. Phys. Rev. Fluids **2**(8), 084603 (2017)
10. Nilsson, E.O., Sahlée, E., Rutgersson, A.: Turbulent momentum flux characterization using extended multiresolution analysis. Q. J. R. Meteorol. Soc. **140**, 1715–1728 (2014)
11. Thomson, D.J.: Criteria for the selection of stochastic models of particle trajectories in turbulent flows. J. Fluid Mech. **180**(1), 529–556 (1987)
12. Vercauteren, N., Klein, R.: A clustering method to characterize intermittent bursts of turbulence and interaction with submesomotions in the stable boundary layer. J. Atmos. Sci. **72**(4), 1504–1517 (2015)
13. Vercauteren, N., Mahrt, L., Klein, R.: Investigation of interactions between scales of motion in the stable boundary layer. Q. J. R. Meteorol. Soc. **142**(699), 2424–2433 (2016)
14. Vickers, D., Mahrt, L.: The cospectral gap and turbulent flux calculations. J. Atmos. Ocean. Technol. **20**(5), 660–672 (2003)

Approximating Turbulent and Non-turbulent Events with the Tensor Train Decomposition Method

Thomas von Larcher and Rupert Klein

Abstract Low-rank multilevel approximation methods are often suited to attack high-dimensional problems successfully and they allow very compact representation of large data sets. Specifically, hierarchical tensor product decomposition methods, e.g., the Tree-Tucker format and the Tensor Train format emerge as a promising approach for application to data that are concerned with cascade-of-scales problems as, e.g., in turbulent fluid dynamics. Beyond multilinear mathematics, those tensor formats are also successfully applied in e.g., physics or chemistry, where they are used in many body problems and quantum states. Here, we focus on two particular objectives, that is, we aim at capturing self-similar structures that might be hidden in the data and we present the reconstruction capabilities of the Tensor Train decomposition method tested with 3D channel turbulence flow data.

1 Introduction

In recent research on multiscale problems low-rank multilevel approximation methods are found to attack high-dimensional problems successfully and they offer opportunities for compact representation of large data sets [3, 11]. Specifically, hierarchical tensor product decomposition methods such as the Tree-Tucker format [4], and the Tensor Train format [5, 13], are promising approaches for application to data that are concerned with cascade-of-scales problems, for instance in turbulent fluid dynamics. Beyond multilinear mathematics, those tensor formats are also successfully applied in e.g., physics or chemistry, where they are used in many body problems and quantum states.

T. von Larcher (✉)
Berlin, Germany
e-mail: thomas.vonlarcher@web.de

R. Klein
Institute of Mathematics, Freie Universität Berlin, Waterloostraat 103A,
3062TJ Rotterdam, The Netherlands
e-mail: rupert.klein@math.fu-berlin.de

M. Gorokhovski and F. S. Godeferd (eds.), *Turbulent Cascades II*,
ERCOFTAC Series 26, https://doi.org/10.1007/978-3-030-12547-9_30

Tensors are multidimensional arrays or mathematically more precisely polylinear formats. For example, vectors are tensors of order $d = 1$, and tensors of order 3 or higher are generally denoted as higher-order tensors. Clearly, the storage requirement of a tensor depends on its order and on the mode sizes, that is, on the number of entries, n, per dimension. A d-dimensional tensor with mode sizes n results in a storage requirement of n^d. Thus, in high dimensional problems or in so-called big data applications one has to deal with a massive storage requirement. Tensor product decomposition methods, first mentioned by Hitchcock (1927) [6], were developed to overcome that *curse of dimensionality*.

Here, we test the capabilities of the Tensor Train decomposition to both, numerically computed and experimentally measured flow profile data. We aim at capturing coherent structures and self-similar patterns that might be hidden in the data, cf. [10]. Our study is concerned with the question of whether Tensor decomposition methods can support the development of improved understanding and quantitative characterisation of multiscale behavior of turbulent flows, cf. e.g. [14]. Results of tests using synthetic data to evaluate the suitability of the method to generally detect self-similar patterns are published in [17].

2 Tensor Product Decomposition Method

The Tensor Train format is a hierarchical tensor format and a specific branch of the hierarchical Tucker format. It is mainly based on the key idea to transform higher order tensors into tensors of order 2 (matrices) that then allow for the application of the matrix singular value decomposition (SVD). Generally, SVD of a matrix $\mathsf{A} \in \mathbb{R}^{m\times n}$ is written as $\mathsf{A} = \mathsf{U}\Sigma\mathsf{V}^{\mathsf{T}}$, where $\mathsf{U} \in \mathbb{R}^{m\times m}$ and $\mathsf{V} \in \mathbb{R}^{n\times n}$. The matrix Σ contains the singular values, σ_i, on its diagonal, $\Sigma = diag(\sigma_1, \ldots, \sigma_{min(m,n)}) \in \mathbb{R}^{m\times n}$, with $\sigma_1 \geq \sigma_2 \geq \sigma_{min(m,n)} \geq 0$. The number of singular values unequal 0 defines the rank r of the matrix A: $rank(A) = r$. SVD often enables compact representation by truncating $\mathsf{U}, \Sigma, \mathsf{V}$ with respect to rank r, i.e., the size of the matrices is truncated with respect to the singular values unequal 0.

Tensor Train decomposition makes use of the compact SVD in successive steps. Figure 1 shows a sketch of the step-by-step procedure that we apply here to transform a Tensor (of dimension 4 in this example) into the Tensor Train format. In the first step, the input Tensor, $\mathsf{A}(n_1, n_2, n_3, n_4)$, is reshaped into a 2-dimensional $n_1 \times (n_2 n_3 n_4)$ matrix A_1 to which a compact SVD is applied, that is, a parameter r (so-called TT-rank) is set which compresses the size of the matrices. The factor matrix $\mathsf{U}_1 \in \mathbb{R}^{n_1\times r_1}$, so-called first core, is stored and the remaining part $\Sigma_1 V_1^{\mathrm{T}} = \mathsf{A}_2 \in \mathbb{R}^{r_1\times n_2 n_3 n_4}$ is used for the second step. In the second step, A_2 is reshaped into a $r_1 n_2 \times n_3 n_4$ matrix to which again a SVD is applied leading to the second core $\mathsf{U}_2 \in \mathbb{R}^{r_1 n_2\times r_2}$. Finally, the

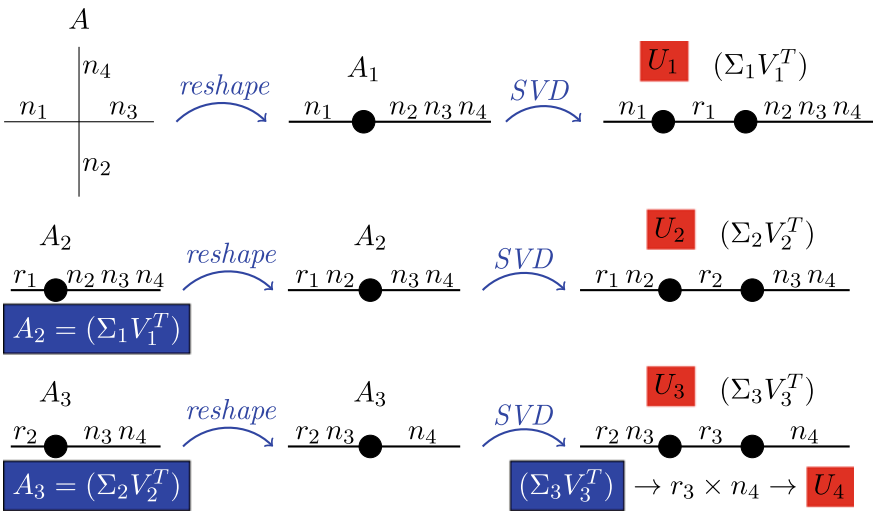

Fig. 1 Scheme of the tensor train decomposition. Note that $r_1 = r_2 = r_3$

step-by-step procedure gives 4 cores $\mathsf{U}_1, \ldots, \mathsf{U}_4$ that are used for writing the Tensor A in the Tensor Train format

$$\mathsf{A}(n_1, n_2, n_3, n_4) = \sum_{k_1=1}^{r_1} \sum_{k_2=1}^{r_2} \sum_{k_3=1}^{r_3} U_1(n_1, k_1)\, U_2(k_1, n_2, k_2)\, U_3(k_2, n_3, k_3)\, U_4(k_3, n_4). \tag{1}$$

Note, that the core tensors are linked by the TT-rank r which is kept fix in all steps of the step-by-step procedure. The cores are tensors of order 3 except the first and the last core which are of order 2.

3 Results

We begin this section with an exemplary demonstration of the Tensor Train decomposition method, that is, we apply it to numerically computed data of a Taylor-Green Vortex flow. Then, we show results of application to in-situ data of the atmospheric stable boundary layer. Finally, we analyse data of a direct numerical simulation (DNS) of a channel turbulence flow.

We write the relative error between the original data Tensor and the approximated Tensor in the Frobenius norm that reads

$$||\mathsf{A}|| = \sqrt{\sum_{n_1=1}^{N_1} \sum_{n_2=1}^{N_2} \cdots \sum_{n_d=1}^{N_d} x^2_{n_1 \cdots n_d}}, \tag{2}$$

where A is a d-dimensional Tensor with entries $n_1, \ldots, n_d$. Then, the relative error reads

$$e = \frac{||(\mathsf{Y} - \mathsf{A})||}{||\mathsf{A}||}, \tag{3}$$

with Y as approximation of A.

3.1 Taylor-Green Vortex

In computational fluid dynamics, Taylor-Green Vortex flow is a classical test bed for at least two reasons. First, it is computed using a fully periodic box with analytical initial conditions. Second, depending on the Reynolds number, it shows a transition from laminar flow to a fully turbulent state and homogeneous, isotropic decay of turbulence with fully developed inertial range.

Here, we use data of a 3D direct numerical simulation; data courtesy of G. Gassner (University of Cologne, Germany). The Reynolds number is $Re = 800$ and the grid size $256 \times 256 \times 256$ in (x, y, z). To demonstrate the capabilities of the Tensor Train approximation, we extract a 2D (x, y) horizontal slice at height $z = 10$. The snapshot is taken at $t = 12$ s; at this time step the flow state shows a mirror symmetric profile in $x-$ and $y-$axis relation (Fig. 2, left panel). We make use of the mirror symmetry and reshape the 2D data set into a Tensor T of order 4, i.e., $\mathsf{T}[2, 128, 2, 128]$. The Tensor Train decomposition is then applied to this input Tensor.

Figures 2 and 3 show results of the approximation of the input Tensor T at various TT-ranks. Already at TT-rank 6 we find a remarkable low relative error ($e \approx 0.02\%$) and the compression factor is about 27 (storage requirement 2382 compared to 65,536 of the original 2D snapshot). At higher ranks also the small-scale structures are getting well resolved, linked with an increase of the storage requirement.

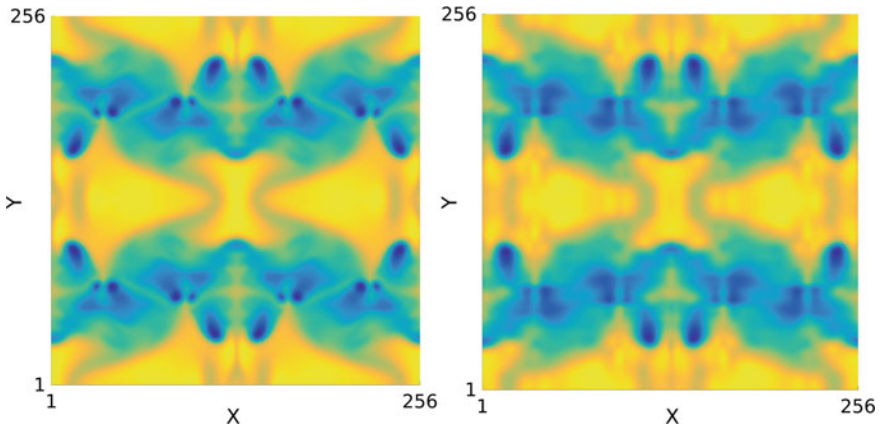

Fig. 2 TGV. Left: (x, y)-slice at height $z = 10$. Snapshot is taken at $t = 12$ s. Right: approximation at TT-rank 6

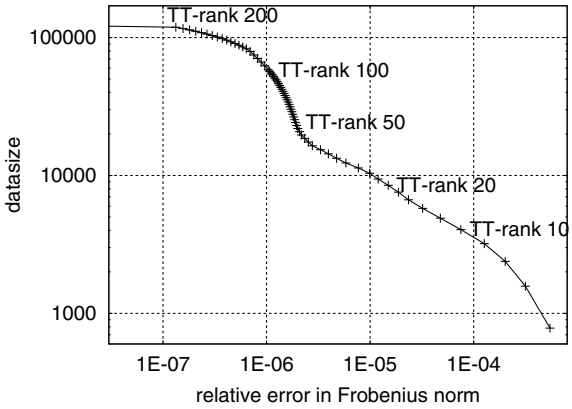

Fig. 3 TGV. Log-log plot of storage requirement against relative error for various TT-ranks. Note that the increment is 2 up to TT-rank 100 and 5 up to 200

3.2 Atmospheric Stable Boundary Layer

During the Snow-Horizontal Array Turbulence Study (SnoHATS) at the Plaine Morte Glacier in the Swiss Alps [1, 12] time series of velocity and temperature data were measured in the atmospheric stable boundary layer (SBL). Analysis of SBL turbulence data [16], shows that data can be clustered according to different interactions of submesoscale wind velocity and vertical velocity fluctuations.

Here, we apply the Tensor Train decomposition to a time series of temperature data of cluster 4 as described in [16]; data courtesy of N. Vercauteren (Freie Universitaet Berlin, Germany). We limit the scalar data series to $2^{18} = 262{,}144$ entries and reshape it into a Tensor of dimension 18, i.e., each dimension has 2 entries. Thus, we ignore any a priori knowledge about the physics hidden in the data that has been described in [16]. Applying the Tensor Train decomposition with a given TT-rank 2 approximates the data series with a relative error of 20.0%, and the storage requirement in the Tensor Train format is 138 which corresponds to a compression factor of about

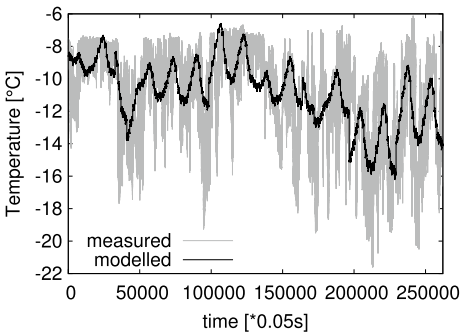

Fig. 4 SBL. Time series of measured temperature data from cluster 4 (gray) in [16] and approximated data modelled with TT-rank 2 (black)

1900. Interestingly, reconstruction of the data series at TT-rank 2 reveals a periodic signal with a cycle length of about 819 s, see Fig. 4. This value is in good agreement with the results of [16] who found both, turbulence motion and wave activity in the cluster under consideration.

3.3 Application to Channel Turbulence Flow

Finally, we consider a fully turbulent 3D channel flow generated in a numerical study by [15]; data courtesy of M. Uhlmann (Karlsruhe Institute of Technology, Germany). The grid size is $600 \times 352 \times 600$ in (x, y, z), the friction-based Reynolds number is $Re_\tau = 590$. We focus on data of vorticity magnitude calculated from the DNS velocity data as turbulence is heavily linked with vorticity.

The Q-criterion [8, 9], a scalar quantity defined to identify vortex (coherent) structures within turbulent flows, represents the balance of shear strain rate and vorticity magnitude. Figure 5 shows iso-surfaces of the Q-criterion. Various vortex tubes of different size and shape, stretched and rotated, can be identified indicating the highly turbulent regime.

To capture the broad range of space scales, the vorticity field is reshaped into its prime factors. Thus, the input Tensor to which the Tensor Train decomposition is applied is of order 18

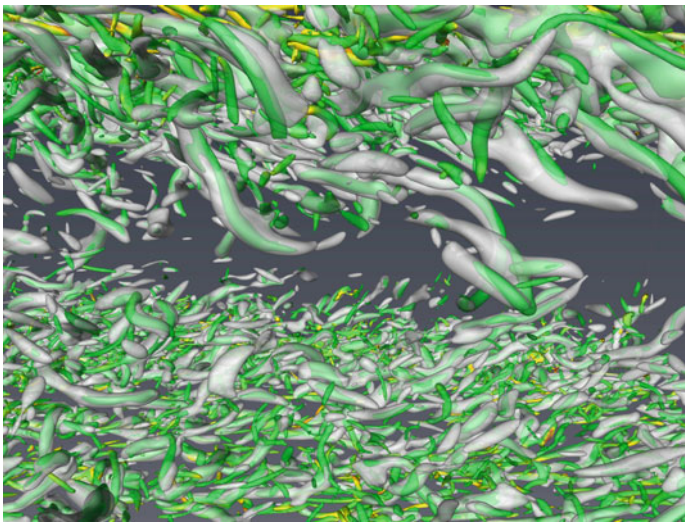

Fig. 5 Channel turbulence flow. Iso-surfaces of the Q-criterion. Colored surfaces represent unfiltered data of $Q = 9$. Gray surfaces (large tubes) represents data of $Q = 2$ filtered with a box-filter of size 10. Colors represents the angle α of vorticity between the unfiltered and the filtered data set, green is $\alpha = 0°$, yellow is $\alpha = 90°$, and red is $\alpha = 180°$, cf. [2]

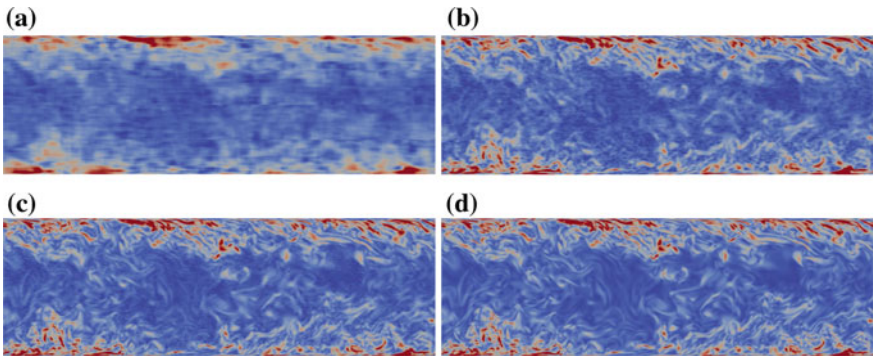

Fig. 6 Channel turbulence flow. (x, y)-slice at z = 300 (mid-channel) of approximated vorticity data. **a** for TT-rank 100 ($e \approx 0.42$), **b** for TT-rank 500 ($e \approx 0.21$), **c** for TT-rank 1000 ($e \approx 0.12$), **d** original data. Note that the colorbar scale is the same for all panels, that is, it is a linear scale from 0 (blue) to 8 (red)

$$\mathsf{T}[n_1, \ldots, n_{18}] = \mathsf{T}[2, 2, 2, 2, 3, 5, 5, 2, 2, 2, 2, 2, 11, 2, 2, 2, 2, 3, 5, 5]. \quad (4)$$

Figure 6 shows (x, y)-slices of the resulting approximated data at various TT-ranks. Qualitatively, the trend of a decrease in the relative error and accompanying increase in the TT-rank is similar to our finding for the TGV flow. However, we find a large relative error at small TT-ranks ($e \approx 0.42$ at rank 100) and the error is still relative large at larger TT-ranks ($e \approx 0.12$ at rank 1000). This is reasonable as vorticity dominates at small scales that are approximated at higher but not at lower TT-ranks. As observed in the previous tests, approximation at low TT-ranks averages also the turbulent vorticity field.

4 Conclusion

In this study, we apply the Tensor Train decomposition method to flow profiles of computational and experimental fluid dynamics. We found the Tensor Train format to be an efficient method to compress big data. The occurrence of (self-)similar structures results in low relative errors at low TT-ranks. Especially, for low-rank approximation of the data the Tensor Train format acts similar to an average filter as the approximated data represent a smooth version of the original profiles. In particular, analysis of the atmospheric SBL data set uncovers a periodic signal that is hidden in the data.

The present results are very promising. In future work, we will apply different multiscale and advanced data analysis methods such as, e.g., shearlets, wavelets, and turbulent event detection methods to detect self-similar structures that might emerge repeatedly in time on different spatial scales.

Acknowledgements This research has been funded by Deutsche Forschungsgemeinschaft (DFG) through grant CRC 1114 'Scaling Cascades in Complex Systems', Project B04 'Multiscale Tensor decomposition methods for partial differential equations'. The authors thank Prof. Illia Horenko (CRC 1114 Mercator Fellow) as well as Prof. Reinhold Schneider and Prof. Harry Yserentant for rich discussions and for steady support. Data analysis was conducted using the Tensor library *xerus* developed by Huber and Wolf [7]. The channel turbulence data were generated and processed using resources of the North-German Supercomputing Alliance (HLRN), Germany, and of the Department of Mathematics and Computer Science, Freie Universität Berlin, Germany. The authors thank Raphael Badel and Christian Hege (both at Zuse Institute Berlin, Germany) for steady support in data processing and data visualisation.

References

1. Bou-Zeid, E., Higgins, C.W., Huwald, H., Meneveau, C., Parlange, M.: Field study of the dynamics and modelling of subgrid-scale turbulence in a stable atmospheric surface layer over a glacier. J. Fluid Mech. **665**, 480–515 (2010)
2. Bürger, K., et al.: Vortices within vortices: hierarchical nature of vortex tubes in turbulence (2013). arXiv:1210.3325 [physics.flu-dyn]
3. Grasedyck, L., Kressner, D., Tobler, C.: A literature survey of low-rank tensor approximation techniques. GAMM-Mitteilungen **36**, 53–78 (2013)
4. Hackbusch, W., Kühn, S.: A new scheme for the tensor representation. J. Fourier Anal. Appl. **15**, 706–722 (2009)
5. Hackbusch, W., Schneider, R.: Tensor spaces and hierarchical tensor representations. In: Dahlke, S., Dahmen, W., Griebel, M., Hackbusch, W., Ritter, K., Schneider, R., Schwab, C., Yserentant, H. (eds.) Extraction of Quantifiable Information from Complex Systems. Lecture Notes in Computational Science and Engineering, vol. 102, pp. 237–361. Springer, New York (2014)
6. Hitchcock, F.L.: The expression of a tensor or a polyadic as a sum of products. J. Math. Phys. **6**, 164–189 (1927)
7. Huber, B., Wolf, S.: Xerus—a general purpose tensor library (2014–2015). https://libxerus.org/
8. Hunt, J.C.R.: Vorticity and vortex dynamics in complex turbulent flows. Trans. Can. Soc. Mech. Eng. **11**(1), 21–35 (1987)
9. Hunt, J.C.R. Wray, A.A., Moin, P.: Eddies, streams, and convergence zones in turbulent flows. In: Proceedings of Studying Turbulence Using Numerical Simulation Databases, vol. 2, Dec 1988
10. Khujadze, G., Nguyen van yen, R., Schneider, K., Oberlack, M., Farge, M.: Coherent vorticity extraction in turbulent boundary layers using orthogonal wavelets. J. Phys. Conf. Ser. **318**(022011), 1–10 (2011)
11. Kolda, T.G., Bader, B.W.: Tensor decompositions and applications. SIAM Rev. **51**, 455–500 (2009)
12. Li, D., Bou-Zeid, E.: Coherent structures and the dissimilarity of turbulent transport of momentum and scalars in the unstable atmospheric surface layer. Bound. Layer Meteor. **140**, 243–262 (2011)
13. Oseledets, I.V., Tyrtyshnikov, E.E.: Breaking the curse of dimensionality, or how to use SVD in many dimensions. SIAM J. Sci. Comput. **31**, 3744–3759 (2009)
14. Ting, L., Klein, R., Knio, O.M.: Vortex Dominated Flows: Analysis and Computation for Multiple Scales. Series in Applied Mathematical Sciences, vol. 116. Springer, Berlin, Heidelberg, New York (2007)
15. Uhlmann, M.: Generation of a temporally well-resolved sequence of snapshots of the flow-field in turbulent plane channel flow (2000). http://www-turbul.ifh.uni-karlsruhe.de/uhlmann/reports/produce.pdf. Accessed July 2017

16. Vercauteren, N., Klein, R.: A clustering method to characterize intermittent bursts of turbulence and interaction with submeso motions in the stable boundary layer. J. Atmos. Sci. **72**, 1504–1517 (2015)
17. von Larcher, T., Klein, R.: On identification of self-similar characteristics using the tensor train decomposition method with application to channel turbulence flow. Theor. Comput. Fluid Dyn. https://doi.org/10.1007/s00162-019-00485-z (2019)

Author Index

M. Gorokhovski and F. S. Godeferd (eds.), *Turbulent Cascades II*,
ERCOFTAC Series 26, https://doi.org/10.1007/978-3-030-12547-9